Understanding density regimes and divertor detachment in ITER relevant conditions

Nicolas Rivals

Aix*Marseille université
Socialement engagée

NNT: 2023AIXM0161

THÈSE DE DOCTORAT

Soutenue à Aix-Marseille Université
le 4 mai 2023 par

Nicolas RIVALS

Understanding density regimes and divertor detachment in ITER relevant conditions

Régimes en densité et détachement dans le plasma de bord d'ITER

Discipline
Physics and Material Sciences

Spécialité
Energy, Radiation, and Plasma Physics

École doctorale
ED 352 PHYSIQUE ET SCIENCES DE LA MATIÈRE

Laboratoire/Partenaires de recherche
Institut pour la Recherche sur la Fusion par Confinement Magnétique (IRFM) - CEA Saint-Paul-lez-Durance, France

Laboratoire de la Physique des Interactions Ioniques et Moléculaires (PIIM) - AMU Marseille, France

ITER Organization Saint-Paul-lez-Durance, France

Composition du jury

Martine BAELMANS KU Leuven	Rapporteur
Detlev REITER Universität Düsseldorf	Rapporteur
Bruce LIPSCHULTZ University of York	Examinateur
Xavier BONNIN ITER Organization	Examinateur
Gwenaël FUBIANI Université Toulouse III	Examinateur
Jérôme BUCALOSSI CEA/IRFM	Président du jury
Patrick TAMAIN CEA/IRFM	Co-directeur de thèse
Yannick MARANDET Aix-Marseille Université/PIIM	Directeur de thèse
Richard A. PITTS ITER Organization	Invité

cea irfm
iter china eu india japan korea russia usa
PIIM Physique des Interactions Ioniques et Moléculaires
EUROfusion

For Aiur

Affidavit

I, undersigned, Nicolas Rivals, hereby declare that the work presented in this manuscript is my own work, carried out under the scientific direction of Yannick Marandet and Patrick Tamain, in accordance with the principles of honesty, integrity and responsibility inherent to the research mission. The research work and the writing of this manuscript have been carried out in compliance with both the french national charter for Research Integrity and the Aix-Marseille University charter on the fight against plagiarism.

This work has not been submitted previously either in this country or in aother country in the same or in a similar version to any other examination body.

Aix-en-Provence, February 12th, 2023,

Liste de publications et participation aux conférences

Liste des publications réalisées dans le cadre du projet de thèse:

1. *"SOLEDGE3X full vessel plasma simulations for computation of ITER first-wall fluxes"*, **N. Rivals**, P. Tamain, Y. Marandet, X. Bonnin, H. Bufferand, R. A. Pitts, G. Falchetto, H. Yang, G. Ciraolo, Contributions to Plasma Physics 2022, 62(5-6), e202100182, https://doi.org/10.1002/ctpp.202100182

2. *"Impact of enhanced far-SOL transport on first wall fluxes in ITER from full vessel edge-plasma simulations"* **N. Rivals**, P. Tamain, Y. Marandet, X. Bonnin, H. Bufferand, R. A. Pitts, G. Falchetto, H. Yang, G. Ciraolo, Nuclear Materials and Energy, Volume 33, 2022, 101293, ISSN 2352-1791, https://doi.org/10.1016/j.nme.2022.101293

3. *"Progress in edge plasma turbulence modelling—hierarchy of models from 2D transport application to 3D fluid simulations in realistic tokamak geometry"*, H. Bufferand, J. Bucalossi, G. Ciraolo, G. Falchetto, A. Gallo, Ph. Ghendrih, **N. Rivals**, P. Tamain, H. Yang, G. Giorgiani, F. Schwander, M. Scotto d'Abusco, E. Serre, Y. Marandet, M. Raghunathan, WEST Team and the JET Team, 2021 Nucl. Fusion 61 116052, https://doi.org/10.1088/1741-4326/ac2873

4. *"Implementation of multi-component Zhdanov closure in SOLEDGE3X"*, H. Bufferand, J. Balbin, S. Baschetti, J. Bucalossi, G. Ciraolo, Ph. Ghendrih, R. Mao, **N. Rivals**, P. Tamain, H. Yang, G. Giorgiani, F. Schwander, M. Scotto d'Abusco, E. Serre, J. Denis, Y. Marandet, M. Raghunathan, P. Innocente, D. Galassi and JET Contributors, 2022 Plasma Phys. Control. Fusion 64 055001, https://doi.org/10.1088/1361-6587/ac4fac

5. *"Numerical modelling of the impact of leakage under divertor baffle in WEST"*, H. Yang, G. Ciraolo, J. Bucalossi, H. Bufferand, N. Fedorczak, P. Tamain, G. Falchetto, **N. Rivals**, J.P. Gunn, Y. Marandet, B. Pégourié, S. Vartanian, Nuclear Materials and Energy, Volume 33, 2022, 101302, ISSN 2352-1791, https://doi.org/10.1016/j.nme.2022.101302

6. *"First 3D modelling of tungsten erosion and migration in WEST discharges adopting a toroidally non-symmetric wall geometry"*, S. Di Genova, G. Ciraolo, A. Gallo,

J. Romazanov, N. Fedorczak, H. Bufferand, P. Tamain, **N. Rivals**, Y. Marandet, S. Brezinsek, E. Serre, Nuclear Materials and Energy, Volume 34, 2023, 101340, ISSN 2352-1791, https://doi.org/10.1016/j.nme.2022.101340

Participation aux conférences et écoles d'été au cours de la période de thèse:

1. **Invited talk:**
   - 6th Asia Pacific Conference on Plasma Physics (AAPPS-DPP), October 9-14, 2022 (online)
2. **Talks:**
   - 32nd ITPA meeting of TG SOL and divertor physics, October 24-28, 2022, Cadarache, France
   - 4th IAEA Technical Meeting on Divertor Concepts, November 7-10, 2022, Vienna, Austria
3. **Posters:**
   - 18th International Workshop on Plasma Edge Theory in Fusion Devices (PET21), September 13-15, 2021, Lausanne, Switzerland (online)
   - 25th International Conference on Plasma Surface Interaction in Controlled Fusion Devices (PSI-25), June 13-17, Jeju, Korea (online)
4. **Summer schools:**
   - Ecole Fusion Pour Tous, IRFM, France
   - Culham Plasma Physics Summer School, CCFE, UK

Résumé

Les propriétés et le comportement du plasma de bord dans un réacteur à fusion nucléaire conditionnent directement ses performances et son fonctionnement. Juste à l'extérieur de la région confinée où se produit la fusion, une couche de plasma se forme et interagit avec les parois de la chambre à vide. Si la majorité du plasma arrive sur le "divertor" spécialement conçu pour supporter des flux de chaleur élevés, une partie peut néanmoins interagir avec le reste de l'enceinte à vide (la "première paroi"). Des flux excessifs peuvent éroder les matériaux et réduire leur durée de vie, et également produire des impuretés susceptibles de contaminer et dégrader les performances du plasma central. Le détachement est un régime d'opération identifié comme solution potentielle pour protéger le divertor. Il s'agit d'un régime à haute densité où l'écoulement du plasma sur les tuiles du divertor génère un nuage de gaz neutre à proximité de celles-ci, permettant ainsi de les protéger des flux de chaleur intenses. Néanmoins, peu d'études existent considérant les impacts au niveau de la première paroi. Par conséquent, des estimations de ces flux sur ces surfaces sont nécessaires en fonction des scénarios envisagés. La physique du plasma de bord est cependant très riche et complexe, et le recours aux simulations numériques est nécessaire pour produire ces estimations.

Dans cette thèse, le code SOLEDGE3X est utilisé pour simuler le plasma de bord d'ITER dans sa première phase d'opération (PFPO-1) avec une combinaison de modèles fluide pour le plasma et cinétique pour les neutres (via le code EIRENE). Le détachement du divertor et les flux/conditions plasma au niveau de la première paroi sont étudiés. En raison de la taille et de la géométrie de la machine ITER, le modèle physique dans SOLEDGE3X a dû être amélioré pour mieux décrire les interactions plasma-neutres, entraînant également des améliorations du schéma numérique.

Les résultats obtenus avec SOLEDGE3X ont été comparés à des cas avec des paramètres similaires dans SOLPS-ITER à partir de la base de données ITER et se sont avérés être en bon accord. Les profils en amont sont proches, ainsi que les profils de densité et de température électronique aux targets. Les profils de température ionique aux strike points sont similaires, mais diffèrent plus loin dans les cas attachés, d'un facteur deux plus faibles dans SOLEDGE3X. Les flux de particules et de chaleur vers les targets correspondent très bien. La pression de neutres dans le divertor est relativement proche dans les deux codes pour les cas attachés, néanmoins l'augmentation est plus faible dans SOLEDGE3X que dans SOLPS-ITER lorsque l'injection de gaz augmente.

Le modèle nouvellement implémenté inclut notamment trois types de réactions entre le plasma et les neutres absentes du modèle simplifié initial : les collisions élastiques entre molécules et ions, l'échange de charge entre molécule et ion, et les

collisions neutres-neutres. Ces additions font apparaître en particulier la recombinaison par l'intermédiaire de molécules ("Molecule Assisted Recombination"), et donne lieu à un rôle plus important de l'ion H_2^+ dans les simulations. Dans les régions basses du divertor, il est également apparu important de traiter la dynamique de ces ions H_2^+, et notamment leur transport. Avec ce modèle, la physique du divertor d'ITER met en jeu à la fois des phénomènes extrêmement rapides de l'ordre de la nanoseconde, alors que l'équilibre du plasma global se trouve de l'ordre de la seconde. De ce constat est venue la nécessité d'améliorer le schéma numérique du code, pour permettre des calculs en temps raisonnables. Les deux principales améliorations ont été, d'une part le passage des termes collisionnels de la fermeture du modèle fluide de Zdhanov vers un schéma implicite, et d'autre part, une estimation du temps pendant lequel les sources de plasma calculées par EIRENE sont valables. Ces cas ITER sont désormais réalisables à l'échelle du mois de calcul.

Pour étudier les mécanismes en jeu dans le détachement, un scan en taux d'injection de gaz est effectué. Une analyse de l'épaisseur de la SOL λ_q est proposée, où il est montré que ce paramètre dépend du régime, conduisant à des recommandations sur le choix des coefficients de transport perpendiculaire pour les simulations de régimes haute-densité. Pour la première fois dans la littérature, une évaluation est proposée des contributions entre neutres et ions dans les taux d'érosion de la première paroi sur la base de simulations autocohérentes. Ensuite, au vu des observations dans les machines actuelles indiquant la possibilité de formation d'épaules en densité dans la far-SOL d'ITER, une étude de sensibilité des résultats précédents est réalisée en augmentant le transport perpendiculaire dans la far-SOL des simulations. Les impacts sur le régime divertor, les conditions plasma, les flux et le taux d'érosion de la première paroi sont analysés. Enfin, des futures étapes pour améliorer les simulations sont proposées, ainsi que les premiers résultats d'une simulation d'un plasma Q = 10 avec impuretés (néon et hélium).

Ensuite, une analyse des régimes de densité a été présentée, allant du régime de high-recycling au régime partiellement détaché, correspondant au maximum de la capacité de pompage de la machine. Au plan médian au-dessus du divertor, il a été observé que la longueur de décroissance de la puissance parallèle des électrons augmentait rapidement de 60% avec la densité, puis même jusqu'à 300% à l'injection maximale. Il en est conclu que pour la simulation de régimes à haute densité, il n'est pas pertinent de fixer les coefficients de transport pour que cette largeur adhère strictement à la loi d'échelle de Eich. L'approche consisterait plutôt à régler d'abord les coefficients de transport perpendiculaire pour qu'ils correspondent à la loi d'Eich dans les simulations en régime sheath-limited, puis à conserver les valeurs obtenues pour les simulations à haute densité. Une telle procédure est alors valable à condition de supposer que les caractéristiques du transport transverse qui sont représentées ici à travers des coefficients de diffusion ne sont pas impactées par les régimes des divertors. Une correction supplémentaire serait nécessaire si c'était le cas. La décomposition des interactions plasma-neutre a été analysée pour les trois régimes : attaché, rollover, et détachement partiel. Lors du rollover, le premier puits de particules dominant est le MAR, tandis que la recombinaison électron-H^+ est négligeable. Cette dernière devient

importante en régime partiellement détaché. Un schéma synthétique des principales réactions pour les trois états est exposé, mettant en évidence les différents rôles des réactions, et en particulier les contributions des ions H_2^+.

La structure des réactions entre le plasma et les neutres est synthétisée dans la figure Figure 1. En régime attaché, toutes les réactions sont localisées juste au niveau de la paroi. Les molécules sont ionisées par les éléctrons en ions H_2^+, qui sont ensuite à leur tour dissociés en ion H^+ et en atomes, et ces derniers sont ionisés à leur tour. Les échanges de charge et l'ionisation des atomes sont les principaux canaux de perte d'énergie pour le plasma. Au rollover, les ions H_2^+ ne sont plus formés par les collisions entre électrons et molécules, mais par échange de charge entre ions et molécules. Le front d'ionisation des atomes se détache de la paroi. En plus de la dissociation des ions H_2^+ en ions H^+ et atomes, un puits de particule net pour le plasma apparaît via la dissociation-recombinaison de ces ions H_2^+ en deux atomes (réaction également appelée Molecule-Assisted Recombination "MAR"). À ce stade la recombinaison électron-H^+ dans le volume est négligeable. La réaction MAR se manifeste donc avant la recombinaison électron-H^+, et c'est elle qui contribue à la saturation et réduction initiale du flux de particule à la paroi avec l'augmentation de la densité dans les simulations. En régime détaché, la recombinaison électron-H^+ devient dominante à proximité immédiate de la paroi, pendant que les autre réactions remontent le long des lignes de champs jusq'au point X. Les réactions MAR sont détachées de la paroi. Les collisions élastiques entre neutres devienent importantes. Dans l'ensemble des régimes la perte majoritaire d'énergie des électrons a pour origine l'ionisation des atomes, avec un coût énergétique moyen de 25 eV constant indépendamment du régime. Même si ce coût augmente fortement avec la température électronique, la fréquence de réaction diminue de même.

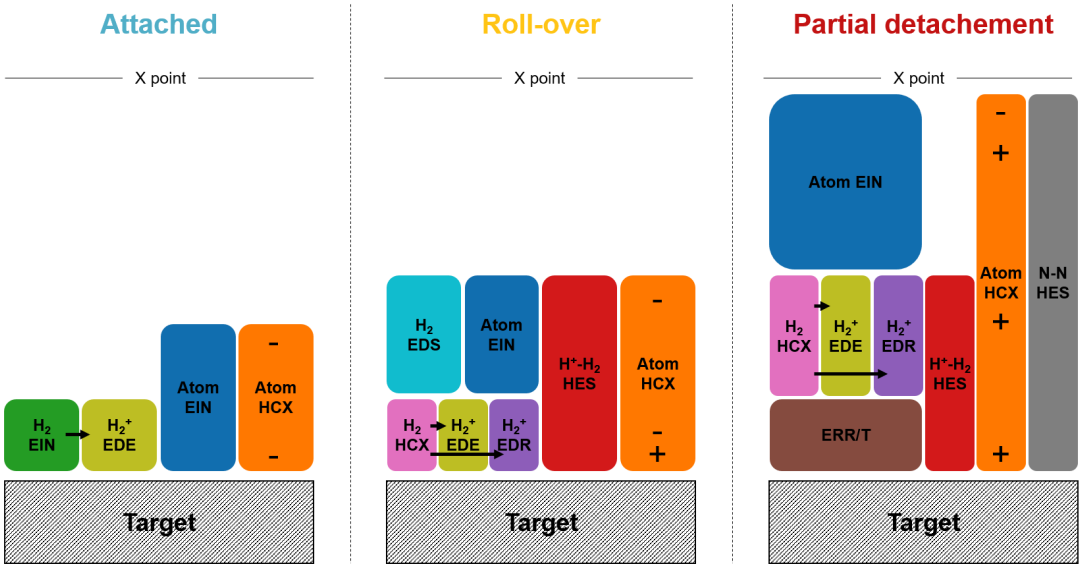

Figure 1.: Vue d'ensemble du processus de détachement avec les réactions clés impliquées, selon trois régimes divertor. Les noms représentent le régime global, mais les comportements représentés sont dérivés de l'analyse d'une seule ligne de champ.

Les simulations permettent également d'analyser les conditions et les flux de plasma au niveau de la première paroi, ainsi que leur évolution en fonction des régimes en densité. Deux effets opposés ont été observés : d'une part les flux de particules augmentent avec l'injection de gaz, mais d'autre part l'énergie des particules diminue. Les flux de chaleur totaux (<10kW/m²) restent largement en dessous des limites du design des composants, malgré leur augmentation avec la densité croissante. Les estimations des taux d'érosion brute de béryllium montrent une multiplication par six entre la valeur la plus faible et la plus haute de l'injection de gaz comme indiqué en Figure 2. Celle-ci est principalement due aux atomes d'échange de charge, car très peu d'ions atteignent la première paroi. La distribution de en énergie des atomes au niveau de la première paroi présente deux populations, une population de Frank-Condon froide de 3 eV et une population d'échange de charge à haute énergie qui peut atteindre 3 ou 4 keV. Cependant, les flux de particules de cette dernière sont extrêmement faibles. Les sections de la première paroi les plus sujettes à l'érosion sont situées au niveau du sommet de la machine, du port d'injection de gaz et les tuiles situées au-dessus du baffle extérieur.

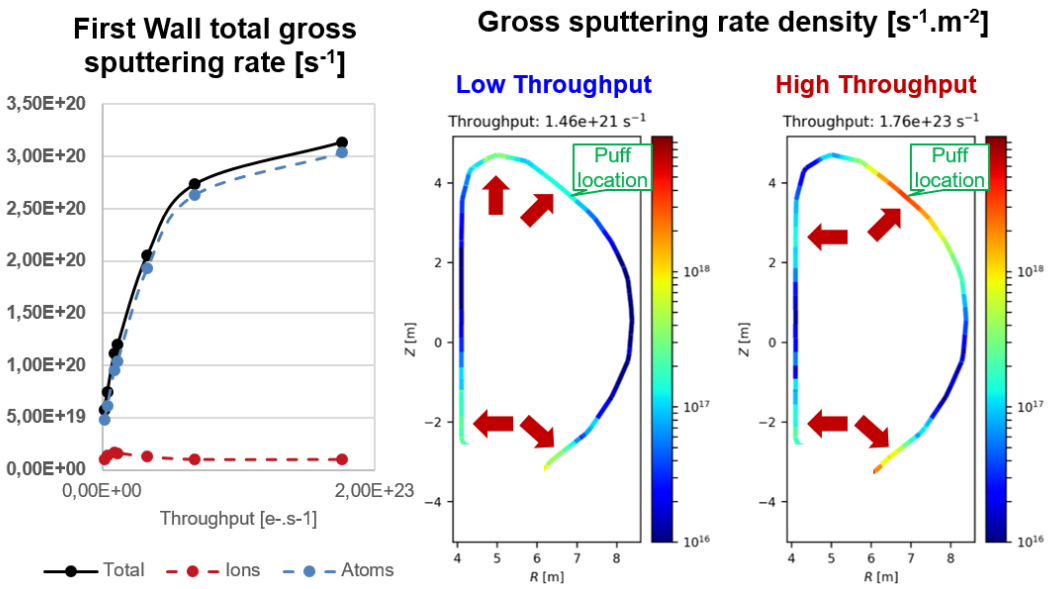

Figure 2.: Impact de l'injection de gaz sur le taux d'érosion brut calculé avec EIRENE. A gauche : Taux total intégré le long de la première paroi, avec la contribution des ions en rouge, et celle des atomes en bleu. A droite : Représentation 2D des taux d'érosion brut le long de la première paroi.

Ensuite, une étude de sensibilité a été réalisée pour évaluer l'impact de la formation potentielle d'épaules de densité dans la far-SOL. Ces dernières sont modélisées en augmentant les coefficients de transport perpendiculaire à quelques centimètres de la séparatrice dans le plan médian. Peu d'effets sont constatés sur les conditions du divertor, le régime reste inchangé. Au niveau de la première paroi, les flux de particules et les énergies sont par contre largement augmentés. Les densités de flux de chaleur augmentent jusqu'à 40kW/m², tout en restant bien en dessous des limites opérationnelles. L'érosion brute est dominée par l'effet des ions, avec une augmentation beaucoup plus forte, d'un facteur 60, entre les différents extrêmes des cas étudiés.

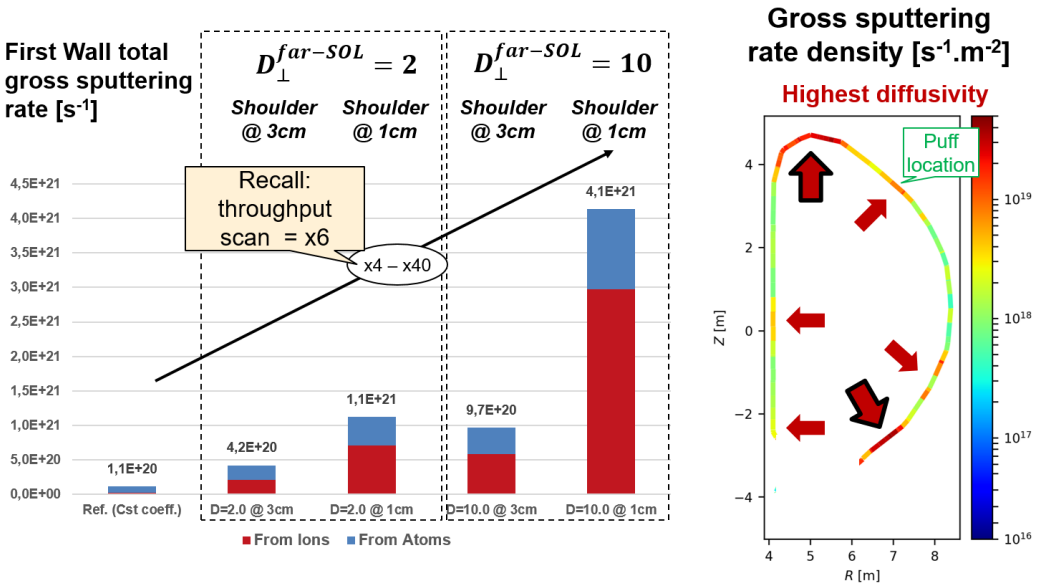

Figure 3.: Impact de la présence d'épaule en densité sur le taux d'érosion brut de la première paroi. A gauche : taux d'érosion brut, à droite : tracé 2D du taux d'érosion brut pour le cas le plus diffusif. La flèche illustre le facteur d'augmentation par rapport au cas de référence.

Enfin, quelques pistes sont données pour la poursuite de ces travaux, notamment : la simulation cas pleine puissance à 100MW avec injection d'impureté de Neon et Helium représentant des scénarios de plasma Q = 10, puis l'utilisation des résultats pour des calculs plus approfondis de l'érosion avec des codes spécialisés comme ERO2.0 ou WALLDYN, l'amélioration du modèle d'interaction plasma-neutre avec l'inclusion de données calculés par des modèles collisionels radiatifs ou la prise en compte des ions H^-, et l'amélioration du modèle du solveur plasma via l'activation de modèles de turbulence réduits.

Keywords: fusion nucléaire, plasma, simulation numérique, plasma de bord, scrape-off layer, ITER, interaction plasma-surface, détachement, épaules en densité

Abstract

The properties and behavior of the plasma edge in a nuclear fusion reactor are critical for its performance and operation. Just outside the boundary of the confined region where fusion occurs, a layer forms which interacts with the vacuum vessel walls. While most of the plasma falls on the so-called "divertor" section of the machine specially designed to sustain high power fluxes, some of it can still interact with the rest of the vacuum vessel (the "First Wall"). Plasma particles impacting surfaces can erode materials, producing impurities that can contaminate the core plasma, degrade fusion performance, and shorten the components' lifetime. To optimize operations, one needs quantitative assessments of the plasma fluxes and conditions at surfaces for different plasma scenarios. As the phenomena involved in the edge plasma are highly diverse and non-linear, numerical simulation tools are required.

In this thesis, we use the SOLEDGE3X code to simulate the behavior of the ITER Scrape-Off Layer in the first non-active operation phase (PFPO-1), with a fluid model for the plasma using the SOLEDGE3X plasma solver, which is coupled to and a kinetic model for neutrals using the EIRENE code. This study specifically focuses on detachment in the divertor and the plasma fluxes and conditions at the beryllium First Wall. Due to the conditions expected in the ITER machine, the physics model in SOLEDGE3X had to be improved to better describe plasma-surface and plasma-neutral interactions in the divertor. The increased complexity of the new model also mandated several improvements to the numerical scheme. Then, following the new ability of the code to deal with ITER cases, a scan over a range of gas injection rates is performed to study the mechanisms at play in plasma detachment. More specifically, the contributions of the plasma-neutral interaction processes are analyzed for the attached/high-recycling, rollover, and partial detachment regimes. Further analysis of the SOL width λ_q indicates that it varies with the divertor regime, giving guidelines on the procedure to set up perpendicular transport coefficients for high-density regime simulations. The contributions of neutrals and ions in the assessed gross beryllium erosion rates are analyzed, including their energy spectra. Then, since observations in current machines point to the possible formation of density shoulders in the far-SOL of ITER, a sensitivity study of the results is carried out by increasing the far-SOL perpendicular transport coefficients in the simulations. The impacts on the divertor regime, conditions, fluxes, and gross erosion rate at the first wall are assessed. Finally, potential future steps to improve simulations are proposed, along with the initial simulation results of a Q=10 plasma with Neon and Helium impurities.

Keywords: nuclear fusion, plasma, numerical simulation, edge plasma, scrape-off layer, ITER, plasma-surface interaction, detachment, density shoulders

Résumé

Les propriétés et le comportement du plasma de bord dans un réacteur à fusion nucléaire conditionnent directement ses performances et son fonctionnement. Juste à l'extérieur de la région confinée où se produit la fusion, une couche de plasma se forme et interagit avec les parois de la chambre à vide. Si la majorité du plasma arrive sur le "divertor" spécialement conçu pour supporter des flux de chaleur élevés, une partie peut néanmoins interagir avec le reste de l'enceinte à vide (la "première paroi"). Des flux excessifs peuvent éroder les matériaux et réduire leur durée de vie, et également produire des impuretés susceptibles de contaminer et dégrader les performances du plasma central. Par conséquent, des estimations de ces flux sur ces surfaces sont nécessaires en fonction des scénarios envisagés. La physique du plasma de bord est cependant très riche et complexe, et le recours aux simulations numériques est nécessaire pour produire ces estimations. Dans cette thèse, le code SOLEDGE3X est utilisé pour simuler le plasma de bord d'ITER dans sa première phase d'opération (PFPO-1) avec une combinaison de modèles fluide pour le plasma et cinétique pour les neutres (via le code EIRENE). Le détachement du divertor et les flux/conditions plasma au niveau de la première paroi sont étudiés. En raison de la taille et de la géométrie de la machine ITER, le modèle physique dans SOLEDGE3X a dû être amélioré pour mieux décrire les interactions plasma-neutres, entraînant également des améliorations du schéma numérique. Un scan en taux d'injection de gaz est effectué pour étudier les mécanismes du détachement. Les contributions des différents processus d'interaction plasma-neutres sont analysées pour les régimes attachés/high-recycling, rollover et partiellement détaché. Une analyse de l'épaisseur de la SOL λ_q est proposée, où il est montré que ce paramètre dépend du régime, conduisant à des recommandations sur le choix des coefficients de transport perpendiculaire pour les simulations de régimes haute-densité. Pour la première fois dans la littérature, une évaluation est proposée des contributions entre neutres et ions dans les taux d'érosion de la première paroi sur la base de simulations autocohérentes. Ensuite, au vu des observations dans les machines actuelles indiquant la possibilité de formation d'épaules en densité dans la far-SOL d'ITER, une étude de sensibilité des résultats précédents est réalisée en augmentant le transport perpendiculaire dans la far-SOL des simulations. Les impacts sur le régime divertor, les conditions plasma, les flux et le taux d'érosion de la première paroi sont analysés. Enfin, des futures étapes pour améliorer les simulations sont proposées, ainsi que les premiers résultats d'une simulation d'un plasma Q = 10 avec impuretés (néon et hélium).

Mots-clés: fusion nucléaire, plasma, simulation numérique, plasma de bord, scrape-off layer, ITER, interaction plasma-surface, détachement, épaules en densité

Remerciements

Je souhaiterais remercier en premier lieu l'IRFM, Aix-Marseille Université, et ITER Organization pour m'avoir accordé leur confiance pendant ces trois années, et avoir permis l'aboutissement mon doctorat.

En tout particulier, je remercie chaleureusement Xavier Bonnin pour sa patience, son temps et ses conseils, et bien sûr Richard Pitts pour son soutien, les discussions, et accompagnement pendant ces trois années. Ces échanges ont été très précieux pour moi.

Un très grand merci à Yannick Marandet pour son encadrement, son soutien, ses conseils, pour ses décryptages de la physique des neutres, et d'avoir été pour moi une pierre de Rosette du langage mythique d'EIRENE et des estimateurs non baisés des approches Monte-Carlo.

Et bien sûr, un immense merci tout particulièrement à Patrick Tamain pour son temps, sa patience et son soutien pendant ces trois années, des discussions sur tous les sujets, physique, numérique, et autres… Longue vie à la #TeamSOLEDGE !

Merci aussi aux autres membres du groupe théorie & simulation tous ceux de l'IFRM avec qui j'ai eu le plaisir d'échanger, en particulier Guido, Hugo, Eric, Gloria, Nicolas, Guilhem, Yannick, Peter, pour les discussions, leur soutien et leur bonne humeur.

I would also like to warmly thank the members of the jury for taking the time to read this 250-page thesis (though with many pictures!), for their patience, questions and remarks: Martine Baelmans, Bruce Lipschultz, Gwenaël Fubiani Jérôme Bucalossi, and also especially Detlev Reiter for our discussions.

Merci également à Nathalie et Valérie pour leur précieuse aide dans la navigation périlleuse de l'administratif au CEA.

Je pense également à mes cothésards-collègues-amis sans qui tout cela n'aurait jamais été au drôle, en particulier Pr. Mathieu Peret et son combo explosif turbulence du plasma de bord + Bigard, Robin la seule personne appréciant les deux minutes du peuple à leur juste valeur, Eléonore "je-suis-beaucoup-trop-gentille" Geulin, Yann Munchy le maillot jaune et son canapé tout confort, Kevin Obrejan fidèle du Plasmapéro, Raffael "l'infiltré double-nationalité" Eller-Düll, Alberto "la classe à l'italienne" Gallo, Hao "It's complex" Yang, Olivier "le rayon de soleil" Panico et tout spécialement à ma co-bureau violette Virginia "la donna torbolenta" Quadri. Merci également aux autres et aux stagiaires que j'ai pu croiser.

Ma gratitude va sans limite à la bande de jeunes gens à la santé mentale douteuse qui ont été là avant, pendant, et seront là après ces trois ans, et en particulier ceux qui sont venus depuis Paris jusque dans le prestigieuse amphithéâtre René Gravier de l'IRFM le jour de Star Wars, vous êtes des chefs.

Je tiens également à remercier évidemment ma famille pour leur soutien en continu au long de ces trois ans.

Enfin, je ne remercie PAS : les serveurs du café le Darius (merci pour le bruit), mon cerveau (il ne maîtrise toujours pas la physique des plasmas), Marconi (tous les jours quelq[SCRATCH IS ALMOST FULL]), le Covid (génial ces 2 années), la machine à café du RDC et ses airs de bandit manchot, et la fuite du réservoir d'Hélium liquide de WEST (bye-bye campagne expérimentale).

Per aspera ad astra in utres,
Nicolas

“ *Donne-moi ton* CORE*, baby ta* SOL*, baby yeah,*
Chauffe avec moi je veux une flamme, MAST-U.”

– TO-K. MARO

Contents

Introduction

0.1. Introduction to fusion energy

0.1.1. Nuclear fusion reactions

Nuclear reactions denote processes that affect the nucleus of an atom. *Fusion* refers to the reaction in which two nuclei merge into a single, heavier one, while the inverse reaction in which a heavy nucleus splits into lighter ones is called *fission*.

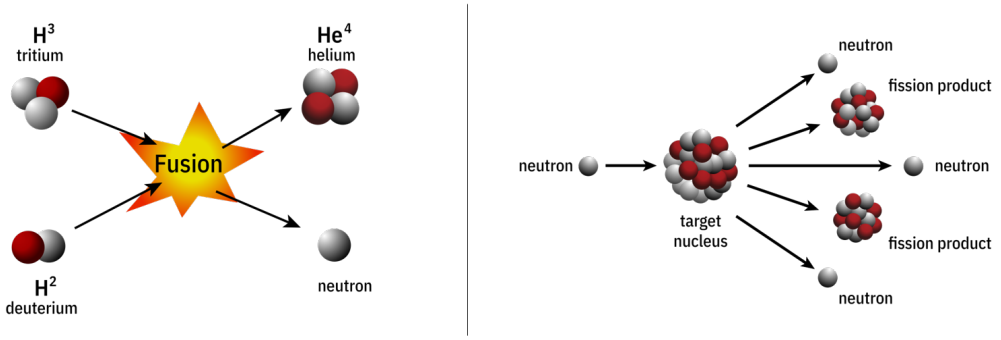

Figure 4.: Illustration of a *fusion* reaction (merging of light nuclei) vs. a *fission* reaction (splitting of a heavy nucleus).

Depending on the size of the nuclei, i.e., their number of constituents called *nucleons* (protons and neutrons), these reactions can either release or consume energy. For a reaction to release energy, the resulting nucleus or nuclei must be more stable than the initial ones. This stability characterizes how efficiently the residual strong nuclear force binds together the constituting protons and neutrons in the nucleus. It is represented by a binding energy, which quantifies the amount of energy necessary to dissociate the nucleus into its individual free nucleons. The products are more stable if the total binding energy is larger for the products than for the initial particles. In this case, energy is released.

The Aston curve Figure 5 illustrates this behavior, which shows the binding energy per nucleon of each chemical element.

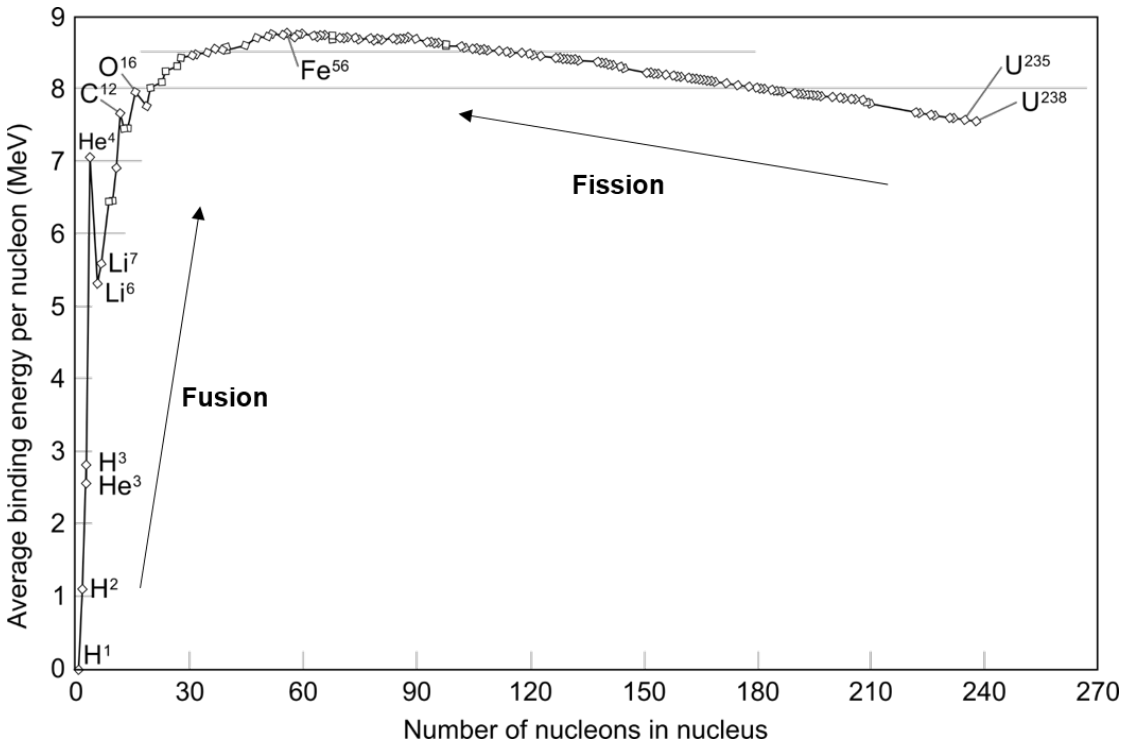

Figure 5.: Aston curve: Binding energy of elements per nucleon. From [1], based on data from [2].

From this, one can see that two reaction types are energetically favorable: fissioning heavy elements into lighter ones (right side toward the left), and fusing light elements into heavier ones (left side toward the right).

The fission of heavy elements is what is done with Uranium in existing power plants. Harnessing the fusion of lighter elements is the goal of nuclear fusion research. While nuclear fusion is one of the most common reactions naturally occurring in nature, as it is the one powering the stars, it is a significant challenge to reproduce and master it on Earth.

Different kinds of fusion reactions are possible. Figure 6 shows the most common fusion reaction cross-sections as a function of the temperature, which can be loosely interpreted as their rate of occurrence under such conditions, i.e., their degree of accessibility. However, even for the most accessible ones, the required temperatures are of the order of tens of keV (10 keV $\simeq$ 100 million degrees C). The requirement for such temperatures, a quantity related to the particles' average velocity, comes from the need to overcome the electrostatic repulsion between positively charged nuclei. In order to fuse, both particles must come close enough to each other, within the very short range of the residual strong nuclear force that binds the nucleus together. However, since the electrostatic force, which acts at a longer range, tends to push them apart with increased strength as they come closer, they must collide with a large enough relative velocity to cross that repulsive region.

The reaction of interest here is the so-called *DT fusion* in blue in the graph, which is

the easiest to achieve, as the others are significantly harder to trigger (much higher temperatures are needed, the x-axis is in logarithmic scale).

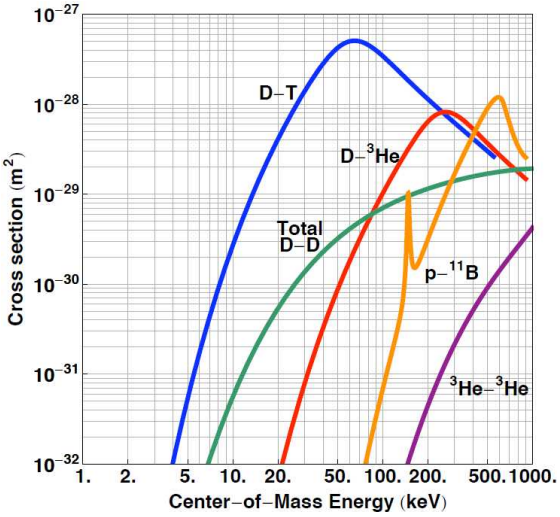

Figure 6.: Fusion cross sections as a function of the energy (temperature) of particles. From [3].

It involves the fusion of two isotopes of hydrogen: deuterium (one proton, one neutron) and tritium (one proton, two neutrons):

$$^{2}_{1}\mathrm{D} + ^{3}_{1}\mathrm{T} \rightarrow ^{4}_{2}\mathrm{He}\ (3.52\ \mathrm{MeV}) + ^{1}_{0}\mathrm{n}\ (14.1\,\mathrm{MeV})$$

It produces a helium nucleus (also called *alpha particle*) and a neutron for a total energy release of 17.6 MeV. The majority is carried by the neutron (80%) and the rest by the Helium nucleus (20%). This process is extremely energy dense: burning a kilogram of DT mixture produces around ten million times more energy than burning a kilogram of coal.

0.1.2. Fusion as an energy source

The DT fusion reaction involves deuterium and tritium in equal parts. While deuterium is vastly abundant in seawater, tritium is very rare. The global yearly production rate is currently on the order of a kilogram, while an industrial-scale fusion power plant would require ~56 kg per GW of fusion power[4]. This aspect is addressed by locally closing the tritium cycle inside the plant. This is done by capturing DT fusion neutrons with a blanket containing lithium, which fissions into tritium and helium. The recovered tritium is then reinjected into the reactor. Neutron multipliers such as beryllium are also considered to compensate for lost neutrons. Thus, the net input materials for current plant designs consist of only deuterium and lithium. The only output is helium.

Fusion energy should play a crucial role in the future of the energy production landscape because of natural resources and for environmental, political, and economic reasons. Although detailed discussions of such matters are outside the scope of this work, the relevance of investing significant efforts into the development of fusion energy can be understood from some of its key properties:

- **Low carbon**: No fossil fuels are involved directly
- **Dispatchable source**: The output of the plant is controllable
- **Limited land usage**: The nuclear nature of the reaction gives it a very high energy density
- **Intrinsically safe**: The reaction cannot run away in an uncontrolled reaction chain in case of failure of the reactor systems, and the products of the reaction are not radioactive. The materials that are activated due to the neutrons do not fall in the category of long-life high-activity waste (HLW) class but rather in the Intermediate-Level-Waste Long-Lived (ILW-LL) class [5].
- **Not weaponizable**: The technology does not enable the creation of thermonuclear weapons (fission elements are necessary).
- **Abundance of fuels**: Deuterium and Lithium are widely available
- **Vector of strategic independence**: Deuterium and Lithium resources are not localized in specific parts of the globe, providing a path to energy independence for many countries and easing energy supply-related political tensions.

Of course, one has to weigh the latter points with known challenges that remain, which current nuclear fusion research aims to address:

- **Scientific challenge**: No consensus exists yet on the optimal approach, due to an incomplete understanding of all physics phenomena involved (this thesis attempts to contribute, at its own scale, to this part)
- **Technology challenge**: First-of-a-kind systems and experiments are required in many cases, involving the successful combination and integration of a wide range of domains and industries
- **Operational challenge**: Neutron fluxes and the associated material activation make such facilities fall in the nuclear installations category, drastically increasing operational complexity. It also includes the management of radioactive waste from the reactor materials. However, these can be seen as a fixed (as opposed to variable) cost because they do not come from the fuel.
- **Financial challenge**: Significant capital is needed to advance the experimental side and demonstrators, which requires the few investors (either public or private) capable of expending such capital to accept the relevance and importance of such term investments.

0.1.3. Performance of fusion reactors

At the temperatures required for fusion, matter is in a state called *plasma*, which is described in more detail in the following section. In DT fusion reactors, the produced alpha particles (helium nuclei) carry a very high energy (3.5 MeV), and can collide with the other D and T particles in the plasma. This effect is beneficial because through this mechanism the plasma in the reactor can heat itself, provided there is a sufficient number of fusion reactions. One commonly used metric to quantify performance or machines is the ratio of the total fusion power generated (neutrons plus alphas) P_{fus} to the power injected by external means in the plasma P_{in}, and is denoted Q.

$$Q = \frac{P_{\text{fus}}}{P_{\text{in}}}$$

Two values of Q are of interest:

- *break-even*: $Q = 1$, as much fusion power is generated as injected power
- *ignition*: $Q = \infty$, the plasma is fully self-heating and does not requires any external power

Reaching ignition is actually beyond the objective of fusion reactors, as the goal is rather to achieve a state where some external heating remains needed, and the plasma simply acts as a controllable power amplifier.

The assessment of the performance of fusion reactors is also possible without having to use costly tritium fuel and directly measuring neutron yields. It can be done by measuring the plasma parameters and calculating the well-known *triple-product* $nT\tau_E$ quantity. This formula actually describes the plasma's projected ability to self-heat. Through this indicator, Lawson was able to devise a criterion that indicates whether a given plasma state would reach break-even if the content had been replaced by a DT mixture [6]:

$$nT\tau_E \geq 3 \times 10^{21} \text{keV.s.m}^{-3}$$

The components of this triple product are:

- n the plasma particle density
- T the plasma temperature
- τ_E the plasma energy confinement time, i.e., how long the plasma holds the energy it is provided. It is computed as the ratio of the energy contained in the plasma W to the injected power $\tau_E = \frac{W}{P_{\text{in}}}$.

From the underlying physics, the triple product is at its minimum (and thus at its optimum) at $T \simeq 26$ keV. Provided one can reach such temperatures, only maximizing density and energy confinement time remains. It is however not necessary to operate at this temperature to reach $Q > 1$.

The current magnetic confinement record in terms of Q is the European JET tokamak with 0.62 in 1997 [7], for a small fraction of a second during a transient spike. The recent JET results of December 2021 showcase, in fact, major improvements and breakthroughs even if a lower value of Q was achieved. $Q = 0.33$ was reached [8], but now in a stable phase which lasted for around five seconds, and furthermore with more reactor-relevant materials inside the chamber (tungsten instead of the now ruled-out carbon used in 1997 because of its tritium retention properties). This change of material brought additional challenges for the plasma performance which were not present in 1997.

To attest to the progress achieved since the beginning of fusion research, one can observe the triple product plot of past, present, and planned machines in Figure 7, displayed as the $n\tau_E$ product as a function of T. Considerable advances have been made, even faster than Moore's law for transistors considering this metric [9].

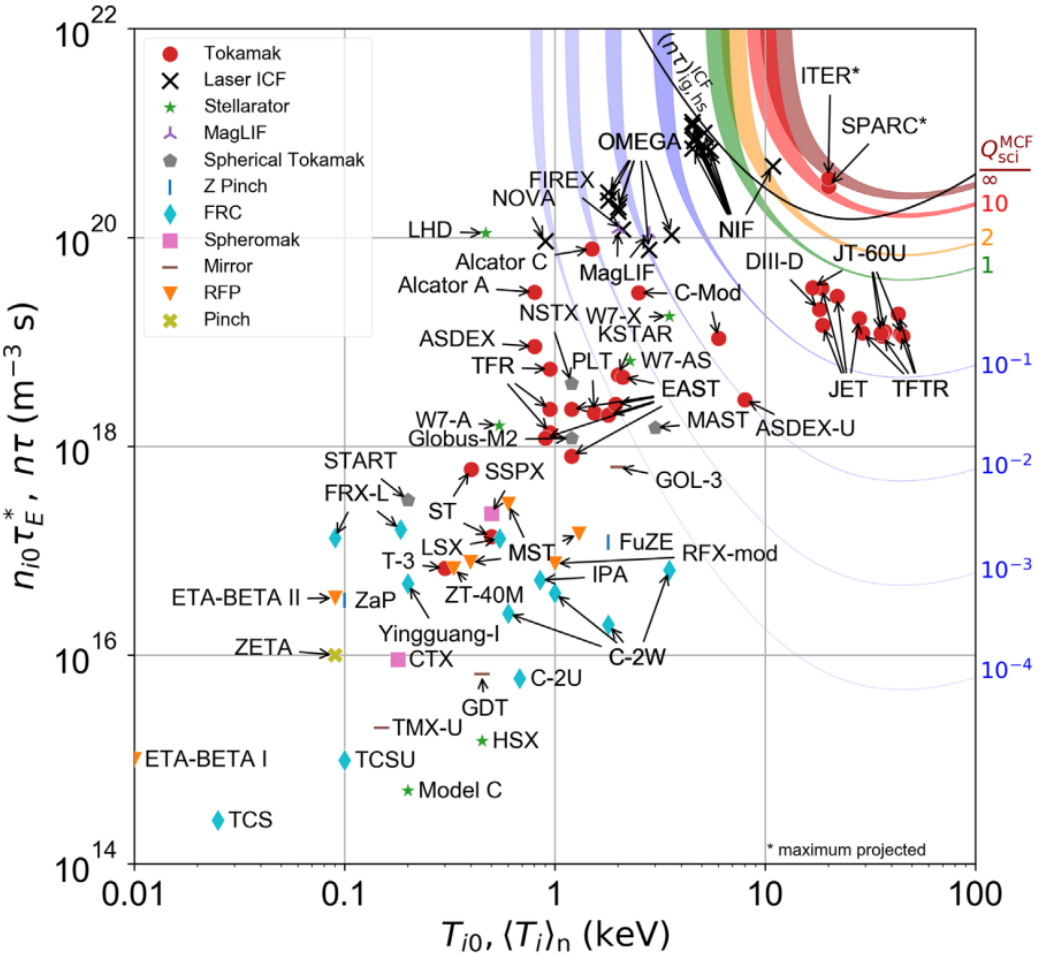

Figure 7.: 2D plot of the $n\tau_E$ product as a function of temperature, for fusion machines, categorized by type, past present, and projected for ITER and SPARC. From [10].

The ITER project, on the top right of the graph, aims at $Q = 10$.

0.2. Magnetic Confinement Fusion

0.2.1. General principle

As seen in the precedent section, fusion requires heating a Deuterium-Tritium mixture to temperatures of around a hundred million degrees. No solid conventional container could hold the mixture at such temperatures without cooling it before any reaction happens. One of the most popular and successful approaches to producing and holding long enough such conditions is called *magnetic confinement*, and is the topic of this work. Other approaches exist but will not be discussed here.

At these temperatures, hydrogen is in the *plasma* state, which denotes the fourth state of matter after the gas state. In such a state, electrons are freed from orbiting the nuclei, forming a soup of free-flying negatively charged electrons and positively charged ions. This is a fundamental difference with respect to a gas, which only includes neutral atoms and molecules. The plasma, however, is still globally neutral, as the densities of positive and negative charges remain evenly matched on a macroscopic level.

Incidentally, charged particles have the property to react to magnetic fields: they follow the direction of the field with helical trajectories Figure 8, as they feel no force from the magnetic field in this direction. The direction parallel to the magnetic field line is called the *parallel direction*, and the perpendicular one the *perpendicular direction* (actually any direction in the plane perpendicular to $\vec{B}$).

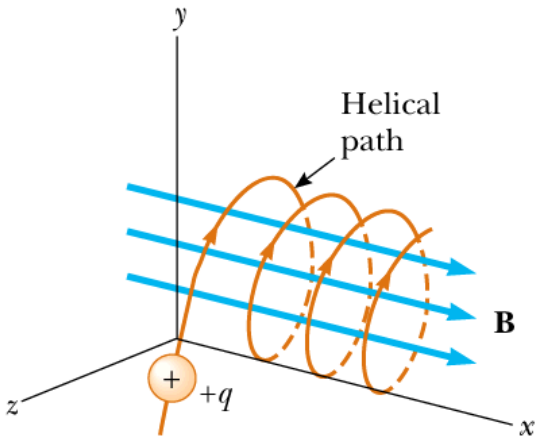

Figure 8.: Helical motion of a charged particle in a uniform magnetic field.

This results in two key properties of charged particles in magnetic fields:

- the particle velocity is unconstrained along the magnetic field direction and can reach large amplitudes
- the radius of the helix, the *gyroradius* or *Larmor radius* ρ is related to its velocity component perpendicular to the magnetic field with the relation below.

$$\rho = \frac{m v_\perp}{qB}$$

Where:

- ρ: the Larmor radius
- m: the mass of the particle
- $v_\perp$: the perpendicular velocity of the particle

- q: the electric charge of the particle
- B: the magnetic field amplitude

It is, in practice, closely related to the particle species' temperature by taking the perpendicular velocity as the thermal velocity at temperature T: $v_{th} = \sqrt{\frac{Te}{m}}$.
With:

- e: the elementary charge
- T: the temperature in eV

It follows that in a plasma, the transport perpendicular to the magnetic field is strongly reduced. It is not fully suppressed, due to other effects that are not detailed here. One can then create magnetic field lines closing on themselves so that particles loop around, then enclose this magnetic configuration in a chamber. A way to achieve this is with the help of electro-magnets around a torus, as is illustrated in Figure 9. This is the base concept for magnetic confinement fusion.

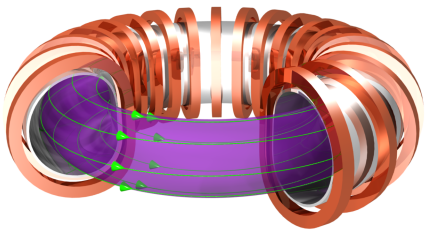

Figure 9.: Simple magnetic configuration, where coils in copper color generate magnetic field lines (green) closing on themselves, encased in a vacuum vessel (in grey) which contains the plasma (purple). Image from Max-Planck IPP, Garching

The following parameters usually characterize such systems Figure 10:

- R_0: the major radius R, distance to the center of revolution, of the magnetic axis located at the center of the vessel
- a: the minor radius, maximum distance in the interior of the chamber

The associate coordinate system is:

- φ: the angle in the so-called "toroidal" direction associated with the major radius
- θ: the angle or coordinate in the so-called "poloidal" direction, associated with the minor radius a

- ψ: a coordinate denoting the distance to the center of the plasma inside the chamber

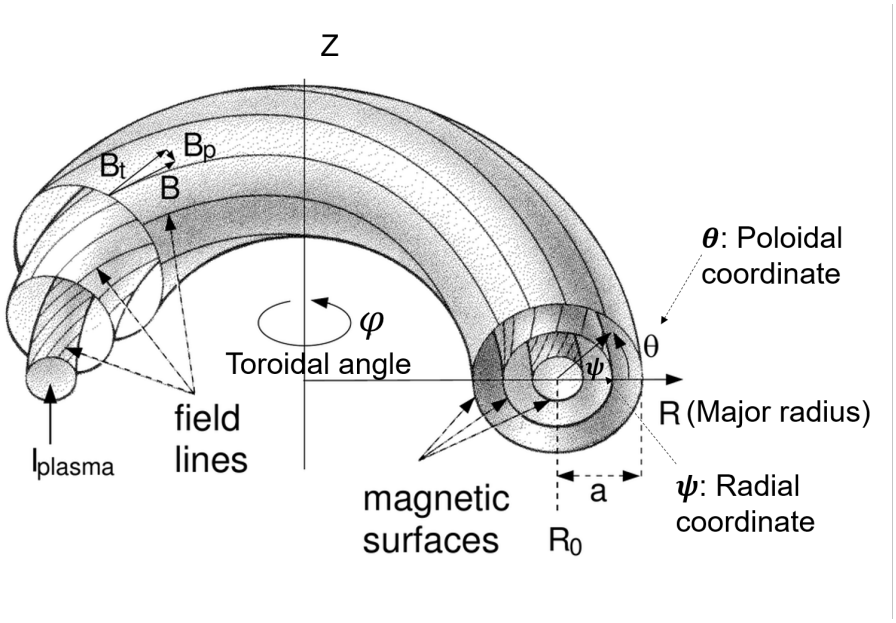

Figure 10.: Diagram of the toroidal (φ), poloidal (θ), and radial (ψ) coordinates, along with the cartesian coordinates in the poloidal plane major radius R and height Z, adapted from [11].

The (ψ,θ) plane corresponds to a vertical slice of the torus, and is referred to as a *poloidal plane*. It can also be parametrized by the cartesian R and Z coordinates, both in meters, R being the distance to the axis of revolution of the machine, and Z the vertical coordinate starting at the center of the chamber.

However, this simple magnetic configuration is not able to hold stable plasmas. To create magnetic field lines that take the shape of closed rings, one has to arrange the coils in a fashion where the inner parts of the coils are closer to each other than the outer parts. This results in a non-uniform magnetic field amplitude across the chamber which decreases with R. In such cases, particles do not follow exactly anymore the field lines and drift rapidly in the vertical direction. The drift direction is opposite for the positive ions and the negative electrons, thus giving rise to charge separation and creating a strong vertical electric field. This electric field induces, in turn, an additional outward drift which makes the plasma particles crash on the outer wall in very short time scales.

The TOKAMAK concept solves this issue.

0.2.2. Tokamaks

Tokamaks aim at modifying the direction of the magnetic field lines by adding a poloidal component, so that they form helical trajectories around the torus Figure 11.

Due to this poloidal component, plasma particles travel along paths forming closed loops when projected on a vertical plane. In 3D, those correspond to tubular surfaces containing a set of magnetic field lines, called *flux surfaces* or *magnetic surfaces*. Three of them are represented in Figure 10 as an example. This schematic view is helpful to illustrate that particles travel very quickly inside flux surfaces, but much more slowly between flux surfaces.

Since this configuration now connects the top and bottom of the chamber via fast parallel transport, the vertical drift of particles when they are located at the top of the machine compensates the drift they undergo when the field line is at the bottom of the machine, resulting in no net transport. This prevents charge separation and the subsequent outward drift.

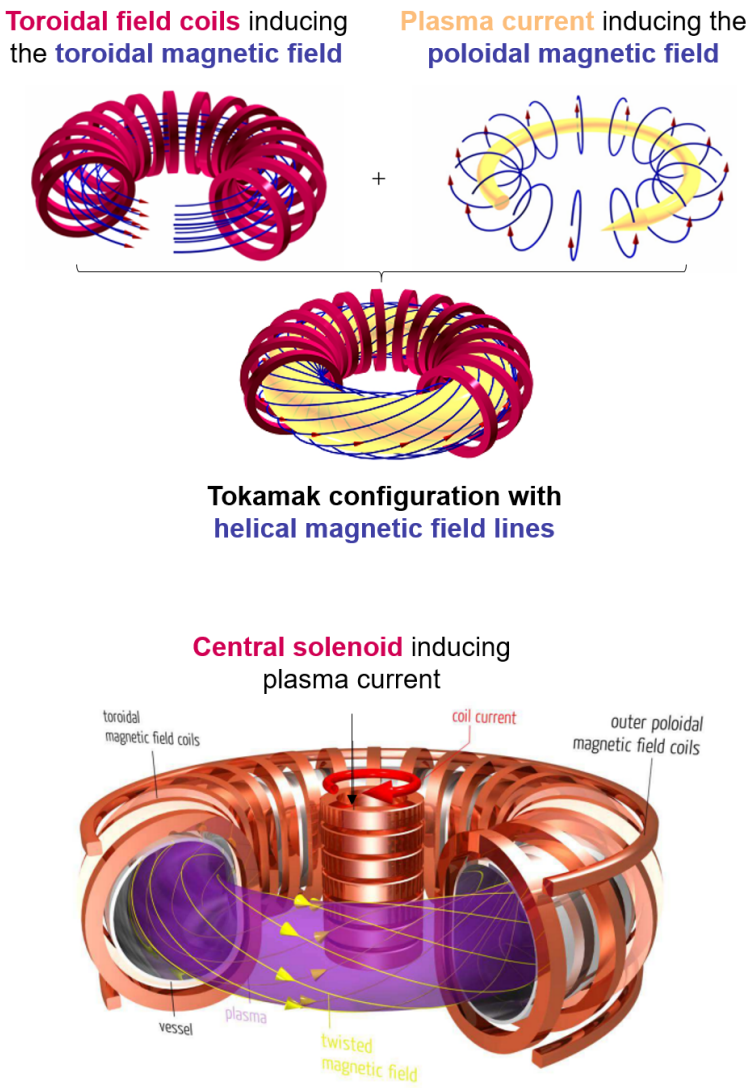

Figure 11.: The tokamak configuration, as the sum of toroidal magnetic field and poloidal magnetic fields, the latter induced by plasma current, itself being induced by the central solenoid coil. Adapted and edited from [12] and from Max-Planck IPP, Garching

Tokamaks creates this poloidal magnetic field by inducing a toroidal current in the plasma through current ramping in a central solenoid. This plasma current denoted I_p, induces in turn the desired poloidal field in the plasma.

This poloidal field can also be directly created via external coils, at the cost of much more complex coil shapes, in a concept labeled *stellarator*, but is outside the scope of this work.

0.2.3. ITER

ITER ("The Way" in Latin), Figure 12, is the largest tokamak project under construction, located in the south of France. ITER will serve as a bridge between current machines and full-scale electricity-producing fusion reactors. In fact, it has already started to play this role, as the completed and ongoing design, systems procurement, and construction phases are intrinsic parts of the fusion power plant life cycle. Thus, lessons learned in the context of ITER are and will be relevant for any fusion reactors, whatever the concept they rely on or their geographic location.

The scientific goals of ITER include the following:

- Achieve the so-called "burning plasma" state, where the plasma becomes largely self-heating for extended durations (400s)
- Reach $Q = 10$, with 500MW of fusion power from 50MW of external heating (i.e. with alpha heating twice the external heating)
- Test tritium breeding systems
- Demonstrate the safety characteristics of the operation of a fusion device in its nuclear phase
- Showcase the key lessons for the successful integration of the wide range of technologies needed for fusion energy production

ITER is a large-scale machine with a major radius of $R = 6.2$m, a plasma volume of 840m^3, and a 5.3T magnetic field at the center of the plasma. The choice of such a size is driven by the need to increase the energy confinement time, for which the major radius (i.e. sim the size) is a very strong driver. The widely used scaling law IPB98(y,2) on energy confinement time [13], which was used for ITER's physics basis includes the major radius to a power of ~ 2.

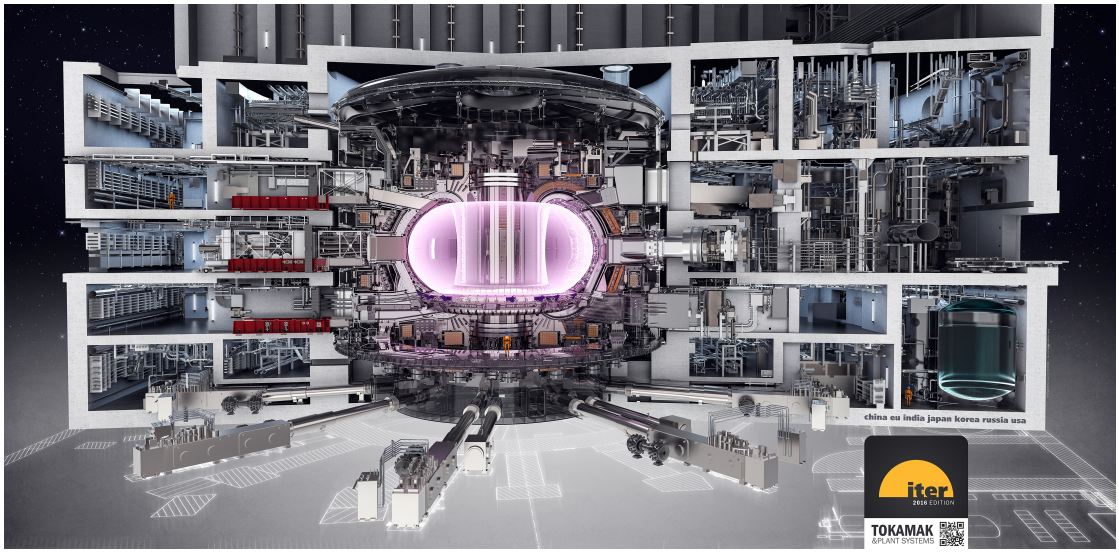

Figure 12.: 3D rendering of the ITER facility, and its vacuum vessel. From https://iter.org/

The project is in its construction phase, and studies related to the clarification of its operational window, and simulations of the behavior of the machine, are being carried out. The present work is set within this context, with numerical simulations of the boundary plasma, and the impacts of the different operating regimes on the plasma-facing components inside the vacuum vessel.

0.2.4. The heat exhaust problem

As it was seen in section 0.2.2, particles in tokamaks travel very quickly in the direction parallel to the magnetic field lines, which when projected in a poloidal plane, live on nested surfaces Figure 10.

In reality, particles also diffuse across field lines in the perpendicular direction, even if at a much slower rate, from the center toward the wall. This behavior stems from many different phenomena which will not be described in this section.

It is then seen that, somewhere along the wall of the reactor vessel, whatever its shape, will exist a location that intersects a field line. This flux surface is called the *separatrix* or *Last Closed Flux Surface* (LCFS).

The shape and location of the separatrix depend on the so-called *magnetic configuration*, which can be of two main types: *limiter* configuration and *divertor* configuration. They are illustrated in Figure 13.

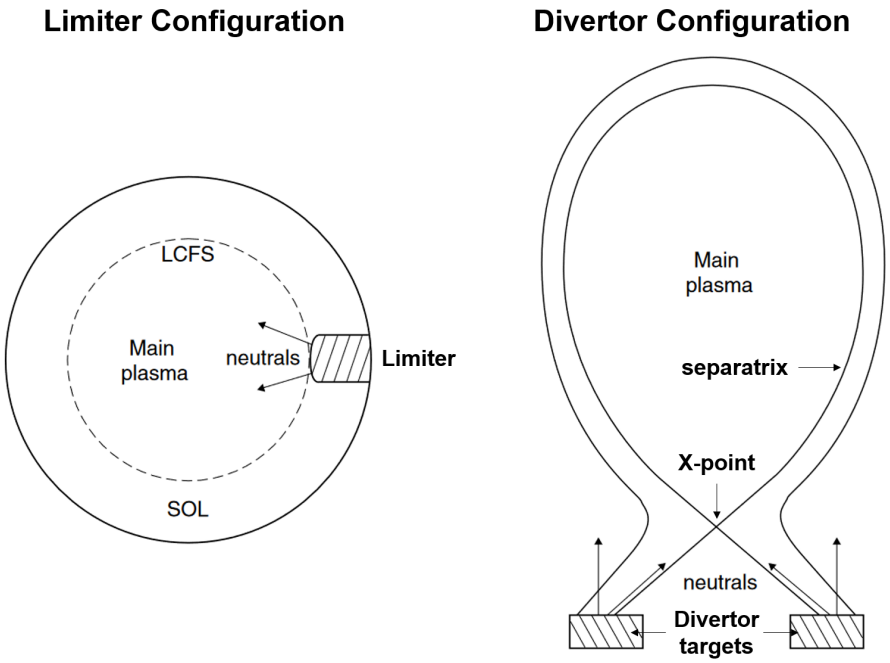

Figure 13.: Left: Limiter configuration. Right: Divertor configuration

The limiter configuration is the simplest, where the flux surfaces are concentric, and one intercepts the top of the limiter. The divertor configuration is obtained by placing an additional coil outside the vessel carrying a current in the same direction as the plasma current, producing a point of zero poloidal magnetic field. The field lines form an "X" shape at this point, which is consequently labeled as the *X-point*. The divertor configuration, even if it is more complex than the limiter one, has the advantage of localizing the contact region between the plasma and the wall farther away from the core plasma. It is beneficial for the performance of the core, as neutrals and impurities which can cool the plasma are produced there.

Due to the efficiency of the parallel transport vs the perpendicular one, the plasma flows outside the separatrix in a very thin layer (in brown in Figure 14 called the *Scrape-Off Layer* (SOL). It has a characteristic length λ_q which varies from a few millimeters to a few centimeters. Thus, the wall sections that intercepts the separatrix will be the only one in contact with the plasma, in is very narrow "wetted" area. Those concepts are further detailed in Chapter 1.

From a simple power balance, for the ITER $Q = 10$ burning plasma phase, 500MW of fusion power gives 100MW of alpha heating to the plasma (400MW are deposited uniformly across the chamber via non-confined neutrons), plus 50MW of external heating, minus 50MW of expected radiation in the core, results in 100MW falling on the plasma-wetted area. From current experimental observations and scaling laws, predictions for the possible size of the wetted area in ITER would be of the order of the square meter. This would lead to heat flux densities around 100MW/m², which is

not tolerable by any currently known material without significant damage and plasma pollution.

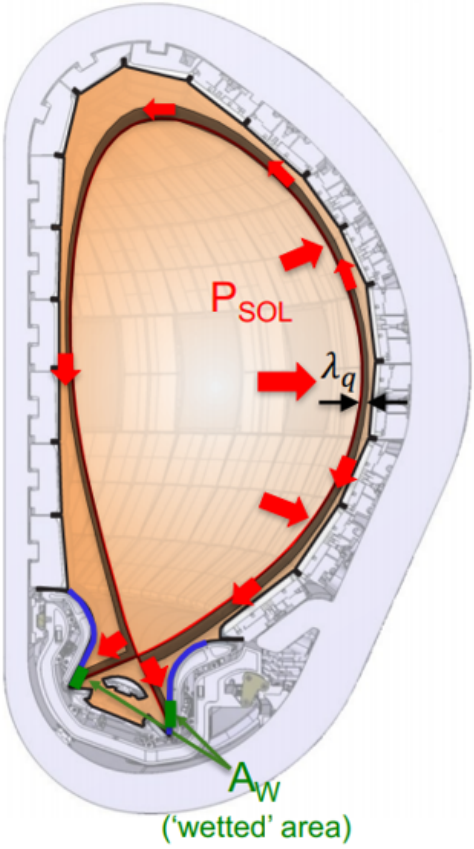

Figure 14.: Diagram illustrating the heat exhaust problem on a poloidal cross-section of ITER: all the power crossing the separatrix, i.e. 100MW in the burning plasma phase, travels in a very thin layer of characteristic width λ_q to the divertor targets. Diagram from C. Theiler (2017)

Therefore, one must find ways to operate the machine that strongly reduces the peak heat flux received by plasma-facing components. This is known as the *heat exhaust* challenge.

Additionally, these methods have to be compatible with the high temperatures and densities in the core plasma, which are necessary to provide the conditions for fusion. This is known as the *core-edge integration* problem.

One way to mitigate these problematic heat fluxes is to operate in conditions leading to plasma *detachment*, which consists in creating a cushion of neutral gas to protect the plasma-facing components. Thus, detached regimes are crucial for the operation of reactors, but are not trivial to access as was observed in current machines. The physics involved in detachment is complex, and not all is fully understood yet, which is why modeling efforts are particularly important for this topic.

Also, even if the majority of the plasma falls on the so-called *strike points* located on the *divertor* at the bottom of the machine, plasma and neutral particles can still be transported to the rest of the vessel wall, called the *first wall* Figure 1.2, potentially leading to erosion and plasma contamination.

The two latter aspects are central topics of the present thesis.

0.3. Thesis objectives and outline

The present work is set in the context of addressing the heat exhaust challenge for ITER. Its goals are:

1. the assessment of the fluxes and the plasma conditions on the first wall of the ITER machine,
2. the study of the detachment mechanisms at play during the different divertor regimes planned for ITER operations
3. the analysis of the behavior of the plasma of the far-SOL
4. the analysis of drivers of the first wall erosion and their sensitivity to two parameters: throughput (operational parameter), and the possible formation of density shoulders in the far-SOL (parameter related to our incomplete understanding of the physics)

More precise definitions of those concepts are given in the following chapters. To support the exercise, an in-depth analysis of the plasma-neutral interactions in the simulations is carried out.

The thesis is structured as follows:

- Chapter 1: The basics of edge plasma physics and of the so-called Scrape-Off Layer are presented, including a description of the different operating (divertor) regimes. The relevant and considered plasma-wall and plasma-neutral interactions are introduced.
- Chapter 2: The numerical simulation tools are presented, consisting of two integrated codes: the SOLEDGE3X plasma solver and the EIRENE plasma-neutral and plasma-wall interactions solver.
- Chapter 3: The challenges of simulating ITER plasmas are then highlighted, and the improvements made to physics model, and the to the numerical aspects of the codes in the context of this work are presented. Results are then compared with those from the well-established SOLPS-ITER code.
- Chapter 4: The mechanisms of the detachment in the simulated ITER cases are studied through the prism of plasma-neutral interactions.

- Chapter 5: Results at the first wall are analyzed and interpreted, by studying the evolution of the plasma profiles in the SOL, and including considerations on the variations of the power decay length λ_q. First wall gross erosion rates and their drivers are assessed.
- Chapter 6: The same exercise as in chapter 5 is carried out, but now with the objective of assessing the sensitivity of results to the possible formation of density shoulders in the far-SOL, a topic where little certainty exists at the moment regarding ITER.

1. Physics of the density regimes in tokamaks

Contents

1.1. Introduction

This chapter introduces the basics of physics at the boundary of tokamaks and a short description of the different divertor regimes. After providing a simplified picture of this plasma region, its boundary conditions (upstream and downstream) are considered. Then, a characterization of the divertor regimes is mentioned using elements of a simple model and experimental observations. Those regimes will serve as an angle of analysis in the following chapters.

1.2. The Scrape-Off Layer (SOL)

1.2.1. Structure of the boundary plasma and the tokamak vessel

The content of this work mainly relates to the *boundary plasma* of tokamaks. This region includes the outer layers of the core confined plasma up to the so-called separatrix (described below), plus its extension toward the wall of the machine, as is shown in poloidal cross-sections in Figure 1.1, as schematic view on the left and more specifically for the case of ITER simulations on the right.

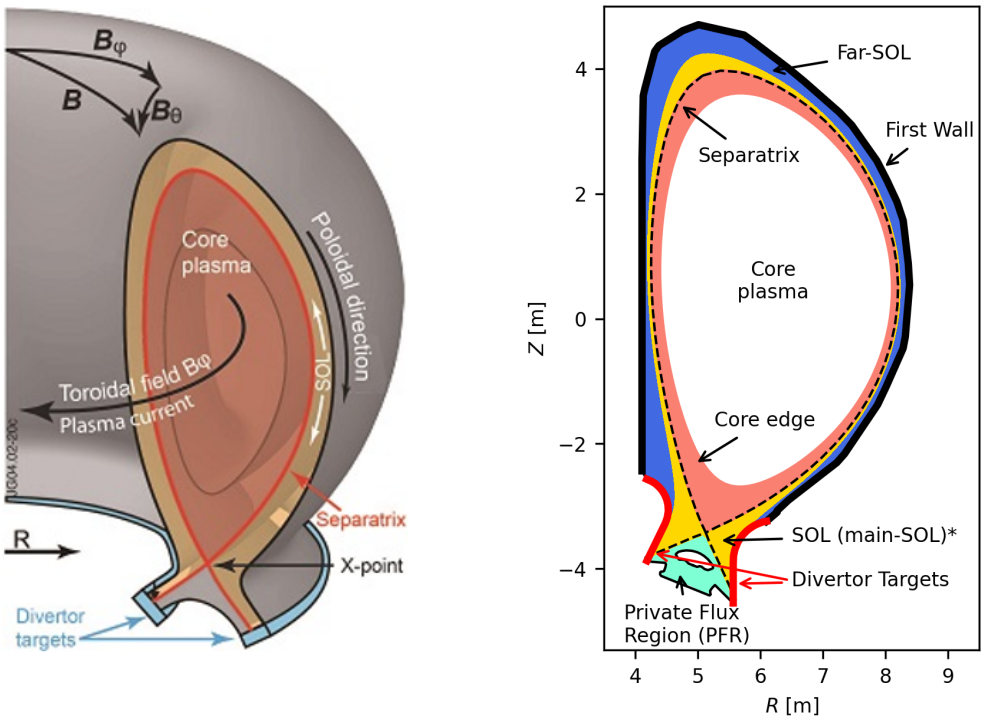

Figure 1.1.: Left: Generic simplified representation of the SOL. Right: Section of the boundary plasma in ITER, represented in the poloidal plane. The "main-SOL" or "near-SOL" is artificially widened here for visibility at the outer midplane to 10cm (main plasma parameters have decay lengths rather of the order of the centimeter or below).

More specifically, the boundary plasma, Figure 1.1, is composed of:

- the *edge* of the confined plasma: the region where field lines are still closed, and so the plasma is transported in the radial direction, until it crosses the separatrix.

- the *separatrix*: this virtual surface delimits the region of closed field lines and the region of open field lines, where plasma is transported toward the wall on its path along magnetic field lines.
- the *Scrape-Off Layer* (SOL), the region where field lines are open and intersect the divertor targets and the first wall. It can be further broken down into two sections:
  - the *near-SOL*: it includes the region of the SOL where the density and temperatures are still close to the ones at the separatrix, and most of the power is transported to the targets through this region. Its width in the perpendicular direction can range from millimeters to centimeters.
  - the *far-SOL*: it includes the rest of the SOL beyond the near-SOL, up to the first wall.
- the *Private Flux Region* (PFR): the region containing the field lines below the X-point.

The wall of the vessel, shown in thick lines in black and red in Figure 1.1, contains two main sections:

- the *divertor*, a region of strong plasma-wall interaction where materials have to be particularly resilient. Figure 1.3 shows the ITER divertor and its main subcomponents: the baffles, targets, reflector plates, and dome. This terminology to label the different parts of the divertor will be used further on.
- the *first wall*, consisting of the rest of the wall facing the plasma, less subject to plasma-wall interaction. Figure 1.2 shows the structure of the first wall in the case of ITER.

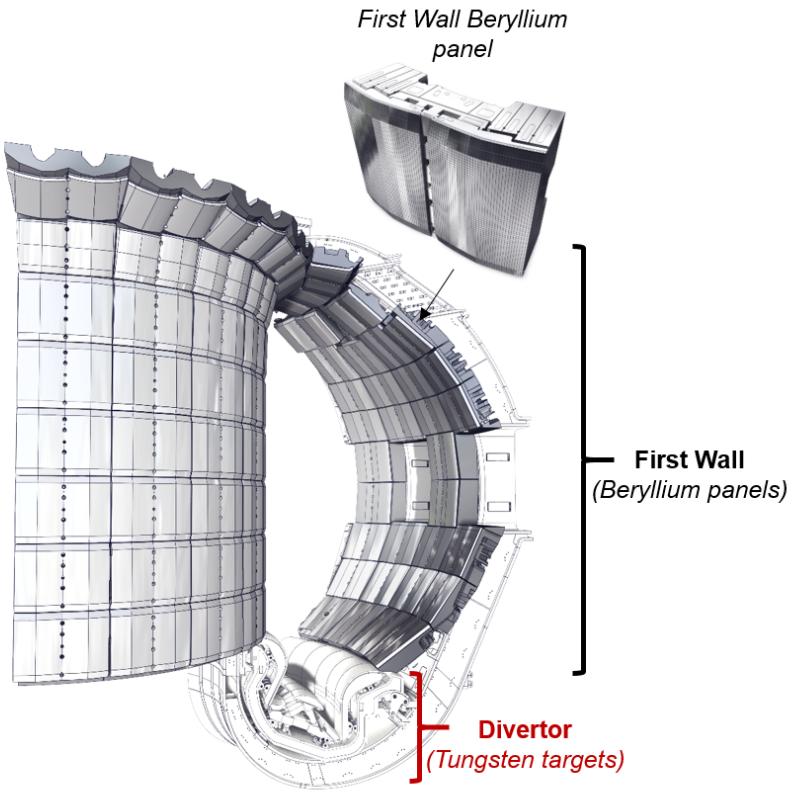

Figure 1.2.: 3D rendering of the interior of the vacuum vessel of ITER, showing the first wall Beryllium tiles and the divertor region. From www.iter.org.

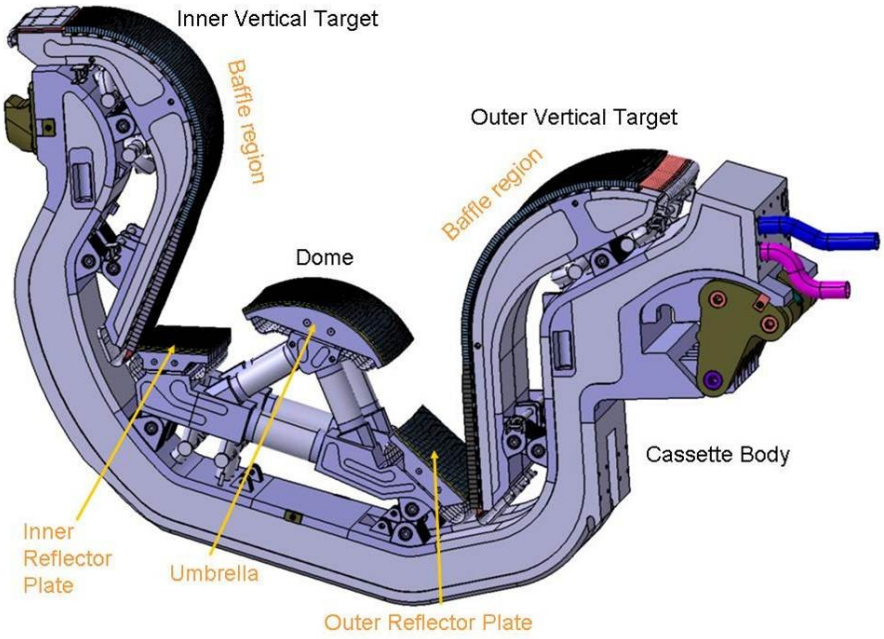

Figure 1.3.: 3D rendering of the divertor of ITER, showing sub-component. Targets, baffle, reflector plates, and dome. From www.iter.org.

1.2.2. Plasma flow along the SOL

As will be seen in the next section, solid surfaces form perfect particle sinks for the plasma. Therefore, once the radially transported plasma particles cross the separatrix (relatively slowly due to the magnetic confinement), they travel very quickly along the field lines towards the targets which are magnetically connected to the separatrix. This phenomenon is illustrated in Figure 1.4, where the SOL has been "straightened out" for clarity. The spatial extension of the particle deposition at the targets depends, if nothing else occurs in the SOL, on the ratio of the parallel transport efficiency to the perpendicular transport efficiency, and on the field line length which is also called the *connection length*.

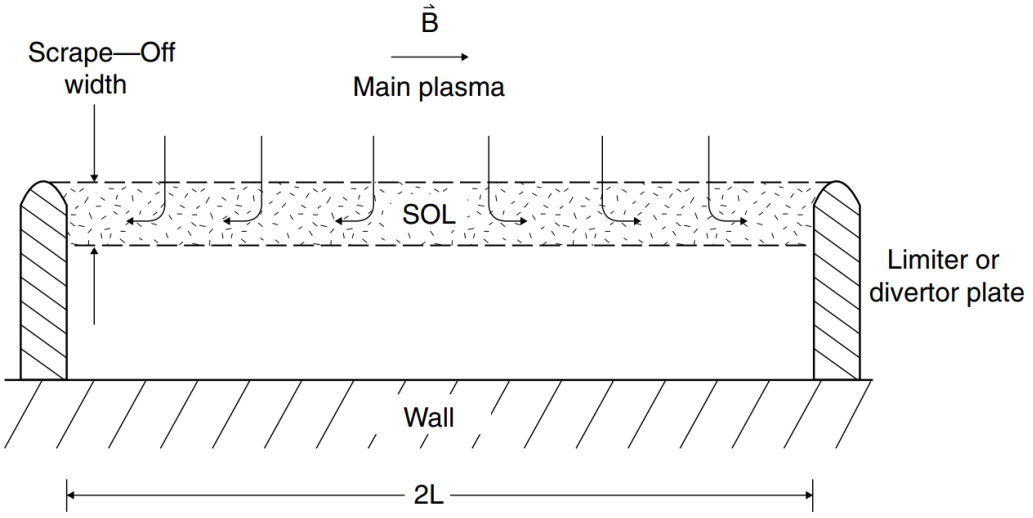

Figure 1.4.: Diagram of the SOL being straightened out for easier visualization and modeling. Particles and heat flow out of the core in the perpendicular direction (here vertically downwards), and are transported in the parallel direction (horizontal) to the targets on the sides. From [14].

From carrying out simple balances and assuming a steady state, one can show (e.g. in [14]) that the particle and energy fluxes out of the core will be deposited on a short characteristic width (denoted the *Scrape-Off Layer width* in Figure 1.4) at the targets. This results in fact in the focusing of the perpendicular flux from the edge that was initially spread over the whole flux surface at the separatrix into this small width at the target.

To pursue the analysis of the behavior of the plasma in the SOL, we model the plasma behavior along a field line, neglecting elements related to the perpendicular direction further out in the SOL. The considered field line extends from the so-called *upstream* location at the intersection of the separatrix and the outer midplane, to the *downstream* location at the targets. The upstream plasma conditions and fluxes are taken as inputs, while the fluxes at the target are considered outputs. The exercise is carried out by invoking and investigating the particle, momentum, and energy conservation equations along this field line, and considering asymptotic behaviors. The geometry is furthermore assumed straight with a constant magnetic field to simplify. First, we turn to plasma fluxes at the surfaces, which form the downstream boundary conditions.

1.2.3. Plasma-Wall interaction part 1: plasma particle and energy outfluxes

Electrons are at least ~ 2,000 times lighter than ions. In a plasma roughly at thermal equilibrium, i.e. where the electron and ion temperatures are not too far apart as is the

case in tokamak boundary plasmas, the electron velocity is around 60 times greater than the ions'. Due to this, when plasmas come into contact with a solid surface, electrons are the first to reach the surface, forming a net negative charge there that is felt by the plasma up to a few micrometers before being shielded. This region is called the *electrostatic sheath*. The ions are then accelerated towards the wall by the resulting electric field, and electrons are repelled. Only the most energetic electrons near the surface can therefore traverse this repulsive field, and reach the wall. The electron and ion particle flux equalize, so that the plasma bulk remains globally neutral.

Under such conditions, it can be shown (as done in [14]) that the particle flow at the sheath entrance has to be at least equal to the plasma sound speed (the so-called *Bohm criterion*).

$$v_{se} \geq c_s \simeq \sqrt{\frac{(T_i + T_e)e}{m_i}}$$

With the following notations:

- v_{se} the plasma fluid velocity at the sheath entrance ("se")
- c_s the plasma sound speed
- T_e the electron temperature, in eV
- T_i the ion temperature, in eV
- m_i the ion mass, in kg
- e the elementary charge

Hereinafter, it is taken in its restrictive form as we assume the plasma is subsonic:

$$\Gamma_t = n_t c_{s,t}$$

- Γ_t is the target particle flux density
- n_t is the plasma density at the target
- $c_{s,t}$ is the plasma sound speed at the target

Following again [14] and the references therein, the power flux to the surface at the sheath entrance for ions and electrons can be approximated as:

$$q_i = \gamma_i T_i e n v_{se} = \gamma_i T_i e n c_s \tag{1.1}$$
$$q_e = \gamma_e T_e e n v_{se} = \gamma_e T_e e n c_s \tag{1.2}$$

where the Sheath Heat Transfer Factors (SHTF) can be taken as $\gamma_e \simeq 4.5$ and $\gamma_i \simeq 2.5$, and $v_{se} = c_s$ is assumed at the sheath entrance.

1.2.4. Plasma-Wall interaction part 2: Recycling

When plasma ions impact the wall, they immediately capture an electron, neutralize, and may undergo several fates Figure 1.5:

- *fast reflection* or *backscattering*: the ion neutralizes into an atom, but is not absorbed in the wall. It retains most of its kinetic energy and is reflected in a direction that depends on the incidence angle of the ion at the wall. This direction is however not the one of the incident magnetic field line because of the electrostatic acceleration in the sheath (see section 4.3.2.2 for a discussion on incidence angles). This produces "fast" atoms coming back into the plasma.
- *thermalization*: the ion neutralizes into an atom but penetrates deeper into the material, where it recombines with another atom to form a molecule. At this stage, all incoming kinetic energy of the ion is transferred to the wall material lattice. Later on, the molecule escapes from the wall back into the plasma with an energy corresponding to the thermal energy of wall material (i.e. the temperature of the wall) atoms in the lattice, hence the term "thermalization". This produces a very "slow" molecule coming back into the plasma, as the wall temperature is much lower than the plasma temperatures.

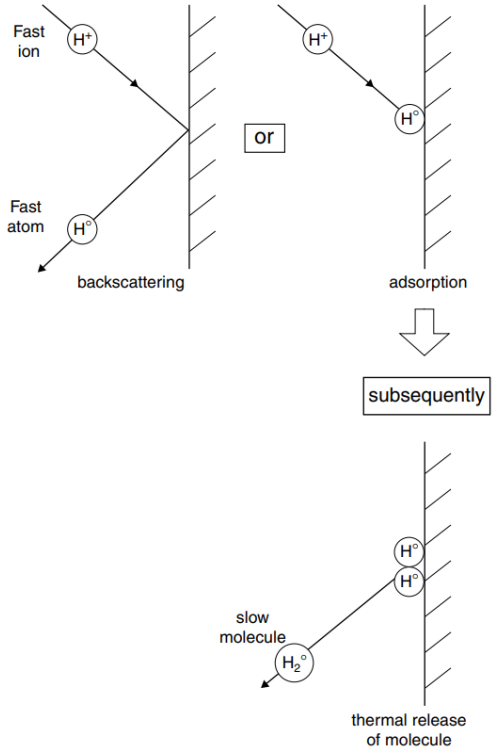

Figure 1.5.: The two kinds of recycling process, from [14] p.39

These neutral particles are then ionized through collisions with the plasma, and are transformed back, or *recycled*, into charged plasma particles. This process requires energy from the incoming plasma flow. Also, the higher the ion flux to the wall, the more neutral particles are generated and reinjected into the plasma. Thus, the incoming plasma loses increasingly more energy and momentum through collisions within this thickening neutral cloud as the target particle flux grows. This topic is addressed in more details in the following paragraphs.

1.3. Divertor regimes

1.3.1. Introduction of regimes

Coming back to a global view of the SOL, we have seen in the previous paragraphs elements related to the downstream plasma fluxes (the outputs). We now focus on how those fluxes change with varying plasma conditions on the upstream side of the SOL at the separatrix. While the power flowing out of the edge into the SOL field line will be taken as constant for the present analysis, specific attention will be paid to the consequences of increasing the upstream plasma density n_u on the plasma conditions at the targets, and especially on the target particle flux density Γ_t.

This approach is used to introduce the so-called *divertor regimes* in this subsection. Those aim at describing broad categories of plasma behaviors near and at the divertor targets, as a function of upstream plasma conditions. In the rest of this manuscript we will use references to these regimes to describe the overall plasma state in our simulations.

The reason for choosing the upstream density as an input parameter relates to its close relation to an operational control parameter of tokamaks, where midplane density measurements can be made to create a feedback controller on the fuelling rate to reach desired values.

Four regimes are introduced and characterized in the following sub-sections, in order of increasing upstream density, at fixed upstream heat flux and magnetic and wall geometry. They are summarized in Figure 1.6.

The key quantity chosen here to define them is the particle flux to the target (vertical axis in the figure) as a function of the upstream density. This choice here stems from the fact that its evolution, as will be shown later, allows on its own to identify each regime. The regimes themselves are characterized by two dimensions: the dominant mechanism determining the parallel heat transport, and the importance and effect of the presence of neutrals on the particle, momentum and energy balance of the plasma.

Each of the next subsections mentions the identifying feature of the regime from the target particle flux evolution as a function of the upstream density.

Especially for high upstream density regimes, other definitions exist, as mentioned in [15, 16], but are not detailed here. For example one can use the target temperature or target heat fluxes, and are relevant depending on the quantities of interest. In this

document, we will restrain the considerations to the target particle fluxes.

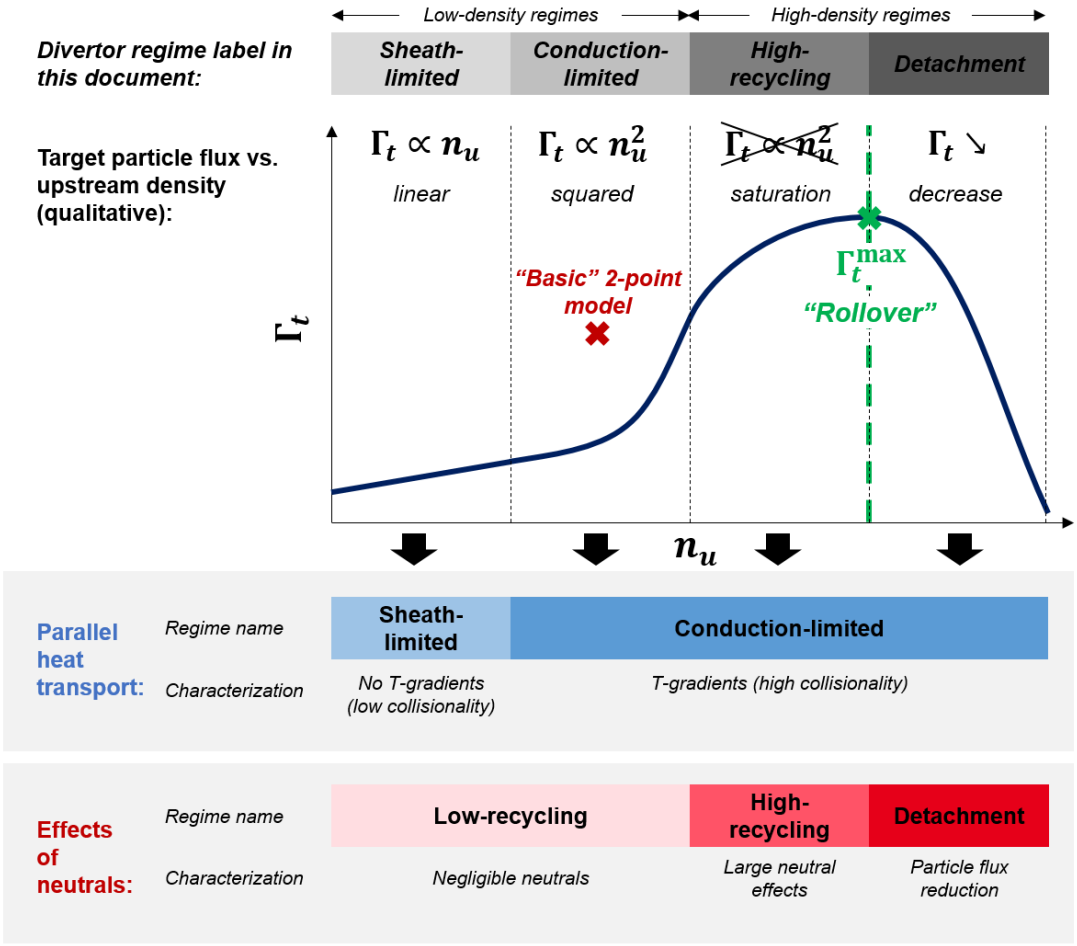

Figure 1.6.: Summary of the divertor regimes considered here, from definitions relating the heat transport mechanism in the SOL, the importance of effects from neutrals, and the target particle flux as a function of the upstream density.

1.3.2. The Sheath-limited regime

From the analysis of the SOL presented above, one can derive an approximate criterion to assess the existence of parallel gradients of the temperature [14] (relations 4.112 and 4.113) along the SOL field lines between the upstream and the target. This quantitative criterion scales with $n_u^{-\frac{7}{4}}$, and thus for very low-density regimes, one can assume an isothermal SOL. This comes from the strong increase in the plasma conductivity with temperature, especially the electron's ($\kappa \propto T^{\frac{5}{2}}$, see next section the Spitzer-Harm expression). At fixed input power, the upstream temperature rises with decreasing density, and very low gradients are sufficient to conduct the heat flow. At the sheath however, its electro-static repulsion effect on the electrons acts as a insulator and thus

"limits" the ability of the plasma to exhaust heat without high enough temperatures, hence the name.

Also, since no phenomena involve loss of momentum along field lines, the total pressure (static and dynamic) is conserved. Assuming equal temperatures for ions and electrons $T_i = T_e = T$, a zero upstream plasma flow velocity, plus the Bohm criterion at the targets, one obtains:

$$p = p_{stat} + p_{dyn} = 2nTe + m_i n v_{\parallel}^2 \tag{1.3}$$

$$p_u = p_t \tag{1.4}$$

$$2n_u Te = n_t Te + \frac{1}{2} m_i n_t c_s^2 \tag{1.5}$$

$$2n_u Te = n_t Te + \frac{1}{2} m_i n_t \frac{2Te}{m_i} \tag{1.6}$$

$$n_u = 2n_t \tag{1.7}$$

Where:

- p is the total pressure
- p_{stat} is the static pressure
- p_{dyn} is the dynamic pressure
- n_u is the upstream density
- n_t is the target density

This gives the target particle flux:

$$\Gamma_t = 2n_u c_{s,t}$$

In the sheath-limited regime, the target particle flux scales linearly with upstream density.

1.3.3. The Conduction-limited regime

Increasing further the upstream density, the previous criterion regarding the absence of temperature gradients breaks down, and the isothermal assumption is dropped. At lower temperatures, it is rather now the conductivity of the plasma which determines ("limits") the temperature profile in the SOL, and the effects of the sheath can be neglected. The $T_i = T_e$ assumption is still retained.

Adding into the model the conducted heat flux via the classical Spitzer-Harm formula:

$$q^{cond} = \kappa_0 T^{\frac{5}{2}} \nabla_{\parallel} T \tag{1.8}$$

Where:

- κ_0 is the thermal conductivity coefficient
- $\Gamma_\parallel$ is the parallel particle flux density
- $\nabla_\parallel T$ is the parallel temperature gradient

From there, one can obtain the so-called *basic two-point model*:

$$n_u T_u = 2 n_t T_t \tag{1.9}$$

$$T_u^{\frac{7}{2}} = T_t^{\frac{7}{2}} + \frac{7}{2}\frac{q_\parallel L}{\kappa_{0,e}} \simeq \frac{7}{2}\frac{q_\parallel L}{\kappa_{0,e}} \tag{1.10}$$

$$q_\parallel = \gamma T e n_t c_{s,t} \tag{1.11}$$

Where:

- $q_\parallel$ is the parallel heat flux entering the SOL from upstream (taken equal to the integrated radial outflux from the core edge)
- L is the connection length
- $\kappa_{0,e}$ is the electron thermal conductivity coefficient (60 times larger than the ion's)
- γ is the total sheath heat transfer factor ($\gamma = \gamma_e + \gamma_i$)

The approximation for the upstream temperature in Equation 1.10 is relevant because of the $\frac{7}{2}$ exponent.
This gives the target particle flux density:

$$\Gamma_t = \frac{n_u^2}{q_\parallel^{\frac{3}{7}}}\left(\frac{7}{2}\frac{L}{\kappa_{0,e}}^{\frac{4}{7}}\right)\frac{\gamma e^2}{2 m_i} \propto n_u^2$$

In the conduction limited regime the target particle flux density scales now as the square of the upstream density.

As one can expect, raising the upstream density can not increase the target particle flux indefinitely, and other mechanisms come into play which were neglected until this point: the interactions with neutrals through recycling.

1.3.4. The high-recycling regime

Experimentally, it was observed that increasing farther the upstream density would lead, after the n_u^2 dependency range corresponding to the conduction-limited regime, to a saturation of the target particle flux. It would then go through a maximum, and finally "roll over" and decrease significantly.

The high recycling regime refers to divertor regimes associated with larger ionization rates inside the SOL subdomain, in which particles undergo several cycles of wall recycling-ionization before being pumped out from the system. At this stage, the target particle flux grows more slowly than the n_u^2 relation and starts to saturate. The number of ionizations and collisions with neutral particles become so large that a non-negligible part of the plasma energy is transferred to the neutrals (and also exhausted through radiation). Thus, the remaining energy in the plasma reaching the target is reduced, and consequently so is the heat flux to the target materials.

Thus, this regime was identified as a way to protect the targets in future reactors.

In the high-recycling regime, the target particle flux density stops scaling with the two-point model square relation, still increases but goes to saturation.

1.3.5. Detachment regime

At a certain upstream density, the target particle flux is maximum, and increasing n_u further decreases Γ_t. This maximum point is called the *rollover*. At this stage, the power flux is already reduced significantly, but can still be too large for reactor-relevant scenarios, or may involve too high ion temperatures resulting in erosion (see in the next section). After the rollover, the heat and particle fluxes can become so weak that the surfaces almost do not see the plasma. This regime was therefore coined *detached regime*, in which the plasma density moves up the divertor legs instead of being in contact with the targets.

This phenomenon is illustrated by measurements in JET Figure 1.7, with the comparison to the conduction-limited regime extrapolation using the relation $\Gamma_t \propto n_u^2$.

The detachment regime starts after the rollover of the target particle flux, where the latter decreases with the upstream density.

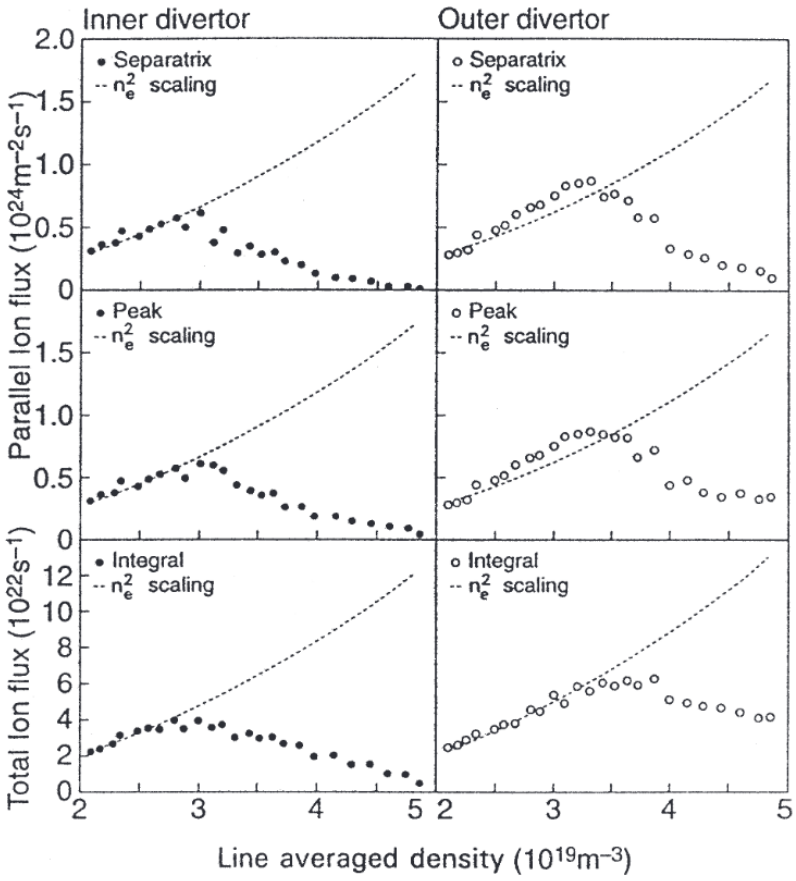

Figure 1.7.: Observations of the increase, rollover, and decrease of the target particle flux in JET (first line: flux density at the separatrix, second line: peak flux density, third line: integral flux) on the inner and outer targets, and comparison with the n_u^2 relation. From [17]

This behavior can also be enhanced by the voluntary addition of impurities in the SOL through the gas injection valves (e.g., Nitrogen, Neon, Argon), this process is called *seeding*. The rationale for doing so is to promote the removal of power by the radiating impurities, leading to easier access to detachment.

While it is clear that impurity radiation and increased interactions with neutrals play a role in the reduction of the target particle flux, many different root causes and mechanisms may exist to produce the "detachment" phenomenon, involving many different parameters for the plasma (conditions, composition, etc.) and the geometry (size, incidence angles from the magnetic configuration and the target inclination, divertor closure, etc.) [14, 18, 19]. Because of this, no exhaustive description of plasma detachment exists currently.

The chapter 4 will attempt a study of the plasma-neutral interactions at play during the detachment modeling of the ITER simulations considered. The following sections will focus on specific matters of plasma-neutral interactions.

1.3.6. Partial detachment

The term *partial detachment*, or *partially detached* regime, refers to the early stages of the detached regime while considering the whole plasma profile over the target in 2D, and not a single flux surface. The "partial" part of this expression denotes the fact that for the early stages after the rollover of the integrated particle flux across the target, some flux surfaces are detaching, i.e., have passed their rollover, while others have not and remain attached, with their particle flux density continuing to increase with upstream density. Each of the field lines at the target follows the same particle flux increase-rollover-decrease behavior, but not simultaneously in terms of upstream density: the farther the field line from the strike point, the stronger the field line rollover is shifted toward high upstream densities.

This effect is illustrated below in Figure 1.8, where a normalized particle flux from the outer target is plotted from the ITER cases simulations that will be considered in the following chapters. The left plot gives the position of the field lines with colors in 2D, and the right plot shows the particle flux as a function of the upstream density (at the separatrix at the outer midplane, not depending on the field line). Each particle flux is normalized by its maximum across the upstream density scan, showing that field lines exhibit that their rollover upstream density increases with the distance to the strike point (in color). The global rollover (across the whole target) is rather close to the one of the first field line, because the particle flux is much larger in absolute value there than on other flux lines. For the highest density case, the orange and red field lines which are the farthest from the strike point have not yet passed their rollover, and their particle flux continues to increase: they are still attached. Thus, the phrase "partially detached" will be used to denote this regime globally, because it is not yet in the globally "detached" regime where all field lines are detached.

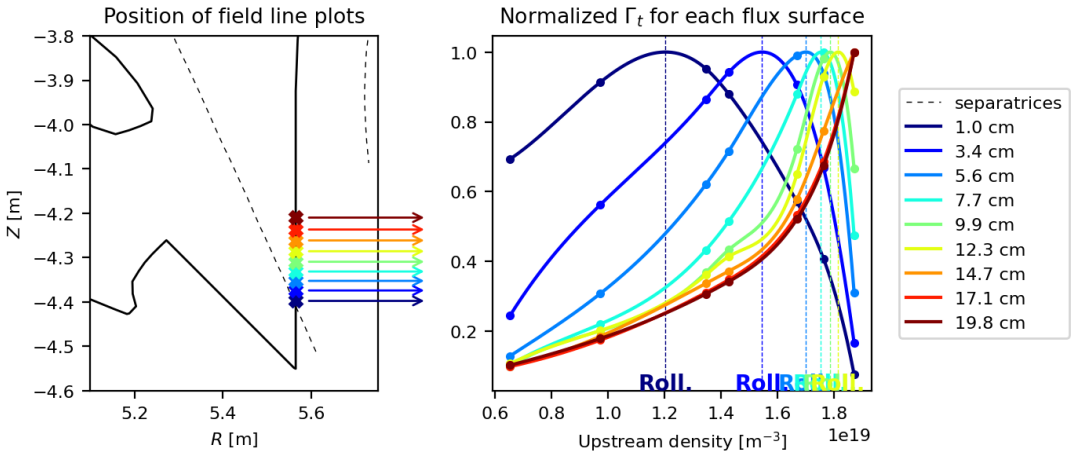

Figure 1.8.: Illustration of the partial detachment with the sequential rollover of each field line, with increased density. Left: the "x" marks represent the 2D position of the field lines of the right plot, at the outer target. Those are from the ITER simulations that will be considered in the next sections. Right: particle flux for each field line at the outer target normalized to its maximum across the upstream density values. Each color represents a distance from the strike point, which is given in the legend in centimeters. Lines are artificially smoothed for better legibility, and points from simulations are noted with a dot marker.

1.4. Plasma-Neutral interactions

Plasma-neutral interactions encompasses the different types of collisions (also denoted here *reactions*), between plasma particles and neutral particles. Their description has two objectives:

1. to account for their effect on the plasma itself
2. to assess their own contribution to metrics of interest that are not directly related to the plasma (e.g. neutral pressure, neutral heat fluxes, erosion, radiation, etc.)

Collisions are usually classified into two types of collisions:

- **Elastic collisions**: such collisions are characterized by the conservation of the total momentum and kinetic energy of the particles involved, without any modification of either the nature of the particles or any of their internal attributes[1].
- **Inelastic collisions**: on the contrary, inelastic collisions involve the creation, removal of particles, or change in internal attributes. Such internal attributes can include:

[1]Resonant symmetric charge transfer reactions may also be labeled as "elastic", since the projectile and the product particle species are the same.

- binding energy (electron-ion i.e. ionization energy, molecular binding energy)
- atomic or molecular electron excitation state
- molecular vibrational state
- molecular rotational state

Internal attributes can be summarized as contributors to the total *internal energy* of the considered particle, and can be represented as different levels of a *potential energy*. The zero point of this potential energy is set to the energy of a neutral molecule in its fundamental state (i.e., no excitation of any type).

During inelastic collisions, the total energy is conserved, i.e. the sum of the kinetic energy and potential energy.

As an example of an inelastic collision, let us consider the atom ionization, which creates a new plasma ion and electron from an electron impact on a neutral atom.

$$H + e^- \rightarrow \mathrm{H}^+ + e^- + e^-$$

For these types of reactions, the electron mass is usually neglected (as is the case in the model which will be used in the present work, except in specific cases), which results in the absence of momentum and kinetic energy transfer between the electron and the ion. Therefore, the momentum and kinetic energy of the created ion are those of the initial atom. The momentum conservation gives:

$$m_i \vec{v}_{atom} = m_i \vec{v}_{\mathrm{H}^+}$$

In terms of energy, one has to also take into account the potential energy. The ionization energy of the hydrogen atom (13.6 eV) is a binding energy between the ion and the electron. It is taken from the kinetic energy of the electron during the collision, and a new ion with a 13.6 eV potential energy is created:

$$E_{\mathrm{kin,atom}} + E_{\mathrm{kin,e^{-pre}}} = + E_{\mathrm{kin,e^{-post}}} + E_{\mathrm{kin,ion}} + E_{\mathrm{p,ion}} \tag{1.12}$$

$$E_{\mathrm{p,ion}} = E_{iz} \tag{1.13}$$

with:

- E_{th}: the thermal energy density
- $E_{\mathrm{kin}^{\mathrm{pre}}}$: the pre-collision kinetic energy density
- $E_{\mathrm{kin}^{\mathrm{post}}}$: the post-collision kinetic energy density
- E_{p}: the potential energy density
- E_{iz}: the ionization energy

General form of collisions in the case of hydrogen A general inelastic collision can be written in the form:

$$\sum_i P_i \rightarrow \sum_j P_j$$

Where P is any particle, of any type between electrons, ions, atoms, molecules, and also photons.

Specific attention is paid to the potential energy. One must consider that internal potential energy can transform into two forms:

- **radiation** (i.e. if there are photons of the RHS in the above reaction): particles in a state above the fundamental energy level can decay into a lower one through the emission of a photon. For example, atoms can radiate through a de-excitation process linked to a change in electronic excitation level.
- **kinetic energy**: during the breakup of molecules and molecular ions, the binding energy between the two nuclei is converted into kinetic energy for the product. This process is labeled *kinetic energy release* (KER) and energy transferred the *Franck-Condon* energy.

Correspondingly, the kinetic energy of an incident particle can also be transferred to internal attributes, and thus elevate the potential energy.

More practically, for the case of hydrogen plasmas, where atoms and molecules are considered, several types of reactions are of interest and are listed below. In the following list, it was chosen to use the standard IAEA terminology and abbreviations for atomic and molecular processes (https://amdis.iaea.org/databases/processes/).

- *Electron impact* processes:
  - **Excitation** (EEX → Electron impact EXcitation): the atom/ion is simply excited upon impact (i.e. the electron in the orbital of the impacted particle reaches a higher energy level) taking the excitation energy from the kinetic energy of the electron. In this case, the decay of the excited atom back to a lower state is very short, and a photon is emitted. This process has a probability to occur whichever electron energy, even if it is above the atom ionization energy. In the rest of this document, this process is included in the "atom ionization" EIN process below, even if it is an extension of the initial meaning. This process is thus a source of new ions and radiation as well.
  - **Ionization** (EIN → Electron Impact Ionization): if the electron is energetic enough, the atom can be ionized, taking the atom/ion ionization energy from the kinetic energy of the electron.
  - **Recombination** (ERR/ERT → Electron Recombination Radiative/Three-body): In this process, an ion captures an electron at low temperatures. The reaction involves exhausting both the incident kinetic energy of the

electron and the potential energy of the ion. The latter represents the decay of the captured electron from a high to a low energy level. This energy release can occur through two channels: either through the emission of a photon (*radiative recombination*), or through a collision with another free electron of the plasma (*three-body recombination*) in which the energy is transferred to the kinetic energy of this plasma electron. This process can be interpreted as the inverse of the EEX. Since the three-body recombination involves the presence of a second electron, this process is more frequent at high electron densities and low temperatures. Furthermore, at low T_e (13.6 eV $\gg T_e$), the electron population can be heated by this transfer, stabilizing the electron temperature, since the recombination rate drops with increased temperature.

  - **Dissociations** (EDI/EDE/EDR → Electron Dissociative Ionization/Excitation/Recombination): These processes cover the splitting of molecules or molecular ions. Several variants exist depending on the type and state of the outgoing particles: e.g. Dissociative Ionization, Dissociative Excitation, and Dissociative Recombination. These reactions are specific in the sense that they involve transforming the molecule binding energy into kinetic energy for the products. As a result, the outgoing atoms or ions can have up to a few eVs of energy even if the molecule was very slow initially.

- *Heavy particle impact* processes:
  - **Elastic Scattering** (HES → Heavy Elastic Scattering): This is a synonym for elastic collisions, i.e. without change of internal state.
  - **Charge Transfers** (HCX → Heavy Charge eXchange): These are collisions between an ion and a neutral particle (atom or molecule), in which an electron from the neutral particle is transferred to the ion in a collision similar to an elastic collision[2]. This process creates atoms born at velocities similar to the one of the local ion. Correspondingly, ions are created. This process can be viewed, in some approximation, as an elastic collision, except that the momentum and energy are simply swapped instead of being shared accordingly to the masses of particles involved.

Photon impact processes (for example *photo-excitation* or *photo-ionisation*) are not mentioned here and the plasma is assumed optically thin (see next chapter on modeling), but may also be relevant for high density regimes [20].

The challenge of choosing which processes to focus on to adequately describe tokamak plasmas is discussed in the following chapter section 3.3.1.

[2]This collision is often approximated in modeling as simply a velocity exchange, i.e. a scattering angle of π.

1.5. Erosion/sputtering of wall material

Finally, a specific matter related to plasma and neutral interaction with solid surfaces is introduced here: erosion.

Erosion, or sputtering (these two terms will be used equivalently here), is the process where atoms making up the solid surfaces (Beryllium in our case) are ejected from the lattice when undergoing impacts from incoming particles. For this to happen, the particle must have a high enough energy so that collision can break the chemical bond between the lattice atoms. For hydrogen nuclei on beryllium surfaces, the sputtering threshold energy is at 13eV [21, 22] (447eV for H on W), therefore incident particles arriving at the wall at an energy of this order of magnitude will produce erosion.

This topic is key for reactor performances as it is a driver in two particular matters:

- It determines the components' lifetime before they are too severely damaged and have to be replaced, which requires long downtimes and complex operations.
- It affects plasma performance by bringing radiating impurities into the plasma (plasma contamination), which could deteriorate the plasma condition in the core if the influx is too important.

Therefore, the following sections will include considerations of the computation of first wall beryllium erosion estimations for ITER plasmas.

2. Modelling the edge plasma with SOLEDGE3X-EIRENE

Contents

2.1. Introduction

A tokamak plasma is formed by a large number of particles (1×10^{21}) of several types, interacting with each other in various ways. In order to design a fusion reactor, one would need the ability to make accurate predictions on the plasma behavior in any

situation, so that one could optimize the parameters of interest, within a set of constraints. Of course, this is not possible from first principles as no analytic formulation is known to describe accurately enough the plasma's behavior. Furthermore, this system is also highly non-linear, and one can not use back-of-the-envelope calculations without over-simplifications beyond what is acceptable to design or operate a machine.

Thus, one has to rely on numerical simulations, which can actually serve two purposes: first, to assess the behavior of the plasma in a given operating scenario and evaluate its performance according to the chosen metrics of interest, and second, to investigate the simulation outputs to learn how the different physics included in the physical model translate ultimately as a result for the plasma.

This chapter introduces the approaches and assumptions of the models implemented in the numerical simulation tools that were used to produce the results presented further in this work. To model the rich physics involved in the scrape-off layers of tokamaks, we rely on two approaches, each of them applied to a different perimeter. The first is the modeling of the plasma charged species via a fluid model with the SOLEDGE3X plasma solver, used here in a mean-field approach. The second is the modeling of neutral particles via a kinetic Monte-Carlo method with the EIRENE code. Both are iteratively coupled, to evolve the system in time, until a steady state is reached, which is taken as the solution. In the following sections, the equations solved by each code are presented, along with consideration regarding their specificities.

2.2. Different approaches to numerical simulation

In the numerical simulation landscape, one has to make a trade-off between fidelity and computation cost:

- **Accuracy**: This point related to two aspects. First, the accuracy of the physics to be described (the *model*), i.e., the list of physical phenomena taken into account in the description of the system. Second, the resolution of the phase and time space, which will determine the discretization/numerical error, and third, coupling tools with different numerical methods (finite-volume and Monte-Carlo as will be seen in the next section) results in additional errors and bias [23].

- **Computation cost**: The computation time and ressources needed to obtain useful results from the simulations.

One can readily guess that it is not feasible for current computers to calculate the individual motion of all 1×10^{21} particles in a tokamak. Therefore reduced models and elaborate numerical methods have to be devised in order to obtain usable results.

Within the landscape of fusion plasmas modelling, several approaches are possible, with different levels of accuracy, which are used complementarily depending on which aspects of the physics the modeler wishes to investigate. The main ones are given here as examples, going from microscopic to macroscopic descriptions:

1. **Particle tracking codes**: the full phase space is described and evolved for each particle in the system, 3 dimensions of spaces, 3 dimensions of velocities, 1 dimension of time. While treating all particles in such a way is beyond the means of current modern computation capabilities, two derived approaches exist. The first is through a statistical approach called Monte-Carlo, and is the basis of the EIRENE code, which is presented in the following section. Another is to deal with "macro-particles", each of them representing many real particles, and is the basis of the *Particle-in-Cell* [24] method.

2. **Kinetic codes**: the full phase and time spaces are described, but now only for certain elements obtained from a discretization (Eulerian or Lagrangian), using and evolving a so-called *distribution function*, a concept that is introduced briefly further on.

3. **Gyrokinetic codes**: The gyromotion of particles in strong magnetic fields is averaged to drop one dimension of velocity, retaining only two dimensions to represent the velocity space: one velocity dimension for the gyrocenter of particles, and one for the magnetic moment.

4. **Fluid codes** Such codes only evolve moments of the distribution functions, i.e., certain integrals of the distribution functions over the velocity space. These moments can give, for example, conservation equations for the density, momentum, and energy. Thus only a few scalar fields are left to be described on only 3 dimensions of spaces and 1 of time. However, in order to obtain such a system with a finite number of equations, one has to introduce a further set of approximations called the closure (as is briefly described further in this chapter). This is the method used in the SOLEDGE3X introduced below.

2.3. The SOLEDGE3X code

This section presents the approach of fluid modeling of the plasma used by the SOLEDGE3X code, and then the equations which are solved in the context of the mean-field transport mode without drifts, which is the mode used for ITER simulations reported in this manuscript.

2.3.1. Moments of the distribution function f_α

The starting point of the fluid modeling is the kinetic equation describing the time evolution of the distribution function.

The *distribution function* of a particle species α corresponds to the number of particles in the infinitesimal volume of the phase space, i.e., with a velocity between $\mathbf{v}$ and $\mathbf{v} + d^3\mathbf{v}$, within the volume between $\mathbf{r}$ and $\mathbf{r} + d^3\mathbf{r}$, at time t.

$$d^6 N_\alpha(t) = f_\alpha(\mathbf{r}, \mathbf{v}, t) d^3\mathbf{r} d^3\mathbf{v}$$

The time evolution of f_α is given by the generalized Boltzmann equation below. It is a "generalized" form in the sense that it combines, for the collisional integrals on the *Right-Hand-Side* (RHS), the elastic collision integral from the Boltzmann equation, and also the inelastic processes S_α integral representing the chemical reactions or changes in quantum states of particles, which is described in the so-called *Wang-Chang–Uhlenbeck* equation (WCU).

$$\frac{\partial f_\alpha}{\partial t} + \mathbf{v}\cdot\boldsymbol{\nabla}_\mathbf{r} f_\alpha + \frac{\mathbf{F}_\alpha}{m_\alpha}\cdot\boldsymbol{\nabla}_\mathbf{v} f_\alpha = \sum_\beta C_{\alpha\beta}(f_\alpha, f_\beta) = C_\alpha^{\text{Coul.}} + S_\alpha \tag{2.1}$$

Where:

- $\mathbf{F}_\alpha$ is the macroscopic force applied on particles of species α. In our case, it is $\mathbf{F}_\alpha = Z_\alpha e\,(\mathbf{E} + \mathbf{v}\times\mathbf{B})$. It is labeled macroscopic because $\mathbf{E}$ and $\mathbf{B}$ are fields that do not depend on $\mathbf{v}$.
- $C_{\alpha\beta}(f_\alpha, f_\beta)$ represents the microscopic collision operator between particles of species α and species β, which includes two types of collisions:
  - $C_\alpha^{\text{Coul.}}$: Coulomb (i.e., elastic) collisions with the other charged species β.
  - S_α: Inelastic collisions, which include ionization, recombination, and interactions with neutrals.

As will be seen later, the $C_\alpha^{\text{Coul.}}$ is included in the fluid treatment of the charged species by the plasma solver SOLEDGE3X through the so-called collisional closure, and the inelastic one S_α by the plasma-neutral code EIRENE[1].

Then, it is possible to derive from Equation 2.1 equations for the plasma density, momentum, and total energy. To do so, one takes the so-called *moments* (Equation 2.2) of this equation, i.e., multiplying it by a power of $\mathbf{v}$ (0, 1, and 2, for obtaining equations on respectively density, momentum and energy), and integrating it over the $\mathbf{v}$ space. This makes moments of the distribution function f_α appear, which are linked to the fluid quantities which will be of interest. The moment of order k of the distribution function reads:

$$\mathcal{M}^k(f_\alpha) = \iiint_\mathbf{v} \mathbf{v}^k f_\alpha(\mathbf{r}, \mathbf{v}, t)\, d^3\mathbf{v} \tag{2.2}$$

More precisely, from the f_α moments of order 0, 1 and 2 comes the definition of the

[1] In the case with multiple ion charge states, SOLEDGE3X also includes the ionization/recombination processes of charge states above 1, which are part of S_α. Those are not present in pure hydrogen plasmas, as is the case in this work.

particle density n_α, fluid velocity u_α, total energy E_α and temperature T_α:

$$\mathscr{M}^0(f_\alpha) = \iiint_{\mathbf{v}} f_\alpha(\mathbf{r},\mathbf{v},t)d^3\mathbf{v} = n_\alpha(\mathbf{r},t) \tag{2.3}$$

$$\mathscr{M}^1(f_\alpha) = \iiint_{\mathbf{v}} \mathbf{v} f_\alpha(\mathbf{r},\mathbf{v},t)d^3\mathbf{v} = n_\alpha(\mathbf{r},t)u_\alpha(\mathbf{r},t) \tag{2.4}$$

For the moment of order 2, it is convenient to multiply by m_α, and at order two, the integrand is now the tensor product $\mathbf{v}\otimes\mathbf{v}$ which gives the total pressure tensor $\overline{\overline{\Pi}}_\alpha$:

$$m_\alpha\mathscr{M}^2(f_\alpha) = \iiint_{\mathbf{v}} m_\alpha\mathbf{v}\otimes\mathbf{v} f_\alpha(\mathbf{r},\mathbf{v},t)d^3\mathbf{v} = \overline{\overline{\Pi}}_\alpha(\mathbf{r},t) \tag{2.5}$$

Decomposing the velocity using the fluid velocity defined in Equation 2.4:

$$\mathbf{v}_\alpha = \mathbf{u}_\alpha + \mathbf{v}'_\alpha \tag{2.6}$$

$$\overline{\overline{\Pi}}_\alpha = \iiint_{\mathbf{v}} m_\alpha\mathbf{u}_\alpha\otimes\mathbf{u}_\alpha f_\alpha d^3\mathbf{v}' + \iiint_{\mathbf{v}} m_\alpha\mathbf{v}'\otimes\mathbf{v}' f_\alpha d^3\mathbf{v}' \tag{2.7}$$

$$\overline{\overline{\Pi}}_\alpha = m_\alpha n_\alpha \mathbf{u}_\alpha\otimes\mathbf{u}_\alpha + \overline{\overline{\mathbf{p}}} \tag{2.8}$$

$$\text{with:} \qquad \overline{\overline{\mathbf{p}}} \equiv \iiint_{\mathbf{v}} m_\alpha\mathbf{v}'\otimes\mathbf{v}' f_\alpha(\mathbf{r},\mathbf{v},t)d^3\mathbf{v}' \tag{2.9}$$

because f_α is symmetric in $\mathbf{v}'$, and introducing $\overline{\overline{\mathbf{p}}}$ as the static pressure tensor.

Now, we define p_α the static scalar pressure as the third of the trace of the pressure tensor, and it is then possible to introduce the temperature T_α, thermal energy E_α^{th} and kinetic energy E_α^{kin} and thus the total energy E_α:

$$p_\alpha \equiv \frac{1}{3}\mathrm{Tr}\left(\overline{\overline{\mathbf{p}}}\right) = \frac{2}{3}\iiint_{\mathbf{v}} \frac{1}{2}m_\alpha\mathbf{v}'^2 f_\alpha(\mathbf{r},\mathbf{v},t)d^3\mathbf{v} = \frac{2}{3}E_\alpha^{\text{th}} \tag{2.10}$$

$$T_\alpha \equiv \frac{p_\alpha}{n_\alpha} \tag{2.11}$$

$$E_\alpha^{\text{th}} = \frac{3}{2}n_\alpha T_\alpha \tag{2.12}$$

$$E_\alpha^{\text{kin}} = \frac{1}{2}m_\alpha n_\alpha \mathbf{u}_\alpha^2 \tag{2.13}$$

$$E_\alpha = E_\alpha^{\text{kin}} + E_\alpha^{\text{th}} \tag{2.14}$$

2.3.2. Moments of the WCU equations and closure

By taking the moment of order k of Equation 2.1, one can obtain the following form for the LHS:

$$\iiint_{\mathbf{v}} \mathbf{v}^k \left(\frac{\partial f_\alpha}{\partial t} + \mathbf{v} \cdot \boldsymbol{\nabla}_\mathbf{r} f_\alpha + \frac{\mathbf{F}_\alpha}{m_\alpha} \cdot \boldsymbol{\nabla}_\mathbf{v} f_\alpha \right) d^3\mathbf{v} = \frac{\partial \mathscr{M}^k(f_\alpha)}{\partial t} + \boldsymbol{\nabla}_\mathbf{r} \cdot \mathscr{M}^{k+1}(f_\alpha) - k \frac{\mathbf{F}}{m_\alpha} \cdot \mathscr{M}^{k-1}(f_\alpha) \tag{2.15}$$

One can note that the k-th moment of the WCU equation automatically involves the moment of order $k+1$, in addition to the moment of order k. In order to be able to solve the system, one would then need an infinite number of equations.

It is then necessary to truncate the system, and apply a *closure* with a set of approximations and assumptions. This closure also deals with the expressions of the Coulomb collision operator integrals on the RHS. This approach was proposed by Grad [25] and pursued by Zhdanov in [26]. In this work, the latter formulated a set of equations more adapted to multi-species plasmas without assumptions on impurity concentrations or mass ratios, which were used in the previous famous work of Braginskii [27]. This more recent closure is now called the *Zhdanov closure*, and is implemented in SOLEDGE3X [28].

This fluid model and closure nevertheless do rely on their own set of assumptions:

- **Collision process scales**: During collision processes (elastic and inelastic), it is assumed that the time scale τ_c over which a single collision occurs (e.g., the actual rotation of the velocity vector) is much shorter than the typical time between two collisions τ_R, and so the collision itself can be considered as instantaneous. In the same way for lengths, it is assumed that the length scales at which the collision process operates λ_c (e.g., the distance of closest approach in an elastic collision) is much smaller than the mean free path of the particles λ_{mfp}.

- **Gradient length and system evolution scales**: In turn, it is assumed that the characteristic time τ_∇ and size λ_∇ of the macroscopic features of the plasma are much larger than the mean free path and frequency of collisions. This situation, identically characterized by a small Knudsen number $\text{Kn} = \lambda_{\text{mfp}}/\lambda_\nabla$, defines the *hydrodynamic* regime. This is usually relevant for tokamaks edge plasmas, even though it may not strictly be valid in the parallel direction.

- **Difference in plasma parameters between species**: The Zhdanov closure still relies on two assumptions concerning the plasma parameters: first, the fluid velocity difference between the ions species is small with respect to their thermal velocity, and secondly, the relative temperature difference between species must be small ($\ll 1$) [29].

2.3.3. The SOLEDGE3X code and equations

The SOLEDGE3X code, which has been developed in recent years at IRFM and Aix-Marseille Université, is born from merging and improving two codes: SOLEDGE2D [30], which focused on 2D-transport simulation with an accurate description of the plasma-wall and plasma-neutral interactions, and TOKAM3X [31], which focused on

first principle 3D turbulence modeling. The rationale for carrying out such a unified approach is two-fold. First, the equations solved in the two initial codes were very similar. Thus, implementing a single set with the option of activating or deactivating terms depending on the case allows sharing benefits of improvements from one side to the other. Second, the progress of edge plasma simulations directly aims at integrating these two aspects, i.e., turbulent simulations and accurate plasma-wall and plasma-neutral interactions. Early applications combination these two aspects with SOLEDGE3X are under development. As a side note, one can also mention that the SOLEDGE project also features the development of another code, solving the same set of equations through a different numerical method and called "SOLEDGE-HDG". The latter uses an unstructured grid with the Hybrid Discontinuous Galerkin method to describe the plasma in the whole chamber with evolving magnetic fields [32, 33].

Due to the history of the project, SOLEDGE3X has been developed as a versatile tool and offers several options in terms of model and geometry. In particular, it can be used either in 2D or 3D geometry, with or without drifts, with a fully consistent description of transverse turbulent transport or under a mean-field approximation, and with a hierarchy of neutrals models, ranging from none to the kinetic model in EIRENE through fluid neutrals.

For the ITER simulation studied here, the code is used in mean-field 2D transport mode without drifts and with a kinetic description of neutrals. This implies:

- **mean-field transport**: The temporal evolution of fluctuations is not represented. The plasma turbulence, which acts as a perpendicular transport mechanism, is emulated via perpendicular diffusion coefficients that can either be prescribed, as is the case in the considered cases, or derived from reduced turbulence models [34]. The dynamics of the system are not considered, only the obtained steady state is of interest.

- **2D**: The system is assumed axisymmetric, and only a poloidal plane is resolved. A further assumption is that all solid surfaces are perpendicular to the poloidal plane. This implies, for example, that no tile shaping (as described in [35]) is taken into account.

- **without drifts**: currents and fluid drifts (which can drive perpendicular flows) are deactivated.

For the simulations within this work, SOLEDGE3X solves the set of equations below. The drift terms are thus not included in the text, even though they are implemented in the code. The perpendicular transport is included via prescribed diffusion coefficients.

2.3.3.1. List of symbols

The following symbols are used in the code equations:

- m_α: mass of plasma species α

- n_α: density of plasma species α

- Z_α: charge state of plasma species α
- $\mathbf{v}_\alpha$: fluid velocity of plasma species α
- $\mathbf{v}_{\perp,\alpha}$: component of the fluid velocity of plasma species α in the plane perpendicular to the magnetic field
- $v_{\parallel,\alpha}$: parallel component of the fluid velocity of plasma species α so that $v_{\parallel,\alpha} = \mathbf{v}_\alpha \cdot \mathbf{b}$
- $\mathbf{b}$: unit vector in the direction of the magnetic field ($= \mathbf{B}/B$)
- $S_{n,\alpha}$: particle source of plasma species α
- $\mathbf{\Gamma}^{an}_{\perp,\alpha}$: Anomalous perpendicular particle flux density plasma species α
- $\mathbf{\Gamma}_{\perp,\alpha}$: Perpendicular particle flux density of plasma species α
- p_α: static pressure of plasma species α ($= n_\alpha T_\alpha$)
- $E_\parallel$: parallel component of the electric field
- Π_α: stress tensor of plasma species α
- π_α: stress tensor coefficient of plasma species α
- R_α: parallel projection of collisional forces between species (friction and thermal)
- $S_{m,\alpha}$: parallel momentum source of plasma species α
- $\nu_{\parallel,\alpha}$: parallel viscosity coefficient α

2.3.3.2. Continuity

The continuity equation is the 0^{th} order moment of the WCU equation. One is solved for each ion species (at a given charge state).

$$\frac{\partial n_\alpha}{\partial t} + \nabla \cdot (n_\alpha \mathbf{v}_\alpha) = S_{n,\alpha} \tag{2.16}$$

$S_{n,\alpha}$ is a volume source of ions from ionization and recombination of other species, including neutrals.

The velocity vector can be decomposed into its parallel and perpendicular components:

$$\mathbf{v}_\alpha = v_{\parallel,\alpha}\mathbf{b} + \mathbf{v}_{\perp,\alpha} \tag{2.17}$$

The parallel velocity $v_{\parallel,\alpha}$ is determined by the parallel momentum balance (see below). The perpendicular velocity $\mathbf{v}_{\perp,\alpha}$ is determined from perpendicular momentum balance using drift ordering when they are activated (which can be either in

turbulent or transport mode). In transport mode, the turbulent cross-field transport is represented by an effective diffusion. In that case, the perpendicular particle flux includes an "anomalous" diffusive part. In transport mode without drifts, it is the only component of the perpendicular particle flux density $\mathbf{\Gamma}_{\perp,\alpha}$.

$$\mathbf{\Gamma}_{\perp,\alpha} = n_\alpha \mathbf{v}_{\perp,\alpha} = \mathbf{\Gamma}^{an}_{\perp,\alpha} = -D_{\perp,\alpha} \boldsymbol{\nabla}_\perp n_\alpha \tag{2.18}$$

The electron density is computed following quasi-neutrality, that is:

$$n_e = \sum_i Z_i n_i \tag{2.19}$$

2.3.3.3. Momentum balance

The parallel momentum balance is the first-order moment of the WCU equation, projected in the parallel direction. This gives:

$$\frac{\partial}{\partial t}\left(m_\alpha n_\alpha v_{\alpha,\parallel}\right) + \boldsymbol{\nabla}\cdot\left(m_\alpha n_\alpha v_{\alpha,\parallel}\mathbf{v}_\alpha\right) = -\nabla_\parallel p_\alpha + Z_\alpha e n_\alpha E_\parallel - \mathbf{b}\cdot\boldsymbol{\nabla}\cdot\overline{\overline{\Pi}}_\alpha + R_\alpha + S_{m,\alpha} \tag{2.20}$$

The R_α term is the force applied to species α by other species, and is given by the Zhdanov closure. Its full expression is detailed in section C. In includes both the friction forces due to the difference in fluid parallel velocity between species, and the thermal forces which depend on the parallel temperature gradient of species.

The $S_{m,\alpha}$ term is the source term stemming from ionization/recombination and interactions with neutrals. The latter can be computed either by a fluid neutral model or by EIRENE.

The stress tensor $\overline{\overline{\Pi}}_\alpha$ can be decomposed in a parallel, gyroviscous, and perpendicular component:

$$\overline{\overline{\Pi}}_\alpha = \overline{\overline{\Pi}}_\parallel + \overline{\overline{\Pi}}_\angle + \overline{\overline{\Pi}}_\perp \tag{2.21}$$

The gyroviscous terms $\overline{\overline{\Pi}}_\angle$ are dropped due to the deactivation of fluid drifts.

$$\mathbf{b}\cdot\boldsymbol{\nabla}\cdot\overline{\overline{\Pi}} = \mathbf{b}\cdot\boldsymbol{\nabla}\cdot\overline{\overline{\Pi}}_\parallel + \mathbf{b}\cdot\boldsymbol{\nabla}\cdot\overline{\overline{\Pi}}_\perp \tag{2.22}$$

The parallel viscosity is given in a form that includes a divergence:

$$\mathbf{b}\cdot\boldsymbol{\nabla}\cdot\overline{\overline{\Pi}}_\parallel = \frac{2}{3}\boldsymbol{\nabla}\cdot\left(\pi_{\parallel,\alpha}\mathbf{b}\right) + \frac{1}{3}\pi_{\parallel,\alpha}\boldsymbol{\nabla}\cdot\mathbf{b} \tag{2.23}$$

where $\pi_{\parallel,\alpha}$ is the stress tensor coefficient for the parallel direction. In the current version of the code it is approximated with the Braginskii formulation:

$$\pi_{\parallel,\alpha} = -3\nu_{\parallel,\alpha}\left(\nabla_\parallel v_{\alpha,\parallel} - \boldsymbol{\kappa}\cdot\mathbf{v}_{\perp,\alpha} - \frac{1}{3}\boldsymbol{\nabla}\cdot\mathbf{v}_\alpha\right) \tag{2.24}$$

$$\nu^{SH}_{\parallel,\alpha} = 2.1\times10^{-7}\sqrt{\frac{m_\alpha}{m_u}}\frac{1}{Z_\alpha}T^{\frac{5}{2}} \tag{2.25}$$

In this formulation, $\nu_{\parallel,\alpha}$ is the parallel viscosity which uses the Spitzer-Härm formulation $\nu^{SH}_{\parallel,\alpha}$ modified with a flux limiter (set to 0.375 in our cases), and $\boldsymbol{\kappa} = (\mathbf{b}\cdot\boldsymbol{\nabla})\mathbf{b}$ denotes the magnetic curvature.

For the considered cases, the terms $\boldsymbol{\kappa}\cdot\mathbf{v}_{\perp,\alpha}$ and $\frac{1}{3}\boldsymbol{\nabla}\cdot\mathbf{v}_\alpha$ are neglected and not activated in the options of the code. Thus, it remains:

$$\pi_{\parallel,\alpha} = -3\nu_{\parallel,\alpha}\nabla_\parallel v_{\alpha,\parallel} \tag{2.26}$$

Thus:

$$\mathbf{b}\cdot\boldsymbol{\nabla}\cdot\overline{\overline{\Pi}}_\parallel = -2\nabla_\parallel\left(\nu_{\parallel,\alpha}\nabla_\parallel v_{\alpha,\parallel}\right) \tag{2.27}$$

For simulations run in transport mode, an anomalous viscosity ν^{an} is added to emulate cross-field transport of momentum by turbulence. This extra-term can be added to the viscous tensor as:

$$\mathbf{b}\cdot\boldsymbol{\nabla}\cdot\overline{\overline{\Pi}}_\perp = \boldsymbol{\nabla}\cdot\left(n_\alpha\nu^{an}_\alpha\boldsymbol{\nabla}_\perp v_{\alpha,\parallel}\right) \tag{2.28}$$

Also, the terms in divergence of p and $\pi_{\parallel,\alpha}$ are transferred in the divergence in the LHS to enable capturing acoustic waves in the numerical scheme. For the pressure, one uses:

$$\nabla_\parallel p_\alpha = \boldsymbol{\nabla}\cdot\left(p_\alpha\mathbf{b}\right) - p_\alpha\boldsymbol{\nabla}\cdot\mathbf{b} \tag{2.29}$$

Finally:

$$\begin{aligned}\frac{\partial}{\partial t}\left(m_\alpha n_\alpha v_{\alpha,\parallel}\right) + \boldsymbol{\nabla}\cdot\left(m_\alpha n_\alpha v_{\alpha,\parallel}\mathbf{v}_\alpha + p_\alpha\mathbf{b} - 2\nu_{\parallel,\alpha}\nabla_\parallel v_{\alpha,\parallel}\mathbf{b} + n_\alpha\nu^{an}_\alpha\boldsymbol{\nabla}_\perp v_{\alpha,\parallel}\right)\\ = \left(p_\alpha + \nu_{\parallel,\alpha}\nabla_\parallel v_{\alpha,\parallel}\right)\boldsymbol{\nabla}\cdot\mathbf{b} + Z_\alpha e n_\alpha E_\parallel + R_\alpha + S_{m,\alpha}\end{aligned}$$

The code solves for the equivalent equation on $\Gamma_\parallel$, which is simply the latter divided by m_α.

The mass of electrons is neglected, so no momentum equation is solved for them. Their mass is however taken into account in the computation of the friction and thermal forces in the collisional closure. To close the system, the parallel electric field is introduced through an instantaneous force balance on the electrons:

$$0 = -\nabla_\parallel p_e - e n_e E_\parallel + R_e \tag{2.30}$$

2.3.3.4. Energy balance

The energy balance is the 2$^{\text{nd}}$ order moment of the WCU equation. For all species, the total energy, including internal and kinetic contributions, is solved:

$$E_\alpha = \frac{3}{2} e n_\alpha T_\alpha + \frac{1}{2} m_\alpha n_\alpha v_{\alpha,\parallel}^2 \tag{2.31}$$

The evolution of this quantity is given by:

$$\frac{\partial E_\alpha}{\partial t} + \boldsymbol{\nabla} \cdot \left((E_\alpha + p_\alpha) \mathbf{v}_\alpha + \overline{\overline{\Pi}}_\alpha \cdot \mathbf{v}_\alpha + \mathbf{q}_\alpha \right) = e n_\alpha Z_\alpha \mathbf{v}_\alpha \cdot \mathbf{E} + Q_\alpha + S_{E,\alpha} \tag{2.32}$$

With:

- $\mathbf{q}_\alpha$: the collisional heat flux, given by the closure, which can be decomposed as:

$$\mathbf{q}_\alpha = q_{\alpha,\parallel} \mathbf{b} + \mathbf{q}_{\alpha,\angle} + \mathbf{q}_{\alpha,\perp} \tag{2.33}$$

  - $q_{\alpha,\parallel}$ is the collisional heat flux, given by the Zhdanov closure. It includes, among others, the parallel conductive heat flux $q^{\text{cond.}\alpha} = \kappa_\alpha^{\text{Zh}} \nabla_\parallel T_\alpha$, where $\kappa_\alpha^{\text{Zh}}$ is the parallel conductivity computed according to the Zhdanov closure formula instead of the Spitzer-Härm one.
  - $\mathbf{q}_{\alpha,\angle}$ is the diamagnetic heat flux and relates to the "diamagnetic cancellation" in the case of drifts. It is not activated here.
  - $\mathbf{q}_{\alpha,\perp}$ is the collisional cross-field heat flux. For simulations run in transport mode, it will take the form of a Fourier law to model the anomalous perpendicular heat flux:

$$\mathbf{q}_{\alpha,\perp}^{an} = -n_\alpha \chi_\alpha^{an} \boldsymbol{\nabla}_\perp T_\alpha \tag{2.34}$$

- Q_α: the local collisional heat flux between species, also given by the closure. It stems from the microscopic collision term $C_\alpha^{\text{Coul.}}$. It contains two contributions: Q_α^{th} the thermal equipartition related to the difference in temperatures between species, and Q_α^W the energy transfer associated with the friction and thermal forces between species. Its complete expression is provided and discussed in section C.

- $S_{E,\alpha}$: the sources associated with inelastic collisions with other species (ionization, recombination, plasma-neutral interactions).

Finally, one obtains:

$$\frac{\partial E_\alpha}{\partial t} + \boldsymbol{\nabla} \cdot \left((E_\alpha + p_\alpha) \mathbf{v}_\alpha + \overline{\overline{\Pi}}_\alpha \cdot \mathbf{v}_\alpha + q_{\alpha,\parallel} \mathbf{b} - n_\alpha \chi_\alpha^{an} \boldsymbol{\nabla}_\perp T_\alpha \right) = e n_\alpha Z_\alpha \mathbf{v}_\alpha \cdot \mathbf{E} + Q_\alpha + S_{E,\alpha} \tag{2.35}$$

2.3.4. Numerical scheme

The code uses a finite-volume method on a field-aligned grid structured by pieces, and the time stepper evolves quantities with a semi-implicit scheme. The terms with very fast dynamics are treated implicitly: the parallel viscous term and the parallel diffusive heat transport (and ionization-recombination between charged states in the case of multiple species, which is not the case here). The rest are treated explicitly. More details about the numerical scheme can be found in [34].

2.4. Coupling with EIRENE

This section provides more details on the interfacing between SOLEDGE3X and EIRENE, in order to include in the SOLEDGE3X equations the sources terms for the plasma:

- $S_{n,\alpha}$ the particle source
- $S_{m,\alpha}$ the parallel momentum source
- $S_{E,\alpha}$ the energy source

The SOLEDGE3X time-stepper includes an explicit section, which includes, among others, the advection scheme for all quantities, followed by an implicit section that computes the parallel diffusion for momentum and energy. At the end of the explicit section, an interface code called STYX takes the relevant plasma quantities from SOLEDGE3X and transfers them to EIRENE's internal input structures. EIRENE computes the source terms, and STYX transfers them back to SOLEDGE3X structures.

To compute the plasma neutral interactions, EIRENE receives:

- For each cell in the volume, each plasma species' density, temperature, and parallel velocity
- For each surface element:
  - Each ion's particle flux, using the fluxes computed in the advection section just before in the current time step
  - Each ion's temperature at the wall. Since SOLEDGE3X is a finite-volume solver, the temperature is defined at the center of cells, not at the edges. To guarantee energy conservation between the SOLEDGE3X outgoing energy flux, and the EIRENE incoming energy flux, T_i at the wall passed to EIRENE is computed from the outgoing wall heat flux in SOLEDGE3X.

To clarify, the ion temperature at the wall is computed to give an equivalent heat flux at the sheath entrance, which is the output given by SOLEDGE3X, and EIRENE

also starts sampling ions at the sheath entrance. This is obtained as the sum of the advected kinetic energy plus the energy given by the sheath heat transfer coefficients:

$$q_{\alpha,\text{wall}} = \Gamma_\alpha \left(\frac{1}{2} m_\alpha M_\alpha^2 \frac{(T_{\alpha,\text{wall}} + Z_\alpha T_e)e}{m_\alpha} e \right) + \Gamma_\alpha \gamma_\alpha T_{\alpha,\text{wall}} e \tag{2.36}$$

$$T_{\alpha,\text{wall}} = \frac{q_{\alpha,\text{wall}} - \frac{1}{2}\Gamma_\alpha M_\alpha^2 Z_\alpha T_e e}{\left(\frac{1}{2}M_\alpha^2 + \gamma_\alpha\right)\Gamma_\alpha e} \tag{2.37}$$

where M_α is the Mach number, $T_{\alpha,\text{wall}}$ the temperature at the wall, γ_α the sheath heat transfer coefficient for ion species α.

Since the total heat flux including the parallel conduction contribution is only available after the implicit section, and the EIRENE call is located in the explicit section, the heat flux $q_{\alpha,\text{wall}}$ is taken as the one at the end of the last time step.

2.4.1. EIRENE calls vs. *short*-cycles

The time step of the plasma solver is usually assumed to be much smaller than the characteristic evolution time of the neutrals system. Therefore, and since EIRENE calls are costly in terms of computation time, the code can be set up so that a full EIRENE call is not triggered at each time step, but rather only once every certain number of time steps. Assumptions on the plasma sources are then made for the steps between the EIRENE calls, which can vary between simply assuming them constant and applying extrapolation schemes. Those methods are detailed in section G. The intermediate time steps, which use an approximation instead of a full EIRENE call, are much faster and are thus referred to as *short-cycles*. These aspects are further detailed in section 3.4.6.

2.5. The EIRENE code

2.5.1. The need for kinetic treatment

Neutral particles play a central role in the behavior of tokamak plasmas at high regimes, as was seen in chapter 1, and understanding the mechanisms they drive is key to the successful design and operation of future machines. In particular, the plasma energy that is transferred to neutrals is deposited on surfaces much larger than the plasma-wetted area on the divertor targets, rendering them beneficial from the protection of plasma-facing components. Their transport also affects the particle balance of the machine: matter can be injected through neutral gas valves and is also removed in the neutral state through the pumping system.

In high density regimes, which are the regimes of interest for ITER, the plasma particle source is largely dominated by the neutral ionization in the SOL via recycling [36], rather than by the neutral-beam and pellet fuelling outflowing from the core or the ionization of the injected gas.

The difficulty in modeling and simulating neutrals is that in typical tokamak conditions, their mean-free path can be much larger than the gradient lengths of the system. Therefore, the fluid approach, which assumes the opposite, cannot be directly applied, and one has to treat them via a kinetic model. The EIRENE code [37] provides such an approach to describe the transport of neutrals and their interactions with plasma particles. It is introduced in this section.

2.5.2. Modeling neutral transport

2.5.2.1. The neutral transport equation

Decomposition of the collision term in the WCU equation Coming back to the kinetic WCU equation Equation 2.1, we apply it to the distribution function of a neutral species f_n:

$$\frac{\partial f_n}{\partial t} + \mathbf{v} \cdot \boldsymbol{\nabla}_{\mathbf{r}} f_n = \sum_{\beta} C_{n\beta}(f_n, f_\beta) \tag{2.38}$$

In the latter, the term related to macroscopic force is dropped, as neutrals are insensitive to electric and magnetic fields (and gravity is, of course, neglected).

The issue is now to address the collision term on the RHS. This can be decomposed into a loss L and a gain G terms.

$$\sum_{\beta} C_{n\beta}(f_n, f_\beta) = -L + G \tag{2.39}$$

Let us consider a generic reaction, in the form of a binary collision between N, a neutral particle against a particle from a background B, with products P_1 and P_2 (in the case of only two products, which is very often the case). The background is usually plasma particles, for which we assume a Maxwellian distribution. The pre-collision and post-collision velocities are written between brackets:

$$N[\mathbf{v}_n^{\text{pre}}] + B[\mathbf{v}_{bg}^{\text{pre}}] \rightarrow P_1[\mathbf{v}_{P_1}^{\text{post}}] + P_2[\mathbf{v}_{P_2}^{\text{post}}]$$

This can represent an elastic collision if P_1 and P_2 are N and B respectively, a charge exchange, or an creation or removal processes depending on the nature of the products. For example, in the case of the atom ionization, N is an atom, and B is an electron, and the RHS P_1 is an ion and P_2 represents two electrons. For a molecule-ion elastic collision, N and P_1 are the molecule, and B and P_2 are the ion.

Associated with this reaction is the differential cross-section $d^2\sigma^{\text{reac}}$ (units of $\text{m}^{-4}.\text{s}^6$), which is used to compute the rate of occurrence of such reactions, depending on the pre-collision velocities $\mathbf{v}_n^{\text{pre}}$, $\mathbf{v}_{bg}^{\text{pre}}$ and post-collision velocities $\mathbf{v}_{P_1}^{\text{post}}$, $\mathbf{v}_{P_2}^{\text{post}}$ of the particles.

$$d^2\sigma^{\text{reac}}(\mathbf{v}_n^{\text{pre}}, \mathbf{v}_{bg}^{\text{pre}}, \mathbf{v}_{P_1}^{\text{post}}, \mathbf{v}_{P_2}^{\text{post}})$$

The superscript "reac" denotes that this σ is specific to this particular reaction. The quantity:

$$d^2\sigma^{\text{reac}}(\mathbf{v}_n^{\text{pre}}, \mathbf{v}_{bg}^{\text{pre}}, \mathbf{v}_{P_1}^{\text{post}}, \mathbf{v}_{P_2}^{\text{post}}) d\mathbf{v}_{P_1}^{\text{post}} d\mathbf{v}_{P_2}^{\text{post}}$$

represents the cross section of the collision of two incident particles with velocities $\mathbf{v}_n^{\text{pre}}$ and $\mathbf{v}_{bg}^{\text{pre}}$ creating outgoing particles at velocities between $\mathbf{v}_{P_1}^{\text{post}}$ and $\mathbf{v}_{P_1}^{\text{post}} + d\mathbf{v}_{P_1}^{\text{post}}$, and $\mathbf{v}_{P_2}^{\text{post}}$ and $\mathbf{v}_{P_2}^{\text{post}} + d\mathbf{v}_{P_2}^{\text{post}}$ respectively.

$\mathbf{v}$ is the variable of the f_n distribution function from Equation 2.38. The following segments focus on $f_n(\mathbf{x}, \mathbf{v}, t)$, which is abbreviated by retaining only the velocity parameter for legibility $f_n(\mathbf{v})$, as time and position are not of interest here yet.

The loss term The loss term L in Equation 2.39 consists of collisions that transform N particles in the $\mathbf{v}$ velocity class into any other velocity class, for any initial and post-collision velocities of the background particles.

$$L = \int_{\mathbf{v}_{bg}^{\text{pre}}} \int_{\mathbf{v}_{P_1}^{\text{post}}} \int_{\mathbf{v}_{P_2}^{\text{post}}} d^2\sigma^{\text{reac}}(\mathbf{v}_n^{\text{pre}}, \mathbf{v}_{bg}^{\text{pre}}, \mathbf{v}_{P_1}^{\text{post}}, \mathbf{v}_{P_2}^{\text{post}}) |\mathbf{v}_n^{\text{pre}} - \mathbf{v}_{bg}^{\text{pre}}| f_n(\mathbf{v}_n^{\text{pre}}) f_{bg}(\mathbf{v}_{bg}^{\text{pre}}) \tag{2.40}$$

In this case, the pre-collision velocity of the neutral $\mathbf{v}_n^{\text{pre}}$ is the one that is the variable $\mathbf{v}$ of the distribution function f_n:

$$L = \int_{\mathbf{v}_{bg}^{\text{pre}}} \int_{\mathbf{v}_{P_1}^{\text{post}}} \int_{\mathbf{v}_{P_2}^{\text{post}}} d^2\sigma^{\text{reac}}(\mathbf{v}, \mathbf{v}_{bg}^{\text{pre}}, \mathbf{v}_{P_1}^{\text{post}}, \mathbf{v}_{P_2}^{\text{post}}) |\mathbf{v} - \mathbf{v}_{bg}^{\text{pre}}| f_n(\mathbf{v}) f_{bg}(\mathbf{v}_{bg}^{\text{pre}}) \tag{2.41}$$

The $f_n(\mathbf{v})$ can be taken out of the integrals. Then since the distribution function of the background is known, because it is assumed Maxwellian, and the behavior of $d^2\sigma^{\text{reac}}$ with the velocities as well from quantum mechanics considerations, it is possible to carry out the remaining triple integration to obtain:

$$L = n_{bg} \langle \sigma v \rangle^{\text{reac}}(\mathbf{v}, T_{bg}) f_n(\mathbf{v})$$

Where v is the relative velocity $v = |\mathbf{v}_n^{\text{pre}} - \mathbf{v}_{bg}^{\text{pre}}|$. The averaged term $\langle \sigma v \rangle^{\text{reac}}(\mathbf{v})$ contains the integrals, and is called the *rate coefficient* of the reaction with units $[\text{m}^3\text{s}^{-1}]$. It depends on the shape of the background particle distribution function, i.e., on T_{bg}, and n_{bg} simply comes out as a scaling factor for the density of background particles. It also still depends on $\mathbf{v}$ because the relative velocity v still includes $\mathbf{v}$.

For reference, this rate coefficient can be linked to the *volume reaction rate* N_{reac} in $[\text{m}^{-3}\text{s}^{-1}]$ after integration over all neutral velocities (which are not yet known here), resulting in an averaged rate coefficient:

$$N_{\text{reac}} = n_n n_{bg} \overline{\langle \sigma v \rangle}^{\text{reac}}$$

This "bar" notation for the average will be omitted in the future, because it is only relevant for the case where the dependency of $\langle \sigma v \rangle^{\text{reac}}$ in the neutral velocity $\mathbf{v}$ is not

neglected, which is always the case except for the atom charge exchange reaction and the molecule-ion elastic collision, see below in section 2.5.3.1 for the rationale of this assumption.

The gain term The gain term G in Equation 2.39 represents all collisions that produce a neutral particle at velocity $\mathbf{v}$, from any velocity class for the incident particles, and for any post-collision velocity of the background particle. This term is much more difficult to treat, as the distribution function of the neutrals f_n cannot be taken out of the integrals:

$$G = \int_{\mathbf{v}_n^{\text{pre}}} \int_{\mathbf{v}_{bg}^{\text{pre}}} \int_{\mathbf{v}_{P_2}^{\text{post}}} d^2\sigma^{\text{reac}}(\mathbf{v}_n^{\text{pre}}, \mathbf{v}_{bg}^{\text{pre}}, \mathbf{v}_{P_1}^{\text{post}} = \mathbf{v}, \mathbf{v}_{P_2}^{\text{post}}) |\mathbf{v}_n^{\text{pre}} - \mathbf{v}_{bg}^{\text{pre}}| f_n(\mathbf{v}_n^{\text{pre}}) f_{bg}(\mathbf{v}_{bg}^{\text{pre}})$$

We are left with:

$$\frac{\partial f_n}{\partial t} + \mathbf{v} \cdot \nabla_r f_n + n_{bg} \langle \sigma v \rangle^{\text{reac}} f_n(\mathbf{v}) = G + S_n \tag{2.42}$$

Applying the Method of Characteristics Equation 2.42 has the form of an "integro-partial differential equation" (IPDE) which contains a differential part on the LHS, and an integral part on the RHS (the G term). By using the "Method of Characteristics" (often used in aerodynamics for solving hyperbolic equations in the context of supersonic flows) which consists in applying a change of variable to parametrize the integration space with a 1D parameter (i.e., carrying out line integrals), it is possible to rewrite the LHS so that this equation now takes only an integral form. To do so, one defines the characteristics as the incoming trajectory of the particles with velocity $\mathbf{v}$ up until a chosen point $\mathbf{r}$, such as $\mathbf{r}' = \mathbf{r} - s\mathbf{\Omega}$, with s the 1D parameter, and $\mathbf{\Omega}$ the unit vector of the direction of $\mathbf{v}$, such that $\mathbf{v} = v\mathbf{\Omega}$, Figure 2.1. This transformation is done to facilitate its numerical resolution with a Monte-Carlo approach, as will be seen in the next section.

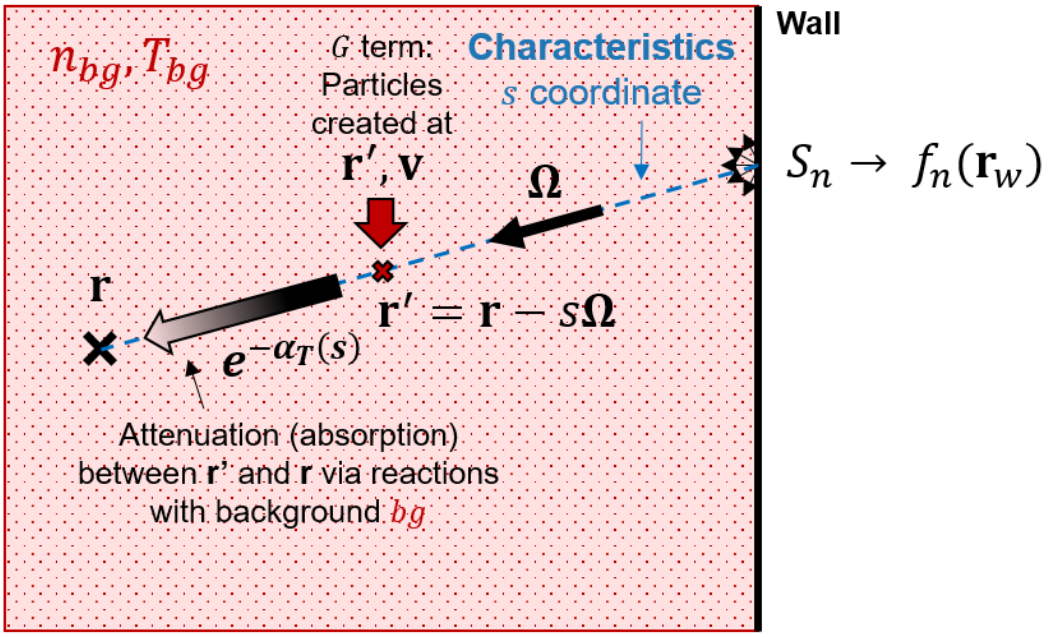

Figure 2.1.: Diagram representing the Method of Characteristics for the integration of Equation 2.38, and the associated coordinate system with s.

We obtain:

$$f_n(\mathbf{r},\mathbf{v},t) = f_n(\mathbf{r}_w,\mathbf{v},t-s_w/\mathrm{v})e^{-\alpha_T(s_w)} + \int_0^{s_w} G(\mathbf{r}-s\boldsymbol{\Omega},\mathbf{v},t-s/\mathrm{v})e^{-\alpha_T(s)}ds \tag{2.43}$$

In the latter, v is the modulus of $\mathbf{v}$ (not the relative velocity v in the context of the collision), and the w subscript indicates the location of the initial source of neutral particles is at the wall in this example, as is the case for recycling. The $\alpha_T(s)$ represents the optical depth of the background, so that the attenuation factor $e^{-\alpha_T(s)}$ is the probability that a particle created at $\mathbf{r}-s\boldsymbol{\Omega}$ and moving in the $\boldsymbol{\Omega}$ direction is not absorbed by any process along its trajectory, and reaches $\mathbf{r}$.

The optical depth thus includes all possible absorption reactions that could lead to the particle being consumed, through the rate coefficient and background density associated with each absorption process:

$$\alpha_T(\mathbf{r},s,\mathrm{v},\boldsymbol{\Omega}) = \int_0^s \sum_{\mathrm{reac}} n_{bg}\langle\sigma v\rangle^{\mathrm{reac}}(\mathbf{r}-s'\boldsymbol{\Omega},\mathbf{v},T_{bg},t-s'/\mathrm{v})\frac{ds'}{\mathrm{v}} \tag{2.44}$$

However, Equation 2.43 is not a closed form of the neutral distribution, as G depends on f_n. It has nevertheless a clear interpretation. The first term comes from the initial ("primary") source of neutral, which is in this case illustrated by the recycling of ions at the wall, in the alignment of the chosen $\mathbf{v}$, so that the particles arriving in $\mathbf{r}$ actually have this $\mathbf{v}$ velocity. The primary source is then simply attenuated through

with line integral of the absorption probability of all included processes. The second term follows a similar reasoning, but now taking as the source the particles created at velocity $\mathbf{v}$ at each point along the characteristic line, then attenuated for the remaining distance until $\mathbf{r}$ (Figure 2.1). The latter depends on the neutrals arriving at $\mathbf{r}'$ from any direction from elsewhere in the domain, and colliding at $\mathbf{r}'$ to get the $\mathbf{v}$ velocity.

2.5.2.2. Resolution via the Monte-Carlo method

Equation 2.42 is well suited for applying the well-known Markov Chain Monte Carlo (MCMC) methods: here the method is based on computing particle trajectories, which actually represent the "characteristic curves" (see previous paragraph) of the PDE part (the LHS) of Equation 2.42. This method can be described as "integration along characteristic lines of the underlying equation". However, other descriptions exit, such as interpreting Equation 2.42 as the "backward equation" representing a Markovian process (in this case the memoryless transitions of particle "states" which include their position, velocity, nature, or other internal properties).

The Monte-Carlo approach is especially attractive in our case as since the plasma solver is a fluid solver, and therefore only takes as input averages over the space inside a cell and over the whole velocity space, so we can in fact avoid computing the full distribution function of the neutrals. Through ensemble averaging, the Monte Carlo method directly provides *estimates* of the average plasma sources and neutral parameters (n_n, u_n, E_n...), which are themselves integrals of the type:

$$\overline{h} = \int_{\mathbf{r}\in\mathscr{C}} \int_{\mathbf{v}} h(\mathbf{r},\mathbf{v}) f_n(\mathbf{r},\mathbf{v},t) \tag{2.45}$$

where $\mathscr{C}$ is the space of a cell in the numerical grid, which has a volume of V. Those are in fact moments of the distribution function which were introduced in the fluid model section in section 2.3.1. The h function is called the *detector function*, and is selected depending on the quantity one wishes to obtain:

$$\overline{h} = n_n \rightarrow\ h_0(\mathbf{r},\mathbf{v}) = \frac{1}{V} \qquad \text{if } \mathbf{r}\in\mathscr{C} \text{ else } 0 \tag{2.46}$$

$$\overline{h} = \mathbf{u}_n \rightarrow\ h_1(\mathbf{r},\mathbf{v}) = \frac{1}{V} m_n \mathbf{v} \qquad \text{if } \mathbf{r}\in\mathscr{C} \text{ else } 0 \tag{2.47}$$

$$\overline{h} = E_n \rightarrow\ h_2(\mathbf{r},\mathbf{v}) = \frac{1}{2V} m_n \mathrm{v}^2 \qquad \text{if } \mathbf{r}\in\mathscr{C} \text{ else } 0 \tag{2.48}$$

Then, the Monte Carlo solver is used to sample N_{part} particle trajectories, by launching them, tracking them, and carrying out collisions until their destruction while adding the contributions of the trajectory segments to the different estimators. These estimators tend to the true value of $\overline{h}$ with an infinite number of trajectories. With only a finite number, the obtained values are not exact, and the solution contains a degree of statistical noise.

The procedure of producing a solution is summarized briefly below (more details are available in [37].

- **Neutral generation**: Neutrals are born with mainly three mechanisms: ion recycling on surfaces, volume electron and background ion recombination, and gas injection. Those three mechanisms are independent, and one can show that the problem is superposable, i.e., one can solve for each generation mechanism, and simply sum the results to get the global solution. Each generation mechanism is solved in its so-called *stratum* (plural *strata*, i.e., "layer"). The recycling of ions is of particular interest, as it generally is the largest contributor. The following sequence is applied to generate the initial conditions of a recycled neutral:
  1. The location of an impacting ion is sampled along the wall through a probability density function corresponding to the ion incident flux.
  2. Its velocity is sampled at the sheath entrance from local plasma conditions (T_i, Mach number, direction of the magnetic field line).
  3. It is accelerated through the sheath by the sheath electric field (computed with the local T_e) up to the wall.
  4. The ion has a probability of being recycled of R_T, or absorbed and lost in the wall.
  5. If it is recycled (with a probability determined by the recycling coefficient R of the surface), it can exit the wall back to the chamber either through backscattering or thermalized reemission. If backscattered, it leaves as an atom and approximately retains its kinetic energy. If thermalized in the wall, it recombines into a molecule and leaves the wall at an energy representative of the temperature of the wall T_{wall}. The probabilities of selecting one or the other behavior, as well as the reemission angles, are tabulated from the TRIM (TRansport of Ions in Matter) database [38] depending on the chemical element of the incoming ion and the of the surface material.

- **Particle tracking**: Once a sampled neutral has an initial position and direction, a random number u is sampled between 0 and 1, and the optical depth integral α_T is incremented in each traversed cell as the particle moves through the grid, until α_T reaches $\ln u$. During this trajectory, it can be reflected on other surfaces. At the location where $\alpha_T = \ln u$, the trajectory ends and an absorption process ("absorption" in the sense of the position and velocity space, to include elastic collisions) is randomly selected among those included in the optical depth according to their contributions. This selected process is then executed. For example, if it is an atom charge exchange, a new velocity is chosen, changing the direction of the tracked particle, if it is an atom ionization, the tracked particle is destroyed and the trajectory ends. Then a new neutral particle is generated from the start. In the case of an elastic collision, the new velocity is randomly sampled in the collision execution, and the tracking continues until the particle is destroyed or absorbed on a surface with a recycling coefficient < 1, such as a non-recycling wall or a pumping surface.

To produce the solution, one has to define how to count the contribution of each

particle to the $\overline{h}$ integral in the traversed cell. This process is known as *tallying*. It is done by incrementing a tally in the cell by the time spent by the particle in it at each of the N_{cross} crossings, multiplied by the representative weight w_i of the test particle i vs. actual particles from the integral value of the primary source (here the integral of total neutral particle influx from the wall Γ_n^{IN}).

$$w_i = \frac{\Gamma_n^{\text{IN}}}{N_{\text{part}}} c_i \tag{2.49}$$

$$n_n(cell) = \lim_{N_{\text{part}}\to\infty} \sum_i^{N_{\text{cross}}} \frac{d_i}{\mathrm{v}_i} w_i h_0(\mathbf{r},\mathbf{v}) = \lim_{N_{\text{part}}\to\infty} \frac{\Gamma_n^{\text{IN}}}{N_{\text{part}}} \sum_i^{N_{\text{cross}}} \frac{d_i}{\mathrm{v}_i} w_i c_i \tag{2.50}$$

$$\mathbf{u}_n(cell) = \lim_{N_{\text{part}}\to\infty} \sum_i^{N_{\text{cross}}} \frac{d_i}{\mathrm{v}_i} w_i h_1(\mathbf{r},\mathbf{v}) = \lim_{N_{\text{part}}\to\infty} \frac{\Gamma_n^{\text{IN}}}{N_{\text{part}}} \sum_i^{N_{\text{cross}}} \frac{d_i}{\mathrm{v}_i} w_i c_i m_n \mathbf{v}_i \tag{2.51}$$

$$E_n(cell) = \lim_{N_{\text{part}}\to\infty} \sum_i^{N_{\text{cross}}} \frac{d_i}{\mathrm{v}_i} w_i h_2(\mathbf{r},\mathbf{v}) = \lim_{N_{\text{part}}\to\infty} \frac{\Gamma_n^{\text{IN}}}{N_{\text{part}}} \sum_i^{N_{\text{cross}}} \frac{d_i}{\mathrm{v}_i} \frac{1}{2} w_i c_i m_n \mathrm{v}_i^2 \tag{2.52}$$

Here c_i is a weight adjustment factor linked to the number of nuclei in the tracked particle, or to other variance reduction techniques (which are not discussed here).

It can be shown that those are indeed unbiased estimators for the quantities on the left-hand side [39].

Regarding the corresponding sources returned to the plasma solver, the parallel direction is often treated separately, as it is the only direction of the velocity which has a dedicated momentum balance equation due to the magnetization of the plasma. Therefore, the parallel projection of the momentum is of particular interest. For example, in the case of an atom ionization, the parallel velocity of the created ion is:

$$v_{\mathrm{H}^+,\parallel} = \vec{v}_{atom}.\vec{b}$$

Where $\vec{b}$ is the unit vector in the direction of the magnetic field.

Since the total energy density of a plasma fluid element is reduced to:

$$E = E_{\text{th}} + E_{\text{kin}} + E_{\text{p}} = \frac{3}{2} nT + \frac{1}{2} m_i n v_\parallel^2 + E_{iz}$$

where E_{iz} is the ionization energy. The kinetic energy related to the perpendicular direction will actually be included in the thermal energy (i.e. the temperature).

2.5.3. Modeling of the reactions

2.5.3.1. Assumptions in the modeling of the rate coefficients $\langle \sigma v \rangle^{\text{reac}}$

In order to compute the probability of reactions for a tracked particle, the values of the collision frequency $n_{bg}\langle \sigma v \rangle^{\text{reac}}$ are needed. In this section, we clarify some of the assumptions and approximations that are used for the $\langle \sigma v \rangle^{\text{reac}}$ coefficients.

These rate coefficients are, in fact, functions of three elements:

- the features of the background particles distribution
- the relative velocity of the two incident particles v, which itself depend on the neutral's velocity $\mathbf{v}$
- the nature of the reaction, i.e., the type of incident particles and also their excitation state (through σ)

Background distribution function In most cases, background particles are plasma particles, which are evolved by the plasma solver in which a Maxwellian distribution is assumed. Therefore, f_{bg} is known and taken to be a Maxwellian, fully determined by T_{bg} and u_{bg}.

Velocities For electron impact reaction, since the electron can be assumed much faster than the heavy particle, then only a dependency in T_e can be retained to model for the relative velocity v. For charge exchange reactions, two cases exist: for molecule charge exchanges, one can neglect the molecule velocity, which can be assumed slow w.r.t. to background ions, and only parameterize via T_i. For atom charge exchanges, the atom velocity cannot be assumed slow w.r.t. the ions', exactly because this reaction can give an ion velocity to an atom. Thus, both T_i and the energy of the incident atom E_0 are retained as parameters.

Excitation states The $\langle \sigma v \rangle^{\text{reac}}$ coefficients are also in fact effective rates taking into account the different possible excitation states of the tracked particle. In the considered model, the so-called Collisional-Radiative regime is assumed, where from the local electron density and temperature, it is possible to calculate the excited population fractions n_i^* with a Collisional-Radiative Model. Using the rate coefficient $\langle \sigma v \rangle_i^{\text{reac}}$ for each specific excitation level i:

$$\langle \sigma v \rangle^{\text{reac}} = \sum_i n_i^* \langle \sigma v \rangle_i^{\text{reac}}$$

Since the population fractions depend on the electron density n_e, now the rates coefficients also depend on it.

Contribution from photons In the considered simulations, the plasma is assumed to be optically thin, meaning photons produced by the processes in the model are simply transported to the wall and absorbed there. Photon processes such as resonance line photo-absorption (which increases the population of excited atoms, which are easier to ionize) could play a role in high-density regimes [20], but were not considered in this work, as it would have required further software developments that were outside the scope of this thesis. They could be included in future models via two options: either using modified rate coefficients for reactions that take into account such processes, or including the tracking of photons with their own set of reactions.

2.5.3.2. Tabulation from databases

Using the assumptions described above, it is possible to pre-compute and tabulate those rate coefficients depending on the chosen parameter dependencies (T_{bg}, n_{bg}, E_{tracked}), and store them in databases, as used by EIRENE [37]. They can be in the form of the nine coefficients of degree 8 polynomials, as is the case for AMJUEL and HYDHEL databases, or in 2D tables of values as in the ADAS database.

2.6. Balances of the system

To better assess the behavior of the studied system, and because they are key to evaluating their convergence of the simulations, we now turn to particle and energy balances.

The first step is to define the system considered. In this section, it encompasses everything that is modeled in the simulations, i.e., the sum of:

- Ions (including H_2^+ ions)
- Electrons
- Neutrals (molecules and atoms)
- Photons (not tracked, but still needed to take into account as an energy form)

The boundaries of the systems are thus:

- The boundary at the core edge
- The walls: in the following, 'wall' denotes any surface interacting with the plasma and neutrals. In practice, it includes the first wall, the divertor targets, the pump, the dome, and the dome pillars (the latter only interacts with neutrals).
- the gas injection points

2.6.1. Particle balance

The particle balance of the system is represented in Figure 2.2 and considers ions and neutrals. The latter includes both atoms and molecules, which are not distinguished in the diagram for legibility.

The input consists of two boundary sources: the particle outflow from the core Γ_{core}^{ion}, and the gas puff injection $\Gamma_{\text{Gas Puff}}^{neutrals}$. Neutrals reaching the core edge boundary are assumed ionized there, and are reinjected into the system as ions $\Gamma_{iz,core}^{ion}$. Their net effect is thus zero.

To count the output, one has to do a net sum of all incident particles to the walls $\Gamma_{inc.}$, minus all particles coming back into the chamber $\Gamma_{emit.}$. The ions incident to the wall are recycled as neutral particles with a ratio of R which depends on the surface.

Identically for neutrals, incoming particles are reinjected in the chamber with this probability. This ratio is strictly less than unity for the pumping surfaces, and since the R coefficient for the rest of the wall is exactly 1, this net effect at the pumping surface is the only exit channel for particles. Only neutrals exist at the location of the pump, therefore it is a good approximation to state that the plasma ions are fully recycled, and only the neutrals are pumped.

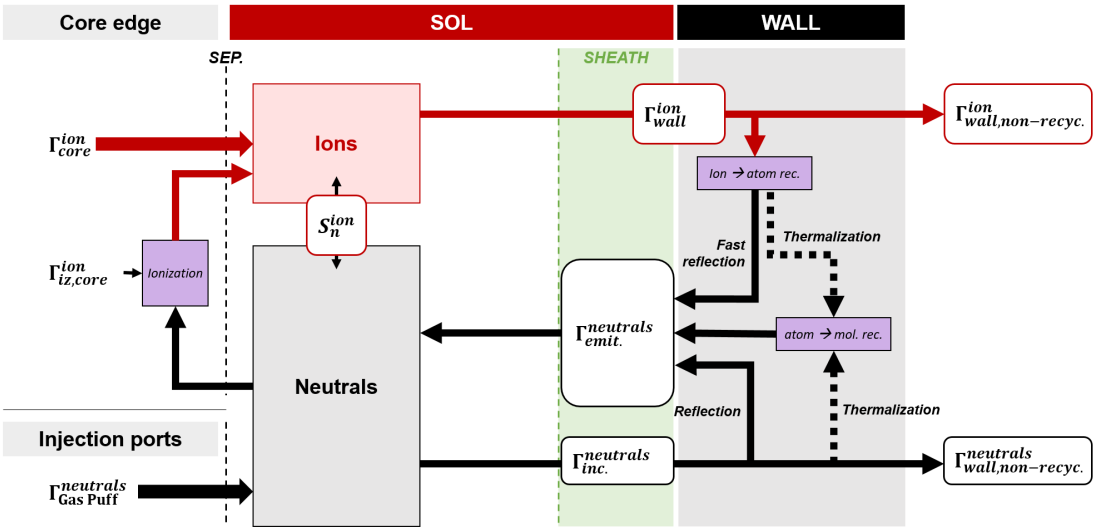

Figure 2.2.: Particle balance of the simulation system, for a single ion species plasma, assuming ambipolarity (i.e., electrons are not represented as ion and electron particle densities and fluxes are assumed equal.)

2.6.2. Energy balance

The energy balance is somewhat more complex. The key point is to take into account everywhere both the kinetic energy of particles and their potential energy. This potential energy is attributed to the ions and neutrals. To do so, the zero potential energy level is assigned to the molecule state. The excited states are not described here, but were they, one would also have to account for them in the potential energy of particles. To describe the potential energy of the atom, the binding energy of the molecule is split in two: $E_{mol}^{bind} = 4.5eV = 2E_{atom}^{pot}$ [40]. The potential energy of the H^+ ion is thus the sum of the latter and the hydrogen ionization energy (13.6 eV). The potential energy of the H_2^+ ion is its ionization energy at 15.4 eV from the H_2 molecules, and its binding energy is 2.7 eV (visible [40] on p.128). The potential energies are summarized in Table 2.1.

The diagram for the energy balance of the system is represented in Figure 2.3.

Regarding inputs, one has now to take into account that the kinetic energy of the neutrals reaching the core is reflected and added to the corresponding ionized particle flux, but the ionization energy of these neutrals $P_{iz,core}^{ion}$ has to be counted. In practice,

Table 2.1.: Summary of potential energies for particles for a hydrogen plasma and neutral gas. Values from [40].

Particle	**Potential Energy E_p [eV]**
e^-	0
H_2	0
H_2^+	15.4
H	2.25
H^+	15.85

this term is also always negligible in ITER cases because of the core edge temperatures and density. Also, the gas puff injection also contributes to the energy input, but with a negligible contribution.

Regarding outputs, one can obtain the kinetic energy deposition from the neutrals again by calculating the net sum of the incident energy $P_{inc.}^{neutrals}$ minus the re-emitted energy $P_{emit.}^{neutrals}$. This takes into account the thermalization (where particles are emitted at energies following a distribution at T_{wall}) and reflection channels. The potential energy differences that are not transferred to the kinetic energy of particles are turned into photons, which are recovered at the wall via volumetric radiation mapping to the surfaces $P_{vol.\,rad}^{neutrals}$.

The potential energy of particles appears in the wall recombination radiative heat flux of the ion and atoms (H_2^+ also, but are not represented, their fluxes to the wall are usually negligible). Depending on the behavior of the incident ion, it can either recombine into an atom through a fast reflection and deposit only a 13.6 eV photon in the wall and then come back in the chamber, or thermalize in the wall and further recombine with another atom to form a molecule, depositing an additional 2.25 eV (per single atom, 4.5 eV per molecule), before re-exiting the wall.

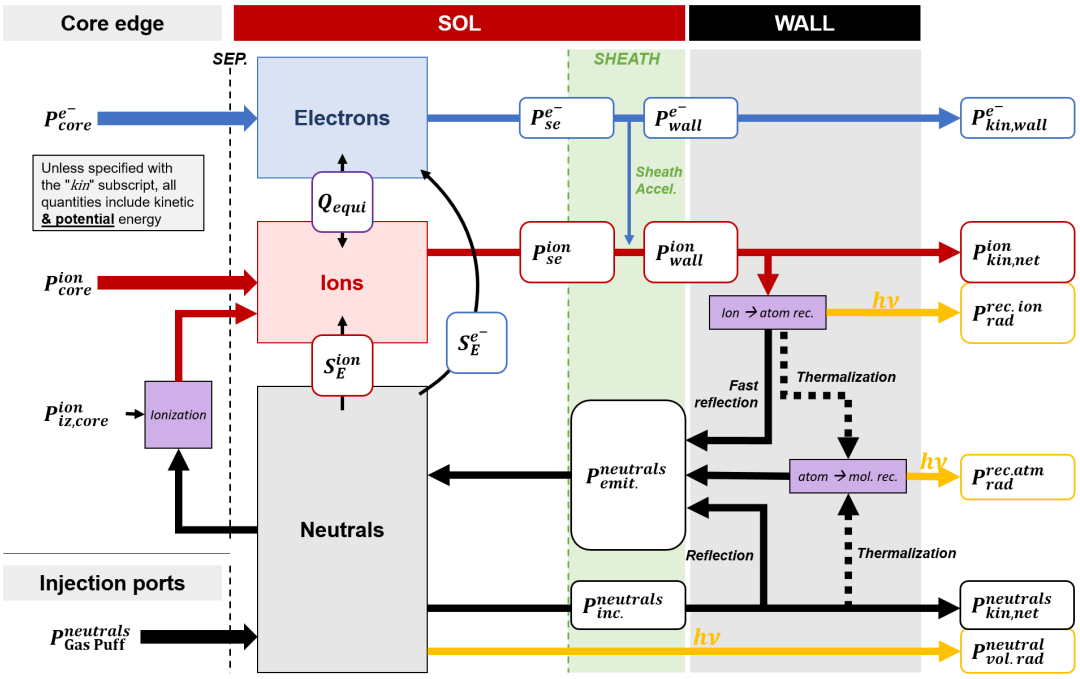

Figure 2.3.: Energy balance of the simulation system, for a single ion species plasma. See the text for the description of the terms.

The picture is more complex with multiple ion species but is not detailed here.

3. Setup of ITER cases and improvements to the codes

Contents

3.1. Introduction

This chapter focuses on the setup of the code to model the considered ITER cases, and the improvements that were designed and implemented to carry out these simulations. It is structured as follows:

- First, the setup of the ITER cases is presented, with a description of the parameters and assumptions.
- Then, we discuss the improvements made to the SOLEDGE3X physics model so that it contains the elements that were identified as necessary for simulating large-scale machines such as ITER.
- As a consequence of the new physics and the characteristics of the ITER machine, improvements to the numerical scheme were necessary, and those are presented.
- Lastly, the results obtained with SOLEDGE3X are compared with similar SOLPS-ITER runs from the ITER database, thus providing some comparability for the quantitative and qualitative results in this work.

3.2. Simulation setup

3.2.1. Common parameters

The main code parameters with which the presented cases were run are summarized in Table 3.1.

The flux-surface aligned mesh (see Figure 3.1) is based on the magnetic equilibrium of Pre-Fusion Power Operation (PFPO) discharges using the baseline $q_{95} = 3$ ($I_p = 5MA$, $B_T = 1.76T$) scenario, in which the geometry of the field lines is identical to the one in the Full Power Operation (FPO) $Q = 10$ plasma scenario. Only the magnitude of the magnetic field is scaled down by a factor of 3 in PFPO-1. This scaling does not affect the considered transport simulations, as fluid drifts are not included. However, it indirectly impacts the choice of transverse transport coefficients which depends on the targeted SOL width, itself expected to scale as $1/I_p$ [41]. In our cases, the values of the prescribed perpendicular diffusion coefficients were selected to match current ITER projections for L-mode SOL width [42], and are also identical to the ones used in the ITER SOLPS simulation database.

Unless specified otherwise, the magnetic equilibrium and the wall contour are from the 2021 updated scenario, which includes a reduced radial distance between the two separatrices at the outer midplane of $dr_{sep} = 6.5$cm, and a thickened inner central wall. The data for those can be found in the ITER IMAS database (magnetic equilibrium: #135011 run 7, wall: 116000 run 2). A comparison between simulations run with the equilibrium and wall used in [42] and the updated ones is provided in appendix section A.

Figure 3.1 shows the field-aligned grid of the SOLEDGE3X plasma solver (left), and the unstructured triangle grid of the EIRENE Monte-Carlo solver (right). The unstructured grid of EIRENE enables to model plasma-wall and neutral-wall interactions in realistic (2D-axisymmetric) wall geometry, which is not possible with the field-aligned grid of the plasma-solver. The plasma-wall boundary in SOLEDGE3X is aligned to the actual wall geometry only at the targets, where the majority of the fluxes fall. Elsewhere, as it is impossible to align everywhere, the wall shows a staircase-like pattern in the plasma solver. A mapping and weighting procedure is implemented in the code coupling routines to enable exchanges between SOLEDGE3X plasma flux data and EIRENE surface elements.

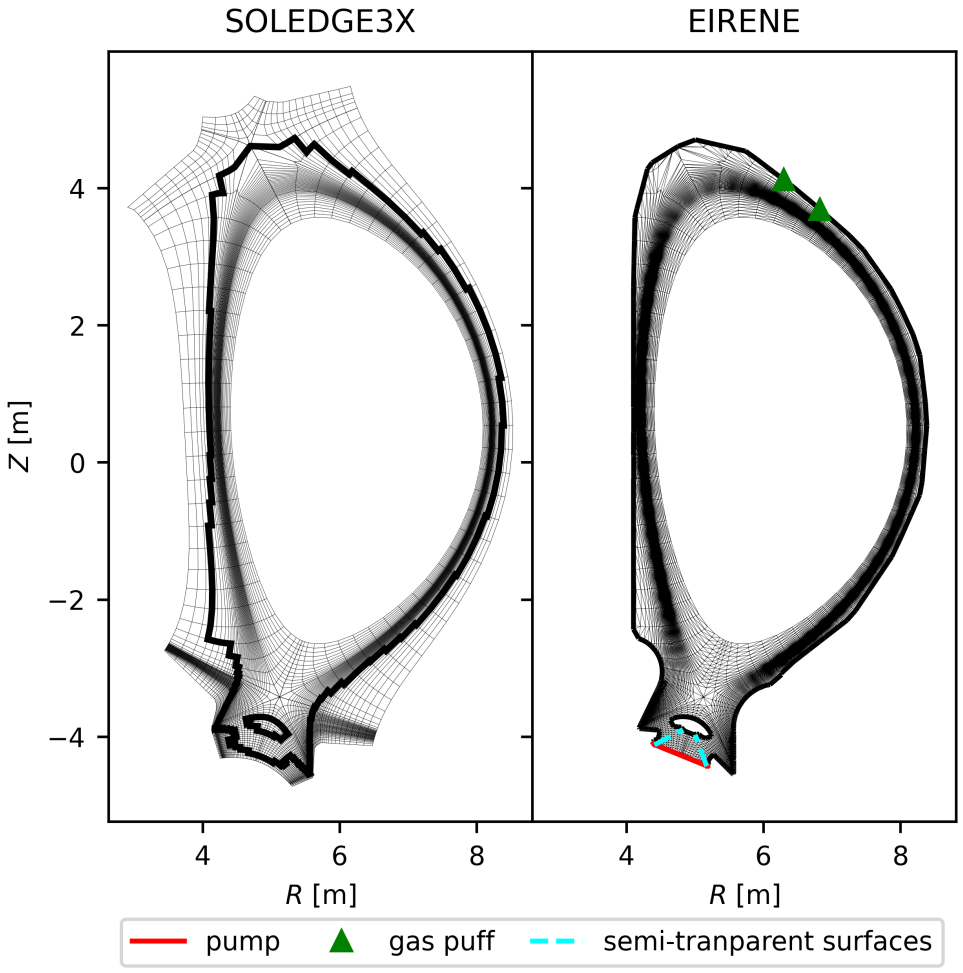

Figure 3.1.: SOLEDGE3X-EIRENE plasma domain mesh for the ITER machine. Left: the plasma solver SOLEDGE3X domain. Right: the EIRENE domain. The red segment represents the pumping surface, the green triangles represent gas puffing locations. Cyan dashed lines are semi-transparent surfaces with a reflection probability of neutral particles of 50%, used to represent the non-axisymmetric dome support structures (pillars).

Table 3.1.: Summary of simulation parameters

Parameter	**Value**
Particle perpendicular diffusivity $D_\perp$	0.3 $m^2.s^{-1}$
Perpendicular viscosity $\nu_\perp$	0.2 $m^2.s^{-1}$
Perpendicular heat conductivity $\chi_{\perp,e}$	1.0 $m^2.s^{-1}$
Perpendicular heat conductivity $\chi_{\perp,i}$	1.0 $m^2.s^{-1}$
Parallel viscosity	ON
Conduction heat flux limiter coeff. for electrons	0.2
Conduction heat flux limiter coeff. for ions	OFF
Viscosity heat flux limiter coeff. for ions	0.375
Neutral Model	Kinetic (EIRENE)
Drifts	OFF
Collisional closure	Zhdanov
Turbulence	OFF
3D	OFF
Content	Pure H
Input power	20 MW (10MW e^- + 10MW H^+)
Particle input from the core	6.13×10^{20} s^{-1}
Sheath Heat Transmission Factors	e^- : 4.5 ; H^+ : 2.5
First Wall material	Beryllium
First Wall material temperature	500 K (uniform)
Targets material	Beryllium
Targets material temperature	500 K (uniform)
Target, first wall, dome recycling coefficient	1.0
Dome material	Beryllium
Dome material temperature	500 K (uniform)
Dome pillars material	Iron
Dome pillars reflection probability	0.5
Pump material	Iron
Pump recycling coefficient	0.9928
Gas injection location	Top outer port

The perpendicular diffusion coefficients are common to cases in chapter 3, chapter 4 and chapter 5, but are varied in chapter 6

Note on the choice of Beryllium for the targets This choice comes from the assumption that eroded Beryllium particles from the first wall will be transported with the plasma flows and also redeposited at the target plates [35]. A further assumption is added that no re-erosion will occur there to remove the Beryllium deposit and expose the Tungsten surface again, an argument supported by WALLDYN simulations of ITER burning plasmas, except for the outer target at low density regimes [35, 43]. In the considered simulations, however, both targets are nonetheless modeled as Beryllium for simplicity across the scan.

3.2.2. Throughput scan

To produce simulations of the different divertor regimes, a set of cases which scans the gas injection rate, or equivalently throughput (because of the steady state assumption), is used. The rates for the gas injection from the top port (see Figure 3.1), summarized in Table 3.2, range from qualitatively very low throughput (1.46×10^{21} e^-/s) to around the maximum throughput allowed by the projected capacity of the pumping system ($\sim 1 \times 10^{23} e^-/s$[44, 45]) at 1.76×10^{23} e^-/s. Even though the two lowest throughput values are not considered viable scenarios for ITER due to too high temperatures obtained on the targets, they are retained as part of the scan because they are the only ones describing conditions before the particle flux rollover, and therefore complement the analysis.

SOLEDGE3X IMAS Shot	Magnetic Eq. & Wall	Corresponding SOLPS-ITER Shot	Gas puff rate [e^-/s]	Transport coefficient $D_\perp$ [m²/s]
106000	dr_{sep} = 6.5cm (2021)	n.a.	1.46×10^{21}	0.3 uniform
106001	dr_{sep} = 6.5cm (2021)	n.a.	3.81×10^{21}	0.3 uniform
106002	dr_{sep} = 6.5cm (2021)	n.a.	8.85×10^{21}	0.3 uniform
106003	dr_{sep} = 6.5cm (2021)	n.a.	1.13×10^{22}	0.3 uniform
106004	dr_{sep} = 6.5cm (2021)	n.a.	3.31×10^{22}	0.3 uniform
106005	dr_{sep} = 6.5cm (2021)	n.a.	6.80×10^{22}	0.3 uniform
106006	dr_{sep} = 6.5cm (2021)	n.a.	1.76×10^{23}	0.3 uniform
106007	dr_{sep} = 6.5cm (2021)	n.a.	8.85×10^{21}	far-SOL: 2.0 from 1cm
106008	dr_{sep} = 6.5cm (2021)	n.a.	8.85×10^{21}	far-SOL: 2.0 from 3cm
106009	dr_{sep} = 6.5cm (2021)	n.a.	8.85×10^{21}	far-SOL: 10.0 from 1cm
106010	dr_{sep} = 6.5cm (2021)	n.a.	8.85×10^{21}	far-SOL: 10.0 from 3cm
106011	dr_{sep} = 11cm	n.a.	1.46×10^{21}	0.3 uniform
106012	dr_{sep} = 11cm	n.a.	3.81×10^{21}	0.3 uniform
106013	dr_{sep} = 11cm	103027	8.85×10^{21}	0.3 uniform
106014	dr_{sep} = 11cm	103028	1.13×10^{22}	0.3 uniform
106015	dr_{sep} = 11cm	103029	3.31×10^{22}	0.3 uniform
106016	dr_{sep} = 11cm	103030	6.80×10^{22}	0.3 uniform
106017	dr_{sep} = 11cm	103034	1.76×10^{23}	0.3 uniform

Table 3.2.: Table of IMAS shot number of the simulations considered in this work, with the associated version of magnetic equilibrium and wall, the IMAS number of the SOLPS-ITER run using similar parameters (when available), the gas puff rate, and the values of the particle perpendicular diffusion coefficient. The shots 106007 - 106010 are related to the cases considered in chapter 6, but are included here as well for convenience. The cases 106011 - 106017 are run on a geometry identical to the one used in the SOLPS-ITER runs in the ITER database (dr_{sep} = 11cm), to enable a comparison between the two codes, see section 3.5

3.3. Improvements to the SOLEDGE3X physics model for ITER relevant simulations

This section presents the improvements of the SOLEDGE3X physics model to better describe high-density regimes in ITER: the implementation of the so-called Kotov model, and a specific treatment of the dynamics of the H_2^+ molecular ion.

3.3.1. Model for the ITER simulations with SOLEDEGE3X and SOLPS-ITER: the "Kotov" model

For the purpose of numerical simulations, one can not hope to model every possible collision type including all parameters, as this would prove to take unreasonable amount of computing time, and not all the necessary data exist to the level of detail this would require. The challenge is then to identify the processes that play a significant role, and include only those. The reaction set used for the simulations in this work is detailed in Table 3.3, and was presented by Kotov and al. in [46]. It is often referred to as the *Kotov model* in the EIRENE community, and includes improvements upon a simpler version of the set that was used before 2004 [46] (also known as the 'EIRENE 1996' model in the literature). This 'EIRENE 1996' simpler model is very similar to the one initially implemented in SOLEDGE2D and SOLEDGE3X and is currently used for studies of medium-sized tokamaks. It is shown in Table 3.4.

While this simplified model was derived for small machines, the improvements and additions that were made in the early/mid-nineties specifically targeted processes necessary to describe high-density regimes in larger machines such as JET, and with ITER in mind [46].

Thus, this more detailed model was implemented in SOLEDGE3X in the context of this PhD, so that the SOLEDGE3X ITER run would be executed more accurately, and with the same model for neutrals as in the SOLPS code suite that was involved in the divertor design. Following this, SOLEDGE3X now includes the possibility to switch between the simplified model and the Kotov model.

The Kotov model includes three additional reaction types [47] in comparison to the previous reaction set, which were identified as relevant for ITER and JET cases:

1. the Molecule Charge Transfer (molecule HCX, also referred to in the literature as 'ion conversion'): $H_2 + H^+ \rightarrow H_2^+ + H$. If this reaction is followed by the molecule EDR, it results in a net particle sink. In that case, the reaction chain as a whole is labeled *Molecule-Assisted Recombination (MAR)*. The MAR reaction can also include the negative H^- ion as an intermediary, but this channel is not considered in this work.

2. the Molecule-Ion HES (a.k.a. molecule-ion elastic collisions)

3. Neutral-Neutral HES (a.k.a. neutral-neutral collisions). The subsection below does a specific focus on those.

Furthermore, some of the reactions that were already in the simplified model are also modified:

- The collision rate coefficients for the processes involving molecules or the H_2^+ molecular ions now include a dependency in electron density, to account for population effects, which will increase those rates at higher densities.
- The atom charge exchange rate coefficient now includes a dependency on the velocity of the atom (recall that the reaction rate coefficient $\langle \sigma v \rangle$ is a function of relative velocity, and the velocity of the neutral cannot be neglected for fast CX atoms).
- The molecule dissociation rate coefficient is now based on the multi-step model from Sawada/Fujimoto/Greenland [48].

Neutral-Neutral collisions Initially, the reduced model for neutrals that was implemented in SOLEDGE3X (see section 3.3.1) did not include neutral-neutral collisions. Developments have been carried out in the context of this work to automatically include those collisions in the STYX interface between SOLEDGE3X and EIRENE, and in accordance with the plasma composition. This was done for the ITER cases to be consistent with SOLPS, and in this section this addition is discussed, and we show that these are indeed relevant for the medium to high throughput ITER cases.

To assess the relevance of neutral-neutral collisions, one can calculate the Knudsen number $K_n = \lambda / L$, where λ is the neutral particle mean free path with respect to collisions with other neutrals, and L is the characteristic size of the system. It was shown in [47] from SOLPS simulations that in regimes expected in the ITER's divertor, neutral particle density would reach values leading to Knudsen numbers as low as 0.1. In this case, neutral-neutral collisions cannot be assumed negligible and must be included in the model.

The importance of these reactions can be checked a posteriori: Figure 3.2 shows the volume reaction rates, after activating neutral-neutral collisions, of the most significant reactions along the first flux tube above the separatrix incident to the outer target, for a high throughput case (equivalent to SOLPS-ITER case IMAS #103030). In the close proximity of the target, the collisions between the recycled neutrals (label n-n HES "Heavy Elastic Scattering", see Table 3.3) become the third most-probable process.

Table 3.3.: Summary of reactions included in the EIRENE setup (also referred as the "Kotov model")

Reaction[1]	**IAEA reaction classification**	**Name**	**EIRENE identifiers**[2]
$H + e^- \rightarrow H^+ + 2e^-$	Ionization (EIN)	Atom EIN	AMJUEL H.4,10 2.1.5
$H + e^- \rightarrow H^* + e^- \rightarrow H + e^- + h\nu$	Excitation (EEX)	*included in above*	*included in above*
$H^+ + e^- \rightarrow H + h\nu$	Radiative Recombination (ERR)	Ion ERR/T	AMJUEL H.4,10 2.1.8
$H^+ + 2e^- \rightarrow H + e^-$	Three-Body Recombination (ERT)	*included in above*	*included in above*
$H + H^+ \rightarrow H^+ + H$	Charge Transfer (HCX)	Atom HCX	HYDHEL H.1,3 3.1.8
$H_2 + e^- \rightarrow H_2^+ + 2e^-$	Ionization (EIN)	Molecule EIN	AMJUEL H.4 2.2.9
$H_2 + e^- \rightarrow 2H + e^-$	Dissociation (EDS)	Molecule EDS	AMJUEL H.4 2.2.5g
$H_2 + e^- \rightarrow H + H^+ + 2e^-$	Dissociative Ionization (EDI)	Molecule EDI	AMJUEL H.4 2.2.10
$H_2 + H^+ \rightarrow H_2 + H^+$	Elastic Scattering (HES)	Molecule-Ion HES	AMJUEL H.0,1,3 0.3T
$H_2 + H^+ \rightarrow H_2^+ + H$	Charge Transfer (HCX)	Molecule HCX	AMJUEL H.2 3.2.3
$H_2^+ + e^- \rightarrow 2H + h\nu$	Dissociative Recombination (EDR)	H_2^+ EDR	AMJUEL H.4,8 2.2.14
$H_2^+ + e^- \rightarrow H + H^+ + e^-$	Dissociative Excitation[3] (EDE)	H_2^+ EDE[3]	AMJUEL H.4 2.2.12
$H_2^+ + e^- \rightarrow 2H^+ + 2e^-$	Dissociative Ionization (EDI)	H_2^+ EDI	AMJUEL H.4 2.2.11
$H + H \rightarrow H + H$	Elastic Scattering (HES)	Atom-Atom HES	Internal data
$H + H_2 \rightarrow H + H_2$	Elastic Scattering (HES)	Atom-Molecule HES	Internal data
$H_2 + H_2 \rightarrow H_2 + H_2$	Elastic Scattering (HES)	Molecule-Molecule HES	Internal data

[1] The standard naming system maintained by the IAEA is available at https://amdis.iaea.org/databases/processes/.

[2] Notation in EIRENE databases (see www.eirene.de).

[3] The runs are not resolved in terms of excitation levels, however this rate represents the reaction involving excited atom product.

Table 3.4.: Summary of reactions included in the EIRENE setup of the initals "simplified" model in SOLEDGE3X, close to the 'EIRENE1996' model.

Reaction[1]	**IAEA reaction classification**	**Name**	**EIRENE identifiers**[2]
$H + e^- \rightarrow H^+ + 2e^-$	Ionization (EIN)	Atom EIN	AMJUEL H.4,10 2.1.5
$H + e^- \rightarrow H^* + e^- \rightarrow H + e^- + h\nu$	Excitation (EEX)	*included in above*	*included in above*
$H^+ + e^- \rightarrow H + h\nu$	Radiative Recombination (ERR)	Ion ERR/T	AMJUEL H.4,10 2.1.8
$H^+ + 2e^- \rightarrow H + e^-$	Three-Body Recombination (ERT)	*included in above*	*included in above*
$H + H^+ \rightarrow H^+ + H$	Charge Transfer (HCX)	Atom HCX	AMJUEL H.2 3.1.8FJ
$H_2 + e^- \rightarrow H_2^+ + 2e^-$	Ionization (EIN)	Molecule EIN	HYDHEL H.2 2.2.9
$H_2 + e^- \rightarrow 2H + e^-$	Dissociation (EDS)	Molecule EDS	HYDHEL H.2 2.2.5
$H_2 + e^- \rightarrow H + H^+ + 2e^-$	Dissociative Ionization (EDI)	Molecule EDI	HYDHEL H.2 2.2.10
$H_2^+ + e^- \rightarrow 2H + h\nu$	Dissociative Recombination (EDR)	H_2^+ EDR	HYDHEL H.2, AMJUEL H.8 2.2.14
$H_2^+ + e^- \rightarrow H + H^+ + e^-$	Dissociative Excitation[3] (EDE)	H_2^+ EDE[3]	HYDHEL H.2 2.2.12
$H_2^+ + e^- \rightarrow 2H^+ + 2e^-$	Dissociative Ionization (EDI)	H_2^+ EDI	HYDHEL H.2 2.2.11

[1] The standard naming system maintained by the IAEA is available at https://amdis.iaea.org/databases/processes/.

[2] Notation in EIRENE databases (see www.eirene.de).

[3] The runs are not resolved in terms of excitation levels, however this rate represents the reaction involving excited atom product.

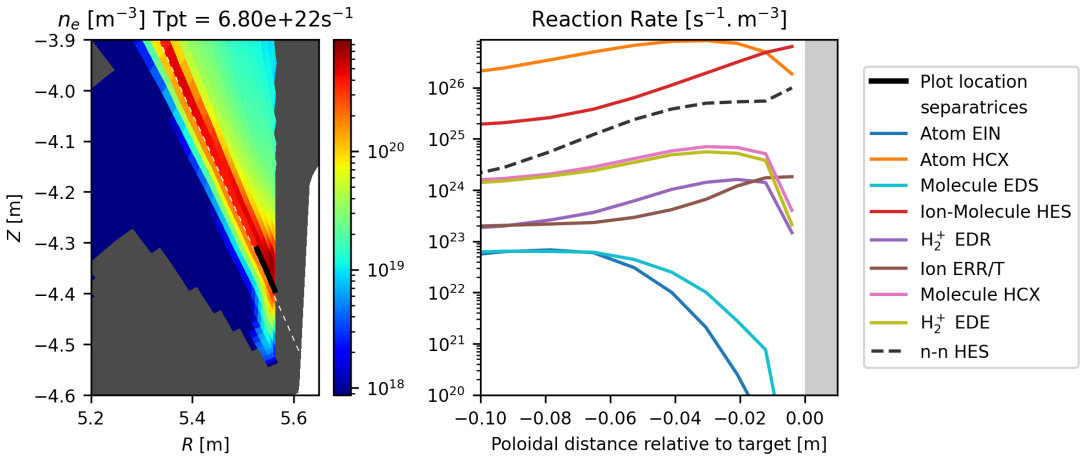

Figure 3.2.: Right: volume reaction rates of the most significant plasma and neutral interactions along the ending portion of a flux tube (in poloidal distance) incident to the outer target, corresponding for the first field line above the separatrix. Neutral-Neutral collisions are plotted with a grey dashed line (label n-n HES 'Heavy Elastic Scattering', see Table 3.3). Left: 2D color plot of the electron density at the outer target with the black line representing the chosen flux tube plot location. The white dashed line represents the primary separatrix.

To account for these reactions, EIRENE uses the Bhatnagar-Gross-Krook ("BGK") approximation through an iterative scheme. In this method, tracked neutral particles have a probability of undergoing elastic collisions with other neutral particles. This probability is computed using the density and temperature of neutrals in the current cell that was obtained at the end of the previous EIRENE call (i.e., at a previous time step) after completing all particle histories. Since the objective is to find a steady-state solution, this process will correctly converge to a consistent description of these collisions, assuming enough iterations of the Monte Carlo solver have been executed. At the start of the simulation or at the moment when neutral-neutral collisions are turned on, no neutral particle background is available, and it is necessary to call EIRENE a sufficient number of times to build a first realistic neutral particle background. In practice, it was found that this procedure converges quite fast, and 10 iterations are enough to initialize these reactions at the start of the simulation.

It was found that the addition of these reactions significantly impacts the solution for high throughput cases. Without them, the plasma detaches more abruptly at lower throughput, as can be seen in Figure 3.3, which shows plasma conditions at the outer target for the highest throughput case between runs with and without neutral-neutral collisions. The computed solution with these collisions shows higher temperature and density at the strike point, which indicates that they tend to reattach the plasma. This effect may be the result of the compression of the neutral gas cloud at the targets and at the pump: the neutrals now have a high chance of colliding with other neutrals, which

reduces their penetration into the chamber, and this also increases their probability of getting pumped below the dome, thus lowering the recycling factor and at the same time the loss for the plasma for a fixed gas injection rate.

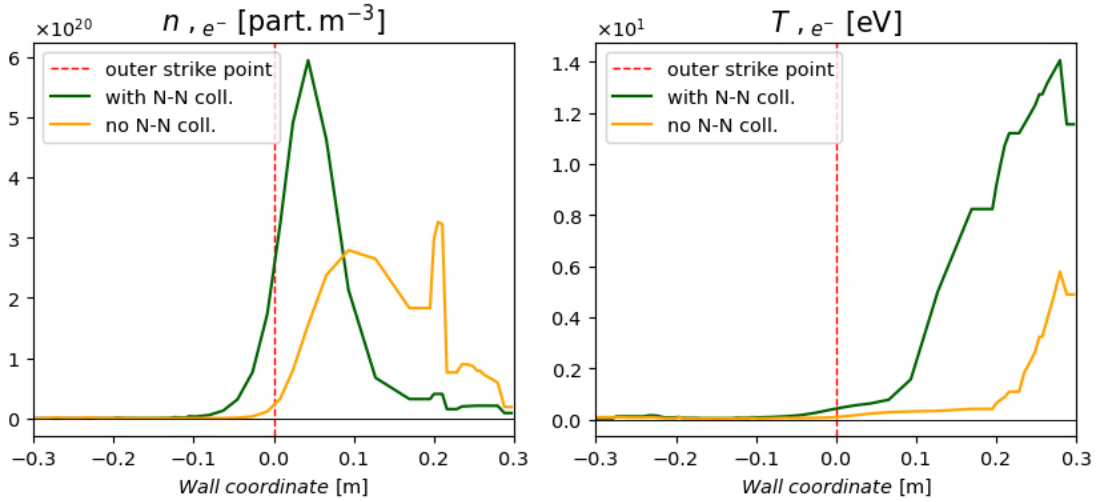

Figure 3.3.: Impact of neutral-neutral collisions: Plasma conditions at the outer target for the #103030 case (high-throughput) for runs with and without neutral-neutral collisions. Without these collisions, the solution obtained is in a more pronounced detachment state. (The secondary density spike is an artifact of the spatial discretization, due to the change in the alignment of the grid at this location.)

Finally, when observing the atom and molecule densities for the maximum throughput case, Figure 3.4, one can observe that molecules tend to accumulate near surfaces in the divertor and where angles are sharp: at the corner of the target and the reflector plates, and also near the angles below the dome and at the pump. The latter pattern was not observed without neutral-neutral collisions. Also, the effect of the semi-transparent surfaces (the dome pillars) is clearly visible and contains the molecules below the dome.

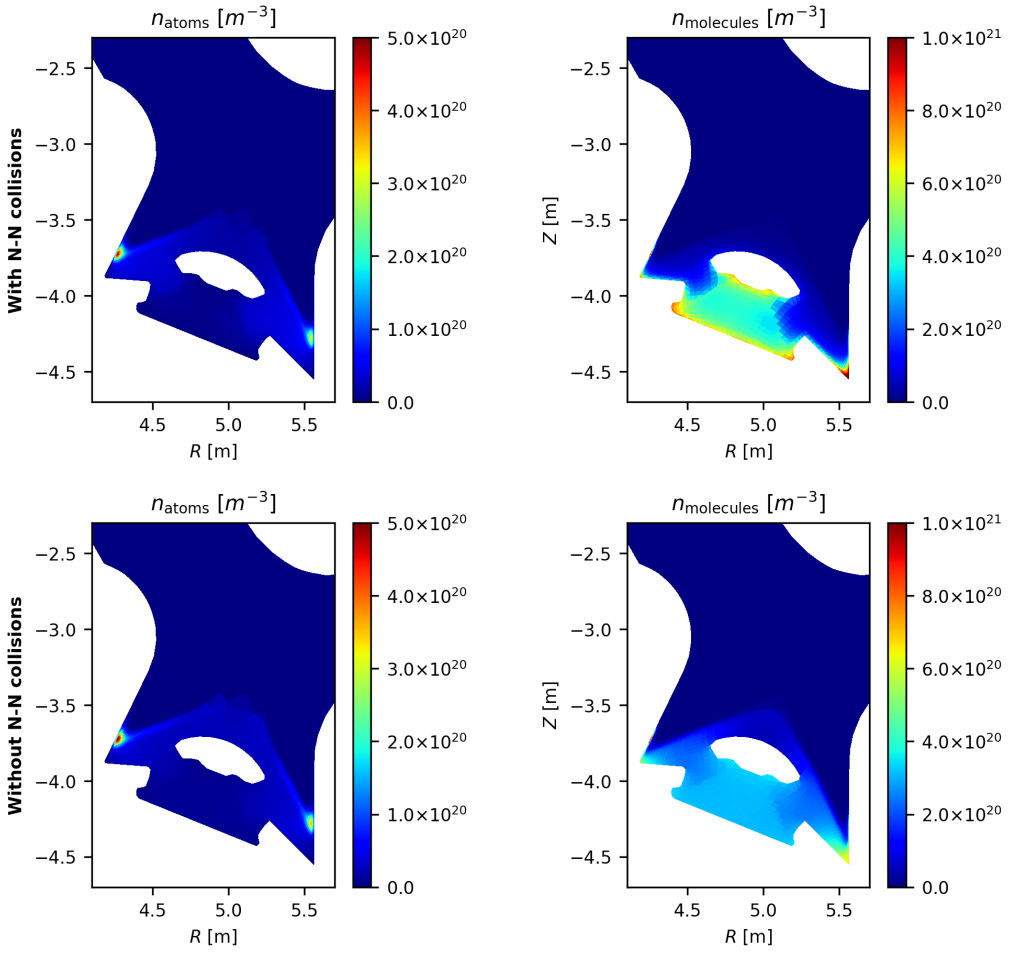

Figure 3.4.: Atom density (left) and molecule density (right) for the highest throughput case at 1.76×10^{23} e^-/s using the full Kotov model with neutral-neutral collisions.

3.3.2. Including the dynamics of the H_2^+ ions

We turn now to an addition that was not in the Kotov model, but was identified in SOLEDGE3X because of the extension of the numerical grid further out in the divertor.

One of the initial issues encountered when attempting to run high-density regime ITER cases with the molecule charge transfer included in the EIRENE reaction set was the random appearance of unphysically high particle sources in the form of point-like spikes below the divertor legs, between the edge of the dome and the reflector plates (i.e., near the edge of the SOLPS-ITER numerical domain). This behavior would destabilize the case, even prevent convergence, and was related to the accumulation of H_2^+ ions in unreasonable densities in certain cells. This was found to be caused by a dangerous combination of two approximations: the EIRENE sources were kept constant for many time steps without calling EIRENE, and the H_2^+ were treated in the

so-called *static approximation*.

The latter involves neglecting the transport of the particles, which are not moved through the spatial grid. Their momentum and energy are however retained and considered in the collision kinetics. This simplification comes from the assumption that their lifetime is very short compared to their transport time from one cell to another (velocity vs. the cell size). This was found not to hold anymore in the lower sections of the divertor legs covered by the SOLEDGE3X grid (see Figure 3.5).

In initial SOLEDGE3X runs, the ions were not transported through the grid to other locations where they could be destroyed, which produces very high densities in the geometry. Therefore, this assumption was relaxed, and the tracking in EIRENE was reactivated, which also required some modifications in EIRENE tracking routines. Once the transport is activated, EIRENE takes into account Coulomb collisions between this molecular ion and other charged particles from plasma species through a Fokker-Planck collision operator as described in section 1.11.2 of [37]. This results in an energy and momentum exchange between the ion background through collisions with these molecular ions. In this regard, the routine used by EIRENE was adapted so it would also apply to H_2^+ (or D_2^+ ions). For hydrogen and deuterium plasmas, the expression of ν_ε which governs the thermalization characteristic time, is given in the EIRENE documentation [37] in (1.106):

$$\nu_\varepsilon = \tilde{\nu}_\varepsilon \delta_{a,b} = \tilde{\nu'}_\varepsilon n_b T_b^{-\frac{3}{2}} = 1.36 \times 10^{-7} Z_a^2 Z_b^2 \frac{\sqrt{\mu_b}}{\mu_a} \lambda_{a,b} \delta_{a,b} n_b T_b^{-\frac{3}{2}} \tag{3.1}$$

$$\tilde{\nu'}_\varepsilon = 1.36 \times 10^{-7} Z_a^2 Z_b^2 \frac{\sqrt{\mu_b}}{\mu_a} \lambda_{a,b} \delta_{a,b} \quad \text{with} \quad \delta_{a,b} = 1 + \frac{\mu_b}{\mu_a} \tag{3.2}$$

a is the index of the test ion and b the index of the background. mu is the mass in a.m.u. For hydrogen, one obtains $\tilde{\nu'}_\varepsilon = 1.02 \times 10^{-6}$, and $\tilde{\nu'}_\varepsilon = 7.21 \times 10^{-7}$ for deuterium, and $\tilde{\nu'}_\varepsilon = 9.03 \times 10^{-8}$ [1].

The associated momentum exchange was also added, so that the $v_\parallel / v_\perp$ is conserved.

Activating the transport of H_2^+ ions resulted in the smoothing of the sources at these locations and the disappearance of the point-like sources. This contributed to a significant improvement of the stability of simulations and appears as a necessary ingredient for the stability of simulation with a plasma domain extending up-to-the-wall, especially in the private flux-region.

An evaluation of the importance of treating self-consistent H_2^+ ions dynamics is proposed below.

Dynamics of the H_2^+ molecular ions To assess how important the related physics are in our simulations, we take the example of one of the obtained simulations. Figure 3.5 shows the difference, for the rollover case (analysed in more detail further in section 4.3) in the inner divertor leg, between the H_2^+ density computed via Monte Carlo (1 million particles) by EIRENE in the static approximation (left), with tracking

[1] This value corresponds to 8.8×10^{-8} in the documentation which uses a rougher rounding

enabled as was effectively used in our simulations (center-left), and the post-processed density computed assuming local equilibrium from reaction rates assuming no transport (center-right). It is readily seen that the H_2^+ density in the static approximation shows density spikes between the reflector plate and the edge of the dome. These features contributed to the numerical instabilities encountered in our initial runs. With tracking enabled, these features are not there and are replaced by a smooth density. The no-transport post-processed density is also much higher in this region than in the tracking-enabled Monte Carlo simulation, which supports the assumption that transport becomes important there. H_2^+ created at this location are in fact removed via parallel transport (both the parallel transport time to the reflector plate and the lifetime of an H_2^+ at T_{wall} =500K are of the order of the millisecond). Thus activating the transport of H_2^+ ions seems to be necessary to capture reliably the physics occurring in remote divertor areas in up-to-the-wall simulations.

A possible reason the static approximation density does not show a density map similar to the post-processing is the low probability of particle creation there, and finite amounts of particles in the simulation cannot explore all possibilities. Indeed, the post-processed density is a ratio of creation to consumption rates, both of which are very small in this case. Therefore, creating enough H_2^+ particles there to produce satisfying statistics would require unreasonable amounts of particles.

As a note, the smoothness of the tracking-enabled solution, which is more physical, also improves the stability of the code. However, it is unclear if activating it is absolutely necessary regarding all other improvements to the code that have been made, see chapter 3.

Finally, the presence of high H_2^+ density below the divertor legs interrogates whether there could be H_2^+ consumption processes that should be relevant but not currently included in the model. Since the density of neutrals there is very high, this may be the case for the process opposite to the molecule charge exchange: i.e., an atom transfers its electron to an H_2^+ ion ($H_2^+ + H \rightarrow H_2 + H^+$). This process could be included in future work, as data for the rate coefficient is included in the AMMONX database[49]. Other destruction processes of the H_2^+ ion could involve the H_3^+ ion as an intermediary ($H_2^+ + H_2 \rightarrow H_3^+ + H$ then $e^- + H_3^+ \rightarrow H_2 + H$)[50]. However only the first reaction ($H_2^+ + H \rightarrow H_2 + H^+$) removes the need for tracking a positive ion, since the created H^+ belongs to the plasma background.

Also, in these regions where the H_2^+ transport is important, the plasma density is low, and the H_2^+ density becomes significant with respect to the plasma density. Therefore, this may render invalid the assumption that the system considered by the plasma solver (i.e., the sum of H^+ ions and electrons) is electroneutral because the plasma solver assumes the electron density equal to the H^+ density only, and does not take into account the presence H_2^+ ions.

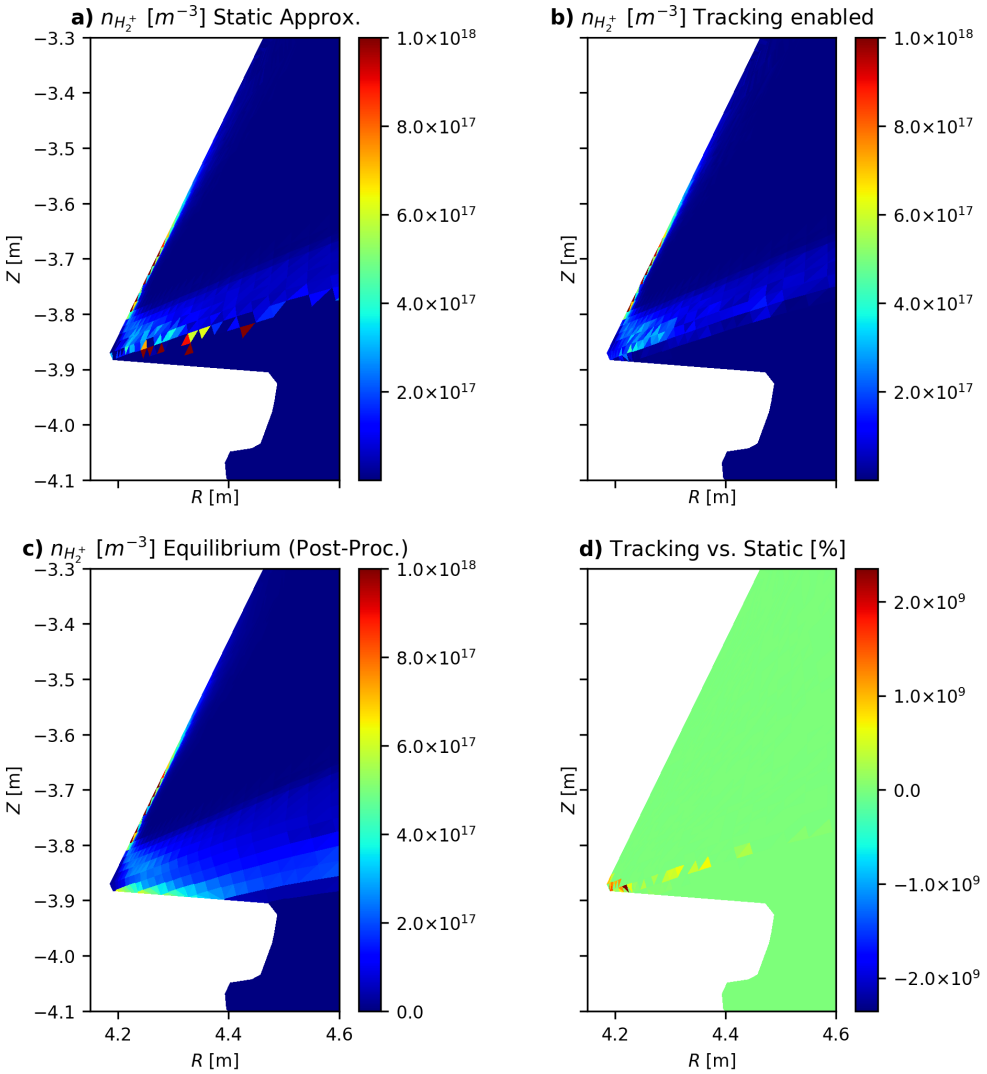

Figure 3.5.: Density of H_2^+ ions computed at rollover with the static approximation (a), with tracking enabled (b), and via post-processing with reaction rates assuming no transport (c). The (d) graph shows the relative difference in % between the static approximation (a) and tracking enabled (b).

3.3.3. Outlook for future improvements on the physics model side

The changes brought to the model enhanced the fidelity of the physical description of the system. Furthermore, from the lessons learned from their implementations and the open discussions in the community, some elements were identified as potential future steps in the improvement of the modeling for high-density regime edge plasmas regarding the neutrals:

- The inclusion of the inverse molecular charge transfer ($H_2^+ + H \rightarrow H_2 + H^+$) in the atomic & molecular model could be investigated to assess whether this process is indeed relevant. In fact, the regions with accumulated H_2^+ ions also show large atom densities, which could make this process significant. If so, adding this process might enable to turn on again the H_2^+ static approximation.
- Since plasma conditions can extend to sub-eV temperature, the validity of the database fits at such low temperatures may be worth investigating.
- Many discussions involved the parametrization of the reaction rates and the kinetics of those (some elements are also mentioned in [51]). Efforts and comparison to a full Collisional-Radiative Model (CRM) are being actively investigated [52], and development is ongoing for inclusion in EIRENE.
- It was found that radiation trapping could impact the simulation of high regime divertor plasmas [20, 53], which could be included in future simulations.
- The modeling of the sheath and the magnetic pre-sheath and its coupling with fluid codes, especially at grazing angles, could be improved by leveraging results from PIC codes [30].
- Finally, lifting the steady-state assumption and rerunning the simulations with time dependant kinetic neutrals would enable the simulation of detachment dynamics.
- The molecule-assisted recombination can also involve the channel where the negative H^- ion is the intermediary instead of the H_2^+ ion. This has been shown to play a role in detached divertors in TCV and MAST-U [51, 54]. Including this reaction in the model could help assess if such a process could be important in ITER as well.
- For multispecies plasmas, the SOLEDGE3X plasma solver could include charge exchange between different chemical elements to enable the capture by an H^+ of an electron belonging to a low-charge-state impurity.
- Finally, the use of reduced turbulent models such as the $k-\varepsilon$ model in SOLEDGE3X instead of prescribed perpendicular transport coefficients should be investigated.

3.4. Improvements of the numerical aspects

Even though the SOLEDGE3X code has been widely used to model medium-sized tokamaks [34, 55–58], running ITER simulations proved to be a challenge significantly harder to tackle. Plasma parameters for PFPO-1 cases are not entirely different from what is obtained in high-power experiments for JET, therefore a probable root cause for the difficulty in simulating the ITER plasmas considered here is the size of the machine.

The rationale for putting forward this assumption is briefly discussed in the following sections. While this should be confirmed by a more in-depth analysis that is outside the scope of this work, the actual observed effect was the considerable increase and sensitivity of collisional processes (both electron-ion exchanges and plasma-neutral interactions), which proved to be a challenge to describe. Practically speaking, this translated into very slow and unstable simulations, rendering it impossible to converge cases. Thus, some elements of the numerical method were revised.

In the context of this work, solutions to these issues were devised and implemented, pertaining to a wide range of topics across the three main blocks of the SOLEDGE3X-EIRENE tool: in the SOLEDGE3X plasma solver, in the EIRENE neutrals solver, and in the STYX interface code dealing with the coupling of the two solvers. They are presented in this section.

3.4.1. Numerical grid optimization and the multigrid approach

This first section briefly discusses optimizations related to the numerical grid and focuses on two aspects. First, we address the optimization of the meshing and the consequences on the computation time. Second, the so-called *multigrid* approach used to converge the considered cases in the next chapters is presented.

3.4.1.1. Optimizing the plasma-solver numerical grid

In the course of this thesis, many improvements have been made in the mesh generator software used to construct discretization grids for our simulations. While many of these changes consisted of adding new features to ease the mesh generation process and will not be discussed here, others directly impacted the numerical stability of the code and the computing time. We here make a quick note on the optimization of the poloidal size of mesh cells, as it proved to be the most effective improvement related to the computation speed. It is also important guidance for future users of the code.

The size of the smallest cell in the grid determines the time step duration in the SOLEDGE3X plasma solver, because many terms (especially advection and perpendicular diffusion) are treated explicitly. This imposes a Courant–Friedrichs–Lewy (CFL) condition defining the maximum allowed time step, which is constrained by the smallest cell across the grid to prevent numerical instabilities. The "cell size" is defined here as the Euclidian distance between two radial or poloidal edges, as opposed to the length of radial or poloidal edges. The two notions differ for slanted cells.

The smallest cell for ITER grids is located at the top of the outer baffle, where the requested alignment with the wall ends. Thanks to various changes in the algorithm used in the mesh generator, the size of the smallest cell was increased from 0.05 mm in the initial mesh generated in 2017 to 1.0 mm, i.e., a 20x increase.

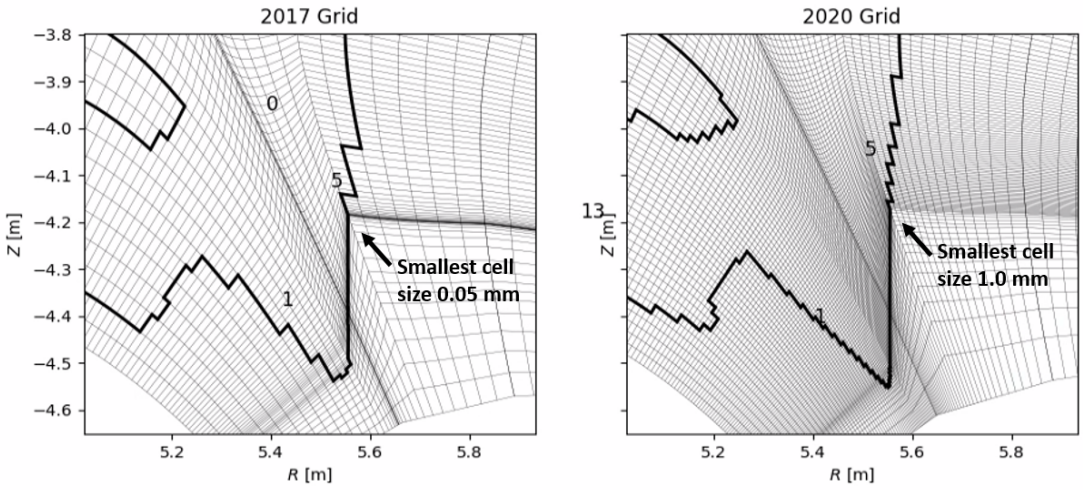

Figure 3.6.: Location of smallest cell size in ITER mesh (2017 mesh & 2020 mesh)

As a result, the new mesh runs in the near convergence phase with a time step of 2.66×10^{-8} s vs. 6.07×10^{-9} s in the 2017 mesh, i.e., increased by a factor 4. The full factor of 20 on the cell size is not recovered since other factors come into play. The desired resolution at the target dictates the size of the smallest size in the poloidal direction, giving rise to a trade-off between accuracy and computation speed.

The cell size cannot be increased indefinitely, however, as is discussed in the section D.

3.4.1.2. The Multigrid approach

Multigrid method *Note: the numbers presented in this section were obtained using the reduced atomic & molecular model in EIRENE (i.e., without molecule charge exchange, ion-molecule elastic collisions, and neutral-neutral collisions), as this consisted of the initial starting point of this work, before the implementation of the complete set of reactions in Table 3.3. These times differ from what would have been obtained with the full set (Kotov model), as longer computation times are required, but the reported trends remain relevant.*

The overall idea of what will be called here the "multi-grid approach" is simple: converge the case with a very coarse mesh with large cell sizes, then interpolate the results on a finer mesh, converge it, then repeat until reaching the desired mesh resolution. It is inspired by the multi-grid schemes developed for the iterative resolution of large linear systems[59]. This terminology is only used to reflect the general idea, and the current implementation represents a first step and does not include advanced schemes as the ones used in the literature for solving complex-non linear systems, or V- and W- cycles. This is also due to the long computation time of running a single convergence step, even on a coarse mesh.

The motivation for this approach comes from the observation that reaching the steady state in terms of particle content is the longest mechanism, especially for the

ITER machine, due to its size relative to the particle input and pumping rate. This machine, in a SOLEDGE3X simulation, contains $\sim 1 \times 10^{21}$ particles in $\sim 400 m^3$ (the core is not part of the domain, otherwise one would have expected the better-known value of $820 m^3$), while puff rates are of the order of 1×10^{21} to 1×10^{23} particles/s, pointing at a need of the order of a second of plasma simulation time to achieve convergence for the low-density cases. Indeed, for the #102294 case (medium/low density), it has been found that convergence is reached in ~1.5 s, whereas for small machines such as WEST, cases can be converged in 0.2 s of plasma. Additionally, the very large sensitivity of collisional processes (plasma-neutrals & electron-ion exchanges) to small temperature variations in the ITER divertor tends to strongly decrease the time step, due to the CFL condition in the early transient phase. Also, the edge plasma in ITER is nearly opaque to neutrals as opposed to WEST, rendering the gas puff input largely inefficient to quickly propagate changes in density. Therefore, reaching a steady state on a very coarse grid, which utilizes a good approximation of the particle content, provides a reasonable approximation of the actual solution that would be obtained with the desired finer grid. Using a coarser grid enables the use of a much larger time step (fine mesh the time step "dt": $dt = 4 \times 10^{-8}$ s vs. coarse mesh: $dt = 2 \times 10^{-7}$ s i.e., an increase by a factor 5.7), and also required less time to compute each time step, including gains from the number of mesh cells to handle in SOLEDGE3X in the plasma solver, and also in EIRENE (although less intuitive as EIRENE is a particle-tracking Monte-Carlo code but it still manipulates arrays for mesh related computations). Once a steady state has been reached on the coarse grid, one then interpolates the solution to a finer grid and restarts the simulation to run it until it converges again. The process should be stopped once the solution does not evolve significantly from one grid to the other.

In practice for our ITER simulations, a set of 3 meshes has been produced and used, illustrated in figure Figure 3.7. We will refer to them as the coarse, medium, and fine grids.

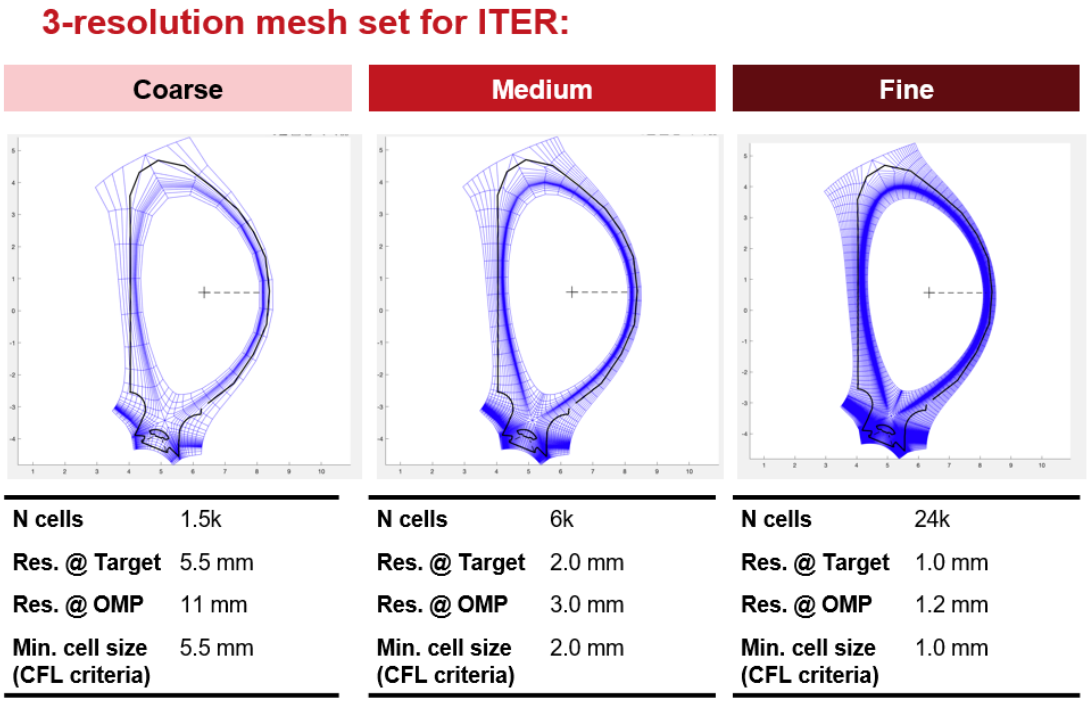

Figure 3.7.: Illustrations of the set of three grids generated on the dr_{sep}=11cm equilibrium and wall geometry, a coarse resolution mesh (left), a medium resolution mesh (center), and a fine resolution mesh (right)

Gain on computation time The results in terms of speed gains are summarized below in Figure 3.8. On that figure, one compares the time necessary to reach a steady state on the fine grid, by running a simulation directly on the fine grid or by adopting the multi-grid approach presented before, resulting in a gain of a factor three on the computing time. These cases were much faster to compute than the ones presented in the following chapters because here we recall that the simplified model for the neutrals was used (not the Kotov model), which did not include MAR, ion-molecule and neutral-neutral elastic collisions. All cases were run on a single node (28 CPUs) on the ITER cluster ("gen9" partition), with 80,000 particles in total in EIRENE (note: this exercise was carried out before investigations on the optimization on the number of particles section 3.4.5).

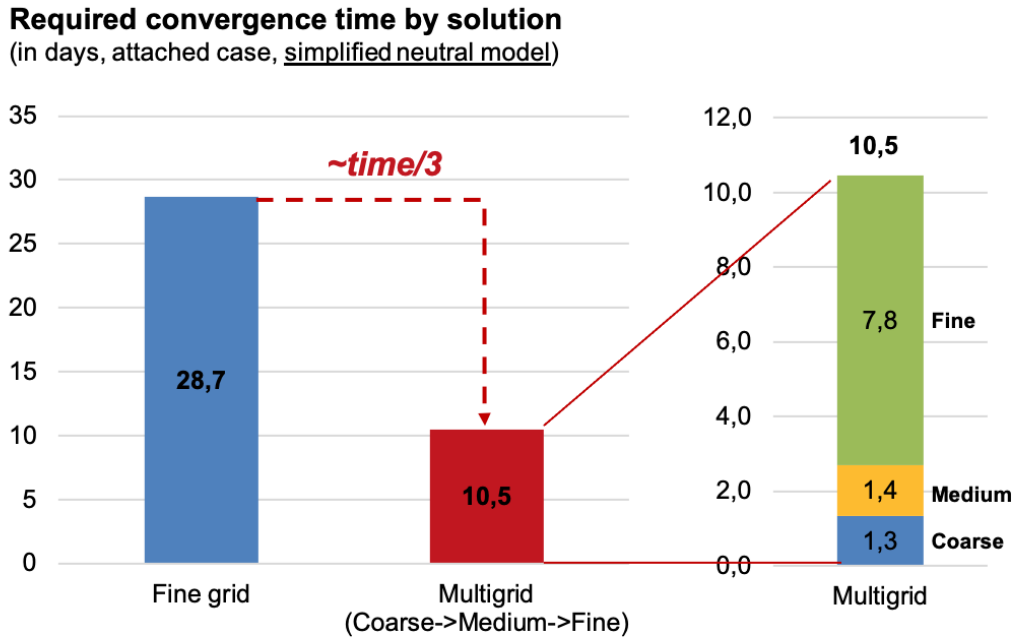

Figure 3.8.: Summary of computation time acceleration, for the case at a throughput of $3.81 \times 10^{21} e^{-}/s$ with the simplified A&M model (i.e., without molecule charge exchange, ion-molecule elastic collisions, and neutral-neutral collisions), between a run done fully on the fine grid, and a run done in the multigrid approach based on a coarse, medium, and fine grid.

Grid resolution impact on the solution To assess the convergence of the multigrid procedure, we first analyze the difference in the solution found on each grid. Figure 3.9 shows the particle and total heat flux at the inner and outer strike points for the coarse, medium, and fine grid. While results between the medium and fine grids are almost identical, the results using the coarse grid show between 20% and 30% underestimations, especially on the heat flux. However, the solution still is quite close to the final solution. Further comparison should be made at other throughputs, as extensive studies with the SOLPS code in [23] showed that the discretization error was throughput-dependent, and also had an impact on the throughput value of the rollover point.

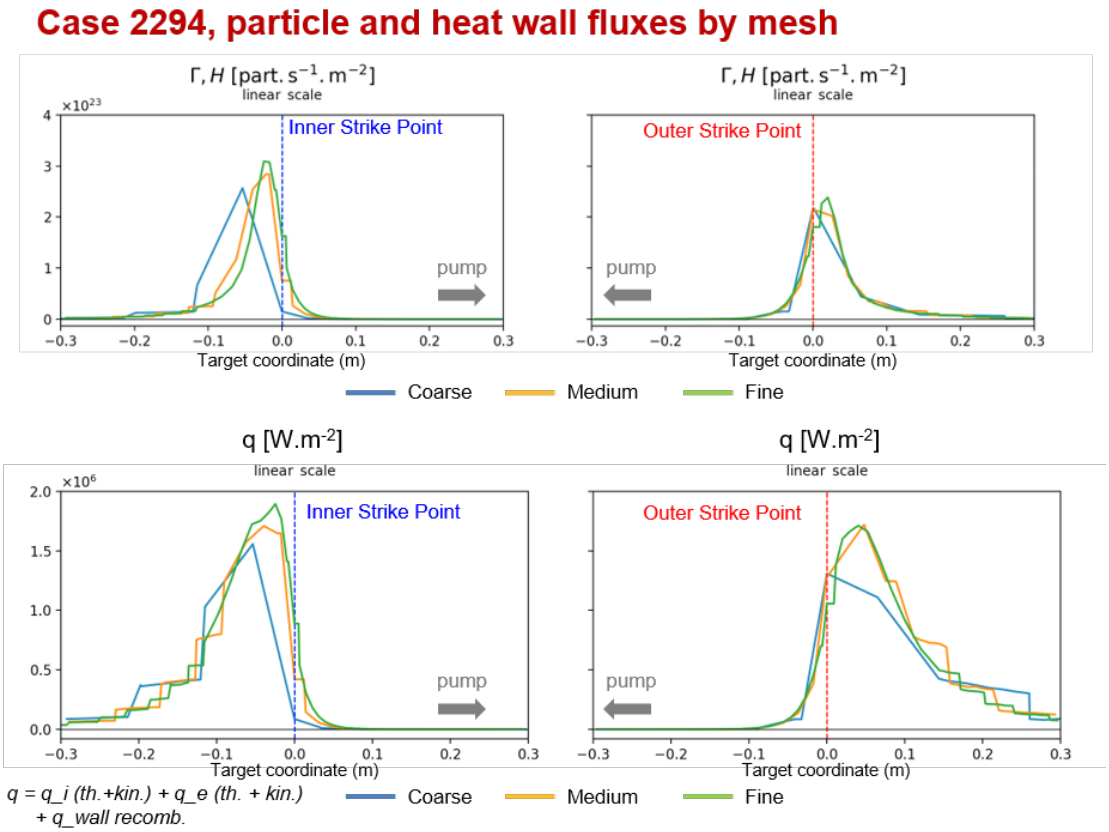

Figure 3.9.: Toroidally symmetric particle flux (top row) and total heat flux (bottom row), at the inner (left) and outer (right) targets, for the coarse, medium, and fine resolution grids

In conclusion, going up to the "fine" grid is not justified, as the results are almost identical to the ones with the "medium" grid (3 mm at the strike point). In the rest of this manuscript, results will be shown on the medium grid resolution.

3.4.2. Stabilizing the collisional closure exchange terms

Caveat: The reader is advised that at the time of writing, this implementation of the Zhdanov closure in SOLEDGE3X cannot be considered final, as there are on-going discussions on the definition of the temperatures and the Q_α^W term.

3.4.2.1. Introduction

The fluid collisional closure derived by Zhdanov [26] and implemented in SOLEDGE3X [28] provides formulations for the momentum and energy exchange between plasma species R_α and Q_α in section 2.3.3.

These terms, due to their collisional nature, tend to become very large when the density rises and temperature decreases, which are exactly the conditions that appear

in the vicinity of target plates in ITER simulations. While for simulations of current smaller machines these terms are too weak to pose a challenge to the code, attempts at running ITER cases rapidly demonstrated the need for a specific treatment of those. For PFPO-1 cases, only the energy equipartition between ions and electrons was necessary to address, as the friction force between electrons and ions[1] is weak. For $Q = 10$ Neon seeded cases with Helium at high power (100MW), the need arose to also stabilize the friction forces between Neon, Helium, and Deuterium.

The three terms considered here are:

- for the momentum equation:
  - R_α^{fric}: the local parallel friction force, resulting from the local difference in parallel velocities between species
- for the energy equation:
  - Q_α^{th}: the thermal energy equipartition heat flux, resulting from the local difference in temperatures between species (in addition to the electrons, each ion and charge state species has its own temperature in SOLEDGE3X)
  - Q_α^{W}: the energy exchange associated with the friction force, which takes the form of a work term.

As a note, the collisional closure for the momentum balance actually includes also a force from the parallel temperature gradients of the species. However, this one was not found to be problematic.

In partially detached regimes in the considered ITER simulations and the transients (in the sense of the evolution of the simulation's initial state towards the final converged solution), the plasma conditions obtained by the code show between 0.1 and 0.3 eV of difference between T_e and T_i. This apparently small difference is enough, at temperatures of the order of 1eV and densities of 10^{21} m^{-3} near the targets to generate strong exchange heat fluxes from one species to the other, of the order of 10^9 W.m^{-3}. In the converged state, the electron energy density evolution characteristic time from this term is about 10^{-8}s (see Figure 3.10), however in the transient phases this time scale was found to be rather of the order of $10^{-9}s$ or less, due to its sensitivity to the temperature difference. As this term is treated with an explicit method in SOLEDGE3X, this characteristic time constitutes a constraint for the plasma solver time step to properly describe its temporal evolution. Thus, the code required a time step of at least 10^{-9}s, which is unreasonable with respect to the computing time.

[1] No momentum equation is solved for the electrons, this force balance is closed via the parallel electric field, see section 2.3.3

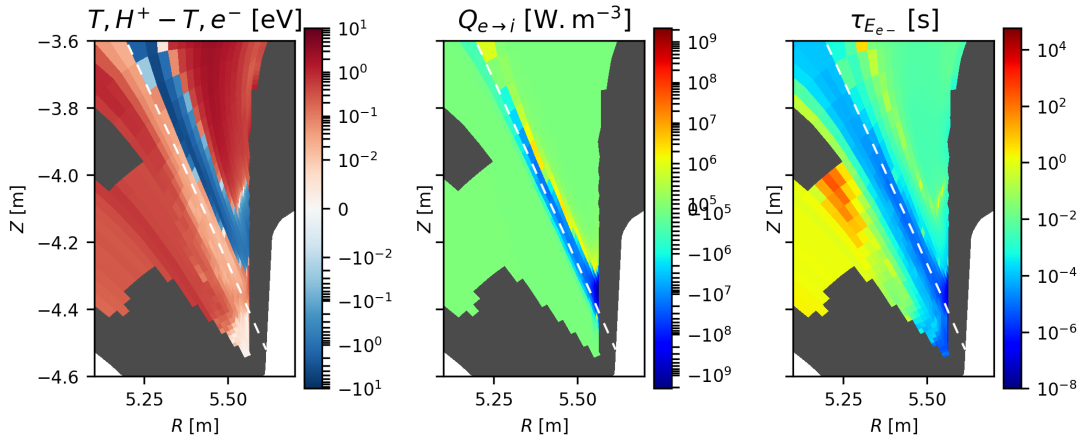

Figure 3.10.: [Plots shown in the converged state] Left: Electron to ion local collisional heat exchange terms in the divertor. Right: Electron energy evolution characteristic time defined as electron energy divided by the electron-ion heat flux, for the case #103030 (high throughput)

SOLEDGE3X initially treated these terms in a fully explicit manner. To stabilize these, the appraoch was taken to design and implement an implicit scheme.

3.4.2.2. Local implicit scheme

Below is summarised the list of symbols used in the following sections, for reference:

- α: a species index
- β: another species index
- $Q^{th}_{\alpha\beta}$: the thermal energy equipartition heat flux from species β to species α
- $Q^{W}_{\alpha\beta}$: the work of the total collisional forces (friction and thermal) from species β to species α
- $Q_{\alpha\beta}$: total collisional heat flux (equipartition and work) from species β to species α
- $R^{\text{fric}}_{\alpha\beta}$: the friction force from species β to species α
- $R^{\text{therm}}_{\alpha\beta}$: the thermal force arising from the parallel gradient of the temperature of the species β, applied to species α
- $R_{\alpha\beta}$: the total collisional forces (thermal + friction) from species β to species α
- $A_{\alpha\beta}$: coefficient for the energy equipartition from species β to species α, see Equation C.19

- $B_{\alpha\beta}$: coefficient for the friction force from species β to species α, see Equation C.11
- Z_α: charge number of the species α
- e_α: charge of the species α ($= Z_\alpha e$)
- Z_{eff}: effective charge
- T_{eff}: effective temperature
- m_α: particle mass of species α
- $\mu_{\alpha\beta}$: reduced mass of species α and β
- $\mu'_{\alpha\beta}$: mass fraction of species α in the α,β couple
- n_α: density of species α
- T_α: temperature of species α
- u_α: fluid velocity of species α
- $\overline{u}$: common fluid velocity
- w_α: fluid velocity of species α relative to the common fluid velocity, $w_\alpha = u_\alpha - \overline{u}$
- $\Lambda_{\alpha\beta}$: Coulomb logarithm of species α and β
- γ_α: square of the thermal velocity of species α
- $\gamma_{\alpha\beta}$: reduced square of the thermal velocities of species α and β
- $\tau^{-1}_{\alpha\beta}$ inverse collision time between species α and β

The approach for implicitation of the equipartition heat flux and the friction force follows the same method, and use the fact that all the quantities involved are local in a cell, no spatial dependency is present. The thermal force related to temperature gradients is kept in the explicit part of the scheme.

Both of these terms R^{fric}_α and Q^{th}_α represent fluxes of two quantities solved by the code (resp. $\Gamma_\parallel$ and E), resulting from local differences in the associated intensive quantity (resp. $v_\parallel$ and T). Due to their collisional nature, they both include a $n_\alpha n_\beta$ product as a factor, which makes it possible to express the fluxes using their extensive quantity:

$$X_\alpha = n_\alpha I^X_\alpha, \quad X_\alpha : \text{"Extensive quantity"}, \; I_\alpha : \text{"Intensive quantity"} \tag{3.3}$$

$$\phi^X_{\alpha\beta} = A n_\alpha n_\beta (I^X_\beta - I^X_\alpha) = A(n_\alpha X_\beta - n_\beta X_\alpha) \tag{3.4}$$

In the expression above, X represents any of the two extensive quantities between the parallel momentum or thermal energy (the code actually solves for the total energy,

see in the next paragraphs), ϕ^X the flux of this quantity from one species to the other,i.e. the friction force or equipartition heat flux, and I represents the associated intensive quantity: respectively the parallel velocity and the temperature. More explicitly, the objective is to formulate these two terms with the following forms:

$$Q^{\text{th}}_{\alpha\beta} = \frac{3}{2} A_{\alpha\beta} n_\alpha n_\beta (T_\beta - T_\alpha) = A_{\alpha\beta}(n_\alpha E_{\text{th},\beta} - n_\beta E_{\text{th},\alpha}) \tag{3.5}$$

$$R^{\text{fric}}_{\alpha\beta} = B_{\alpha\beta} n_\alpha n_\beta (v_{\parallel,\beta} - v_{\parallel,\alpha}) = B_{\alpha\beta}(n_\alpha \Gamma_\beta - n_\beta \Gamma_\alpha) \tag{3.6}$$

The $A_{\alpha\beta}$ and $B_{\alpha\beta}$ coefficients actually depend on many other quantities because the system is highly non-linear. However, in the solving process, they will be assumed constant (i.e., computed explicitely from the values at the previous time step) as part of the linearization method.

The details of their full expression and of the associated systems are provided in section C.

3.4.2.3. Solving the system

We note that the Γ system Equation C.16 is not dependant on the energy. Thus, it is possible to solve it first, and then use the obtained values for Γ in the RHS of the energy system Equation C.26. After this, the E system is solved.

For the complete time derivative of Γ and E, we also consider the contributions that have already been computed in the numerical scheme $\partial_t^{\text{expl.}}\Gamma$ and $\partial_t^{\text{expl.}}E$, and include them as constants on the right-hand side in Equation 3.7. In SOLEDGE3X's numerical scheme, these other contributions are located in the explicit scheme section as well. They contain the advection, and also more particularly the sources related to neutrals (e.g. as computed by EIRENE), which can become very large in detached cases in large machines such as ITER).

We also note that we include also in the RHS the thermal force term $R^{\text{th},\Gamma} = R^{\text{th}}_\alpha / m_\alpha$ in ∇T from the collisional closure, the expression of which is kept in the explicit part of the numerical scheme because of its spatial dependence.

The system to solve, for Γ is finally:

$$\partial_t \Gamma = R^{\text{fric},\Gamma} + R^{\text{th},\Gamma} + \partial_t \Gamma^{\text{expl}} \tag{3.7}$$

$$\partial_t \Gamma = M^R.\Gamma + R^{\text{th},\Gamma} + \partial_t \Gamma^{\text{expl}} \tag{3.8}$$

and for the energy:

$$\partial_t E = Q^{th} + Q^W + \partial_t E^{\text{expl}} \tag{3.9}$$

$$\partial_t E = M^Q.E + C_{kin} + Q^W + \partial_t E^{\text{expl}} \tag{3.10}$$

The standard implicit method of solving linear systems is carried out for the two

systems, which are now in the same form:

$$\partial_t X = M.X + X_c \tag{3.11}$$

It is done by taking the right-hand side at time step $n+1$:

$$\frac{X^{n+1} - X^n}{dt} = M.X^{n+1} + X_c \tag{3.12}$$

$$(\mathbb{I} - dt.M).X^{n+1} = X^n + X_c.dt \tag{3.13}$$

$$X^{n+1} = (\mathbb{I} - dt.M)^{-1}.(X^n + X_c.dt) \tag{3.14}$$

New values of Γ are obtained, the energy RHS terms depending on Γ are computed, then the E is solved. We then wish to recover the Γ and E rates from this collisional closure to feed back into the total time derivatives. For Γ, we retrieve R^Γ the friction force contribution to Γ from Γ^{n+1} computed at the last step:

$$\frac{\Gamma^{n+1} - \Gamma^n}{dt} = R^{\text{fric},\Gamma} + R^{\text{th},\Gamma} + \partial_t \Gamma^{\text{expl}} \tag{3.15}$$

$$R^{\text{fric},\Gamma} = \frac{\Gamma^{n+1} - \Gamma^n}{dt} - R^{\text{th},\Gamma} - \partial_t \Gamma^{\text{expl}} \tag{3.16}$$

For the total energy E, we retrieve the total exchange rate Q which includes the thermal equipartition and the work of the collisional forces in the same way:

$$Q = Q^{th} + Q^W \tag{3.17}$$

$$\frac{E^{n+1} - E^n}{dt} = Q + \partial_t \Gamma^{\text{expl}} \tag{3.18}$$

$$Q = \frac{E^{n+1} - E^n}{dt} - \partial_t E^{\text{expl}} \tag{3.19}$$

Overall this method requires the computation of the coefficients, and the resolution of two linear systems of size $N_{species}$

3.4.2.4. Observed results

This procedure produces a set of converging temperatures, therefore preventing any overshoot or uncontrolled divergence, independently of the time step length.

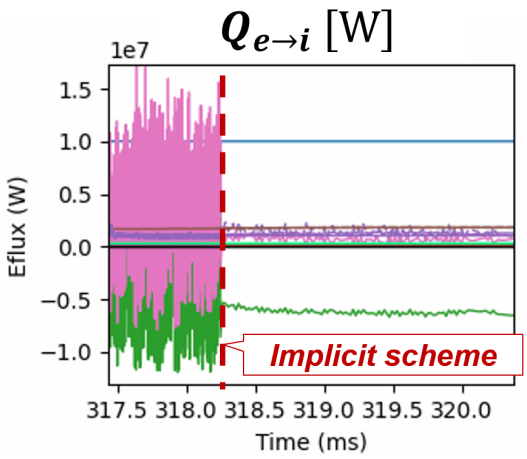

Figure 3.11.: Integral over the domain of the electron-ion heat flux, before and after the activation of the analytic method, all with increased time steps, for an ITER 20MW pure H case.

Figure 3.11 shows the effect of activating such a scheme on the volume integral of the electron-ion heat flux, all with increased time step. The time at which the new implicit scheme is activated is marked by the vertical dashed line. The solution showed very large oscillations before the activation of the scheme, making it difficult or even impossible to reach a converged steady-state for the simulation. Activating the implicitation leads to an immediate disappearance of these oscillations. The resulting scheme is also unconditionally stable, whichever time step amplitude is adopted by the plasma solver.

3.4.3. Improved perpendicular diffusion operator

One specific challenge that was encountered when running ITER cases relates to the perpendicular diffusion operator in SOLEDGE3X. The discretization method in the plasma solver is based on a conservative finite volumes approach, where intensive quantities are computed in each quadrangle cell at its center, and fluxes are computed on each quadrangle face. This requires the computation of the gradient of the relevant fields at the location of the quadrangle face center. Initially, this was carried out using a face-centered differencing gradient operator, using a 9-point stencil[2], for any quantity

[2]Note that this discretization choice differs from the 5-point stencil often used in SOLPS simulations and provides a more accurate description (isotropic in the perpendicular plane) of the diffusion terms, especially in the vicinity of target plates where the grid cells can get significantly non-orthogonal. For highly slanted cells, the 5-point stencil discretization leads to a non-isotropic perpendicular diffusion acting along a single direction, while the 9-point stencil preserves the isotropy of the diffusion in the perpendicular plane.

of interest X:

$$\vec{\nabla} X = \frac{\partial X}{\partial \psi}\vec{e^{\psi}} + \frac{\partial X}{\partial \theta}\vec{e^{\theta}} + \frac{\partial X}{\partial \varphi}\vec{e^{\varphi}} \tag{3.20}$$

$$\vec{\nabla}_{\psi-\frac{1}{2},\theta} X = (X_{\psi,\theta} - X_{\psi-1,\theta})\vec{e^{\psi}} + \frac{1}{2}\left(\frac{1}{2}(X_{\psi-1,\theta+1} + X_{\psi,\theta+1}) - \frac{1}{2}(X_{\psi-1,\theta-1} + X_{\psi,\theta-1})\right)\vec{e^{\theta}} \tag{3.21}$$

The second expression provides an example of the computation of this gradient at the center of a psi-facing quadrangle face (i.e., a radial flux). The φ contribution reduces to 0 in the 2D axisymmetric simulations concerned by this work and is omitted here for readability (only 6 points of the stencil are represented), but it is implemented in the code when dealing with 3D cases and is similar to the θ component. It can be noted that for this cross-coordinate component θ, the points used are the simple arithmetic mean of the two cells at ψ and $\psi+1$ of the corresponding θ locations above and below the face considered ($\theta+1$ and $\theta-1$). Figure 3.12 provides a visual representation of this stencil.

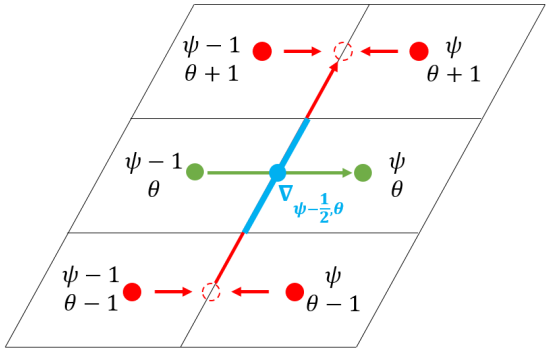

Figure 3.12.: Computation of the gradient on the ψ θ face (in blue) using a 9-point stencil in 2D. Green points represent the direct ψ contribution, and red points the cross-coordinate contribution from θ.

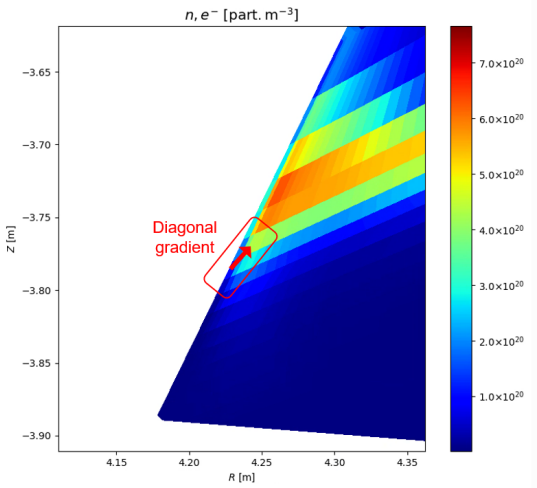

Figure 3.13.: Presence of strong density gradients in the "diagonal" direction with respect to the mesh, which leads to reverse diffusion flows when using the initial operator.

However, this operator is not guaranteed to produce total-variation diminishing results as is expected for a diffusion operator. As detailed in [60], in case of strong gradients in the "diagonal" direction of the mesh in an anisotropic medium, linear centered-difference schemes can produce reverse fluxes from low-density cells to high-density cells, violating for example the second law of thermodynamics in the case of heat fluxes. This behavior was observed for particle fluxes when attempting to run high-throughput ITER cases, at the edge of the plasma dense region below the strike points, between the target and reflector plates Figure 3.13. At this location, sharp density gradients develop in the "diagonal" direction of the field-aligned mesh, leading to reversed fluxes from empty cells toward plasma-dense cells. Such a situation is highly unstable for the discretization scheme as it can lead to a "run-away" situation where already empty cells get non-physically emptier by diffusion, eventually leading to the crash of the simulation or to a drastic drop of the time step.

Ref. [60] then proposes a set of new improved operators, which are guaranteed to preserve the monotonicity of the solution, i.e., without generating reverse flows. These operators rely on non-linear correction terms, so-called "slope limiters", which have been the subject of substantial research. The "slope limited asymmetric centered" operator was therefore implemented in SOLEDGE3X , using the Monotonized Central

(MC) slope limiter function, which is defined as follows:

$$\phi_X\Big|_{\psi-\frac{1}{2},\theta} = -D_X\Big|_{\psi-\frac{1}{2},\theta} J\Big|_{\psi-\frac{1}{2},\theta} \vec{e^{\psi}} \cdot \left(\frac{\partial X}{\partial \psi}\Big|_{\psi-\frac{1}{2},\theta} \vec{e^{\psi}} + \overline{\frac{\partial X}{\partial \theta}}\Big|_{\psi-\frac{1}{2},\theta} \vec{e^{\theta}} \right) \tag{3.22}$$

$$\frac{\partial X}{\partial \psi}\Big|_{\psi-\frac{1}{2},\theta} = X_{\psi,\theta} - X_{\psi-1,\theta} \tag{3.23}$$

$$\overline{\frac{\partial X}{\partial \theta}}\Big|_{\psi-\frac{1}{2},\theta} = \mathrm{MC}\left(\mathrm{MC}\left(\frac{\partial X}{\partial \theta}\Big|_{\psi-1,\theta+\frac{1}{2}}, \frac{\partial X}{\partial \theta}\Big|_{\psi-1,\theta-\frac{1}{2}} \right), \mathrm{MC}\left(\frac{\partial X}{\partial \theta}\Big|_{\psi,\theta+\frac{1}{2}}, \frac{\partial X}{\partial \theta}\Big|_{\psi,\theta-\frac{1}{2}} \right) \right) \tag{3.24}$$

$$D_X\Big|_{\psi-\frac{1}{2},\theta} = \frac{2}{\frac{1}{D_X|_{\psi-1,\theta}} + \frac{1}{D_X|_{\psi,\theta}}} \tag{3.25}$$

$$\mathrm{MC}(a,b) = \mathrm{minmod}\left(2\,\mathrm{minmod}(a,b), \frac{a+b}{2} \right) \tag{3.26}$$

$$\mathrm{minmod}(x,y) = \begin{cases} \min(x,y) & \text{if } x,y > 0 \\ \max(x,y) & \text{if } x,y < 0 \\ 0 & \text{if } xy \leq 0 \end{cases} \tag{3.27}$$

Where:

- X : any quantity of interest, e.g. n, T, or $v_{\parallel}$
- $\phi_X\Big|_{\psi-\frac{1}{2},\theta}$ is the flux of X through the $\psi-\frac{1}{2},\theta$ face
- D_X: the diffusion coefficient for the quantity X
- J: the Jacobian of the metric tensor
- $\vec{e^{\theta}}$, $\vec{e^{\psi}}$: the contravariant basis vectors
- MC: the slope limiter function
- "barred" partial derivatives are the interpolated results from the limiter function, while "non-barred" partial derivatives are simple 2-cell differences.

It can also be noted that the diffusion coefficient for the face is computed as a harmonic mean instead of an arithmetic one, which further increases stability. Following the implementation of this new operator, reverse fluxes were not observed again, and a monotonic density and temperature decrease from the strike point toward the reflector plate was recovered. More importantly, the implementation of the slope limiter removed any occurrence of numerical instabilities arising from under-dense cells fuelling neighboring over-dense cells through reversed diffusive fluxes, thus strongly improving the numerical stability of simulations.

3.4.4. Management of thresholds

3.4.4.1. Thresholds handling in the plasma solver

The SOLEDGE3X fluid plasma code solves the evolution of extensive quantities for each plasma species: density, parallel momentum (in fact, parallel particle flux), and total energy (thermal plus kinetic). However, the time derivative of such quantities is often computed from associated intensive quantities: parallel velocity for the momentum and temperature for thermal energy. Since these require dividing by the density, in practice, the latter must not be allowed to reach arbitrarily low values.

From a numerical scheme point of view, the plasma density would never reach zero if the model's equations are discretized appropriately, as all sink terms have a proportional relation to the density (advection, recombination reactions). The density could exponentially decrease but never reach zero.

An adequate discretization in time would therefore impose that the time step does not exceed a fraction of the shortest characteristic time $n/\frac{\partial n}{\partial t}$ across the numerical grid.

However, this criterion can be problematic in the case of an explicit coupling with a Monte Carlo code that involves a degree of statistical noise. This can be interpreted intuitively: at the edge of the plasma-dense regions, especially below the divertor legs toward the pump, the plasma density is very low, and the noise level of the sources computed by EIRENE can become of the order of the plasma density.

If such a criterion is kept, the time step becomes very small to accommodate for the adequate description of those very low density cells. Those do not play a key role in the global solution of the plasma, and such small time steps would require very long computation times.

Consequently, some finite thresholds are chosen for the density and temperature. Those are set respectively to $1 \times 10^{10}\mathrm{m}^{-3}$ and 0.03 eV in the presented cases.

However, in the cells where a threshold is applied, the equations solved by the code are modified with the addition of an artificial source term S_n^{thresh}. If the density goes below the threshold during a time step, it brings the density back to the threshold value:

$$\frac{\partial n}{\partial t} + \nabla \cdot (n\mathbf{v}) = S + S_n^{\mathrm{thresh}}$$

This does introduce a bias in the solution if this term becomes significant. Thus, these source terms are stored and tracked, and a solution can only be seen as valid if this term is zero or negligible compared to the smallest input term (i.e., for particles, the outflux from the core, or the gas puff rate).

Also, when such artificial particle sources are applied, the higher moments have to be impacted consistently:

$$S_m^{\mathrm{thresh}} = S_n^{\mathrm{thresh}} v_\parallel^0 \tag{3.28}$$

$$S_E^{\mathrm{thresh}} = S_n^{\mathrm{thresh}} \frac{3}{2} T^0 \tag{3.29}$$

where for impurities, $v_{\parallel}^{0}$ and T^{0} are those of the main ion (if it is the main ion reaching the threshold, they are taken as zero).

In practice, these threshold terms are largely negligible in the converged states of the presented cases.

3.4.4.2. Consistency between the plasma solver and the neutrals solver

In the process of computing the reaction rates, EIRENE also uses thresholds for the minimum allowed values of temperature and density. Those are not modifiable by the user, and are set to 0.02 eV and $1 \times 10^{8}\mathrm{m}^{-3}$, respectively. If a plasma species has a temperature or a density lower or equal to these values, all reactions related to this species (e.g., electron impact reactions for electrons, ion impact reactions for ions) will be turned off. Therefore one must take care to set up the plasma solver with thresholds strictly above (due to the "or equal") 0.02 eV and $1 \times 10^{8}\mathrm{m}^{-3}$. Otherwise, problematic situations can arise, such as the appearance of H_2^+ anomalously large densities because it was generated through an ion impact (molecule charge exchange), and cannot be consumed if T_e is below the threshold and the transport is deactivated (static approximation). This was initially observed under the divertor legs in ITER cases in the private flux region (beyond the radial extent of the SOLPS-ITER mesh).

3.4.5. Computation time optimization with coupled Monte Carlo neutrals

For the considered ITER runs, most of the computation time is spent in EIRENE calls. A SOLEDGE3X time step takes of the order of 1×10^{-2} s to execute, while EIRENE calls are rather of the order of one to ten seconds. This is the case even when the so-called short-cycling scheme is used, which consists in executing multiple plasma solver time steps without calling EIRENE. In such cases, at maximum, and only for low density regimes, a few tens of SOLEDGE3X iterations can be done without calling EIRENE. For reference, this number can go up to a few hundred in medium-sized tokamaks simulations.

Thus, the computation time approximately boils down to the EIRENE computation time. It is determined by the number of EIRENE calls, times the duration of a single EIRENE call. The latter is itself driven by the number of particles launched per CPU, multiplied by the average computation time per particle. The following discussion will not consider matters related to CPU parallelization, as it is outside the scope of the present work.

Computation time for each particle This has to be considered as an input, as no free parameter can change it in the considered runs. This is a purely serial process in the Monte-Carlo procedure and cannot be parallelized. Since operations done at this step involve the particle's behavior, this aspect is related to the chosen physics model, i.e., the set of reactions a particle can experience, or the way those are calculated. It also strongly depends on the plasma conditions. In the context of this work, the efforts

that were carried out on this matter were dedicated to improving the initial reduced reaction set in SOLEDGE3X and implementing the full "Kotov model" summarized in Table 3.3. Therefore no further improvements of the latter will be discussed in this section.

The computation time per particle was found to be very dependent on the regime, with a factor ~10 increase when going from low density regime to partial detachment. EIRENE calls with the same number of particles (10k) take around a fraction of a second at the lowest throughput and a few seconds at the highest throughput in pure hydrogen. This comes from the very large increase of elastic collisions and atom charge transfers in high throughput regimes, in the cold and very dense plasma near the target. It especially highlights the relevance of going to hybrid fluid-kinetic approaches, as is being developed [61] [62] [63] [64], which removes the need of executing a large number of such collisions by the particle tracker in highly collisional conditions.

Number of particles per EIRENE call Increasing the number of particles reduces the statistical noise and smooths obtained source. As the noise scales with $\sqrt{N_{\text{particles}}}^{-1}$, this process quickly becomes very expensive.Optimizing this parameter then relates essentially to using the lowest number of particles that enables the plasma solution to converge correctly, i.e., without creating destabilizing transients and without biasing the solution. The sensitivity of finite volume plasma solver solutions to Monte-Carlo statistical noise has been extensively studied in recent years [65], [66], [67]. Empirically and in the context of these ITER runs, it was found that increasing the number of particles almost never had any beneficial effect on stability, and that reducing it to around 1,000 would not change the solution. However, it must be noted that experience of some runs with the SOLPS code in other machines and conditions (e have observed otherwise: increasing the number of particles led to a change in the solution [50]. The quantification of this under-sampling error is currently an open question.

The 20MW pure H cases presented in the rest of this document were however run with 10,000 particles per EIRENE stratum (the sensitivity study on the number of particles was carried out later in the context of going to FPO plasmas in multispecies, see section D). Then, once the case is converged, the solution is smoothed with 1 million particles for a time step at the end to retrieve more accurate results for quantities computed by EIRENE. However this sudden change of number of particle did not produce any transient over a few time steps in the solution (except smoothing), which would indicate that no biasing occurred.

Frequency of EIRENE calls in plasma time If the number of particles did not seem to be central to the stability and correctness of the solution, the plasma time between two EIRENE calls was found to be of crucial importance. Increasing this time beyond 0.5 µs proved to cause strong noise and instabilities.

A similar effect was observed for the FPO 100MW multispecies case and an illustra-

tion is provided in section D.

This behavior is in line with [67], where it is shown that the statistical error scales with the square root of the time step, and with [68], where it is argued that the statistical noise does not introduce a bias in the solution if EIRENE is called frequently enough, whereas if noisy source maps are retained for too long (i.e., short cycled), then a bias in the solution is observed through the "filtering" effect of the plasmas system.

Conclusion The value/cost ratio of increasing the particle number in the Monte Carlo procedure was found to be very poor, as it provides little increased stability beyond 1,000 particles per stratum, but linearly increases the computing time. However, the duration between EIRENE calls was observed to be the factor determining the stability and validity of the solution. This one can be optimized and is a promising lead for computation time improvements. section 3.4.6 provides a first attempt at calculating an optimal value. Overall, the strategy can be summarized as running with a very low number of particles (1,000) with the maximum time possible between EIRENE calls.

3.4.6. EIRENE calls optimisation through computation of sources characteristic time

As mentioned in section 3.4.5, it was observed that increasing the number of particles in EIRENE was not an effective method to increase stability beyond 1,000 (10,000 were used, i.e. a sufficient number stability-wise), and that the most important parameter was rather the frequency of calls. Therefore, in this section, we focus on the matter of the frequency of EIRENE calls.

The key question to address is knowing the duration for which the computed sources are approximately valid for a given plasma state. Computing this duration would enable executing the costly EIRENE calls a minimum number of times while still preserving the stability of the code and without biasing the solution. This type of investigations were already started in the 1990's [69], albeit with different criteria.

It can be stressed here that the care and effort of optimizing this matter have proved to be a necessity due to the specificity of ITER cases, and due to the high sensitivity of plasma-neutral interactions in this machine with small plasma conditions changes. Runs for smaller machines with simpler atomic and molecular models could be set up with much more ease and show no issues with computing time or convergence.

The SOLEDGE3X code describes the temporal advancement of the plasma at each time step, with a time step duration that is dynamically adjusted at each iteration to optimize speed. This duration is computed from a Courant-Fredrich-Landau (CFL) condition to ensure maximum time step length without endangering stability.

It is assumed that the plasma solver time step is much smaller than characteristic evolution time of the neutrals. Therefore, for simulations of current smaller machines, the setup of the code would make the plasma solver iterate a fixed number of times (a few hundred usually, set in the parameter file) between EIRENE calls and keep the

computed plasma source constant in the meantime. This approach, which proved sufficient until now for machines such as WEST, TCV or even JET, would not allow computing ITER cases due to numerical stability issues. On the other hand, calling EIRENE at every time step would lead to an unreasonable amount of computing time, thus the number of calls had to be optimized.

The new approach described here consists of computing dynamically the number of time steps the plasma solver can execute before re-calling EIRENE. To do so, one needs to estimate the simulation time during which the sources do not change significantly. This time can be estimated as the EIRENE sources characteristic time, defined similarly as a characteristic evolution time of any physical quantity:

$$\tau_{EIR} = \frac{S_X}{\frac{\partial S_X}{\partial t}} \tag{3.30}$$

Where:

- τ_{EIR} is the EIRENE source characteristic time after which an EIRENE call needs to be triggered
- S_X is the EIRENE source of any quantity X (particle, momentum, or energy)
- $\frac{\partial S_X}{\partial t}$, the time derivative of this source

The main difficulty comes from computing this time derivative at the time of the EIRENE call.

$$\frac{\partial S_X}{\partial t} = \frac{\partial \left(\sum_{i_{REAC}} n_{ispec_1} n_{ispec_2} \langle \sigma \nu X \rangle_{i_{REAC}} \right)}{\partial t} \tag{3.31}$$

This expression can be approximated by introducing four simplifications:

1. most of the change in these terms comes from the reaction rate coefficient, which is very much non-linear, versus the linear dependency in the two densities, therefore only the derivative in the reaction rate coefficient will be retained
2. for this reaction rate coefficient, its main dependency comes from temperature, thus others (density or neutral energy) will be dropped.
3. the reactions with no sharp change in rate coefficients can be excluded to focus only on those with strong variations in regions where large densities of neutrals are expected, which is to say at low temperatures. From these considerations, only the volumetric recombination, the atom ionization, and the molecule charge exchange can be retained in the scope.
4. it was observed that one of the reactions which cause the largest instabilities was the volumetric recombination, because it has such a sharp variation below

1eV and can cause very large electron energy source due to the recombination electron population heating (at low temperature) during the three-body-recombination. Thus, only this one will be retained. However, more precise computation could be achieved by including the other two.

5. Since the volumetric recombination is mainly sensitive to T_e, then only the electron energy source time derivative is retained

Finally, we obtain:

$$\tau_{EIR} \approx \frac{S^{RC}_{E,e^-}}{\frac{\partial S^{RC}_{E,e^-}}{\partial t}} \tag{3.32}$$

$$\frac{\partial S^{RC}_{E,e^-}}{\partial t} = \frac{\partial S^{RC}_{E,e^-}}{\partial T_e}\frac{\partial T_e}{\partial t} \tag{3.33}$$

Where $\frac{\partial S^{RC}_{E,e^-}}{\partial T_e}$ can be computed from additional routines reading the EIRENE databases (AMJUEL, HYDHEL) or other external databases used by EIRENE (e.g. ADAS), and $\frac{\partial T_e}{\partial t}$ will be extracted and passed from the SOLEDGE3X plasma solver. The full formula and computation for the derivative of the fit w.r.t. T_e can be found in section F.

In the code, the time since the last full EIRENE call is tracked and compared at each time step to the EIRENE source characteristic time τ_{EIR}. As soon as the former exceeds the latter, the plasma solver exits the short-cycling procedure and triggers a new call to EIRENE.

This procedure has proven very effective in automatically tuning the frequency of calls to EIRENE and guaranteeing the stability of ITER cases even at high throughput. For example, this criterion led for the upper range of the scan to transition from the order of $\sim 1\times10^{-6}$s at roll-over to $\sim 1\times10^{-7}$s at maximum throughput, when attempts to run at $\sim 1\times10^{-6}$s for the maximum throughput were unsuccessful. However, we also found that the criterion used is not optimal for low throughput cases for which the computed characteristic time does not increase as much as it could. For example, in the most attached case, the automatic procedure leads to an EIRENE call every $\sim 5\times10^{-7}$s while the simulation can run to the same converged state without stability issue if one manually imposes a call every $\sim 5\times10^{-6}$s (a factor 10 longer). The root cause for this underestimation is under investigation. Further studies will be necessary to define a criterion to efficiently tune the frequency of EIRENE calls that would be valid across the whole range of divertor regimes.

3.4.7. Outlook for future improvements on the numerical side

The presented schemes strongly improved the numerical robustness of simulations and helped reduce the computing time by optimizing the time spent in the Monte Carlo solver. In the same way as for the modeling of the physics, some potential future

next steps were also identified for the numerical side. Let us list the most salient ones rapidly:

- The derivation of a physics driven maximum time interval between calls to EIRENE is a very effective way of determining an optimum path between the opposite constraints of increasing the numerical stability and reducing the computing time. The criterion proposed in in section 3.4.6 seems well adapted to stiff high throughput case but further refinement is needed to make it optimal through the whole range of divertor regimes.

- As was seen in the reaction counts section and the computation time optimization section, the development of hybrid kinetic-fluid models is crucial to avoid computation of a very large number of elastic collisions in high collisionality conditions [61] [62] [63] [64].

- Further in this direction, a particular point would be to investigate the relevance of using a two-fluid representation for atoms (a Franck-Condon population and a charge-exchange population) as will be highlighted in the following chapters.

- Even further in the fluid direction, one could also investigate the relevance and feasibility to build a fluid model involving the same species and reactions as the Kotov model considered here with EIRENE.

- One could further leverage the lessons learned in [70] and [71] on the optimization of coupling strategies and implement them in SOLEDGE3X.

- The relevance and accuracy trade-offs of using combined rates for molecular assisted processes instead of describing the H_2^+ or H^- in the model could be assessed.

- From the now gained ability to compute derivatives of the reaction rates in the database, one also might attempt to adopt a partially implicit time discretization of EIRENE sources. This would likely allow one to adopt larger time steps in the plasma solver and reduce the frequency of call to EIRENE.

- The parallel nature of particle tracking and its proximity to ray tracing from the world of computer graphics make a strong case for assessing the relevance of porting of the EIRENE Monte Carlo solver to the GPU, even if some aspects will probably remain challenging (e.g. the scoring procedure).

3.5. Comparison of results with SOLPS-ITER

To provide some context on the results obtained with SOLEDGE3X, a comparison is carried out with the existing SOLPS-ITER database on similar cases. Six cases with different throughput values (see Table **??**) are selected for this exercise. The relevant SOLPS-ITER cases were taken from the ITER public IMAS database and

include those described in [42] (the last four cases). They are run with the same magnetic equilibrium, which corresponds to the scenario considered prior to the 2021 update, with $\mathrm{d}r_{\mathrm{sep}} = 11$ cm.

SOLPS IMAS shot	**Gas puff rate [e^-/s]**
103312	1.46×10^{21}
103313	3.81×10^{21}
103027	8.85×10^{21}
103028	1.13×10^{22}
103029	3.31×10^{22}
103030	6.80×10^{22}

Table 3.5.: Identifiers of the SOLPS-ITER cases considered for the comparison with SOLEDGE3X. Gas puff (H_2 molecules) injection rates in electrons per second. For molecules per second, these values need to be divided by two. The corresponding SOLPS case number in the IMAS database is provided in the first column.

3.5.1. Setup matching between both codes

In terms of setup, SOLEDGE3X parameters were chosen to match as closely as possible the SOLPS-ITER runs, both in terms of included physics and parameter values. Most notably, fluid drifts are not activated, and anomalous perpendicular diffusion coefficients for particles, momentum, and heat ($D_\perp, \nu_\perp \chi_{\perp e}, \chi_{\perp i}$) are uniform and their values matched between both codes. Sheath heat transfer coefficients and heat flux limiters values for the parallel conductivity are also identical. H_2 molecules are injected from the same location (top port), and pumping is modeled with a fixed recycling coefficient (< 1) surface below the dome. The list of most important parameters in the runs is summarized in Table 3.1.

While the best effort was made to make these runs comparable, it is still worth mentioning that these two codes are, in essence, widely different in terms of algorithmic, numerical discretization, and treatment of the underlying equations. As a consequence, both approaches do not involve the same types of approximations. Therefore a perfect match cannot be reasonably expected, but the objective is to provide a quantitative estimation of how much the two codes agree on the selected runs.

Below is the list of the identified differences between the two codes that might impact simulation results. Other differences surely exist, but their identification

would require meticulous analysis of both codes, an exercise that is outside the scope of this work.

1. **Full vessel numerical domain**: the considered version of SOLPS-ITER (at the time of writing) does not extend radially to all the wall components and therefore applies a radial boundary condition consisting of a set decay length of 3cm for densities and temperatures. The potential effect of having such boundary conditions is not trivial to assess. It could be estimated by comparing cases with and without the newly developed "extended grid" feature of SOLPS-ITER [72], but cannot be done with SOLEDGE3X as SOLEDGE3X currently does not include the possibility of restricting the domain before the wall.

2. **Parallel currents**: SOLPS-ITER cases solve for the parallel current, while this option is deactivated in the SOLEDGE3X cases, and ambipolarity is assumed. This current results in a limited heat transfer from ions to electrons.

3. **Core particle outflux** The SOLEDGE3X runs use a constant particle outflux from the core at 6.13×10^{20} ion/s to represent pellet fueling, in addition to the neutral particle flux reaching the core boundary of the numerical domain which is re-injected as ions. SOLPS-ITER uses lower and different values for the prescribed additional flux from the core, depending on the case. However, those differences should have little impact on the solutions, especially in the SOL, but might explain the different density levels in the closed flux surfaces and at the separatrix.

4. **Collisional closure** In SOLEDGE3X, an implementation [28] of the Zhdanov collisional closure [26] is included in the code (with also a temperature equation for each ion species), while SOLPS-ITER uses for the considered runs a Braginskii closure (a Zhdanov-type closure has been recently implemented in SOLPS-ITER. [73]). However, while the Zhdanov closure improves the treatment of the equations for multicomponent plasmas, it reduces to the Braginskii closure for single ion plasmas as demonstrated in [28].

5. **Wall temperature**: In SOLEDGE3X, EIRENE is set up so that the wall temperature is uniform at 500K, while in SOLPS-ITER, the majority of the wall is at 580K, with a peaked profile up to 1160K at the strike points. The wall temperature changes the energy of the recycled molecules that thermalize with the wall (but not the velocity of the fast specular reflections of atoms). This temperature difference is very low with respect to plasma temperatures, therefore the impact is probably minimal on the plasma response. A few test cases with different wall temperature confirmed that this parameter has very little impact, even on divertor neutral pressure.

6. **Molecular ion transport & H_2^+-H^+ elastic collisions**: As mentioned in section 3.3, including the transport of H_2^+ molecular ions proved to be necessary to stabilize

the code, especially during transients. In SOLPS-ITER runs, the static approximation is used. This also activates the H_2^+-H^+ elastic collisions, but their contribution is found to remain minor (see section 4.3). At the time of writing, it is not possible in EIRENE to activate the tracking of molecular ions without H_2^+-H^+ elastic collisions, so they are included in SOLEDGE3X-EIRENE simulations even though not present in the SOLPS-ITER runs.

3.5.2. Comparison of results

This section now focuses on comparing the obtained results between the two codes across three sections: upstream conditions, target conditions, and target wall fluxes. Four cases are considered here, from attached conditions at low throughput to partially detached conditions at high throughput, where the varying parameter for the scan in the gas puff rate, with values shown in Table **??**.

3.5.2.1. Upstream conditions

Figure 3.14 shows that obtained upstream profiles are quite similar, and separatrix values are within 15% of difference as shown in Figure 3.15. Separatrix temperatures seem to match, while SOLPS obtains slightly hotter values of T_i in the far-SOL. This may be an effect of the finite extension of the SOLPS-ITER grid, which forces one to apply a prescribed 3cm decay length of T_i and T_e at this location, as the decay length found in SOLEDGE3X and in both codes at the start of the far-SOL is rather of the order of 1.5 to 2.0 cm.

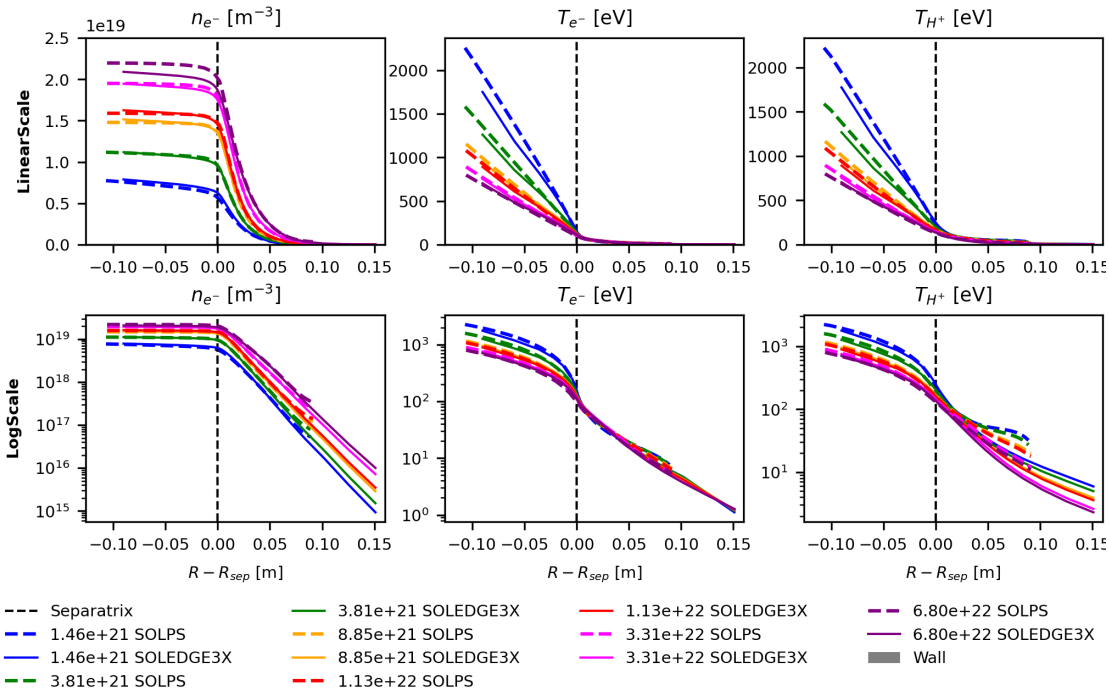

Figure 3.14.: Upstream density and temperatures at the outer mid-plane. Solid lines represent SOLEDGE3X cases, dashed lines represent SOLPS cases. The first row is on a linear scale for the vertical axis, the second row is on a log scale.

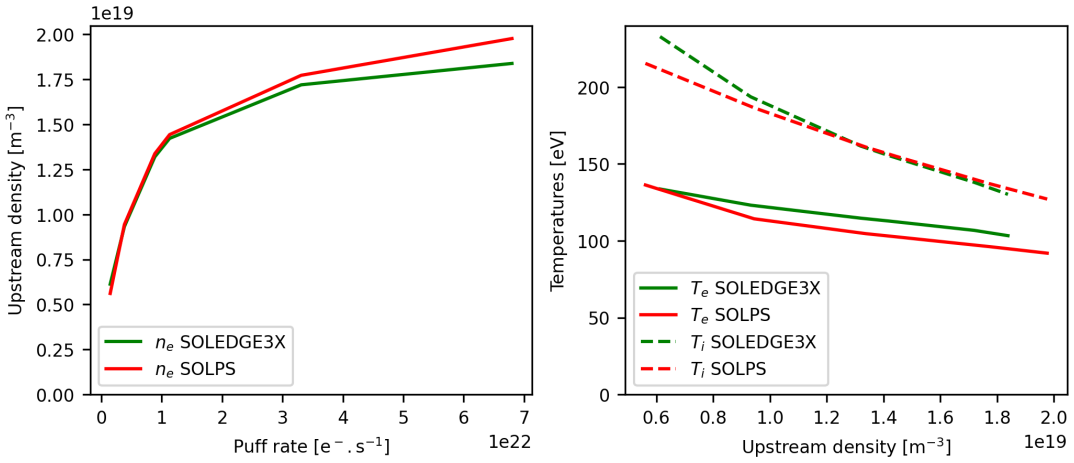

Figure 3.15.: Left: upstream density (separatrix at the outer midplane) as a function of throughput (gas injection rate) in SOLEDGE3X and SOLPS simulations. Right: electron and ion temperatures as a function of upstream density.

3.5.2.2. Target conditions

At the targets (Figure 3.16), density and electron temperature profiles match very well across the scan except for the lowest density case. On the inner target, locally at the strike point, SOLEDGE3X shows 30% to 50% lower T_e (e.g., 0.6 eV vs. 1.1 eV for #103027 SOLPS-ITER) around the rollover, but are more different for the most attached case on the outer target (10 vs 30 eV at the strike point, a factor 2 on the density, with a slightly higher density upstream). However, apart from those, the global patterns, trends, and amplitudes are well-matched. While at the strike points, ion temperatures are similar, when moving away along the baffles, SOLEDGE3X produces a factor two or three lower T_i for attached cases. This difference is strongly reduced when increasing the throughput. However, in low-density cases, particle fluxes in these regions are low, leading to a minor impact on the plasma as well as on plasma-wall interaction. Notably, this increased T_i in SOLPS-ITER is in line with the differences found upstream at the mid-plane in the far SOL. Since the values for the sheath heat transfer coefficients have been matched, whether this difference is due to the imposed decay length radial boundary condition in the far-SOL in SOLPS-ITER or a difference in the plasma-wall interaction model is unknown at this time.

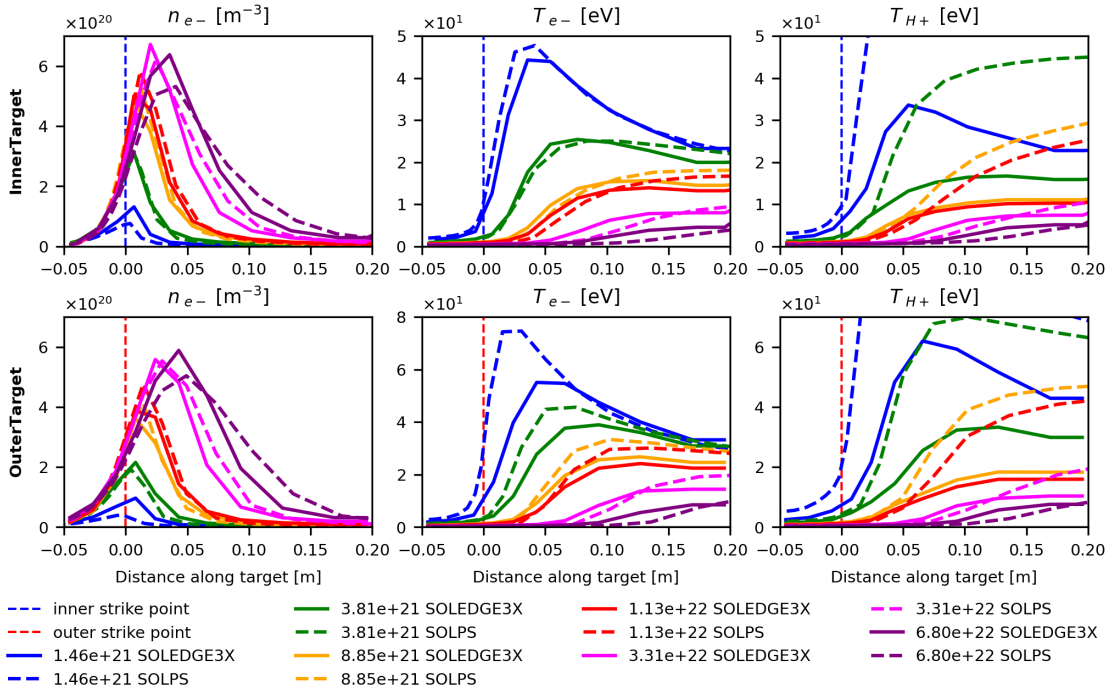

Figure 3.16.: Downstream density and temperature at the inner (top row) and outer (bottom row) targets, for four color-coded throughputs (in $e^-.s^{-1}$) of the throughput scan. Solid lines represent SOLEDGE3X cases, dashed lines represent SOLPS cases.

3.5.2.3. Target particle fluxes

Plasma particle fluxes show very good agreement on targets, expect for the lowest throughput case which shows almost a factor of two difference. Again, profiles at the rollover (yellow) are almost identical between the two codes. At high throughput, fluxes in SOLEDGE3X are slightly higher. Particle fluxes for neutrals show more difference: atom and molecule fluxes are larger in SOLEDGE3X, and these differences increase with the throughput, up to +20% on atoms and a factor of 2 on molecules at high throughput.

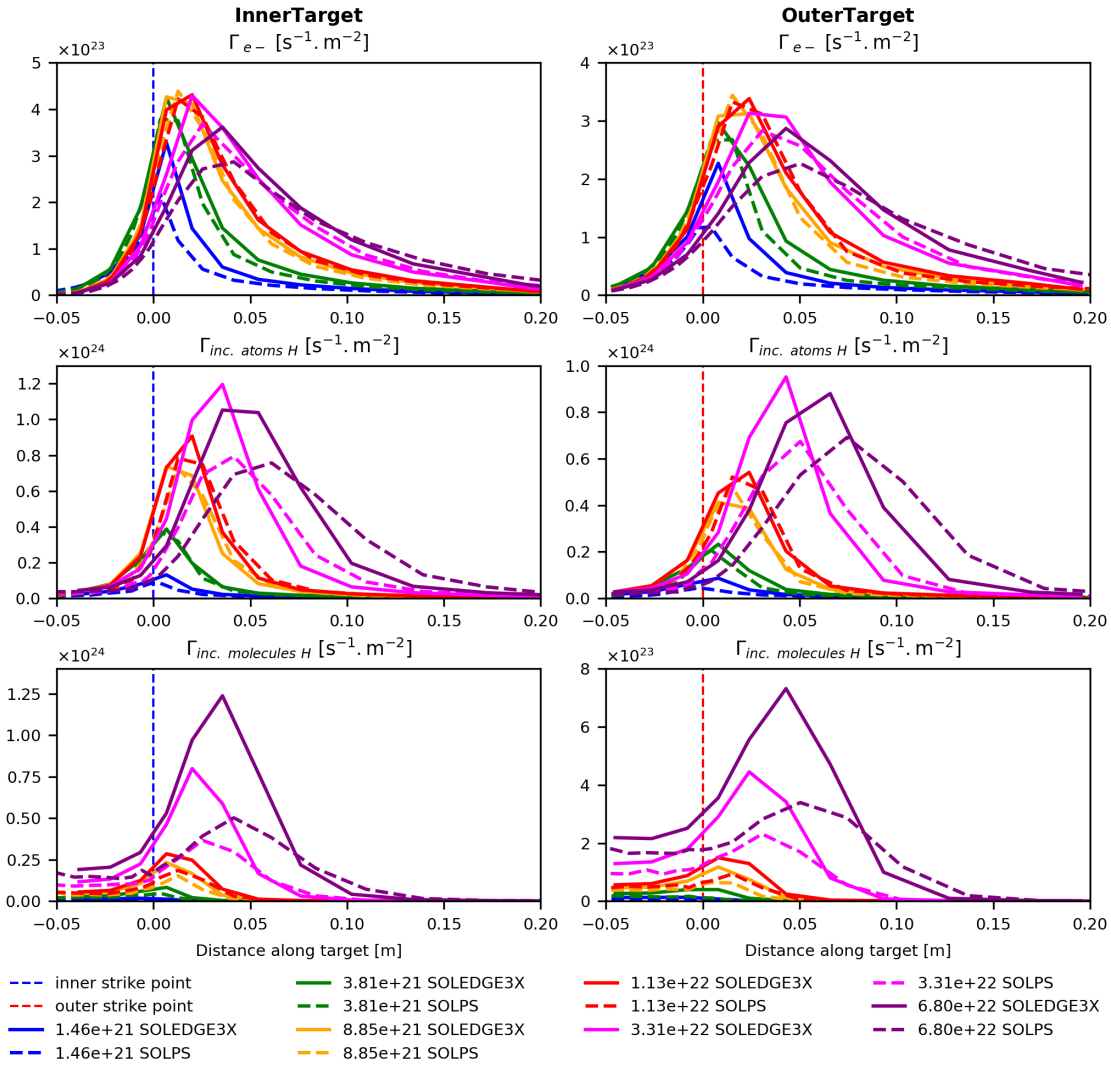

Figure 3.17.: Target ion (left), atomic (middle) and molecular (right) perpendicular toroidally symmetric particle fluxes at inner (top row) and outer (bottom row) targets, for four color-coded throughputs of the throughput scan. Solid lines represent SOLEDGE3X cases, dashed lines represent SOLPS cases.

3.5.2.4. Target heat fluxes

The "total" heat flux mentioned in this section consists of the net sum of all heat deposition channels to the wall: kinetic from ions, electrons, and neutrals, plus the radiation from volume processes and the photons from wall recombination.

Total power deposition profiles on the targets show good agreement for both codes and peak values are very well matched, as illustrated in Figure 3.18, except again for the lowest density case where the inner-outer asymmetry is much less present in SOLEDGE3X, and reversed compared to SOLPS-ITER. At high throughput, power fluxes are higher by 30-40% in SOLEDGE3X, but power fluxes are reduced in these partially detached conditions.

The main difference found comes from the relative weight of the plasma and the neutrals' contributions to the heat deposition at the inner target, see Figure 3.19. While the agreement is quite good on the outer target, the inner target plasma power deposited fluxes in SOLPS-ITER are a factor 2 below those of SOLEDGE3X, even in attached cases. This difference is compensated by the heat flux from neutrals, so that the total power deposited remains similar (except in the lowest density case where the effect of neutrals is much weaker). The difference in inner/outer asymmetry appearing in the total heat flux mentioned above appears to come from the plasma contribution. Neither SOLEDGE3X nor SOLPS runs included drifts for the cases considered here. The cause of this difference is currently under investigation, but it is worth noting that similar results have already been reported in the literature during comparisons between edge plasma codes (see [74] for a comparison between UEDGE, SOLEDGE2D, and SOLPS-ITER, Figure 3d & h).

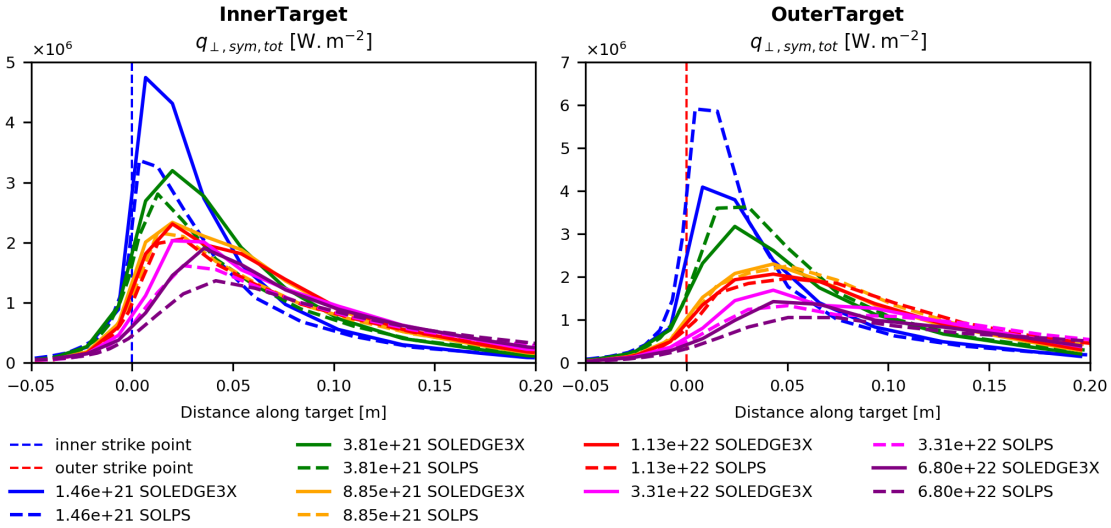

Figure 3.18.: Total perpendicular toroidally symmetric heat flux (including contributions from plasma, neutrals, and radiation) on the inner (left) and outer (right) targets for four color-coded throughputs of the throughput scan. Solid lines represent SOLEDGE3X cases, dashed lines represent SOLPS cases. For SOLPS, this quantity is extracted from `ld_tg_x.dat` files (quantities from IMAS are under investigation at the time of writing): "Wtot" is used.

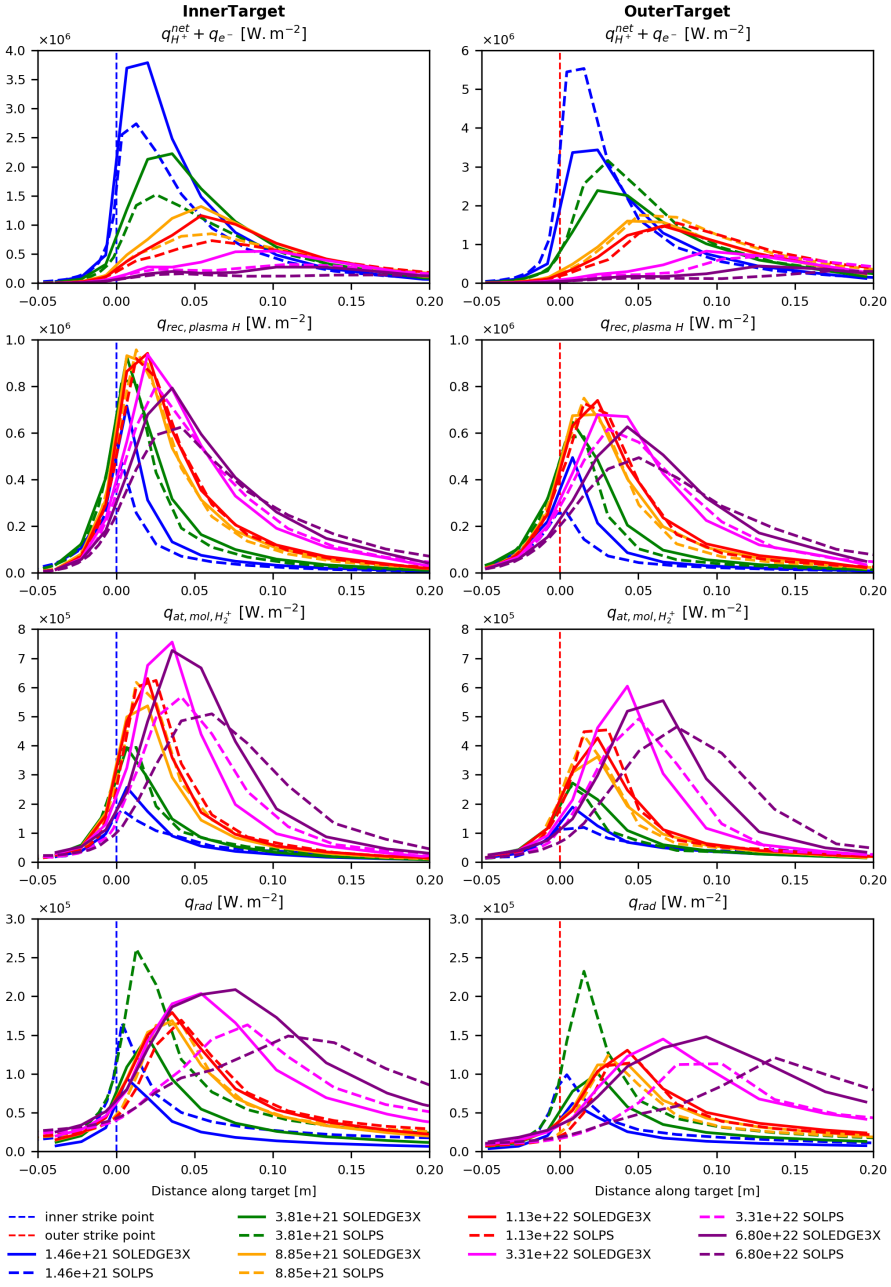

Figure 3.19.: Breakdown of the perpendicular toroidally symmetric heat fluxes (from plasma, neutrals, and radiation) on the inner (top row) and outer (bottom row) targets for four color-coded throughputs of the throughput scan. Solid lines represent SOLEDGE3X cases, dashed lines represent SOLPS cases. For SOLPS, these quantities are extracted from `ld_tg_x.dat` files (quantities from IMAS are under investigation at time of writing): "Whtpl" is used for the plasma heat flux, "Wptpl" for the wall recombination, "Wneut" for the neutrals, "Wrad" for the radiation. The plasma power is given at the sheath entrance, where the "net" superscript for the ion indicates that the energy of the outgoing recycled neutrals from ions has been substracted. The $q_{rec,plasma}$ includes the recombination of all ions into atoms (the additional photon for the step from atom to molecule is in the row below). The q_{at,mol,H_2^+} quantity also includes the recombination at the wall of atoms into molecules (also including the recombination of atoms from ions). q_{rad} from SOLEDGE3X contains the volume radiation received by the wall, from the atom excitation process, the electron-H^+ recombination, and the H_2^+ EDR process.

3.5.3. Divertor neutral pressure

In ITER cases run with SOLPS-ITER and mentioned in the literature, the quantity called divertor neutral pressure p_{div} is computed as the average of the neutral pressure in cells at the edge of the SOLPS plasma domain between the target and the upper part of the dome [35]. For comparability, the same average has been computed with SOLEDGE3X across the scan as shown in Figure 3.20. On the right side is shown the relation between the upstream density and the divertor neutral pressure, showing a very good agreement on this behaviour, especially at low throughput. At high throughput, this pressure as a function of upstream density rises faster in SOLEDGE3X than in SOLPS-ITER, but the trend is very similar, even if differences exist between cases, because the response to throughput is not identical (especially at high throughput).

The two left plots show the 2D distribution of the neutral pressure in the divertor for both codes at the highest throughput case. Tests were carried out with different wall temperatures in SOLEDGE3X (not pictured here), but did not lead to any significant change in divertor neutral pressure. As a consequence, this parameter difference between the two codes can probably be excluded when attempting to explain the difference in p_{div}. An increased penetration of atoms along the field line just below the separatrix is also found in SOLPS, which is not observed in SOLEDGE3X. The root cause for these differences is under investigation.

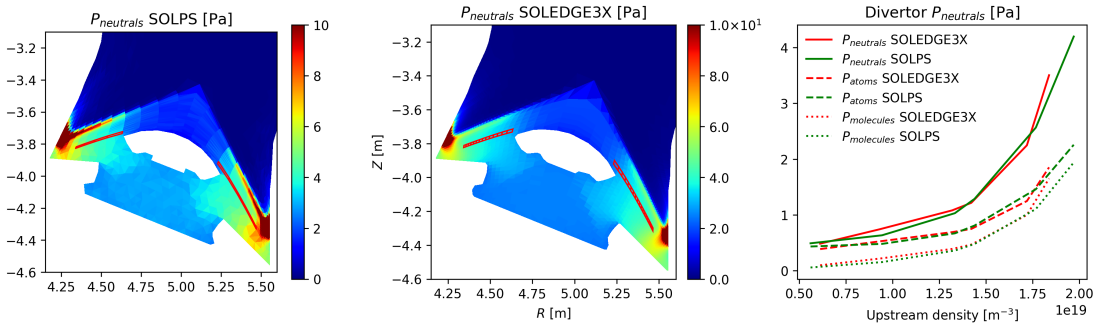

Figure 3.20.: Left-most 2D plots: divertor neutral pressure in the #103030 (6.80×10^{22} $e^{-}.s^{-1}$) case for SOLPS (left) and SOLEDGE3X (middle), red cells are used for computing the average. Right-most plot: divertor neutral pressure as a function of the upstream density for SOLPS and SOLEDGE3X, see in the text for the definition of this measure.

3.5.3.1. Take-aways for the comparison with SOLPS-ITER

In summary, even though some quantitative differences have been found between the two codes, those are not very large, especially for the regimes around the rollover and after which are of particular interest for the operating scenarios of the machine. Furthermore, key results and trends remain unchanged and upstream-to-downstream relations match well. It is rather the response of the upstream to the throughput which

appears to not be exactly identical. One can therefore conclude that it is possible to move forward with the detachment and first wall study in the next sections, without contradiction with published results with SOLPS-ITER.

3.6. Conclusion

In this chapter, we have presented the improvements made to the physics model so that SOLEDGE3X includes the relevant ingredients to better model the boundary plasma in ITER-relevant conditions. These changes mandated improvements and optimizations on the numerical side as well. Thanks to those, simulations of ITER plasmas in pure hydrogen at 20MW require a more reasonable amount of time of the order of two to three weeks. Finally, a comparison of the results with SOLPS-ITER cases showed good agreement on the common part of the domain, strengthening confidence in SOLEDGE3X results. From these observations, the following chapters will dive more into the analysis of the obtained results of SOLEDGE3X up-to-the-wall simulations.

4. Divertor detachment study

Contents

4.1. Introduction and objectives of the study

As mentioned in section section 1.3.5, the transition from the high-recycling regime to the detached regime is a multifaceted phenomenon with many parameters, and some of its driving mechanisms are still under discussion [14, 75]. More specifically, while it is certain that the plasma-neutral interactions play a crucial role in the reduction of the particle and energy fluxes to the targets, there is no definite consensus yet on the role and importance of each underlying process in all the different types of plasma scenarios and machines. This work attempts to clarify what happens in the context of ITER simulations. This section focuses on plasma-neutral processes in the simulations, and builds a high-level picture of those driving detachment in ITER PFPO-1 scenarios. Since detachment involves many other parameters that are not explored here, either because they depend on the machine (target materials, geometry, etc.) or the pulse configuration (input power, magnetic equilibrium, fuel isotope, impurity seeding, etc.), the results obtained here can not claim to provide a picture encompassing all scenarios and in all machines.

This exercise is carried out using a throughput/density scan (the gas injection rate is the actual scanned parameter), and the analysis of the detachment provided in this section is structured as follows:

1. First, results at the targets (fluxes and plasma conditions) are reviewed to assess the divertor regimes obtained across the scan.

2. Then the plasma-neutral interactions are decomposed into the contribution from each of the reactions, for three cases representative of the attached, roll-over, and partially detached conditions, in which the key contributors and trends are identified.

3. Then, from this analysis, a high-level picture of the detachment in our ITER PFPO-1 simulations is constructed as a summary.

4.2. Target fluxes, plasma conditions, and regime identification

Across the throughput scan, a clear particle flux rollover at the targets is seen in Figure 4.1. It occurs simultaneously on the inner and outer sides, and the peak heat load strongly decreases.

As will be seen in the graphs in this section, one can note the strong degree of symmetry obtained across this scan. Here, even if the flux densities of particles and heat are higher on the inner side, both targets roll over at the same throughput. One may have expected the inner side to roll over at lower throughput as is observed in experiments and in SOLEDGE3X simulations of smaller machines. Determining the reason for this noticeable symmetry would require additional investigations.

Before the rollover, the particle flux as a function of the upstream density already starts to saturate with the upstream density increase, which shows that the scan's first point is already well in the high-recycling regime. In the early stages of the conduction-limited regime, an increase of the particle flux scales with n_u^2 section 1.3.3, which is not the case here. At the last point in the scan, target profiles Figure 4.2 (plasma conditions) and Figure 4.3 (fluxes) show that significant plasma density, particle flux and temperatures are still present, however only in the regions further away from the strike point. At the strike point, all quantities are strongly reduced with very low temperatures below 1 eV. In this case, the heat flux is mainly carried by neutrals and radiation Figure 4.4.

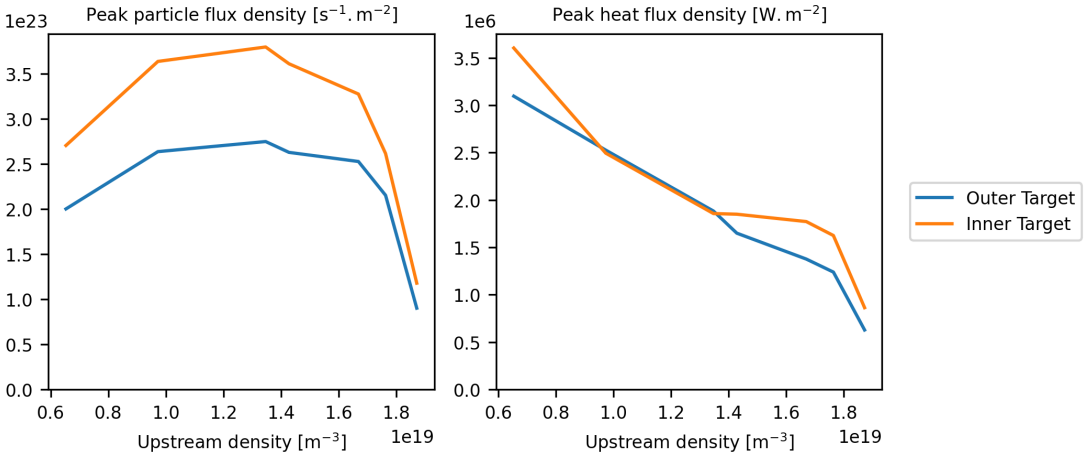

Figure 4.1.: Peak particle (left) and total heat (right) flux density from plasma, neutrals, and radiation at the outer and inner targets as a function of the upstream density at the outer midplane across the throughput scan.

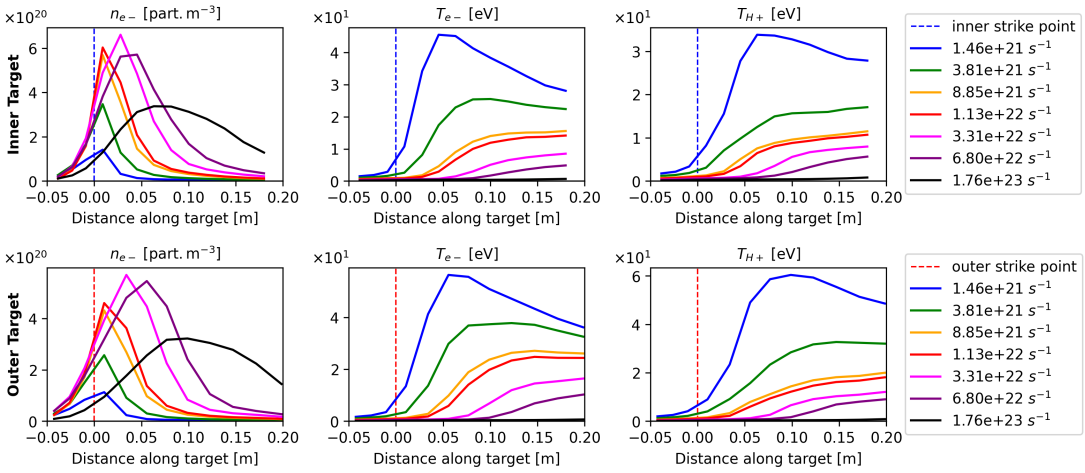

Figure 4.2.: Plasma density, electron and ion temperatures at the inner target (top line) and outer target (bottom line).

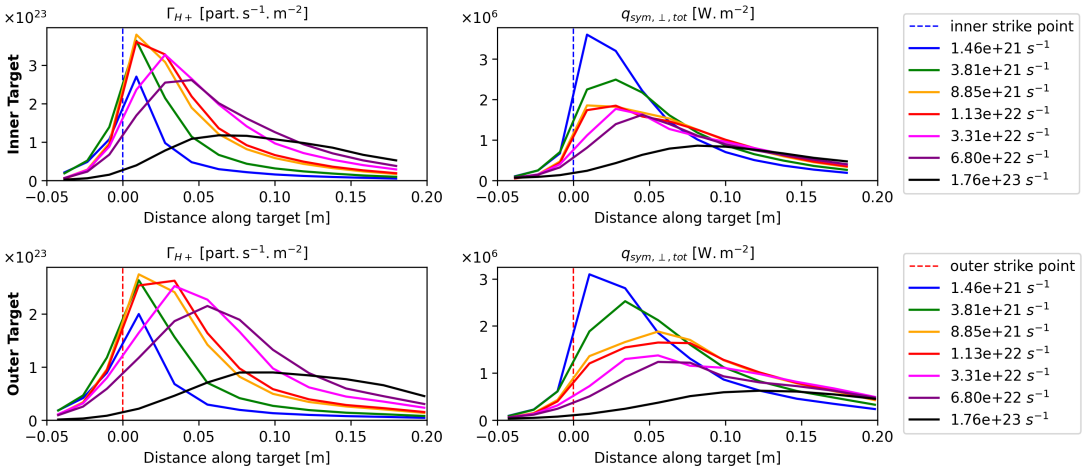

Figure 4.3.: Toroidally symmetric perpendicular (2D-symmetric, i.e., without 3D or tile-shaping shaping effects) ion particle and total heat flux (plasma + neutrals + radiation, incl. wall recombination) at the inner target (top line) and outer target (bottom line).

This pattern, consisting of detached flux tubes near the strike points and attached flux tubes (i.e., with significant plasma density and particle flux) further along the target is characteristic of the so-called *partially detached* regime. None of the cases include a "full"/"deep"/"ultimate" detachment regime where all field lines are detached, and almost no plasma reaches the targets. The last case of the scan being already at the limit of the expected capacity of the machine's pumping system, increasing further throughput would move too far outside the realistic operating window, and therefore is outside the scope of this work.

To summarise, the scan ranges from the high-recycling regime to the partial detachment regime.

One can also note that the two cases before the rollover (at 1.46×10^{21} and 3.81×10^{21} e^-/s) may be less relevant from the operating window of the machine, because of high temperatures above 20 eV away from the strike points where there is still non-negligible particle flux ($\sim 1 \times 10^{23} s^{-1}.m^{-2}$), which may cause an undesirable amount of sputtering even in the case of a tungsten target (which produces less sputtering than beryllium) if the plasma contains impurities there. These considerations are not included in our simulations here, since they only contain a pure H plasma, and the wall is assumed fully coated with beryllium.

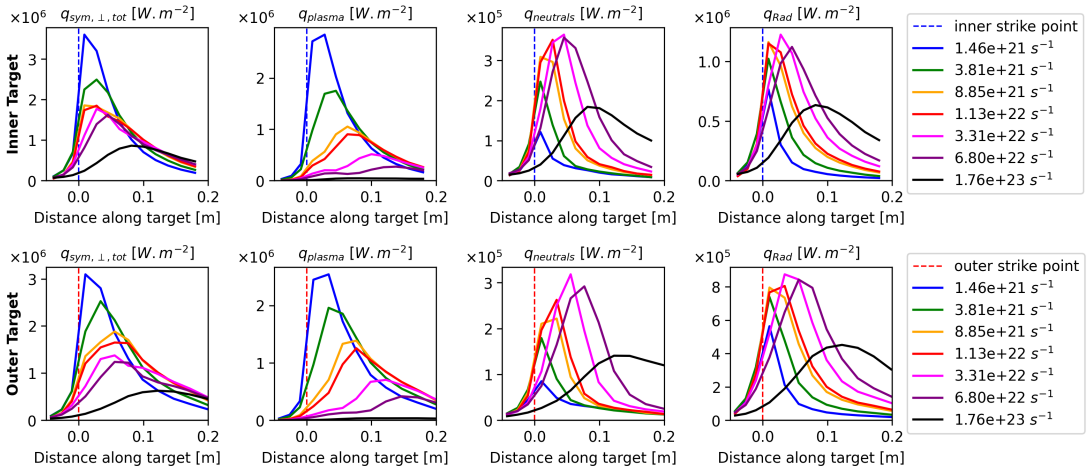

Figure 4.4.: Left-most plot: total toroidally symmetric heat flux on the targets across the throughput scan (inner: top row, outer: bottom row), and its three components: the plasma (electrons + ions), net deposition by neutrals (atoms + molecules), and radiation (volume + wall recombination radiation from plasma and atoms)

4.3. Analysis of the divertor detachment processes in ITER

From the discussion in section section 1.3.5, it was seen that the detachment, in the sense of the reduction of the particle flux at the targets, stems from the increased interaction between plasma and neutrals, which generates particle, momentum, and energy sources and sinks. This section aims at identifying the key processes driving those three sources, in an attempt to build a high-level picture of plasma-neutral interactions in the considered ITER simulations. Notably, specific attention will be paid to the nature of the particle sinks, as well as their relative importance in the different regimes.

For this exercise, we investigate the contributions from each individual reaction/collision included in the plasma-neutral interaction model to the plasma source terms (in the RHS of the equations section 2.3.3). The list of those processes can be found in Table 3.3. Thus, the plasma particle source, momentum source, electron and ion energy sources are decomposed and analyzed both in terms of amplitude and spatial distribution.

4.3.1. Volume integrals of the sources

To get a first overview of cases, the volume integrals over the whole numerical domain of these sources Figure 4.5 are investigated.

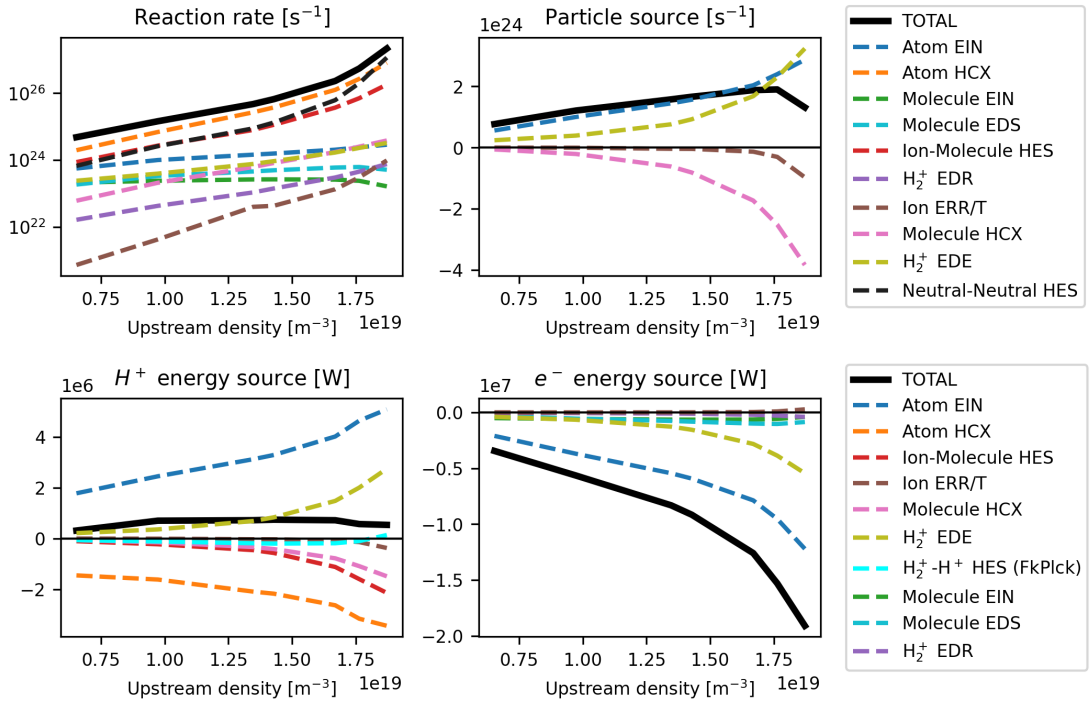

Figure 4.5.: Volume integrals of the reaction rates (i.e. reaction counts) in LOG scale, plasma particle source (linear scale), ion energy source (linear scale), and electron energy source (linear scale) for each of the main reactions included in the EIRENE model used, across the throughput scan as a function of upstream plasma density. Only significant reactions are plotted in each graph. Reaction abbreviations from Table 3.3.

The number of reactions per unit time (top left plot of Figure 4.5, in logarithmic scale), shows that the total number of reactions keeps drastically increasing with the upstream density. The slopes are almost linear for most of the scan, illustrative of exponential growth, and rise even faster at very high throughput. This illustrates the considerable sensitivity and importance of the physics involved with modeling the plasma neutral interactions, translating into the numerical challenge observed in chapter 3 for the code.

Particle source The total net plasma particle source increases with upstream density up to a maximum at around $n_u = 1.8 \times 10^{19}\mathrm{m}^{-3}$, then decreases. Notably, this extremum does not coincide with the target particle flux rollover, which is found at $n_u = 1.3 \times 10^{19}\mathrm{m}^{-3}$. In fact, each reaction's contribution still increases rapidly in amplitude across the whole scan, and the sinks end up more than compensating the positive sources, leading to a net decrease towards the end of the scan.

Electron energy source On the electron energy, however, since the only positive source (the three-body electron-ion recombination at low temperature) is of small amplitude, the total is directly exponentially increasing. It increases from 3MW for the most attached case up to 19MW. In this case, almost all (95%) of the input power (20MW) is transferred to the neutrals. Since there are only three output channels for the plasma energy: the radiation, the neutrals and the wall, the resulting power flux to the wall from the plasma is almost non-existent, indicating that the detachment successfully transfers the energy to neutral species unaffected by the magnetic field. In this case, the power is deposited through radiation and neutrals impacts, but on a much larger surface than the plasma-wetted area.

Ion energy source The net ion energy source total is rather low (< 1MW), because the contributions of the different channels essentially compensate each other. It is maximum at the particle rollover.

Reaction rates The top left graph in Figure 4.5 shows the reaction rates in log scale, where all significant individual reactions in the model are plotted, so that their relative importance can be compared. This complements the analysis as not all reactions appear on every plasma source graph (e.g., the molecule ionization only appears on the electron energy source and not in the particle source). One can make five observations from this graph:

1. the molecule charge exchange (molecule HCX in pink) increases very rapidly to become one of the major processes, and the molecular ion dissociation (H_2^+ EDE in light green) even overtakes the atom ionization (atom EIN in blue) in terms of ion particle source for the most detached case.

2. the electron-H^+ recombination (in brown) is much lower than the H_2^+ dissociative recombination (H_2^+ EDR in purple, which is the MAR), except for the last point in the scan.

3. for the most attached case, the amplitude of the H_2^+ dissociation (main consumption mechanism of H_2^+) matches with the amplitude of the molecule ionization via electron impact (molecule EIN, in dark green), while the molecular charge exchange (pink) is non-existent. This means that the process which creates the H_2^+ ions for attached cases is the electron impact on molecules. Further along in the scan, beyond rollover, this creation process is replaced by the molecular charge exchange, i.e., H_2^+ ions are created via ion impact and not electron impact, because T_e is not high enough anymore.

4. The H_2-H^+ elastic collisions (Ion-Molecule HES, in red) and atom charge exchange (atom HCX, in orange) are important all across the scan, even for attached cases, being major contributors to both the momentum and energy sources. This also illustrates a helpful point for the investigation of the detachment mechanism: no ion collision process can result solely in a momentum loss

or solely in an energy loss. Both are fundamentally linked and therefore have to be considered simultaneously.

5. Neutral-neutral collision rates (Neutral-Neutral HES, in dark grey) are high across the scan, however it will be seen in the next section that they are not significant at the targets in attached cases. The large volume integral in the graph comes from their large frequency down in the divertor near the pump for all cases.

4.3.2. Reaction profiles at the outer target

To provide a more precise picture of the reactions in the detachment process, and especially investigate spatial effects, we now turn to the decomposition near the outer target. For this purpose, the present section uses plots of the volume reaction rates and sources along the first flux surface above the separatrix (see Figure 4.7) in the outer divertor, for the last 10 cm poloidally next to the target. Three cases representative of the detachment process are used: one at the lowest density (in blue in Figure 4.6, at $1.5 \times 10^{21} e^- / s$) for the attached plasma, one at rollover (in yellow, $8.8 \times 10^{21} e^- / s$), and one at the maximum throughput (in dark red, at $8.8 \times 10^{23} e^- / s$) for the partially-detached plasma. Figure 4.7 shows the location of the plots at the first field line, and the associated density and temperature profiles. The density shows a clear maximum at the rollover, and temperatures decrease largely from a few tens of eVs, to a few eVs, and finally to below 1 eV.

For the last case, the considered field line itself is in the detached state, as the particle flux density at this location is very strongly reduced compared to the value at rollover (-93%), but field lines on the rest of the target are still attached with significant temperatures and particle fluxes (left plots of Figure 4.6), hence the "partially detached" label for the global plasma state (this term does not apply to individual field lines). Also, the particle flux rollover for this field line (right plot in Figure 4.7) coincides with the rollover as defined in Figure 4.1, which considered the peak over the whole target whichever the field line.

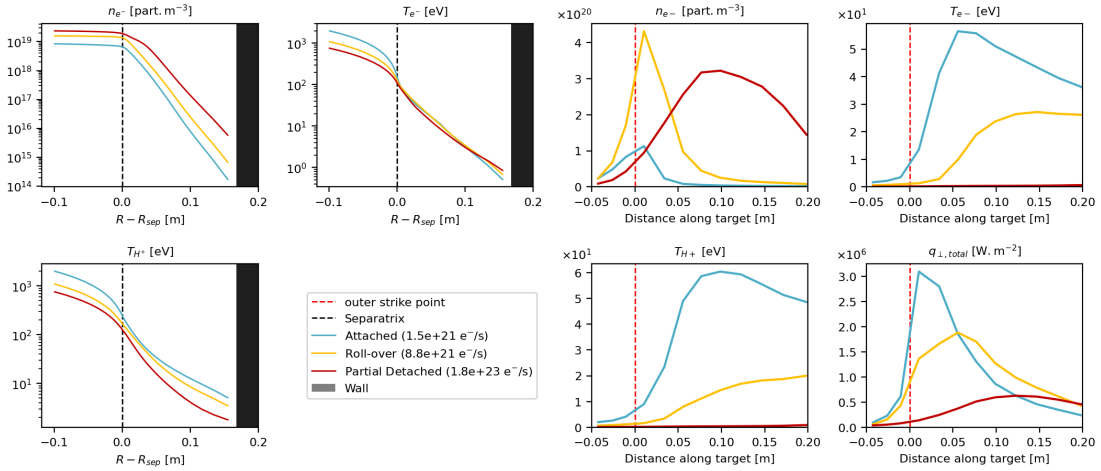

Figure 4.6.: Left 3 plots: upstream profiles at the outer midplane of density, electron and ion temperatures of three representative cases of the detachment process. 4 right plots: Outer target profiles of density, electron and ion temperatures, and total toroidally symmetric heat flux density. Figures in the legend correspond to the throughput, which corresponds to the following upstream densities: blue: $0.65 \times 10^{19} \mathrm{m}^{-3}$, yellow:$1.35 \times 10^{19} \mathrm{m}^{-3}$; red:$1.87 \times 10^{19} \mathrm{m}^{-3}$

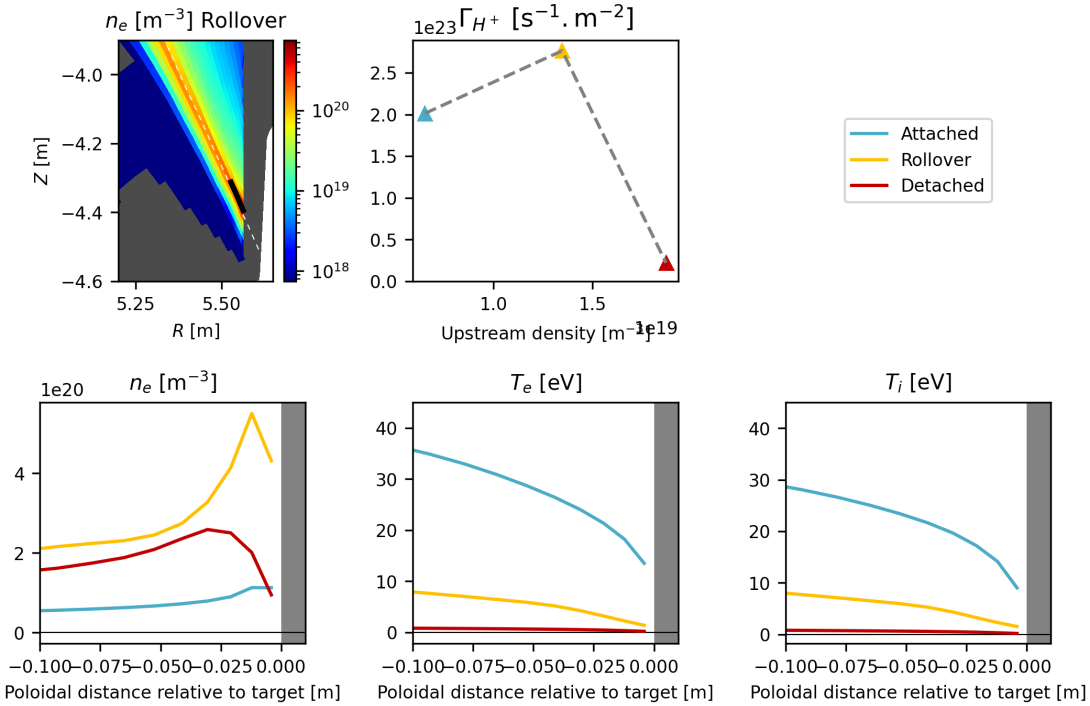

Figure 4.7.: Left-most plot: The thick black line is the location of the reaction profiles plots in the divertor considered in this section. 1D plots on the right: profiles along this black line (in poloidal distance) to the outer target for density, electron and ion temperatures. Right-most plot: target ion particle flux density at the field line, as a function of upstream density.

4.3.2.1. Ion particle sources & reaction rates

Figure 4.8 shows the contributions for each individual reaction to the particle source, where we observe a similar trend as on the volume integrals: there is a significant contribution from the molecular ion H_2^+ channel and its dissociation. For the attached case, all the source is located within 2cm of the target, with atom ionization as the main contributor. In this case, the H_2^+ dissociation is actually a net source because the H_2^+ is generated via electron impact. This is not the case if the H_2^+ is created by a molecule charge exchange, in which case the reaction chain (molecule charge exchange $\rightarrow$ H_2^+ dissociation) results in a net zero ion particle source.

As we go to rollover, it is interesting to note that the atom ionization front already detaches from the target, and the molecular ion dissociation source moves at the target. When summed, the total particle source may seem attached to the target forming one ionizing region, but it actually consists of two separate zones, a colder part near the target where the molecular-assisted processes dominate, and another one farther away in the plasma where the electrons are hotter and the atom ionization is the majority process.

This is even more pronounced for the partially-detached case, where atom ionization still makes up for the largest contributor when integrated over the whole divertor, but is now very much spread out over the field line up to the X point, and very weak near the target. At this location, the particle source is dominated by molecular ion dissociation and is now also detached from the plate. It is only at this detachment level that the electron-ion recombination becomes significant, in the direct vicinity (~3 cm) of the target.

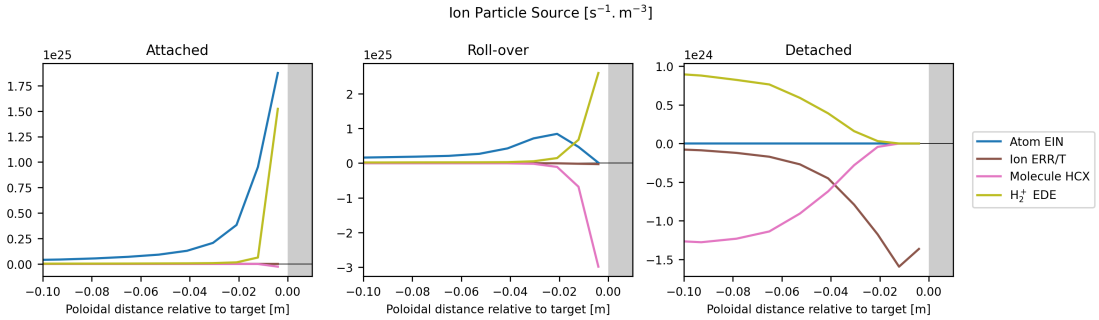

Figure 4.8.: Volume particle source along the outer divertor leg up to the target. See Figure 4.7 for the location of the plot in 2D. Only significant reactions are plotted.

Figure 4.9 shows the volume rates at the outer target (in log scale), i.e. reaction counts. Similarly to volume integrals, the creation process of the H_2^+ ion at this location shifts from electron impacts (molecule EIN in dark green) to ion impact (molecule HCX in pink).

Then, remarkably only at rollover, molecules that have traveled further away from the plate where T_e is higher are dissociated directly into two atoms by electrons (molecule EDS reaction in cyan), without going through the H_2^+ intermediate. This is not the case for the attached and detached states, where the H_2^+ channel largely dominates.

Finally, Figure 4.10 focuses on particle sources to highlight the sinks. The left graph shows the particle source associated with atom ionization, electron-H^+ recombination ("ERR/T"), and the net sum of all processes involving the H_2^+ ion ("H_2^+ proc."). The latter can be either positive or negative, depending on the reaction chain (examples: molecule EIN → H_2^+ EDE: +1; molecule HCX → H_2^+ EDE: 0; molecule HCX → H_2^+ EDR: -1). This plot helps identify which is the dominant particle sink process. The processes involving the molecular ion are the first to dominate at the target at rollover, while the electron-H^+ recombination is still minor. The negative net source from H_2^+ processes actually comes from the molecule-assisted recombination (MAR), i.e., the chain involving H_2^+ EDR, whose reaction rate is plotted directly on the right graph of the same figure. Then, only at partial detachment when T_e has sufficiently dropped below ~ 1eV, the electron-H^+ recombination increases and takes over at the target, while the MAR rather occurs in farther hotter regions.

Finally, neutral-neutral collisions at the target only become significant for the most detached case.

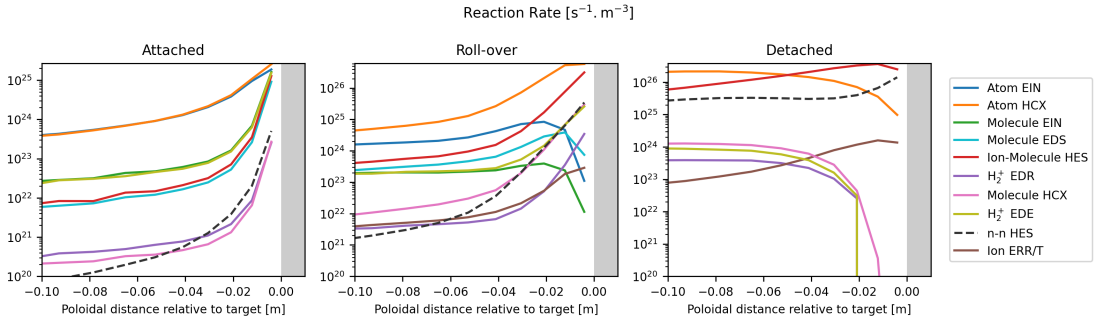

Figure 4.9.: Volume reaction rates (counts) along the outer divertor leg up to the target. See Figure 4.7 for the location of the plot in 2D. Only significant reactions are plotted.

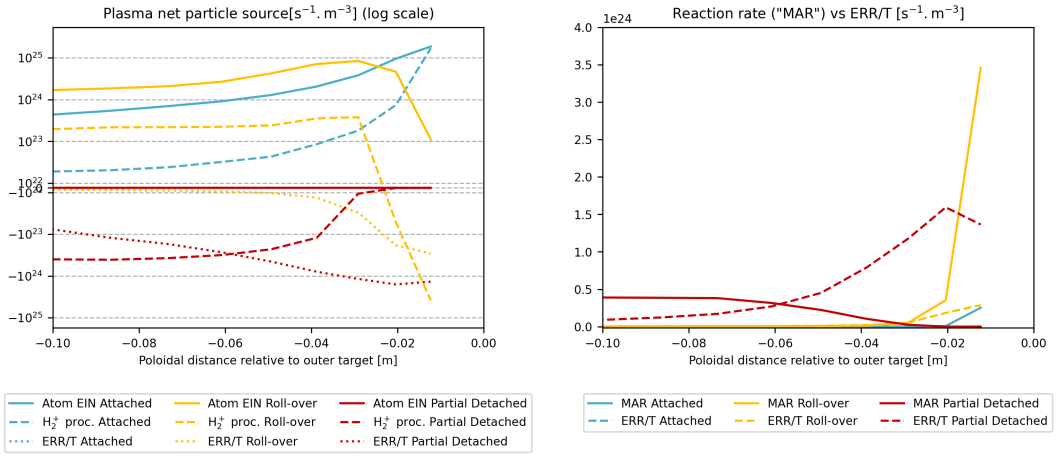

Figure 4.10.: Profiles along the first SOL field line near the outer target, see Figure 4.7 for the location of the plot in 2D. Left: breakdown of the plasma particle source between the atom ionization (EIN), the net sum of all processes involving H_2^+ ions (see the list in Table 3.3, and the H^+-e^- recombination (ERR/T). Right: reaction rate of the H_2^+ Dissociative Recombination (EDR), a.k.a. "MAR".

4.3.2.2. Ion momentum sources

Figure 4.12 shows the ion parallel momentum source contributions. For the attached case, the dominant loss process is the atom charge exchange, directly at the plate.

The atom ionization also contributes significantly as a positive source of momentum in the fluid, linked to the creation of plasma particles with a positive parallel velocity,

although this does not induce an acceleration of the fluid cell overall. This effect is interpreted through the angle of incidence on ions at the target and the fast ion reflections. The parallel momentum source from ionization reactions corresponds to the parallel momentum of the ionized atoms. Incoming ions from the bulk of the plasma arrive at the sheath entrance with a guiding center motion aligned with the magnetic field. Then, because of the gyromotion and the acceleration by the sheath, the actual angle of incidence when of the ion when it impacts the surface is not the one given by the magnetic field.

Left of Figure 4.11 shows the average computed incidence angle after the sheath for ions as computed by EIRENE, which takes into account the sheath acceleration in the Monte-Carlo procedure [37]. The average angle is in fact almost always close to 60°. Averages of the second deviation angle in the plane of the material surface (not pictured), are found to be close to zero. This behavior is also unchanged by the divertor regime, i.e. independent from the plasma conditions at the targets. Thus, ions that undergo fast reflections into atoms are back-scattered into the plasma on average in the direction which corresponds to the specular reflection of this 60° incidence. Then, its velocity retains a large positive parallel component, as shown in the diagram on the right of Figure 4.11. Modeling the ion incidence angle at surfaces is a topic of active research, in particular with the help of PIC codes [76, 77], and efforts have been made to implement such results in fluid codes [30].

When the atom is ionized later, that parallel moment is transferred back to the plasma, resulting in a positive contribution to the source. While the parallel component of the reflected atom is still largely positive, its amplitude is smaller than before the reflection (i.e., smaller than that of the bulk plasma). Therefore, the ion population will slow even in the presence of a positive momentum source as more particles with a lower parallel velocity are added. Furthermore, if a charge exchange occurs, since the parallel velocity of the incoming ion is larger, the collision will result in a momentum loss for the plasma. In this case, the charge exchange contribution to the momentum source is negative, even if the ionization one is positive.

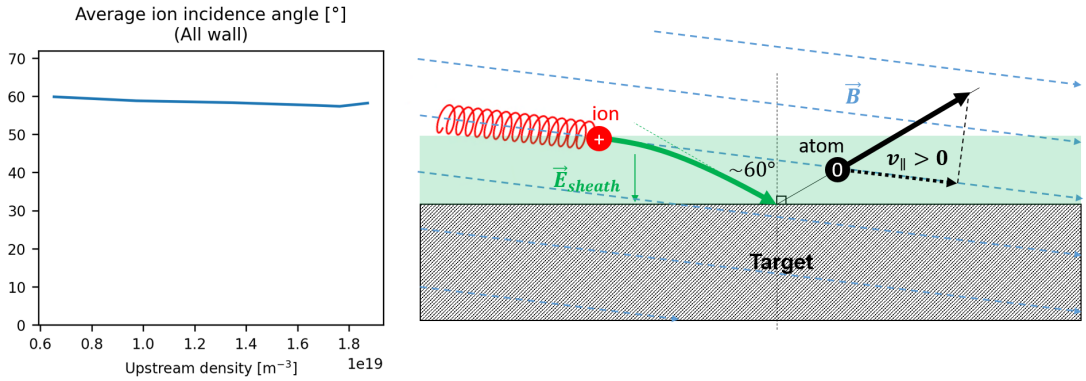

Figure 4.11.: Left: average ion incidence angle to the solid surfaces after the electrostatic sheath acceleration, as computed by EIRENE, across the whole wall (first wall and targets). Diagram of the associated parallel velocity of an atom after an ion fast reflection. The parallel velocity of the atom is still positive, but moved away from the wall in the (R, Z) plane.

At rollover, the ion-molecule elastic scattering starts contributing largely, while the peak of the atom charge transfer component detaches slightly from the target. For the partially detached plasma, the ion-molecule elastic scattering becomes very large, and extends largely away from the target. While these collisions only form a momentum sink, the sign of the atom charge exchange contribution depends on the location. Away from the target, where the parallel plasma velocity is larger, it is a sink, while closer to the plate, where the parallel velocity is lower, it is a source. In partially detached conditions, charge exchange atoms are therefore responsible for a transfer of momentum from regions away from the target to the vicinity of the target.

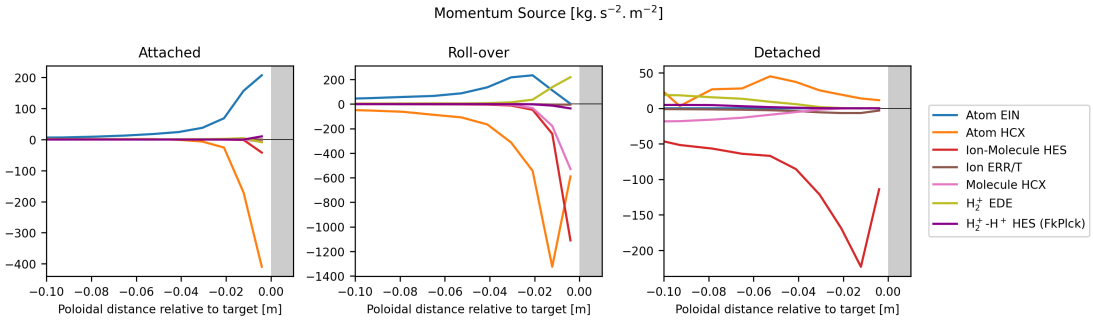

Figure 4.12.: Volume ion momentum source along the outer divertor leg up to the target. Only significant reactions are plotted.

4.3.2.3. Ion energy sources

Turning now to the ion energy source (Figure 4.13), one finds that the three dominant processes throughout the throughput scan are the same as for the parallel momentum:

the ion creation through atom ionization, the atom charge transfer, and the ion-molecule elastic scattering. In attached cases, it is dominated by atom ionization (including of high energy charge transfer atoms) acting as a positive source with the same reasoning as with the momentum source (i.e., this still leads to plasma cooling), with a significant negative contribution of the atom charge transfer within 2 cm of the target.

Then at rollover, the atom charge exchange contribution becomes a source near the target, while its momentum contribution is still a loss with respect to the incoming plasma flow toward the target. Thus, atoms near the target transfer a portion of their parallel kinetic energy to their thermal energy. In addition to this, the plasma is also heated by the fast atoms that have undergone charge exchanges, further upstream or on other field lines where the plasma is hotter. The plasma can also be possibly heated from the back-scattered atoms from fast reflection after their accelerations by the sheath. At partial detachment, this positive contribution extends largely towards the X-point, but also becomes a positive momentum source, which indicates the increased contribution of the fast atoms from the upstream regions.

The molecule-ion elastic scattering, however, only takes the form of a sink. Indeed, the molecules can not reach high kinetic energies in the same way atoms do, because of their slow velocity when they enter the plasma ($T_{\text{wall}} \ll T_{\text{atoms}}$). Furthermore, they do not survive in hotter regions and are consumed by other processes before they can collide with very hot ions. In fact, molecule-ion collisions only occur where cold ions exist near the target. This also coincides with the region where atom charge transfers are reheating ions. Therefore, atoms and molecules have opposite contributions to the ion energy balance (heating and cooling respectively) in this regime. A similar region is observed at partial detachment, but now spreads up halfway toward the X-point.

On a final note, the H_2^+-H^+ elastic scattering ("H_2^+-H^+ HES" on the graph) is not very large, which indicates that it should not drive differences with the SOLPS runs (section 3.5), for which H_2^+ is static, and this channel does not exist.

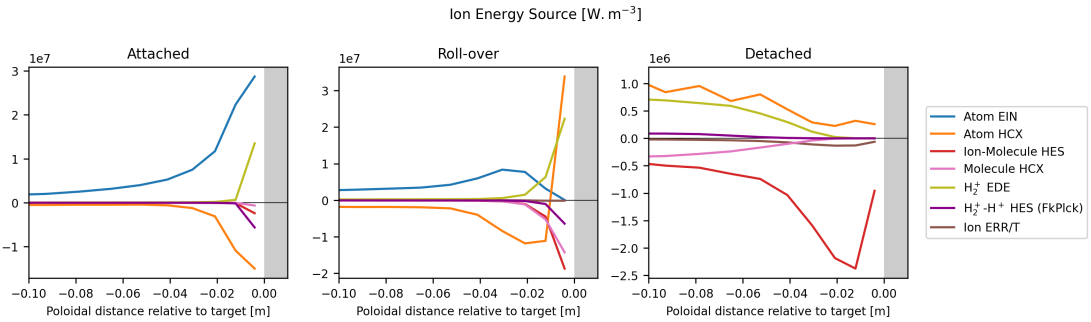

Figure 4.13.: Volume ion energy source along the outer divertor leg up to the target. Only significant reactions are plotted.

4.3.2.4. Electron energy sources

The electron energy loss picture is much simpler (Figure 4.14), as all reactions involving electrons produce a cooling effect except for the volumetric recombination at low temperature (three-body recombination).

Atom ionization is the largest contributor. The electron energy loss per ionization event is about 20 to 25 eVs at temperatures above 10 eV, but can increase sharply to several tens of eVs when T_e decreases. Oppositely, when n_e rises, this cost is significantly lowered because of collisional excitation effects. Figure 4.15 shows this dependency along with the associated collision rate coefficients on the left. However, as can be seen on the plot on the far right, the average electron loss per ionization is almost unchanged at ~25 eV, whatever the regime in the ITER simulations. With increased upstream density, divertor density increases, and the density dependence of the collision rate coefficient makes the ionization occur at lower temperatures ("Atom Iz. weighted T_e" on the figure), and at higher density ("Atom Iz. weighted n_e"). Because this ionization cost also includes both opposite dependencies in density and temperature, the effects cancel out, and the unitary cost remains at 25 eV on average.

For attached cases, atom ionization is the dominant process due to its significant cost per event. It is located directly at the target. The other contributors are the H_2^+ dissociative excitation, and also notably the molecule ionization, both within a centimeter of the target. At rollover, the H_2^+ dissociative excitation strongly increases at the target, the atom ionization detaches from the target, and the molecule ionization disappears, as is consistent with what was seen in the particle source and reaction rates section section 4.3.2.1. One can note that even though the H_2^+ dissociative recombination is large near the target (Figure 4.10), it does not entail a large electron energy loss: this is because this reaction occurs at rather low temperatures, so that for this process low energy electrons in the distribution function are the main contributors (see [48], reaction H.8 2.2.14).

Then at partial detachment, the electron-H^+ recombination and the H_2^+ dissociative recombination appear near the target, the former as a source, the latter as a sink. When looking at the net source, there is now actually a positive heating source to the electrons directly at the plate because of the three-body recombination. The major contributor in this region is the H_2^+ dissociative excitation, while when integrated over the whole volume the atom ionization still dominates (it is not visible on Figure 4.14 because this reaction is widely spread out over the divertor).

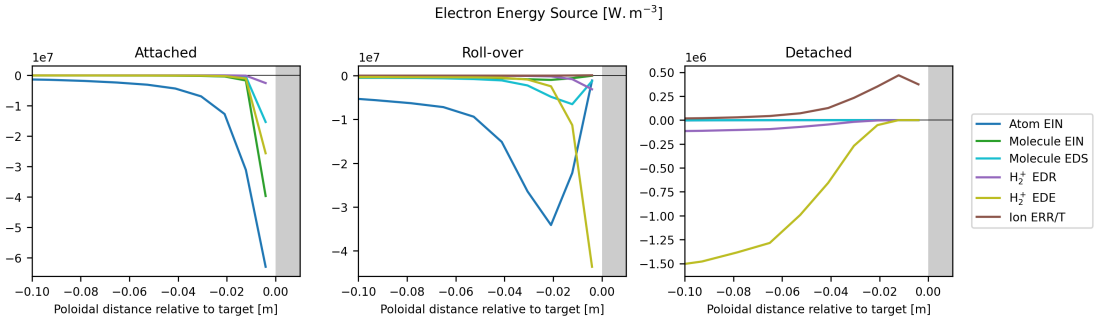

Figure 4.14.: Volume electron energy source along the outer divertor leg up to the target. Only significant reactions are plotted.

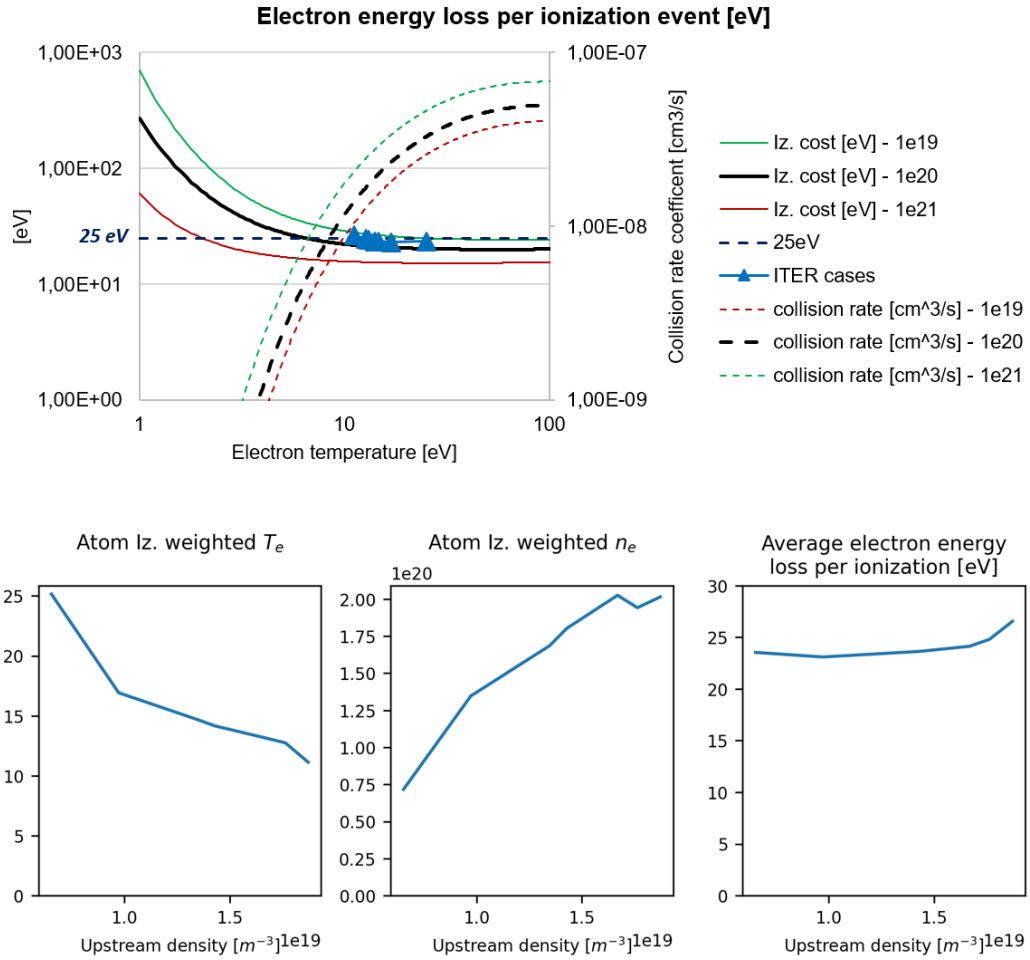

Figure 4.15.: Top: Electron energy loss per atom ionization event (left axis) and collision rate coefficient (right axis), for three values of density 1×10^{19}, 1×10^{20}, and 1×10^{21} m^{-3}. Blue triangles indicate the position of averages for the considered ITER cases (data on the plots on the right). Bottom plots: Electron temperature and density averaged across the whole volume with the occurrence of atom ionization (ex: $\overline{T_e} = \int N_{Iz} T_e / \int N_{Iz}$) and average ionization cost ($\int SE_{e^-,Iz} / \int N_{Iz}$) as a function of upstream density.

4.3.3. Overall picture of the neutral driven plasma detachment in ITER PFPO-1 simulations

It is now possible to summarize the main phenomena observed through the detachment process in the considered ITER simulations, in Figure 4.16.

- **In all regimes**: The strongest electron energy loss is the atom ionization, due to

its high cost per event (~ 25eV on average, increasing with T_e = decreasing in cold regions, but decreasing with density, vs. 15eV cost of ionizing a molecule).

- **Attached regime/high-recycling**: Atom ionization is the largest contributor to the ion particle source, followed by the already significant H_2^+ dissociation (H_2^+ EDE). Because T_e is large enough, H_2^+ are created by electron ionization, and thus the H_2^+ dissociation is a net ion source. All plasma-neutral reactions happen directly at the targets. The electron energy loss is mainly composed of the expensive atom ionization, the molecule ionization, and the H_2^+ dissociation. The ion energy and momentum sources are only losses, driven by the atom charge exchange.

- **At rollover**: At rollover, the atom ionization front detaches, while the H_2^+ dissociation increases and stays at the target. However, T_e decreases, and n_i increases enough so that the H_2^+ creation mechanism completely switches from electron impact to ion impact (i.e., through molecule charge transfer). Molecule electron ionization disappears, thus the H_2^+ dissociation becomes a net zero particle source. Molecules are now also significantly dissociated directly into two atoms further away from the plate. The rest of the H_2^+ are consumed by dissociative recombination (MAR), which becomes significant at the target as a particle sink. Electron-H^+ recombination remains very weak. Ion-molecule elastic scattering is now a large momentum sink, and the energy transported by the atom charge exchanges starts to heat the cold target plasma after taking energy upstream.

- **Partially detached**: Finally, at maximum throughput, the atom ionization is largely spread out up to the X-point, and does not occur close to the strike point. The H_2^+ dissociation front detaches and spreads. The molecule dissociation into two atoms disappears. Electron-H^+ recombination becomes a large particle sink near the target, and the H_2^+ dissociative recombination (MAR) detaches from the target where the H_2^+ density is high (but still several orders of magnitudes below n_i). Electron energy now includes a small source directly at the plate from the three-body recombination. Strong losses include atom ionization on the whole divertor leg, and the H_2^+ dissociation near the target. The atom charge transfer adds now momentum and energy in a larger region between the X-point and the target, while the molecule-ion elastic scattering makes a large and wide momentum sink at this location, which also results in pushing the molecules back to the target. Neutral-neutral collisions become large at the target at this stage.

In order to highlight two specific points about the investigations of the detachment mechanism, it is observed that:

1. MAR is the particle sink that appears at the rollover while electron-H^+ recombination is not significant, and the latter becomes dominant on the field line only at detachment, and closer to the target.

2. The molecule-ion elastic collisions and atom charge exchange are each responsible for both very large momentum and energy sources, and these two types of sources are directly linked and cannot be addressed as independent effects.

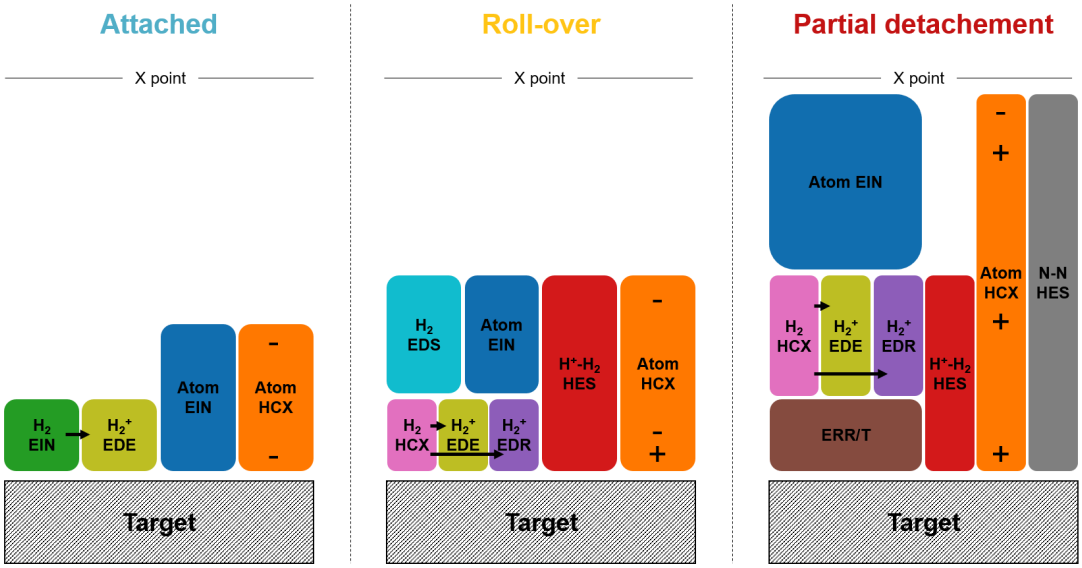

Figure 4.16.: Overview of detachment process with key reactions involved, depending for three divertor regimes. Note that the labels in color represent the different regimes, but the behavior represented are derived from the analysis of a single field line. Thus the "partial detachment" label relates to the regime, while the considered field line is itself simply "detached". Arrows represent the H_2^+ creation-consumption reaction chain. See Table 3.3 for the list of abbreviations.

4.3.4. Specificity of ITER cases

Even if the latter analysis only focuses on the ITER machine, and does not include simulations of plasmas in current, smaller machines, it is possible to note a key observation that makes ITER cases different: the plasma sources (particle, momentum, and energy) related to plasma neutral interactions are generally much more localized in the divertor than in current, smaller devices. This comes from the fact that both the sources' position with respect to the targets and spatial extent do not depend on the size of the machine, but rather on the mean free paths of these processes, which only depend on the plasma conditions. Those are not so different from what is found at high power in current machines for the low-power ITER cases (this may not apply to high-power burning plasma ITER cases). Therefore, the relative spatial extension of the sources with respect to the machine and divertor size is much smaller in ITER than

in current devices. Even for partially detached cases, sources are still well contained in the divertor, as is shown in Figure 4.17.

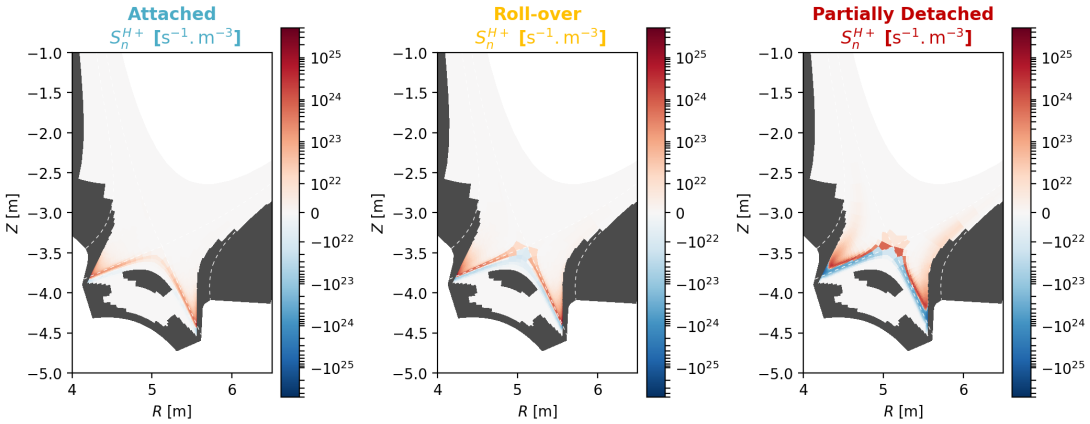

Figure 4.17.: 2D plots of the plasma particle source from plasma-neutral interactions (from EIRENE), for 3 cases representing the throughput scan, at the following upstream densities: blue: $0.65\times10^{19}\mathrm{m}^{-3}$, yellow:$1.35\times10^{19}\mathrm{m}^{-3}$; red:$1.87\times10^{19}\mathrm{m}^{-3}$.

4.3.5. Relation between momentum and energy fractions

From this density regime scan, it is also possible to evaluate the fraction of momentum f_{mom} and energy f_{power}[1] remaining in the plasma between the upstream and the target.

Those fractions are defined as such:

$$f_{\mathrm{mom}} = \frac{p_t^{\mathrm{tot}}}{p_u^{\mathrm{tot}}} \tag{4.1}$$

$$p^{\mathrm{tot}} = n(T_i + T_e)e + \frac{1}{2}\frac{\Gamma^2}{n} \tag{4.2}$$

$$f_{\mathrm{power}} = \frac{q_{\parallel,t} f_x}{q_{\parallel,u}} \tag{4.3}$$

In the latter expression, f_x is the flux expansion between upstream and the target.

The results for the throughput scan are plotted in Figure 4.18. As is shown in the left two graphs, both f_{mom} and f_{power} decrease drastically with increasing upstream density as expected. More notably, when plotting f_{power} against f_{mom} (the right part of the figure), one can see that for high-density regimes near and after the rollover f_{power} is proportional to the square of f_{mom}. This observation seems to support the

[1] In the literature, the symbol f_{power} may also refer to the $1 - f_{\mathrm{power}}$ used here. The notation here is defined to be consistent between momentum and energy.

point that in the considered simulations, at high-density regimes both fractions are closely linked. Thus, they cannot be arbitrarily varied independently from each other in reduced models to derive conclusions. This squared relation recalls the relation between momentum $\mathbf{p}$ and energy $E \propto \mathbf{p}^2$, illustrating an energy loss associated with momentum losses. However, more detailed investigations would be needed to better understand this observed link between the two fractions.

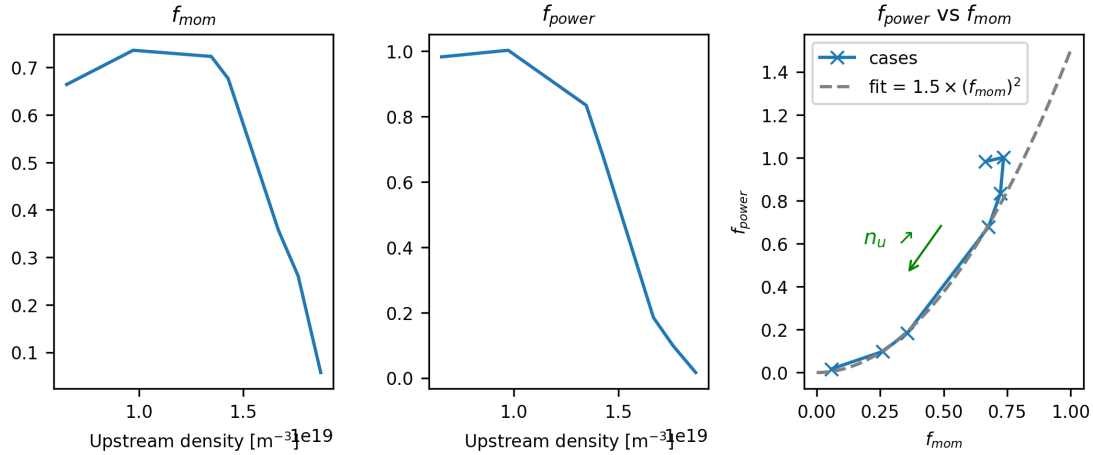

Figure 4.18.: Momentum fraction and energy fraction as a function of upstream density, and energy fraction as a function of the momentum fraction for the throughput scan.

Additional simulations could be carried out with the recombination mechanisms (MAR and electron-H^+) turned off to assess their role in the reduction of the particle flux to the targets in our simulations, to compare with the investigations in [19], [18], [78] and [79].

5. First Wall fluxes and plasma conditions

Contents

5.1. Introduction to first wall matters

As mentioned in section 1.5, two of the key challenges of the first wall are: first, the optimization of the life expectancy of the plasma-facing components by minimizing the damage from the plasma, and second, the minimization of the plasma contamination from sputtered particles from the wall material.

Both issues are linked to the same origin, and are related to the rate at which the beryllium panels will be eroded by the plasma discharges, which is directly driven by the plasma and neutral processes occurring in the vicinity and at the first wall. Also, the sputtering at the targets can be increased by sputtering of the first wall: even if the plasma hydrogen ions are much more likely to erode the beryllium surfaces than the tungsten ones (due to the lower sputtering energy threshold for H on Be), the eroded beryllium ions can be transported to the target and induce tungsten sputtering there (Be on W has a lower energy threshold than H on W).

This chapter discusses the results obtained at the first wall. As those are dictated by the outward radial evolution of the plasma from the edge towards the wall, a first section will focus on the upstream profiles and their evolution through the SOL, and address two points: the observed increase of the λ_q and the insensitivity of the T_e profile to throughput.

Then a second section will focus on the erosion of the first wall, by analyzing the plasma conditions there, the fluxes and energy of charge exchange neutrals, and present gross erosion estimations.

5.2. Upstream analysis

5.2.1. Quantities at the separatrix and outer midplane profiles

Density and temperatures at the separatrix at the outer midplane are shown in Figure 5.1, which correspond to the values denoted "upstream".

Separatrix density The left part of Figure 5.1 shows the relation between the throughput and the upstream density. One important feature to note is the saturation of the upstream density towards $\sim 1.9 \times 10^{19}$ m^{-3} with increasing throughput. Those throughput values in the saturation region correspond to the detachment phase at and after the rollover. This seems to indicate that the upstream and the divertor decorrelate even more noticeably in high-density regimes than in low regimes with respect to the density. This saturation behavior is also found in SOLPS-ITER simulations at both low and high power for ITER cases [35, 42]. The origin of this effect would require a more in-depth analysis of the particle balance, which is not done here, but may be an effect of the machine size in ITER which leads to better confinement of the particle source in the divertor. However, this increased decorrelation cannot be generalized for all quantities, as will be seen for the decay lengths in section 5.2.2.

Plots of quantities across similar scans are often made against the upstream density as the x-axis. As this is not directly the scanned parameter (which is the throughput), the link between the two is provided in the left part of Figure 5.1. Since n_u tends to saturate, therefore when other plots are presented as a function of n_u, the points towards the end of the scan are closer on the x-axis, but represent very large increases of the throughput. Similar results are obtained with SOLPS-ITER (see section 3.5).

Separatrix temperatures Both temperatures drop with throughput as expected, but the effect on the ions is much larger than on the electrons. T_i decreases by a factor of two from 230 to 120 eV, but T_e only by 25% (from 130 to 100 eV).

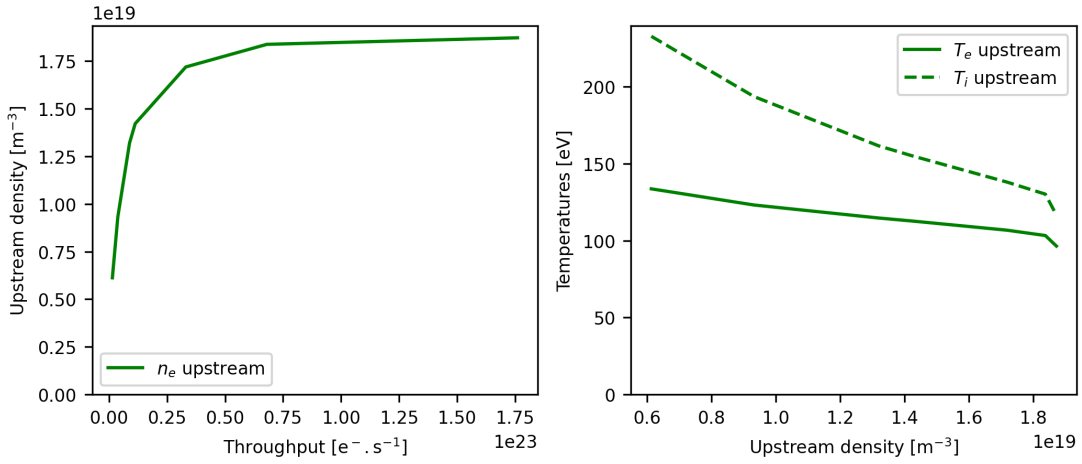

Figure 5.1.: Separatrix density and temperatures at the outer midplane. Left: plasma density as a function of the throughput, right: electron and ion temperatures as a function of upstream density (i.e., the quantity on the left).

Profiles at the midplane Turning now to 1D profiles at the outer midplane, Figure 5.2) shows the expected behavior for this type of transport simulations, i.e., close to exponential decays after a few centimeters from the separatrix. Notably, no density shoulder appears at all in these profiles, which could have been the case even with uniform perpendicular transport coefficients under certain circumstances (for example, if a strong neutral ionization source had been found in the far-SOL). This result is in line with modeling results obtained with SOLEDGE3X and similar set-up (2D transport, no drifts) on medium-sized tokamaks for which mean-field simulations have not been able to exhibit density shoulders without strongly increasing perpendicular transport coefficients in the far-SOL w.r.t. near SOL values (which are constrained by profile measurements).

The ion temperature shows a sharp drop in the near SOL, then a second region with a flatter profile in the very far-SOL. The drop corresponds to the radial region where field lines are connected to the divertor, in which very large energy losses occur due to neutrals, in contrast to the far-SOL where those are not present. The transition between the steep decay and the slowest decay tends to move radially outwards as the throughput increases.

While the electron temperature inside the separatrix decreases with throughput, which could have been reasonably expected, one can observe however that further in the SOL, the T_e profile is almost insensitive to the throughput. The explanation of this effect is discussed in the next subsection.

Finally, at the first wall at the outer midplane, the plasma density increases by a factor of 100 across the scan, from $\sim 1 \times 10^{14}$ to $\sim 1 \times 10^{16}$ m^{-3}, while T_e stays below 1eV, and T_i decreases from 6 to 2 eV.

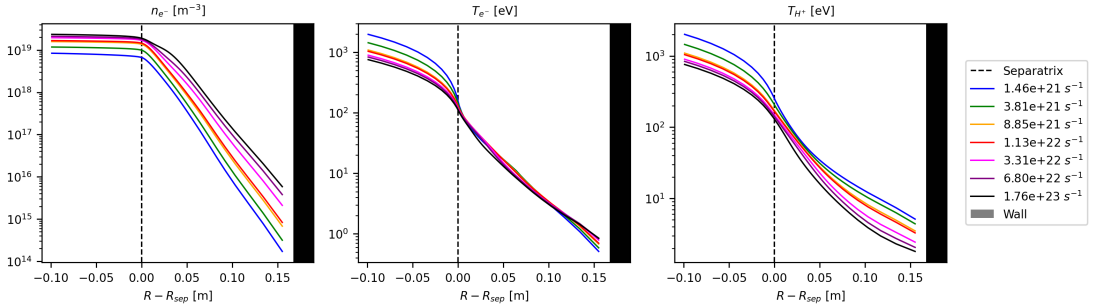

Figure 5.2.: Upstream density and temperature profiles at the outer mid-plane for the throughput scan, with values of throughput indicated in the legend in electrons per second.

2D overview & dense regions in the far-SOL Figure 5.3 presents 2D plots of the density and the electron temperature for a case after the rollover, in order to provide an overview of the solutions. Significant plasma densities are present near the outer bottom first wall plate above the outer baffle and at the machine top near the secondary X-point (see black rectangles in the figure). Consequently, one can expect increased plasma-wall interaction at these locations, as seen in the following sections.

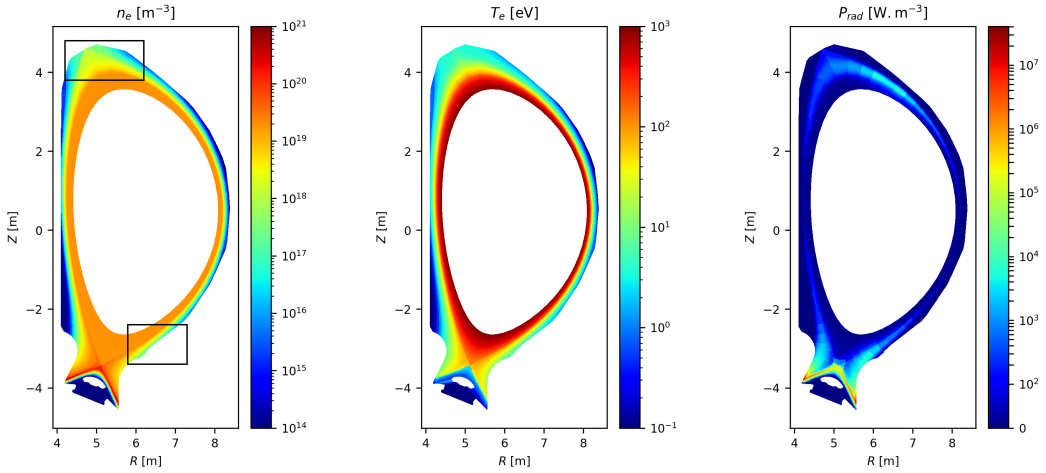

Figure 5.3.: 2D plots of density, electron temperature and volume radiation for a medium-throughput case (after rollover, 3.31×10^{22} e$^-$.s^{-1}). Black rectangles indicate the regions of the first wall where plasma-wall interactions are expected to be significant.

5.2.2. λ_q increase with throughput

The SOL power width λ_q is a central parameter to consider when addressing the heat exhaust challenge, as it is one of the determining factors of the peak heat flux arriving

at the targets. This section focuses on this quantity, where values obtained in the simulations and variations across the scan are investigated.

λ_q as an input parameter to edge mean-field modelling SOL decay length, either for the density, the temperatures or the heat flux, result from the equilibrium between perpendicular and parallel transport processes. While mean-field models describe reasonably well parallel transport mechanisms (under the assumption of a collisional plasma), they rely on a gradient-diffusion closure for the description of perpendicular fluxes to circumvent the lack of information concerning fluctuations and the turbulent transport they drive. The associated diffusion coefficients can be considered as a free parameter of the model. In the absence of theory-based guidance for the determination of their amplitude, one has to rely on other means to determine sensible values to use in edge plasma modelling. When the code is used as an interpretative tools for experiments, profile measurements, either at the target or upstream, provide constraints to determine transport coefficients. When the code is used for predictive study however, as it is the case here for ITER, the only available information stems from experimental multi-machine scaling laws on SOL widths. λ_q can then be seen as an input parameter to the simulation as it is effectively used to tune transverse diffusion coefficients to a sensible value.

The multi-machine inter-ELM H-mode power width scaling To date, the most widely accepted experimental scaling available for the SOL heat flux width is the well-known multi-machine inter-ELM H-mode power width scaling [41]. This scaling only applies to low-density regimes and relies on a fit of the heat flux profile at the target by a function parameterized with λ_q plus a "power spreading" parameter S. In spite of the fit being performed on target profiles, the standard interpretation of this scaling suggests that λ_q can be considered as an upstream quantity determined by transport processes above the X-point while S is determined by divertor transport and dissipative mechanisms. The scaling law is then effectively used to tune diffusion coefficients to achieve a value of the upstream SOL width.

One can attempt to compute the obtained λ_q with this fit in the considered simulations in order to check that the chosen transport coefficients are relevant. However, it will be seen that this approach is not suited here and that one has to use another method. The left part of Figure 5.4 shows the profiles at the targets that are used for the fitting function in solid lines and the best fit in dashed lines with the same color. Apart from the two lowest throughput cases, the fits are poor since the fitting function cannot properly describe the shape of the profiles, and the obtained values for λ_q can not be considered. Furthermore, even for the two first cases, it was seen in section 4.2 that they were actually at the high end of the high recycling regimes. Therefore, the fit of this mathematical function should not be utilized to derive the physical power width as it falls out of the domain of validity of the Eich's scaling law.

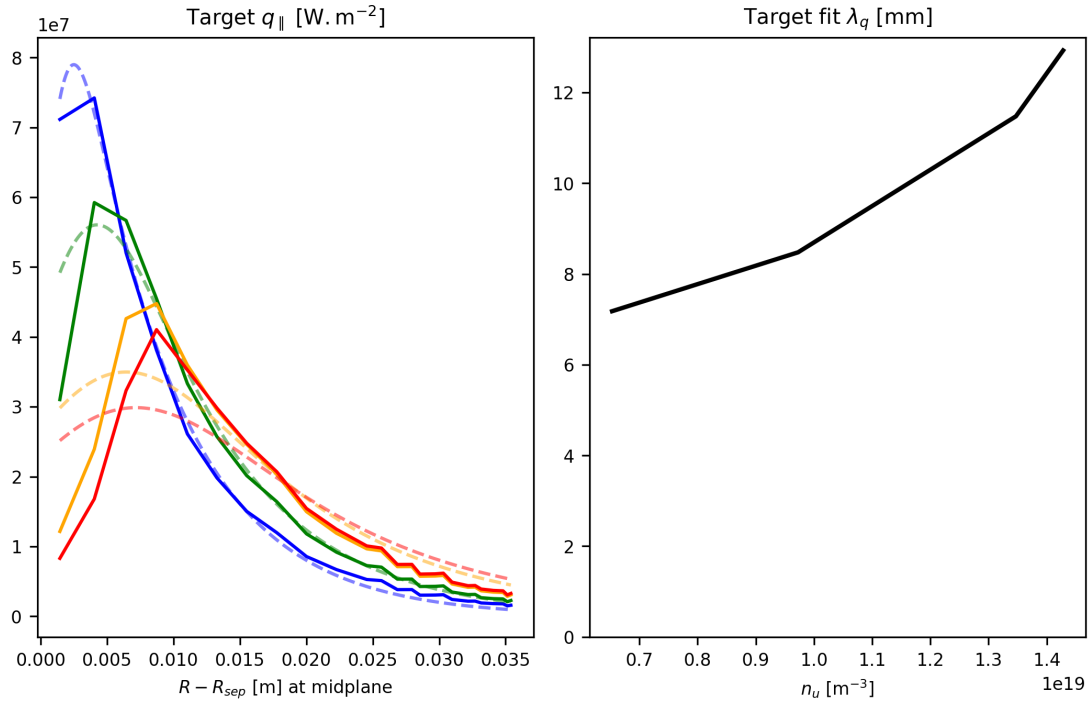

Figure 5.4.: Attempt at fitting the mathematical expression of the target heat flux scaling law [41] on the obtained profiles at the target in ITER simulations for the throughput scan. Apart from the first two cases, the fits are poor and are not relevant. Left is plotted the parallel heat flux data in solid lines for each case, and the function fit in dashed lines. The right plot shows the associated values of λ_q.

A more direct approach is used to compute it from the simulations: λ_q is evaluated via $\lambda_{q,e}$ the characteristic decay length of the electron parallel heat flux density at the poloidal location where it is maximum and then remapped to the outer midplane. This method, as it involves quantities upstream above the divertor, applies to any regime, not only to low densities, and is also used in other analyses based on the SOLPS code [80]. The results are shown in Figure 5.5.

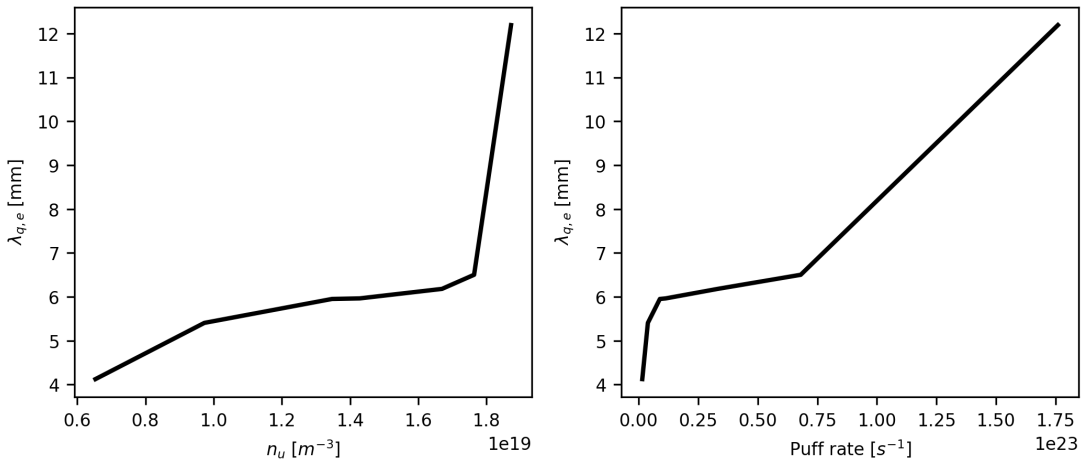

Figure 5.5.: Evolution of the SOL width $\lambda_{q,e}$ with the upstream density (left) and throughput (right). $\lambda_{q,e}$ is defined as the exponential decay length of the electron parallel heat flux taken at the poloidal location where it is maximum. See definition in the text.

The first case gives a value at 4 mm and is roughly consistent with the scaling law, which gives around 2 mm for a 5 MA hydrogen H-mode, a value that needs to be doubled for L-modes [42]. However, it is then found to strongly increase from 4 mm to 6 mm up to the roll-over, and then continue to increase to 6.5mm in a much slower fashion. This behavior was also observed in SOLPS-ITER runs [81]. The last large step to 12mm is only due to the maximum throughput case, where the density rises so much that profiles tend to be significantly flatter. Coming back to the formulation of Eich's fit, since in our cases $\lambda_{q,e}$ was computed upstream above the divertor, this width increase is not supposed to be captured by the spreading factor S, which focuses on divertor effects.

Therefore, this shows that in our simulations, even with identical perpendicular transport coefficients, changes in the divertor regime have a noticeable effect on the shape of the SOL upstream. In such cases, what happens upstream is not independent anymore from what happens in the divertor. However, it is recalled that those are low-power simulations, without impurities, and the latter observation may not hold for high-power impurity-seeded burning plasma cases as seems to be indicated by SOLPS simulations in [35].

The reason for this increase in power width is investigated below.

Interpretation of the $\lambda_{q,e}$ increase Figure 5.6 provides more details on the parallel electron heat fluxes where $\lambda_{q,e}$ is computed. This location is where this flux is maximum in the poloidal direction, labeled "divertor entrance" (left figure), is actually the same for all cases. Then, the radial coordinate is remapped to the outer midplane. The parallel electron heat flux after the separatrix takes the shape of a decaying exponential, and thus it is possible to compute a decay length. This is also the reason for

restricting this quantity to the electrons and excluding the ions: the ion parallel heat flux can be much farther from a decaying exponential because of the flow reversals (inversion of the fluid parallel velocity, flowing upstream instead of downstream, see Figure 5.7) near the separatrix.

The physical origin of these flow reversals could be related to the strong localization of the particle source near the target, which only leaves important radial losses along the first field line in the divertor leg. However, a clear understanding of this phenomenon would require additional analyses which are outside the scope of this work.

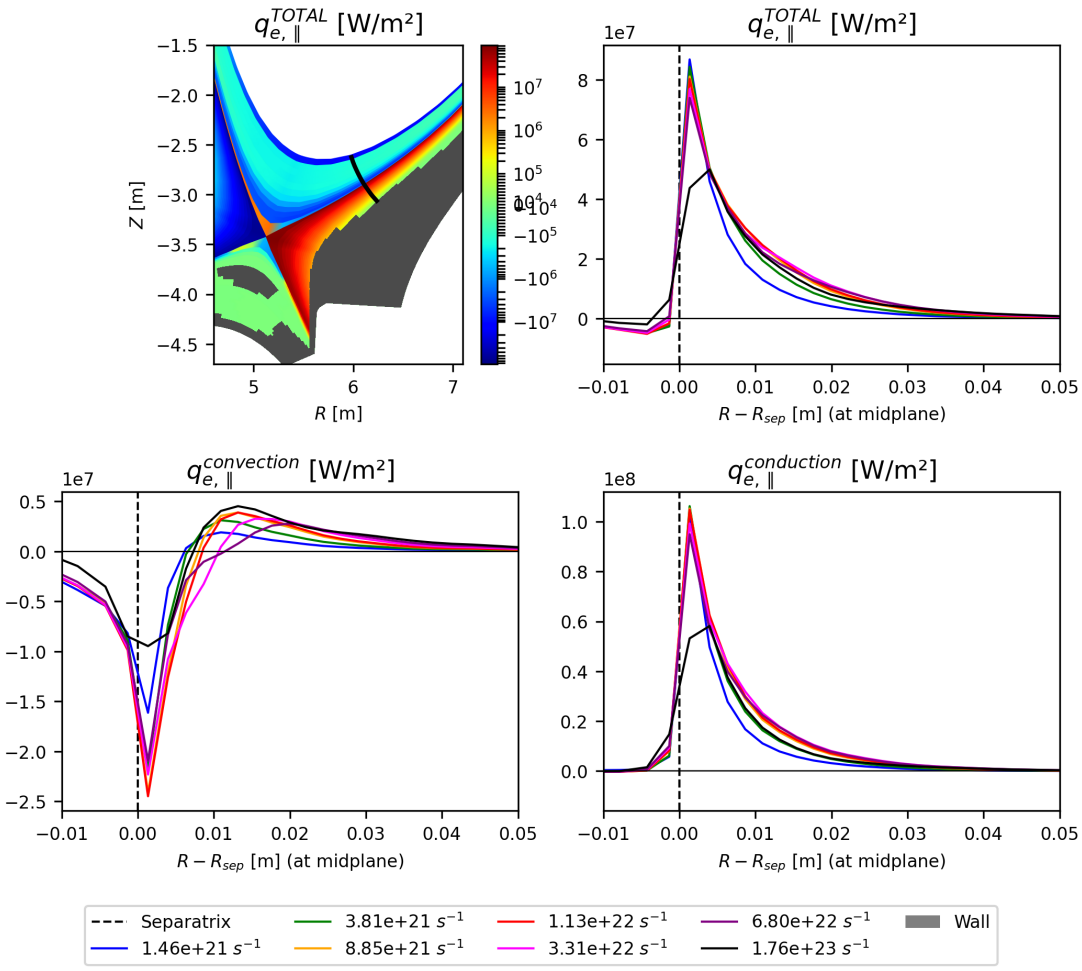

Figure 5.6.: Top left: 2D plot of the parallel electron energy flux; the black line represents the location of the radial profiles on the right, the so-called "divertor entrance", where the electron parallel heat flux density is maximum. 1D plots: Radial profiles of the total electron parallel heat flux (top right) at the outer divertor entrance, and decomposition between its convective (bottom left) and conductive (bottom right) components.

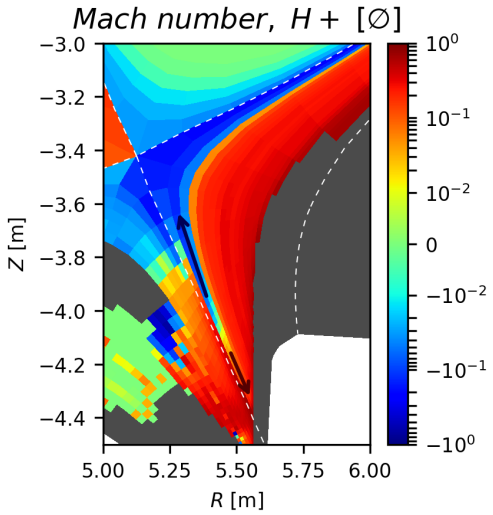

Figure 5.7.: Mach number for the rollover case, as illustration of the appearance of a flow reversal in the SOL. Arrows emphasize the change of sign of the parallel velocity near the separatrix in the divertor.

The heat flow patterns result from a balance between the parallel and perpendicular fluxes. From a simple energy balance, one can obtain the following relation to assess variations of $\lambda_{q,e}$ from these two contributions:

$$\nabla \cdot \vec{q} = 0 \quad \Rightarrow \quad \frac{\partial q_\parallel}{\partial s_\parallel} = -\frac{\partial q_\perp}{\partial s_\perp} \quad \Rightarrow \quad \frac{q_\parallel}{L_\parallel} \sim \frac{\chi_{\perp,e} n_e}{\lambda_{T_e}^2} \tag{5.1}$$

$$\text{from} \quad q_\perp = K_\perp \frac{\partial T_e}{\partial s_\perp} \quad \text{with} \quad K_\perp = -\chi_{\perp,e} n_e \tag{5.2}$$

$$\lambda_{q,e} \sim \lambda_{T_e} \sim \left(\frac{n_e \chi_e T_e L_\parallel}{q_\parallel} \right)^{1/2} \tag{5.3}$$

where the relation $\lambda_q \sim \lambda_{T_e}$ is justified in [14].

Figure 5.8 show this approximation computed at the divertor entrance (left plot) and is found indeed to follow the same trend as the $\lambda_{q,e}$ computed previously. It still has a factor 10 difference in absolute value in comparison to Figure 5.5 which is probably due to the coarseness of the model, however it is rather the trend that is of interest. Since this approximation is a ratio, the relative evolution of each term across the scan can be evaluated to interpret the evolution (right plot). One can see there that the perpendicular transport is strongly enhanced because the density rises significantly while the electron temperature only slightly decreases. Since, in absolute terms, the amplitude of the perpendicular transport is much lower than the parallel one, the associated relative reduction of the parallel transport is rather weak.

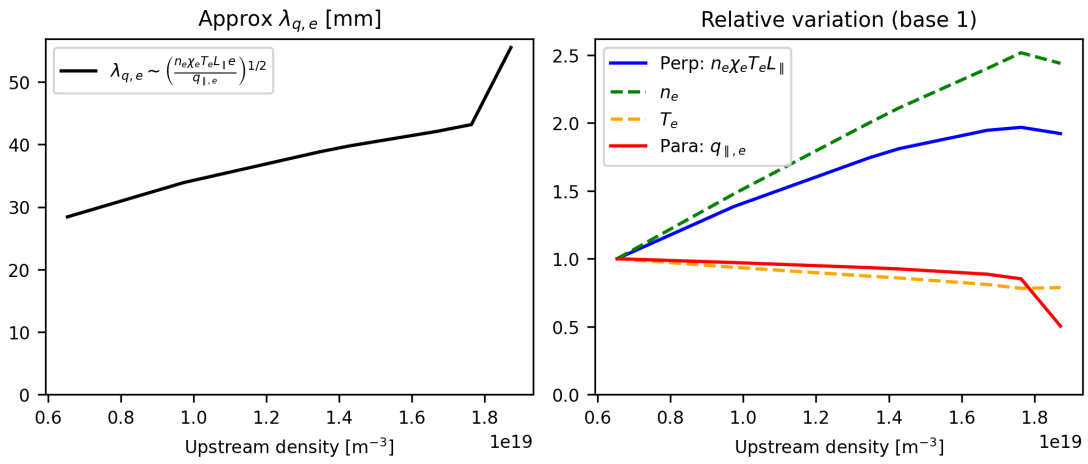

Figure 5.8.: Left: Approximation of the $\lambda_{q,e}$, see the text the derivation and assumptions. Right: relative variations of the parallel electron heat flux, electron temperature and density at the separatrix at the divertor entrance (see Figure 5.6) for the exact location) across the throughput scan, as a function of upstream density.

Next, the reasons for the reduction of parallel transport are investigated. Figure 5.9 shows the decomposition of the electron parallel heat flux as a function of the upstream density for two flux surfaces ($R - R_{sep} = 4.0$mm and $R - R_{sep} = 6.4$mm), normalized to the perpendicular heat flux entering the flux surface $q_\parallel / Q_\perp$. This enables the comparison of the efficiency of the conductive and convective parts of the parallel transport.

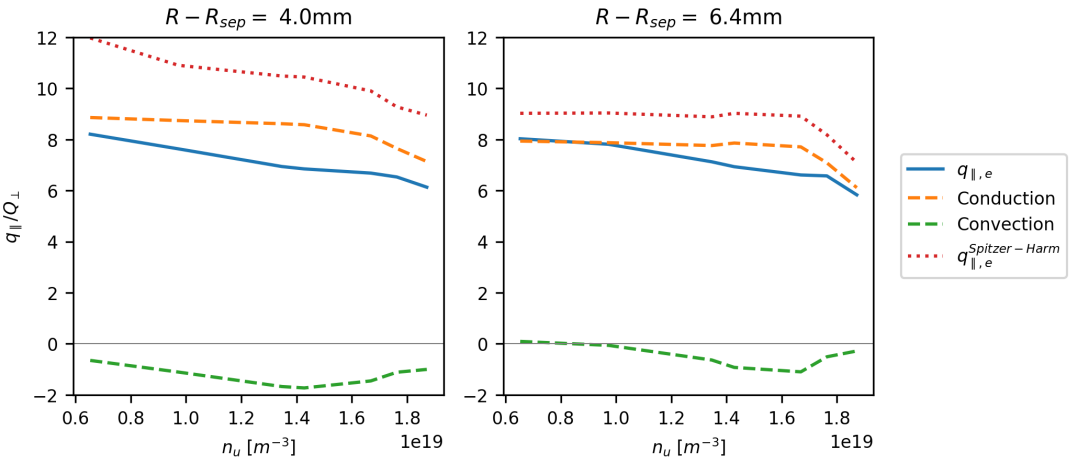

Figure 5.9.: Ratio between the parallel heat flux density to the integrated perpendicular heat flux entering the flux surfaces $q_\parallel / Q_\perp$, for two flux surfaces close to the separatrix, extending from the inner divertor entrance to the outer divertor entrance.

Until the last point of the scan, the conductive part is constant (in dashed orange), while the convective part (dashed green) is negative and increases in amplitude. Thus, this contribution is responsible for the observed increase $\lambda_{q,e}$ for this part of the scan. Indeed, this mechanism transports energy in the opposite direction (upstream) because of a local flow reversal, countering the conduction effect.

At maximum throughput, the picture is reversed, and conduction decreases significantly while the flow reversal amplitude decreases. However, in this case, the conduction effect is much larger than the change of flow reversal.

Also, Figure 5.9 shows that the conductive transport on these flux surfaces is actually set by the flux limiters [82]. In our cases the flux-limiter α parameter is set to 0.2 for the electrons (and deactivated for ions). The choice for this value is justified in [14], as it gives the best match with kinetic simulations. The Spitzer-Harm formula, plotted in dotted red, would give higher values.

Conclusion In low-density regimes, the standard interpretation of Eich's scaling law suggests that the SOL power width is independent from divertor dissipative mechanisms that rather determine the spreading factor S of the profiles at the targets. In ITER's highly dissipative divertor regimes, such an assumption does not hold, and the power decay length presents significant variations with the throughput. Indeed, the shape of the power channel upstream is changed by two effects: the increase of the perpendicular heat transport with rising density, and the reduction of the parallel one via, first, convective flow reversal, and then, conductivity reduction.

Therefore, returning to the original question of setting up the perpendicular transport coefficients for future machines, one can tune them to match λ_q with the scaling in very low-density sheath-limited regime simulations and retain these values for

other regimes. Then for simulations of highly dissipative divertor regimes, λ_q may increase without being fundamentally inconsistent with the scaling law, which is not applicable at this stage. In the case where one wishes to simulate directly dissipative regimes, one should not tune transport coefficients to match the scaling law, which would lead to over-constraining the simulations.

5.2.3. Insensitivity of the T_e profile in the SOL

In section 5.3.2.3, the electron temperature at the first wall is found to be insensitive to throughput. This section investigates the origin of this effect. The T_e value at the wall is a consequence of its radial evolution in the near and far SOL, shown in Figure 5.2 at the midplane. In this figure, one can observe that contrary to the ion temperature profiles, the electron temperature profiles a few centimeters after the separatrix are almost identical and reach the first wall at approximately the same value.

To interpret such a result, one can invoke two arguments:

1. First, at the separatrix, T_e is lower and much less sensitive to density than T_i, as seen on the left of Figure 5.10, which plots the temperature profiles at the midplane, due to the higher parallel conductivity of the electrons [14].

2. Second, further in the SOL, the energy equipartition term between ions and electrons ($T_e < T_i$) is positive for electrons, and increases with density.

The latter point is illustrated in the right plot of Figure 5.10. It shows the ratio between two characteristic times: the parallel energy loss characteristic time $\tau_{\parallel,e} = \frac{\mathscr{E}_e^{th}}{\gamma_e n c_s T_e e} = \frac{3L}{2\gamma_e c_s}$, and the collisional energy exchange characteristic time $\tau_{\text{equi.}} = \frac{\mathscr{E}_e^{th}}{Q_e}$. This ratio decreases with density, and when $\tau_{\text{equi.}}$ becomes of the same order of magnitude as $\tau_{\parallel,e}$, then its effect is seen on the profile of T_e, and this mechanism heats the electrons significantly. Two factors drive its increasing importance: its n^2 dependency, and the radially increasing temperature difference between electrons and ions in SOL because of the difference in the sheath heat transmission factors.

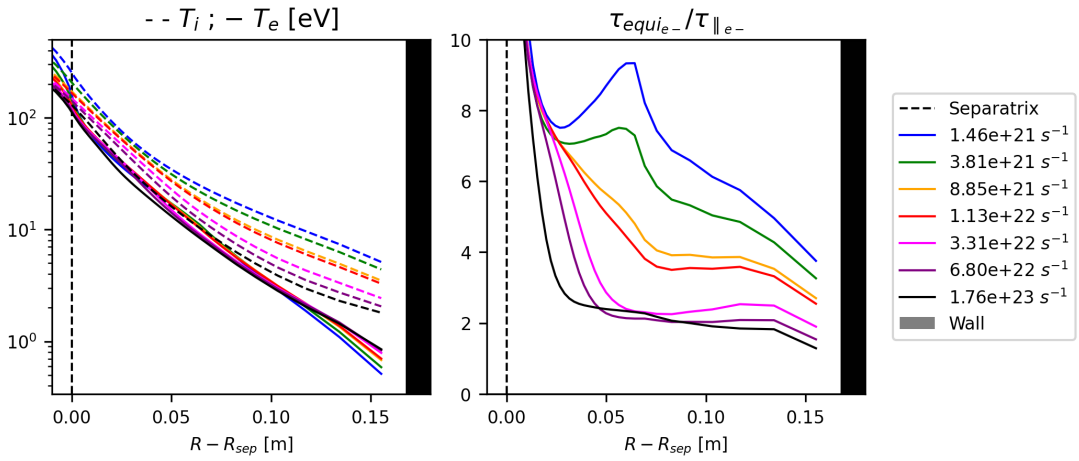

Figure 5.10.: Profiles at the outer midplane. left: Electron (solid lines) and ion temperature (dashed lines), right: ratio of collisional energy equipartition characteristic time to parallel energy loss characteristic time (under the approximation of a constant connection length of 100m). See in the text for definitions.

This actually reduces the T_e decay rate in the SOL with increasing density. Since T_e at the separatrix decreases with density, but the gradient in the SOL decrease at the same time, the radial profiles tend to cross and overlap. One can also note that because of this crossing, which occurs at around 12 cm from the separatrix (left of Figure 5.10) $T_{e,wall}$ increases slightly with density, in contrast with what happens at the separatrix.

In conclusion, T_e values in the SOL and at the first wall are very close, but this results from a coincidence related to the difference in the behavior of the two species (different conductivity and wall heat losses) and the energy coupling between them.

5.3. First wall: heat loads and erosion analysis

5.3.1. Heat loads on the first wall

Let us now investigate plasma conditions and loads at the first wall, starting with the power fluxes. Figure 5.11 shows in a 1D plot, as a function of the curvilinear coordinate along the wall, of the total toroidally symmetric heat flux received by the wall. This flux includes contributions from the plasma, neutral particles, and radiation (both from volume processes and recombination at the wall). Target heat flux densities stay between 1 and 3 MW/m², around 100kW/m² for the reflector plates, and 20 to 30 kW/m² for the rest of the baffles. For the rest of the first wall, heat fluxes stay below 5kW/m² with maximum values reached at the top of the machine, i.e., well within the design limits of the panels (5MW/m² at the inner wall, 3MW/m² at the outer wall, and 2MW/m² at the machine top [83]).

Increasing throughput not only spreads the power load at the target themselves, but remarkably also increases the power received by the rest of the wall (cf. totals below).

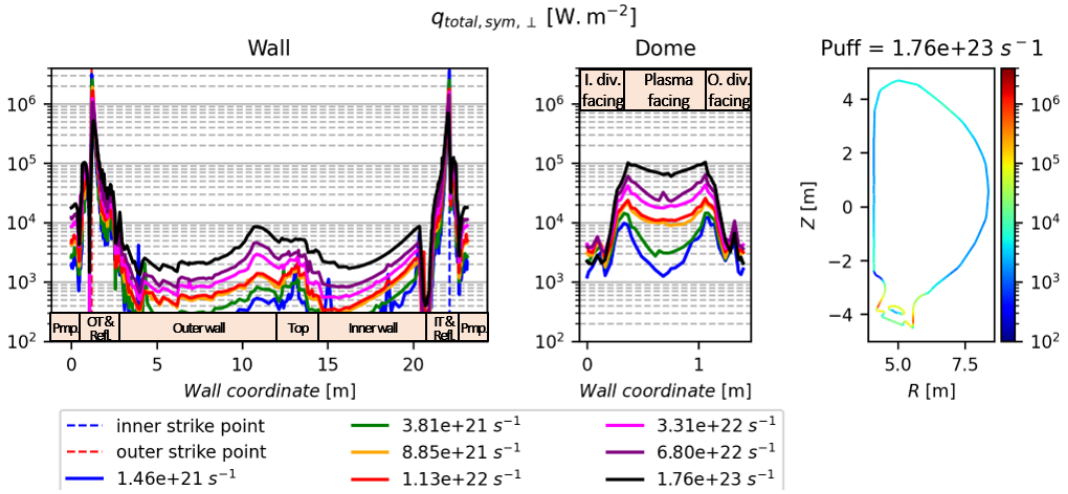

Figure 5.11.: 1D plot of the total perpendicular toroidally symmetric heat flux (including contributions from plasma, neutrals, and radiation) against the wall curvilinear coordinate for the throughput scan. The wall coordinate starts at the bottom of the machine (pump) and evolves counter clockwise, from the outer side to the inner side. Each color represents a case with a specific throughput. Left: profile along the vacuum vessel wall. Middle: profile along the divertor dome. Rightmost plot: the same quantity in 2D for the highest throughput (i.e., the black curve on the previous plots). This heat flux does not include radiation from the core region (not included in the numerical domain), which would add ~10kW/m² (~10MW spread over ~1000m²) on top of the plotted quantity.

Looking at integrated figures (Figure 5.12), a significant portion of the input power arrives at the first wall: from 5% to 28%, increasing with throughput. This deposition is driven by the atoms and radiation, with the radiation contribution increasing with throughput (up to 70% of the power arriving at the first wall, Figure 5.13). The dome receives negligible power in the lower part of the scan, but up to 13% at maximum throughput, driven by radiation and atom wall recombination into molecules.

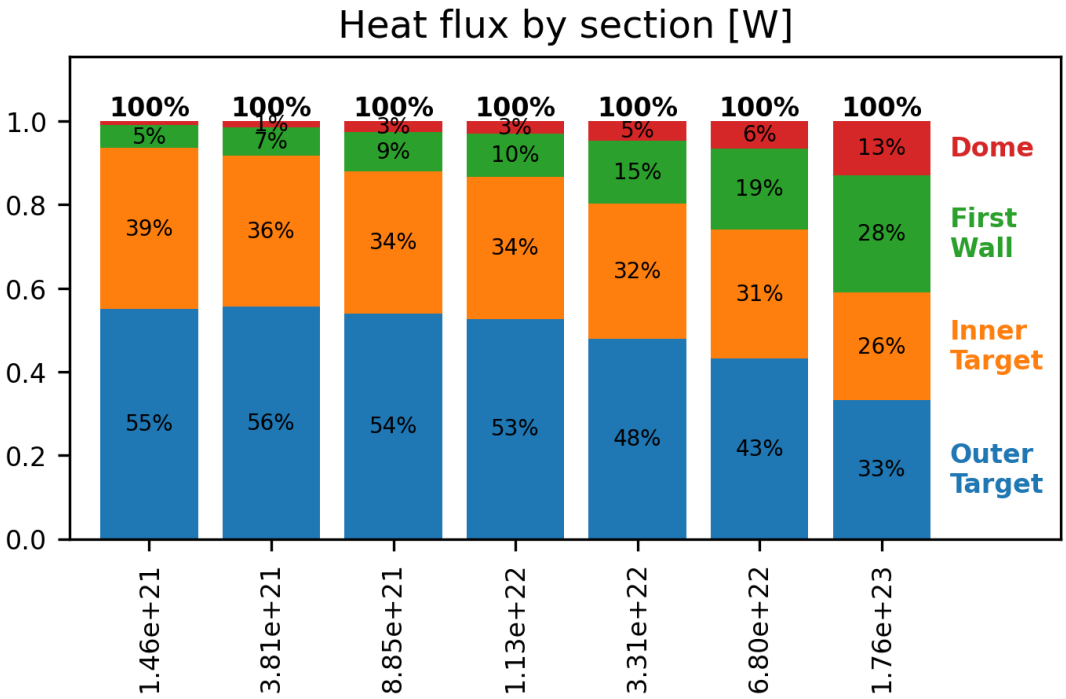

Figure 5.12.: Breakdown of the total (plasma + neutrals + radiation + wall recombination) heat flux received by each section of the machine, as a percentage of the total heat flux arriving on the whole wall. Columns are labelled with the throughput in e^{-}/s

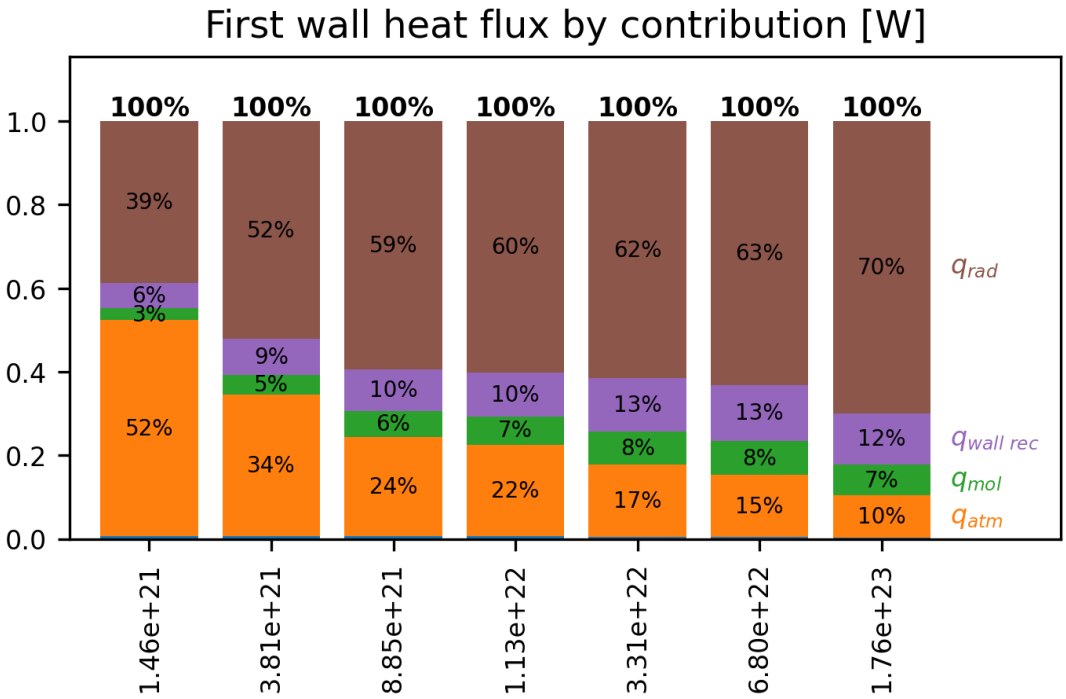

Figure 5.13.: Components of the heat flux (plasma, atoms, molecules, radiation, wall recombination radiation) received by the first wall, as a percentage of the total heat flux arriving on the first wall. Columns are labelled with the throughput in e^-/s

5.3.2. Impact on Beryllium gross erosion estimations

5.3.2.1. The erosion process

One of the goals of carrying the present simulations is to provide the fluxes and plasma backgrounds in the far-SOL and at the first wall with SOLEDGE3X, to be used as input for erosion-specialized codes [43, 55, 84]. Regarding this matter, the simulations in this work, which include a self-consistent plasma solution from the edge up to the wall, are the first of this type.

It is possible, however, to set up EIRENE in SOLEDGE3X so that it computes a beryllium erosion rate from physical sputtering (no chemical sputtering is taken into account) on each of the wall segments, using the Roth-Bohdansky-Eckstein model [22, 37]. It is, of course, less precise than what the specialized codes can do because of the absence of 3D effects and beryllium self-sputtering (the latter can be done with SOLEDGE3X, but was not activated here).

The motivation for using these estimations with SOLEDGE3X is rather to make a sensitivity study. This can be carried out in a relative way from one case to another, and assess how strong variations are. For this exercise, precise numbers in absolute value are not necessary, as the trends are the main focus of the investigation. Of

course, however, the results obtained here should be checked after running the actual cases with the erosion specialized codes (see the outlook section in the conclusion section 7.2).

It is recalled that in the simulations considered here, all surfaces, including the targets, are made of beryllium (see section 3.2 for the rationale of this assumption).

In the case of the plasma system considered here, two kinds of particles can have a high enough energy to induce sputtering: plasma ions, and charge exchange neutrals (CXN).

Plasma ions Plasma ions arriving at the wall undergo an acceleration due to the electrostatic sheath that was formed (see section 1.2.3). This acceleration is of the order or $3Z_i T_e$ (Z_i being the charge number of the ion), which has to be added to the initial energy of the incoming ion. The ion energy can thus quickly go over the sputtering threshold even for mild plasma conditions. Thus, the sputtering rate also depends on the electron temperature, and not only the ion temperature.

Charge exchange neutrals Fast neutral atoms can also reach the threshold energy. In this case, they do not take their origin near the wall, but rather deeper inside the plasma where the ions are much hotter. Atoms produced by charge exchange collisions will have a kinetic energy of order the local ion temperature. In that case, it can potentially reach the sputtering threshold, and erode the wall if its direction is towards the wall and if it does not suffer another collision or reaction on its flight back.

Therefore, in order to compute the erosion rates, specialized codes such as ERO2.0 and WALLDYN use two key inputs (amongst others): first, the plasma conditions at the wall for the ions sputtering, and second, the fluxes and energy of the charge exchange neutrals reaching the wall. These are the two domains of interest that will be included in the investigation in the next section.

5.3.2.2. Fluxes & energies of charge exchange atoms

Incident atom particle fluxes and energy at the first wall Figure 5.14 (left) shows the atom particle fluxes obtained on the first wall, along with their average energy. The atom particle flux increases, as expected with increasing gas injection, especially at the machine top and in the vicinity of the upper outer tiles, where it increases by a factor of 100 across the scan (from 1×10^{19} $s^{-1}.m^{-2}$ to 1×10^{21} $s^{-1}.m^{-2}$).

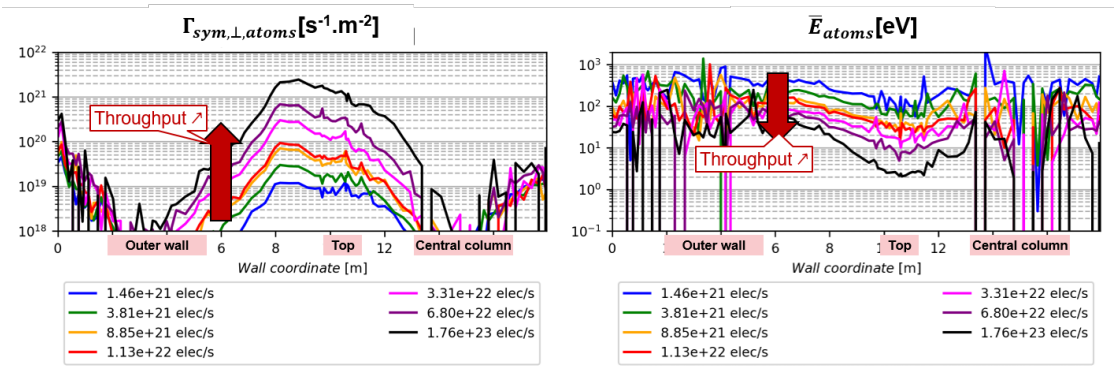

Figure 5.14.: Left: poloidal distribution of the atom perpendicular toroidally symmetric particle flux along the first wall. Right: poloidal distribution of the average energy of incident atoms along the first wall. The curvilinear span across the first wall, starting from above the outer baffle, and ending above the inner baffle. In both plots, each curve corresponds to a different value of throughput in the scan, according to the legend.

The average energy decreases drastically however, as shown on the right plot of Figure 5.14. It changes by a factor of 10 to 100 (depending on the location along the wall) from 200-500 eV down to 20-30 eV and even as low as 3 eV at the machine top (where the particle flux is the largest).

Their energy can actually be related to the birth location of these particles, i.e., where this atom has undergone the last charge transfer collision: most probably where the ion temperature has the value of the energy of the atom at the wall. The observed range of energies indicates that these atoms come from around and even inside the separatrix. For example, the ion temperature at the separatrix at the outer midplane is ~230eV for the most attached case Figure 5.1, atoms on the outer wall are found at around ~400-500 eV. The energy of the atoms seen by the wall does not directly represent the temperature of the ions at the location of the charge exchanges, because collisions involving ions in the distribution function's high energy tail will produce particles that will tend to cross the SOL more easily to the wall.

For the maximum throughput case, however, the atoms seen by the wall (20eV) are below the separatrix ion temperature in that case (~125 eV), indicating that the collisions occur on average further in the SOL.

Such interpretation can be checked more quantitatively through the reaction number count analysis profile at the outer midplane Figure 5.15, where we indeed see that there is a shift of the peaking of the atom HCX reaction count from around and inside the separatrix and outside. In addition to this, the reaction rates also largely increase, and the peak widens, which could indicate that the energy distribution of atoms also spreads.

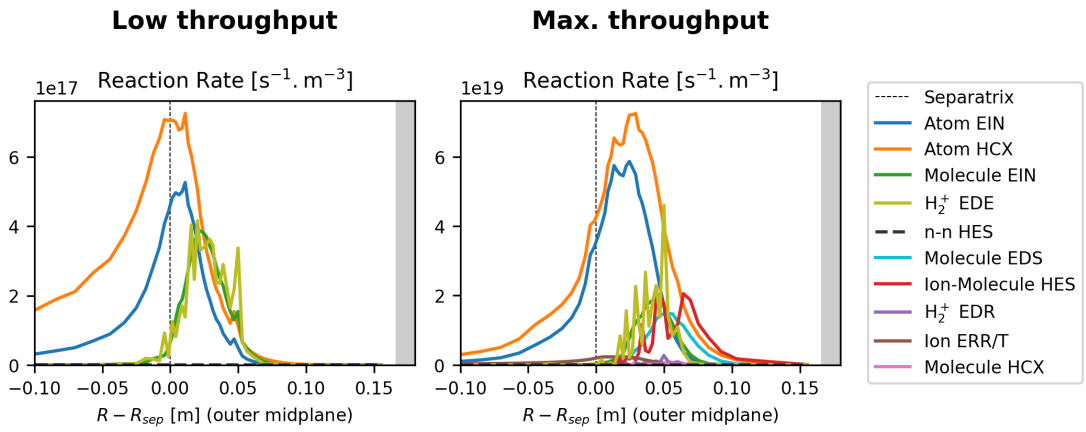

Figure 5.15.: Volume reaction counts profiles at the outer midplane, for a low throughput case (left) and high throughput case (right).

One can attempt to explain this shift by invoking this reaction's rate coefficient $\langle \sigma v^{\text{Atom HCX}} \rangle$ behavior. The inverse mean free path of the atom reads $n_i \langle \sigma v^{\text{Atom HCX}} \rangle / v_a$, and the rate coefficient $\langle \sigma v^{\text{Atom HCX}} \rangle$ is actually only weakly dependant on T_i (see HYDHEL database, reaction H.3 3.1.8), especially at high T_i. Therefore it is predominantly the ion density in the SOL which drives the penetration and origin of these atoms (along with v_a). Furthermore, since the throughput largely increases the density in the SOL (factors of 3 to 10 between the scan's extremes), it is likely that this effect pushes the reaction location outward.

Also, at maximum throughput, other reactions involving collisions and dissociations of molecules begin to take importance, indicating increased neutral density even in the main chamber and not only in the divertor.

Let us note that the discussion above concerns only the average energy. A more detailed investigation would include the actual energy distribution of these incoming atoms, as the averaging could hide potentially dangerous high-energy populations. In the case of erosion, the presence of even a minority of high-energy particles can significantly change the erosion rates. This effect is however included in the gross erosion rates computed in the following section.

Energy distribution of incident atoms The energy distribution of the atoms incident to two sections of the first wall (in columns, see Figure 6.22 for a 2D view) are shown in Figure 5.16, for the three cases representative of the throughput scan (in rows: attached, rollover, and partially detached). It is readily seen that two different populations exist:

1. A 3-4 eV "cold" population which consists of two almost mono-energetic peaks at 2.7 eV and 4.0 eV. These populations come from the dissociation of molecules and H_2^+, which creates atoms at fixed Franck-Condon energies.

2. A hot "CX" population, ranging from tens of eVs to hundreds of eV, and even up to 2 keV in some cases. These are the results of charge exchange reactions in the much hotter regions of the plasma, often behind the separatrix.

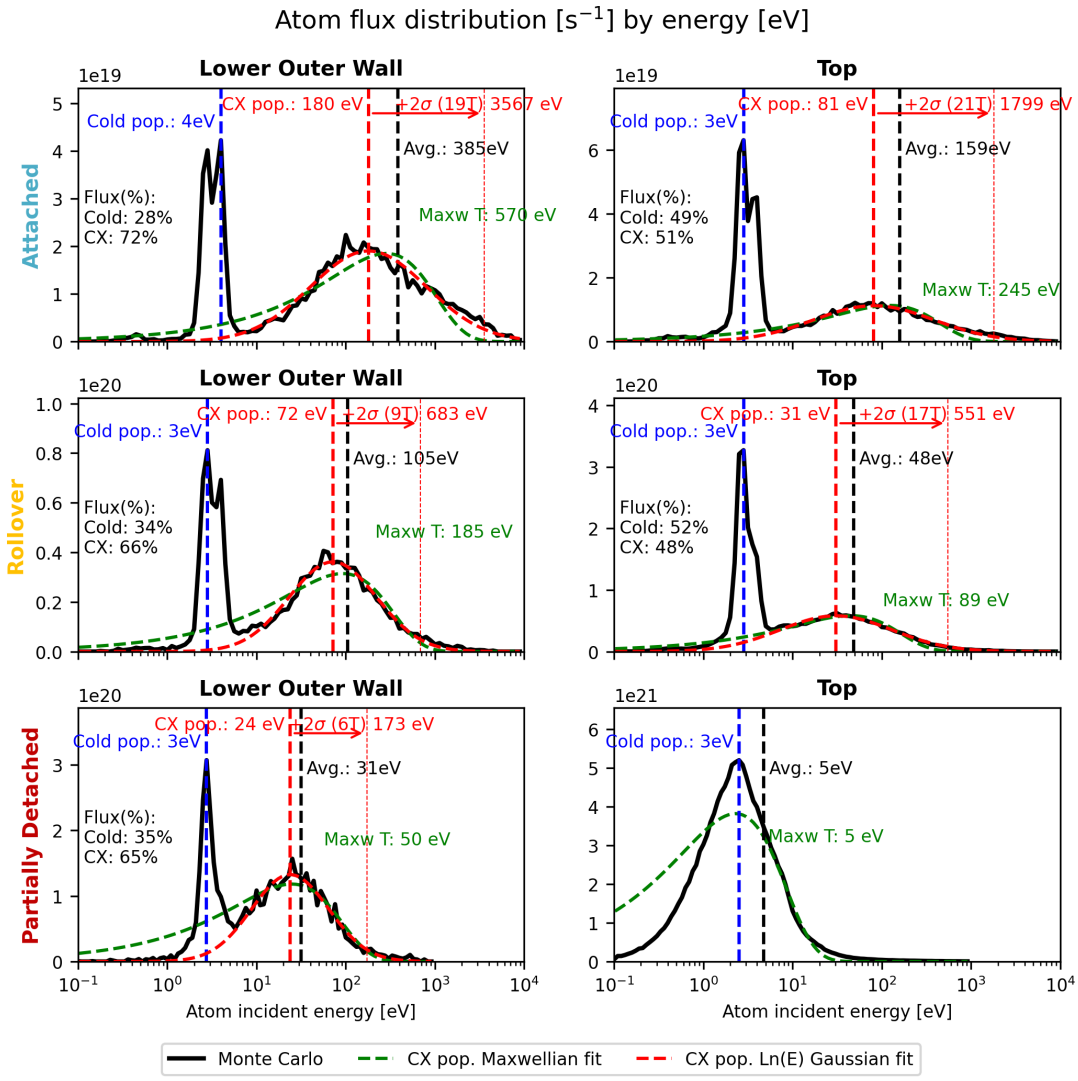

Figure 5.16.: Energy distribution of atoms incident on two of the first wall sections (see Figure 6.22 for a 2D view), for three cases (in rows) representing the attached, rollover, and partial detachment state. The black vertical line is the total average energy. Two fits are carried out: from a Maxwellian distribution ($f_E(E) = 2\sqrt{\frac{E}{\pi}}\left(\frac{1}{T}\right)^{3/2}\exp\left(-\frac{E}{T}\right)$ with T and E in eV) in green with moderate success, and a more successful fit with a Gaussian law in logarithmic space in red. The vertical red dashed line represents the center of this fit, and the red arrow shows the energy upper bound required to capture 95% of the distribution (i.e. 2σ).

Further, the flux weighted average energies (vertical black dashed line and value), show that the estimates in the previous 1D graph Figure 5.14 were quite representative of the energy of charge exchange population, because of its much higher energy.

The CX atoms are almost always the majority population (between 50 and 75 % of the incident particle flux, except for the machine top at maximum throughput).

Notably, the obtained CX distribution shape is not exactly a Maxwellian distribution (in dashed green in the graphs). Such a distribution could have been expected because ions are assumed to follow a Maxwellian distribution in the fluid plasma solver, and are sampled as such in the Monte-Carlo procedure. The obtained CX distribution is missing the lower-end of the Maxwellian distribution, and is closer to a Gaussian law in logarithmic space (red dashed lines). This absence can be interpreted from to the additional collisions in the SOL which are more probable for lower energy atoms, than for high energy ones. Further, the CX location vary with the penetration depth of the atoms so the sampling of CX neutrals actually stems from a superposition of Maxwellians at various temperatures. From the Gaussian fit, the high bound of the energy to capture 95% (i.e. within 2σ) of the flux is evaluated (red arrows) to assess the most energetic atoms in the distribution. Very high values above 1 keV are found for the attached case, however the fluxes are low.

Apart from some exceptions at maximum throughput, a general trend seems to appear: the throughput does not seem to change much the shape of the distributions (i.e., the ratio of CX to cold population, and the width of the CX distribution), whereas it does shift the center of the CX distribution toward lower energies.

Conclusion In brief, in terms of total expectations towards erosion, increasing throughput produces two opposite effects: the atom particle flux at the wall increases, but the average energy of these atoms decreases, therefore no immediate conclusion can be drawn at this point. The actual observed effect after computation will be discussed in the following section section 5.3.2.4.

5.3.2.3. Plasma conditions at the wall

Energies The focus is now turned to the plasma conditions at the first wall Figure 5.17. The throughput increase performed in the scan leads to a large ion temperature drop, by about a factor of 4 for the majority of the wall, to a factor 20 at the top. Maximum values drop from ~20 to ~7 eV. Note that the ion temperature here is the ion temperature at the sheath entrance. For the ion impacting energy after the sheath, one should add $3T_e$ to the T_i displayed here.

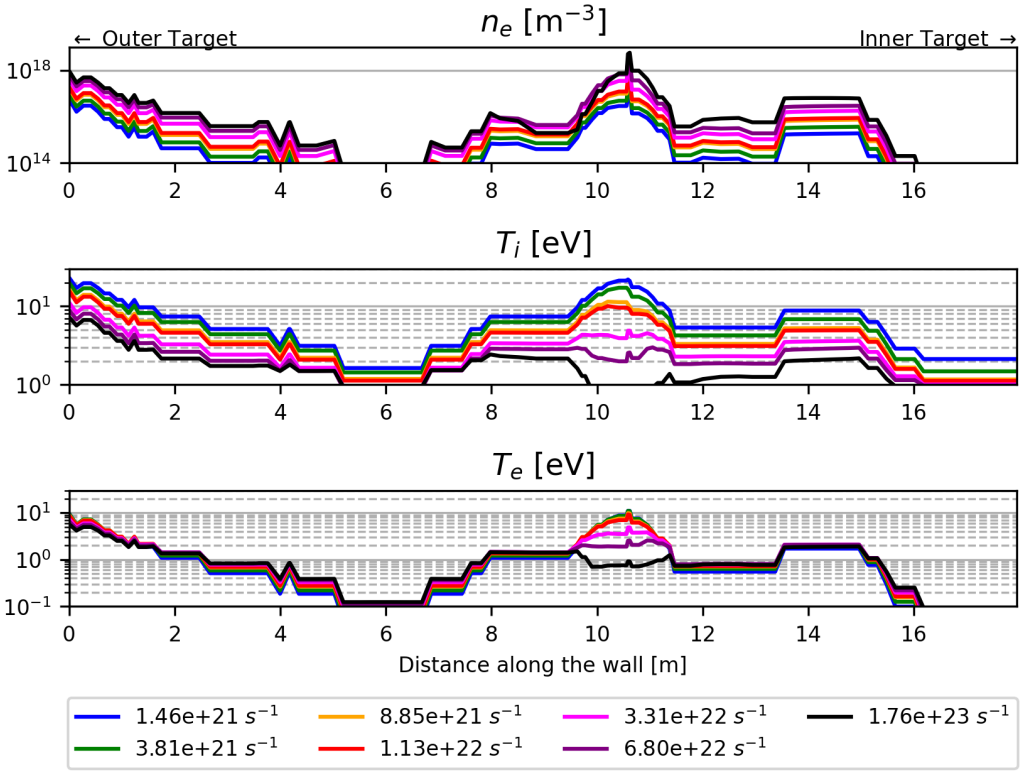

Figure 5.17.: Impact of throughput on the first wall plasma density, ion and electron temperatures (ion temperature at the sheath entrance). The curvilinear coordinate is oriented counterclockwise in 2D: it starts on the left above the outer baffle, and finishes above the inner baffle.

In contrast to T_i, the throughput leaves T_e at the wall almost unchanged. This effect can be explained by the very small sensitivity of upstream outer midplane profiles of T_e in the SOL and far-SOL, see section 5.2.3. The field lines arriving at the first wall (i.e. far from the strike points field lines) are all in the sheath-limited regime because of their low density, which comes with almost no variations of the temperature along field lines. Therefore this insensitivity of the upstream profile is simply cascaded to the first wall. The only place where this is not the case is at the machine top, where a decrease in T_e is observed from 10 to 1 eV. However the assumption of no ionization (and so no electron energy loss) possibly breaks down at this location due the stronger plasma-wall interaction there as well as to the proximity of the gas injection.

Particle fluxes Considering now particle fluxes Figure 5.18, ion fluxes are almost non-existent except at the machine top and the bottom outer panel above the outer baffle. At the top, while the recycling ion particle flux density is still low ($\sim 1 \times 10^{20}$

$s^{-1}.m^{-2}$), the gas injection rate at the end of the scan is of the order of 1×10^{23} s^{-1} leading to significant plasma-neutral interactions. Also, the plasma density there is quite low ($\sim 1 \times 10^{18}$ m^{-3} at the secondary separatrix) therefore even if plasma-neutral interactions remain much lower in amplitude than in the divertor, they can still affect the plasma quantities. Neutral particles, and especially atom fluxes, constitute the majority of the flux. They increase drastically with throughput, gaining up two orders of magnitude from 1×10^{19} to 1×10^{21} $s^{-1}.m^{-2}$ at the top, which can be expected with the increase of density.

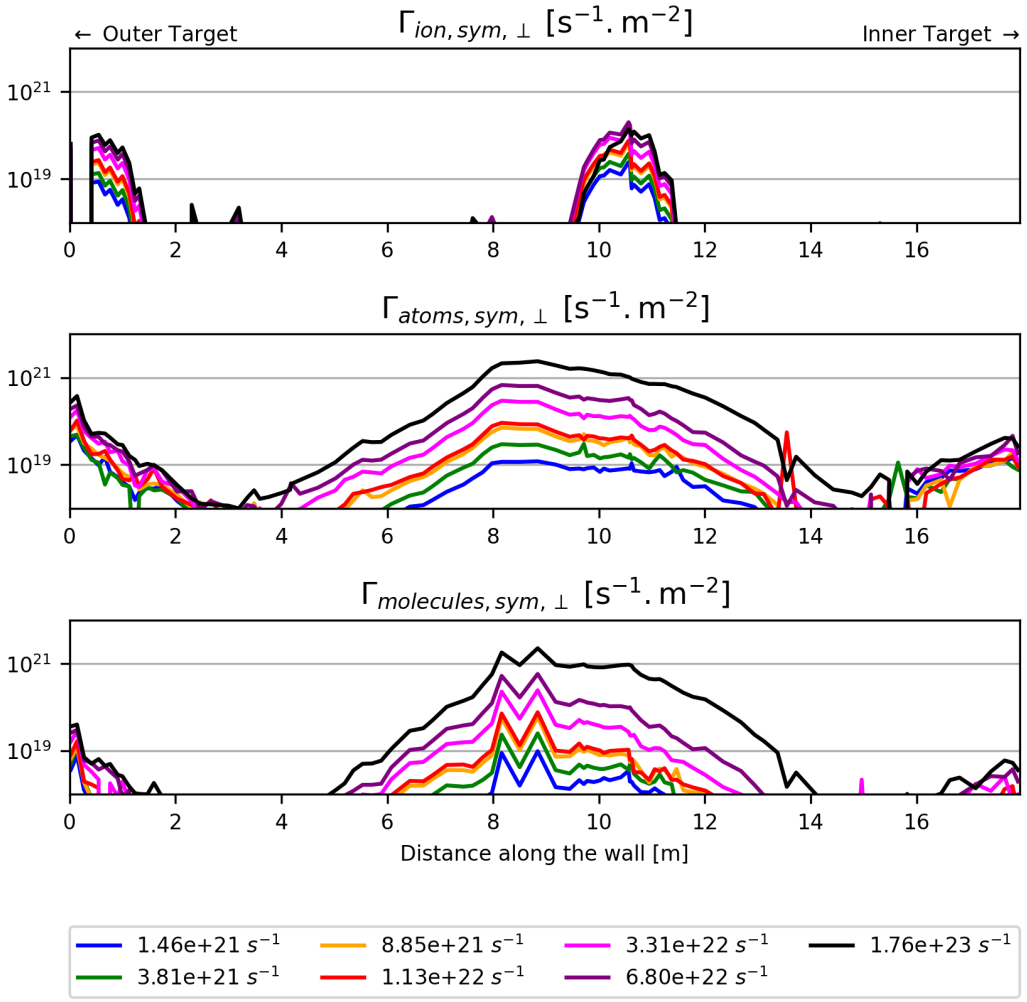

Figure 5.18.: Impact of throughput on incident particle flux decomposition along the first wall between ions, atoms, and molecules. The curvilinear coordinate is oriented counter clockwise in 2D: it starts on the left above the outer baffle, and finishes above the inner baffle.

Overall, when increasing throughput, plasma conditions evolve such that they will have two opposite effects: on the one hand, the ion flux increases, which would tend to increase sputtering linearly; on the other hand, the ion temperature goes down, which should contribute to a decrease of the sputtering. The electron energy, however, except at the top of the machine, stays roughly constant throughout the scan. The latter, combined with the rise of the particle flux, should contribute to an increase in the erosion rate. However, the amplitude of the fluxes and the energy of plasma particles are small compared with those of atoms, and one can expect their contribution to the erosion process to remain minor compared to that of neutral particles.

5.3.2.4. Gross erosion estimations

This section now deals with the gross erosion rate, as computed by EIRENE in the considered runs. It can be viewed as a post-treatment, as no feedback on the plasma is included, i.e. the sputtered particles of Beryllium are not tracked, no Beryllium plasma or neutral gas is included, and associated radiative losses have not been accounted for in the plasma equilibrium.

As a caveat, and as mentioned in section 5.3.2.1 these rates should be taken as rough estimations (no self-sputtering, H+ & H only, no 3D effects), for trend analyses.

Figure 5.19 summarises the obtained results for these rates. The total gross sputtering rate integrated over the FW increases with throughput by a factor of 6 between the scan extremes, ~ 90% of which comes from charge transfer atoms. This seems coherent with the previous section, where it was seen that few ions arrive at the first wall. It is also remarkable that the ion portion of the sputtering is almost independent of throughput.

Figure 5.19 also shows the areas where sputtering is most important. For the case with the highest obtained gross erosion rate (highest throughput), it is the puff location at the top, and the tile above the outer baffle. It can be mentioned here that in reality, the puff location consists of a port and not a flat tile, therefore 3D effects may be important there and are not captured here. Also, the particle injection via the puff is assumed axisymmetric here, and not localized toroidally.

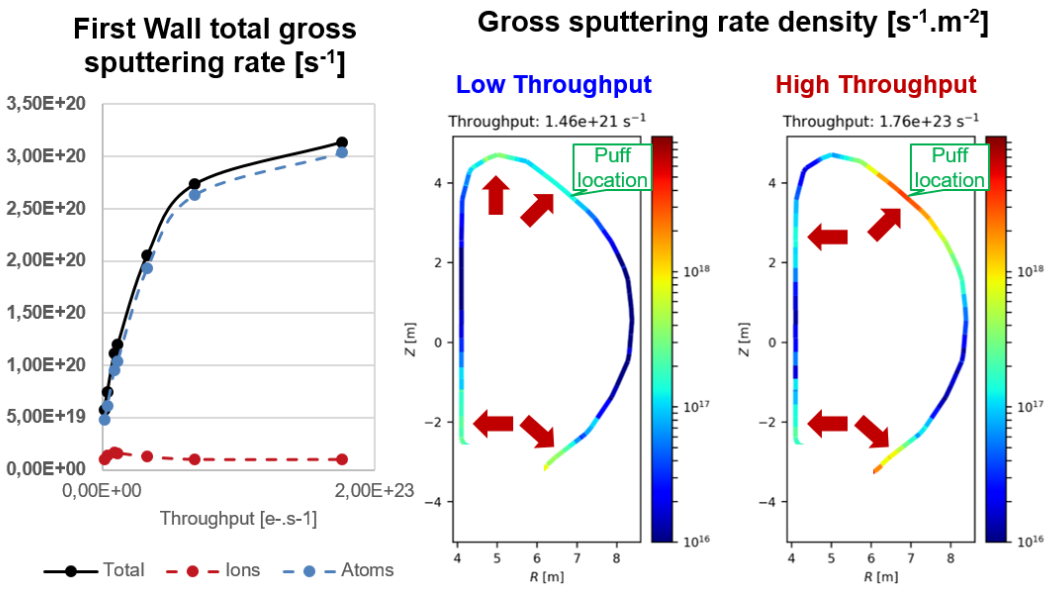

Figure 5.19.: Impact of throughput on the gross erosion rate computed with EIRENE. Left: Total integrated rate across the first wall, with the ion contribution in red, and atoms contribution in blue. Right: 2D representation of gross erosion rate densities along the first wall.

6. Impact of the formation of density shoulders

Contents

6.1. Introduction to enhanced far-SOL transport study

This section considers the impact of increasing the anomalous perpendicular diffusion coefficients in the far-SOL. This exercise follows the many reports made on the formation of density shoulders in the SOL since the 1990's [85], and under high divertor density regimes [86, 87]. In such conditions, plasma is strongly transported towards the main wall in the far-SOL, increasing plasma-wall interactions there. Although the exact conditions in which SOL density shoulders appear and their quantitative impact on plasma transport properties remain open questions for ITER, the current understanding of the conditions in which they appear suggests that they might be present in ITER high-density regimes. This calls for a sensitivity study of first wall conditions and fluxes as a function of far SOL transverse transport coefficients, leveraging again the

advantage of the ability to self-consistently simulate the plasma (modeling turbulent transport using a diffusive approach) at this location with SOLEDGE3X.

6.2. Modelling density shoulders

The understanding of the formation and characteristics of density shoulders is the topic of active research. The flattening of the density profile is related to convective LFS filamentary transport, and several proposed mechanisms are invoked in recent literature [86, 87]. Those works study the correlations between the amplitude of the density shoulders and other parameters: divertor collisionality, recycling in the far-SOL, divertor regime, radial electric fields, particle source in the main chamber, plasma current, safety factor, and midplane neutral pressure. Experimentally, the appearance of density shoulders is correlated with the transition to high-density regimes [86, 87]. However, all across the throughput scan in our simulations with uniform transport coefficients, which goes after the rollover into partial detachment, no sign of shoulder is observed (see the upstream density profiles in Figure 5.2. This implies two possibilities: either a density shoulder would not form in these situations (this is not known), or the simulation lacks a necessary ingredient to form such shoulders. Especially, the latter possibility means that the plasma neutral (recycling) description in our simulations is either incomplete in that regard, or that the recycling mechanism is insufficient to form such shoulders. Answering these questions is outside the scope of this work.

A supplementary caveat is to be noted here: the choice was made here to model the density shoulders by increasing also the perpendicular heat transport coefficients, which translates to a shoulder also on the temperature profiles. This may not be a standard assumption as the presence of density shoulders in experiments is not necessarily associated with a temperature shoulder. Applying a temperature shoulder was rather done with a sensitivity study in mind, to model "pessimistic" cases.

Hereafter, the enhanced transport giving rise to density shoulders is modeled by increasing the perpendicular diffusivity coefficients in the far-SOL from the base value of $D_\perp$=0.3 m²/s.

Two parameters are varied:

- the value in the far-SOL, either $D_\perp^{\text{far-SOL}} = 2.0\text{m}^2/\text{s}$ or $10.0\text{m}^2/\text{s}$
- the distance from the separatrix at the outer midplane where this increase starts: either 1cm or 3cm (translating respectively into $1.8\lambda_q$ vs. $5.4\lambda_q$, with of a λ_q of 5.5 mm for the reference case).

The increase from the base value to the far-SOL value is linear over 1cm in all cases. These midplane profiles are then propagated along the flux surfaces in all the numerical domain, including in the divertor below the X-point. Other diffusion coefficients (χ_e, χ_i, $\nu_\perp$) are scaled proportionally to the $D_\perp$ increase from its base value of $0.3\text{m}^2/\text{s}$, as shown in Figure 6.1. The rationale for choosing such values comes from density

profiles observed in machines such as JET, where the density decay length at the outer midplane λ_n increases by a factor 3 to 4 [87], corresponding to factors of 9 and 16 on $D_\perp$. Similar factors for the cases considered here would give 3 to 5m²/s, however to include additional uncertainties, this range is extended to 2 to 10m²/s. The simulations here could be therefore understood as "best" and "worst" case in terms of diffusion in case of shoulder formation.

Of course, these simulations still stick to a diffusive model in the shoulder even though this may not be a faithful description of the perpendicular transport there, which may be more ballistic ($\Gamma_\perp \sim n\overline{v_{\text{eff},\perp}}$). However, the choice of closure for transverse fluxes matters little, as long as the chosen transport coefficients induce the desired gradient lengths.

In total, 4 cases are considered and compared to the reference case #103027 with constant coefficients ($D_\perp$=0.3m²/s) at a low throughput of 8.85×10^{21} $e^-.s^{-1}$. In this section, the cases are labeled with codes corresponding to the diffusion profiles' features, and are described in Table 6.1.

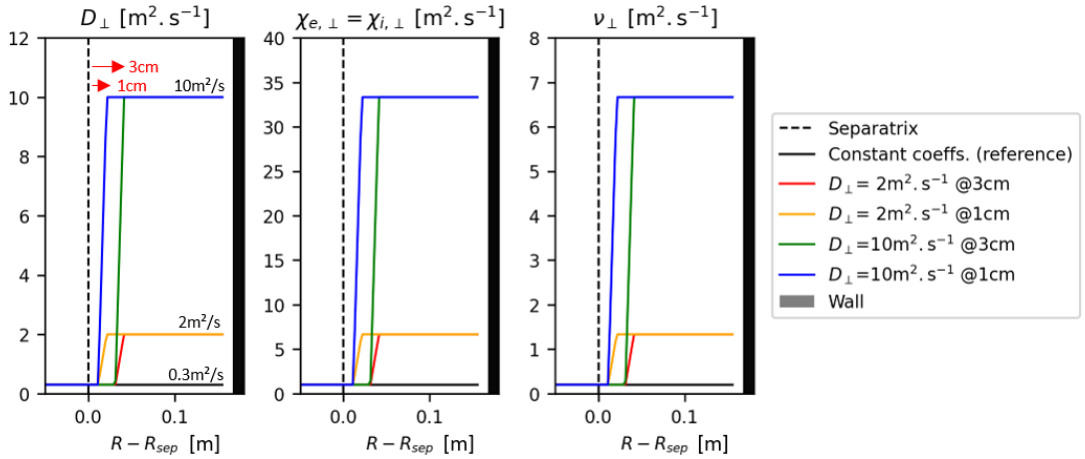

Figure 6.1.: Outer midplane radial profile of far-SOL perpendicular diffusivity coefficients for the far-SOL diffusivity scan: coefficient are increased to higher values (from 0.3m²/s to either 2.0m²/s or 10.0m²/s) from 1 or 3 cm after the separatrix at the outer midplane. These coefficient radial profiles are then propagated along flux lines.

Table 6.1.: Cases labels and corresponding features of the perpendicular diffusion coefficient profiles

Case label	**$R - R_{sep}$ Ramp Start (RS)**	$D_{\perp}^{far-SOL}$
Ref.	n.a.	flat profile (0.3 m²/s)
D02.0_RS0.03	3cm	2.0 m²/s
D02.0_RS0.01	1cm	2.0 m²/s
D10.0_RS0.03	3cm	10.0 m²/s
D10.0_RS0.01	1cm	10.0 m²/s

6.3. Upstream profiles

6.3.1. Plasma parameters

Figure 6.2 shows profiles obtained at the outer midplane, where the temperature and density profiles flatten as expected in the far-SOL.

This changes dramatically the values of density and temperatures at the outer wall, by a factor 1000 for the density, from 1×10^{15} m^{-3} to 1×10^{18} m^{-3}, and a factor of 10 for temperatures (1 to 10 eV for T_e and 3 to 30 eV for T_i).

Inside the separatrix, the stronger the far-SOL transport (closer shoulder, higher values of coefficients), the more the density rises, from 1.6×10^{19} m^{-3} to 2.4×10^{19} m^{-3} (+50%), and the lower temperatures get, from 1100 to 800 eV (-27%) for the electron and temperature. A potential contributor to this is the main wall recycling, which is discussed in section section 6.6.

All quantities are left almost unchanged at the separatrix (Figure 6.3).

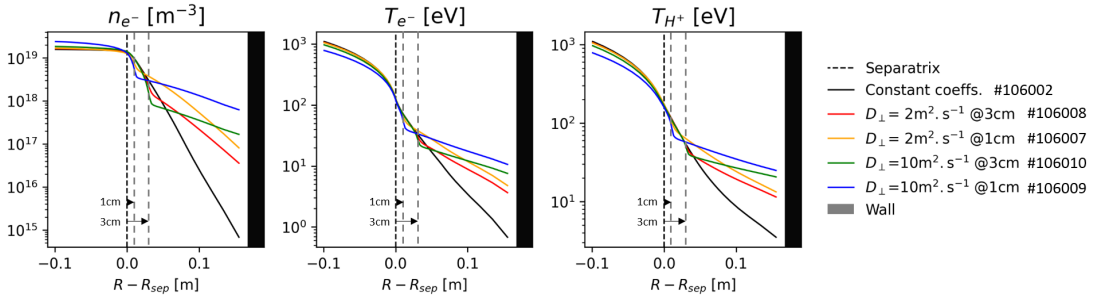

Figure 6.2.: Impact of increasing far-SOL diffusion coefficients on upstream conditions at the outer midplane.

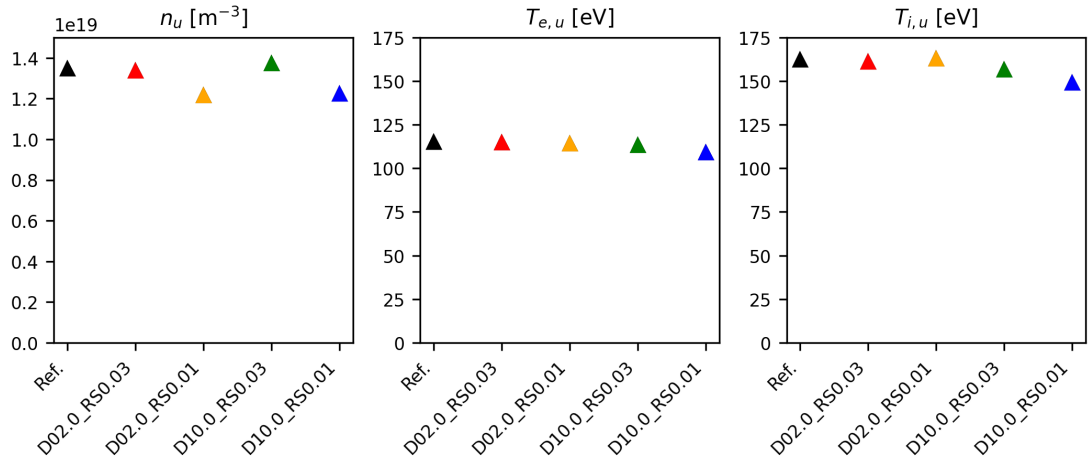

Figure 6.3.: Density, electron and ion temperatures at the separatrix at the outer midplane for the enhanced far-SOL transport scan. See Table 6.1 for the meaning of cases labels

6.3.2. T_i/T_e ratio

In this section the focus is turned to the ratio of ion to electron temperature in the SOL, and especially in the far-SOL at the wall, as it is a key assumption for the erosion-specialised codes. The following paragraphs can be used to compare the assumptions which were used in erosion simulations versus what is obtained here from the up-to-the-wall plasma backgrounds.

Figure 6.4 shows the outer midplane profile for this quantity, for 3 cases to try to cover extremes for the parameters explored in this study. A common assumption is to take $T_i/T_e = 2$ by default in the SOL. The plots show that for models with uniform diffusion coefficients (high and low throughput cases on the graph), this assumption is close to the simulation in the near SOL (within 5 cm of the separatrix) which is around a ratio of 1.5. This quantity decreases with throughput, between 1.6 and 1.2.

In the far-SOL however, the ratio largely increases going towards the wall, and the value at the first wall is actually between 2 for maximum throughput and 5 at the lowest throughput (the first wall is at 15 cm of the separatrix). This behavior comes from the difference in the sheath heat transfer coefficients between the electrons and the ions ($\gamma_e = 4.5$, $\gamma_i = 2.5$), which makes the electrons lose more energy at the wall than the ions under the same conditions. Because of this, the difference between the electrons and ion temperature will tend to increase radially, reaching a maximum at the wall.

In terms of shoulder formation, not much changes in the near SOL, however in the far-SOL and at the first wall, the ratio tends to go towards the values observed for large throughput, indicating that this ratio decreases with density. This comes with the increase of the collisional energy exchange between the two species, which tends to bring the ratio towards unity.

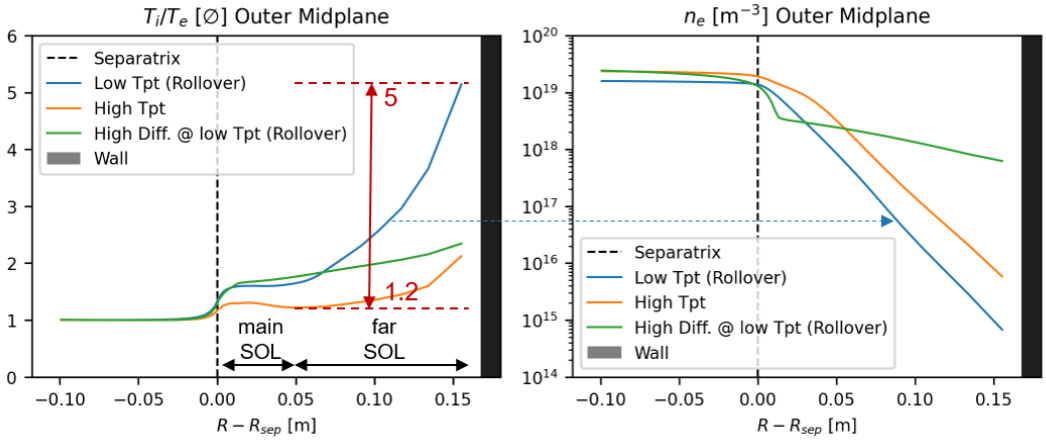

Figure 6.4.: Left: T_i/T_e ratios at the outer midplane for three cases: low throughput (which corresponds to rollover at 8.85×10^{21} e^-/s), high throughput at 1.76×10^{23} e^-/s, and high diffusivity with strongly enhanced far-SOL transport (shoulder @1cm, $D_\perp$=10m²/s in far-SOL). Right side: the associated plasma density profiles.

In conclusion estimates for the T_i/T_e ratio could be provided as follows, depending of a macro "density" indicator of the SOL with respect of the machines' window:

1. In the near SOL: 1.6 to 1.2, decreasing with density
2. In the far-SOL: 2 to 5, decreasing with density

6.4. Impact on the divertor

Figure 6.5 presents the profiles at the targets of plasma conditions (density and temperatures), and total heat flux density. It shows that quantities at the targets are most sensitive to the shoulder start location. This is to be expected, given that target conditions essentially depend on the power outflux from the core and the local target recycling, none of which directly depend on what occurs radially further out in the SOL after a few characteristic SOL-widths. In this case, the impact can only be indirect and of weaker amplitude, through increased interaction with neutrals from the far-SOL, either from downstream along the targets or from the first wall, coming back into the main SOL. In the case of a shoulder close to the separatrix, however, it can be noted that the heat transport Figure 6.6 seems more susceptible to the variations in the transport coefficients than the particle transport Figure 6.7, as the target profiles show lower temperatures for close shoulders (red and yellow), but retain the same values for the density. For shoulders positioned farther at 3 cm (green and red), an opposite but weaker trend appears when transport is enhanced farther into the SOL starting from 3cm (5-20% increase). A reason for this could be an interaction with more energetic neutrals at the first wall, although this would require further analysis.

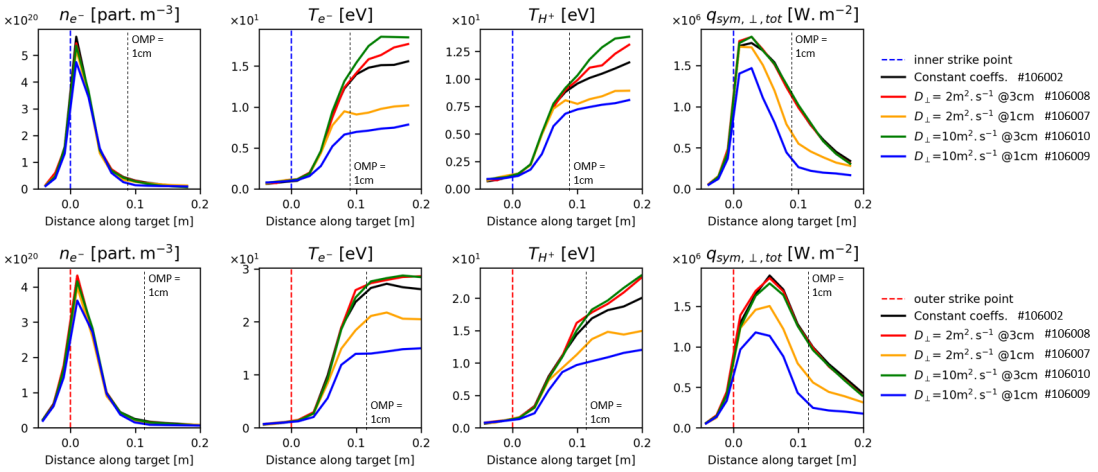

Figure 6.5.: Impact of increasing far-SOL diffusion coefficients on the inner (upper row) and outer (lower row) target electron density and temperature, ion temperature, and total perpendicular heat flux. Same color scheme as in Figure 6.1.

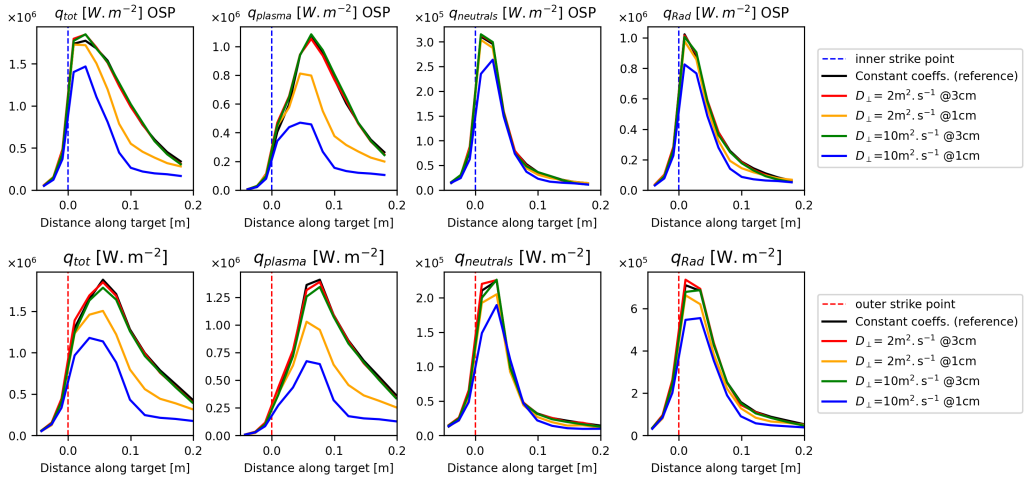

Figure 6.6.: Impact of increasing far-SOL diffusion coefficients on the inner (top row) and outer (bottom row) target heat fluxes, total, and by components: plasma, neutrals, and radiation (incl. wall recombination)

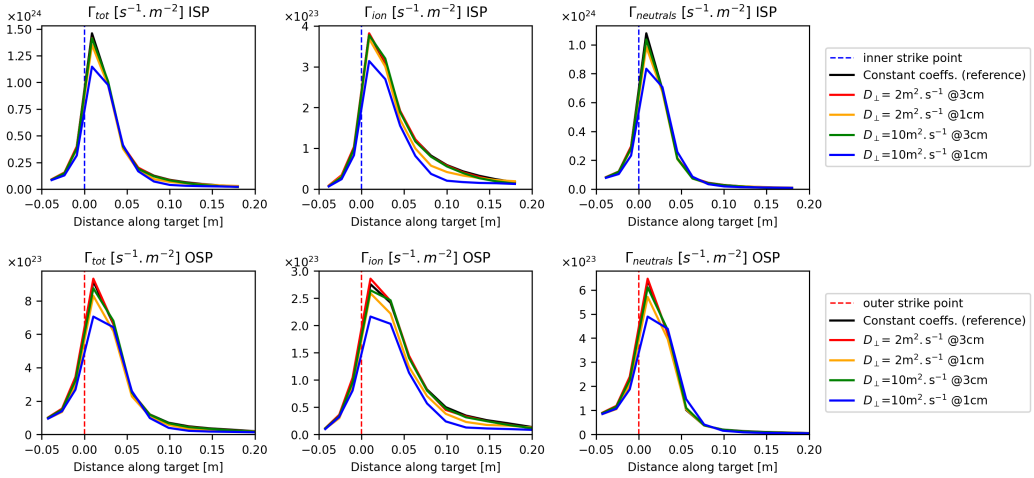

Figure 6.7.: Impact of increasing far-SOL diffusion coefficients on the inner (top row) and outer (bottom row) target particle fluxes, total, ion and neutrals (atoms + molecules) components.

6.4.1. Impact on the plasma-neutral reactions structure

The reduction of the target heat flux and temperature for the cases with the shoulder starting 1cm away from the separatrix raises the question of a change in the divertor density regime with respect to the reference case.

First, the upstream density and the particle flux at the target do not decrease significantly, so the quantification of detachment through this metric does not seem to be sensitive to the enhanced far-SOL transport. Only the target heat flux is reduced. This indicates that the degree of detachment, as defined through the relation between the upstream density and the target particle flux in [17], has not changed.

Then, assessing the structure of the plasma-neutral interaction processes in the same way as was done in the throughput scan section section 4.3, Figure 6.8 shows the reaction contributions to the particle and ion energy sources along the first field line next to the separatrix at the outer target. The overall shapes of the curves and relative amplitude are conserved, and the same processes appear. Therefore, little difference is found in the structure of the reactions. The amplitudes of the reaction contributions are simply scaled down for the case with increased diffusivity. A possible reason for this is the simultaneous decrease of both the parallel particle and energy flux densities upstream, due to the increased perpendicular transport.

In conclusion, the presence of shoulders in the far-SOL does not seem to change the divertor regime.

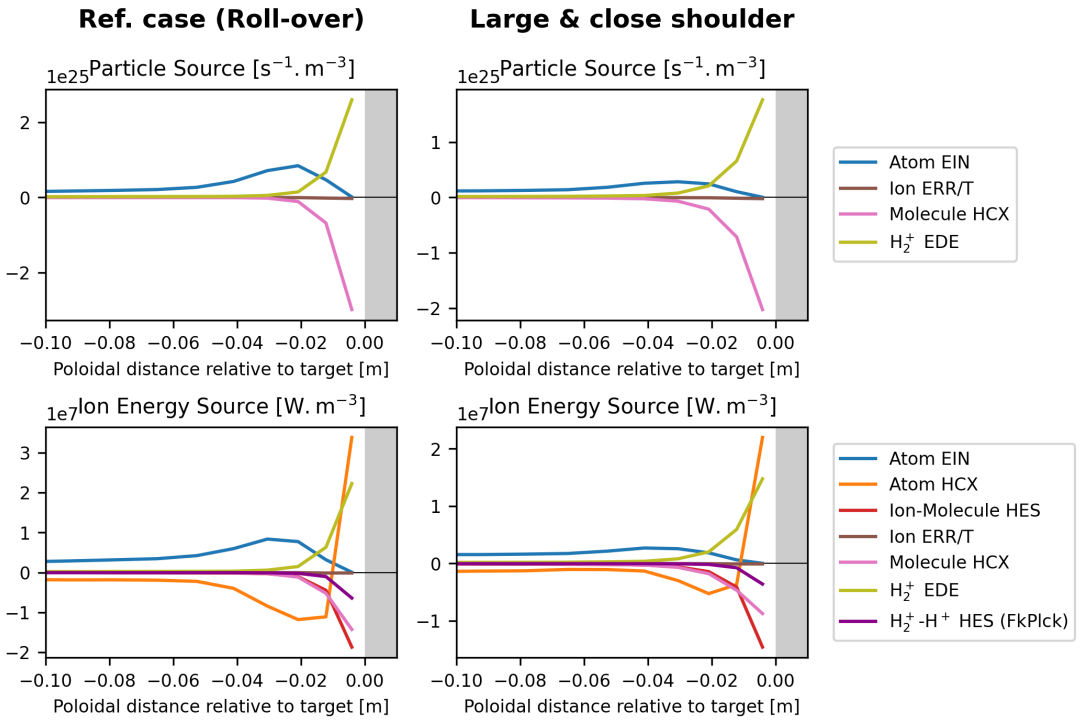

Figure 6.8.: Plasma-neutral reactions contributions to the particle source (top row) and ion energy source (bottom row) for the reference case (roll-over) and the most diffusive one (shoulder at 1cm of the separatrix, $D_\perp$=10m²/s in the far-SOL)

6.5. Results on the First Wall

6.5.1. Fluxes and conditions at the First Wall

In contrast to the divertor, it is the highest values of the diffusion coefficient in the far-SOL that have the largest impact on quantities on the first wall, rather than the shoulder start location.

Plasma temperatures This is especially visible on the temperatures in Figure 6.9, where values at a fixed far-SOL value (2 or 10m²/s) are quite close to each other even with different shoulder locations (1cm and 3cm translating into $1.8\lambda_q$ vs. $5.4\lambda_q$). Indeed, we observe that, for the upstream midplane profiles in Figure 6.2, increasing the shoulder start location translates as a downward vertical shift, while the value of the far-SOL coefficients controls the slope of the profiles. When the first wall is far enough away from where the profile breaks, the difference induced by the shoulder location becomes small compared with the cumulative effect of the slope change.

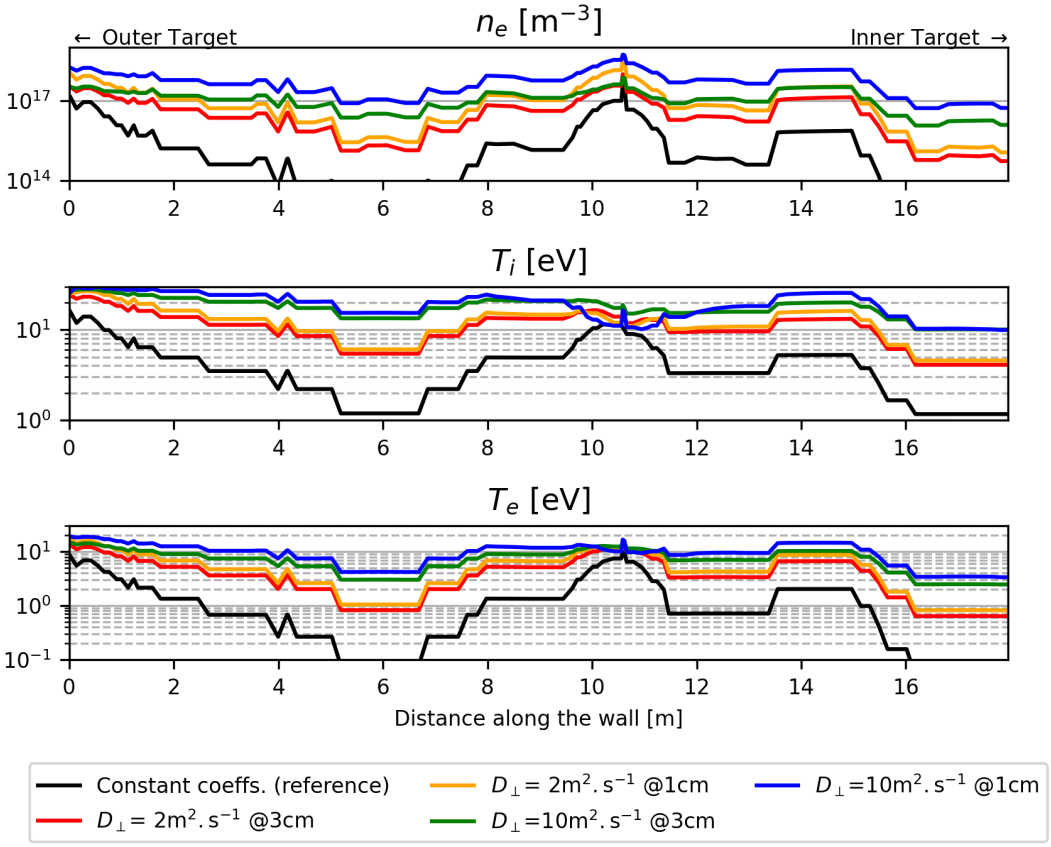

Figure 6.9.: Impact of enhanced far-SOL transport on plasma density, ion and electron temperatures, along the first wall coordinate. The curvilinear coordinate is oriented counterclockwise in 2D: it starts on the left above the outer baffle, and finishes above the inner baffle. Same color scheme as in Figure 6.2.

Quantitatively, enhancing the far-SOL transport has a large impact on temperatures. T_i increases to 30 eV and T_e to 20 eV almost uniformly across the whole wall contour, while in the reference case, only local peaks were observed (at 20 eV and 10 eV for T_i and T_e respectively). The highest temperatures in the cases with the highest far SOL diffusion are found on the bottom part of the outer wall above the outer baffle, the top of the machine, and the upper part of the central column.

Particle fluxes Total particle fluxes (incident plasma and neutrals) Figure 6.10 increase as well, by a factor of 10 to 100 with respect to the reference case. However these fluxes remain low in magnitude, of the order of 10^{21} m^{-2}.s^{-1}, compared to those at the target of 10^{24} m^{-2}.s^{-1}, with peak values at the top of the machine.

The ion fluxes are the most visibly increased, by around factors of 100 across the wall. Atom fluxes also increase, by factors of 10 to 100 depending on the location. This is expected to translate into both a strong rise of ion-induced sputtering, which

may become significant (it was not in the case of constant diffusion coefficients), and increase atom-induced sputtering.

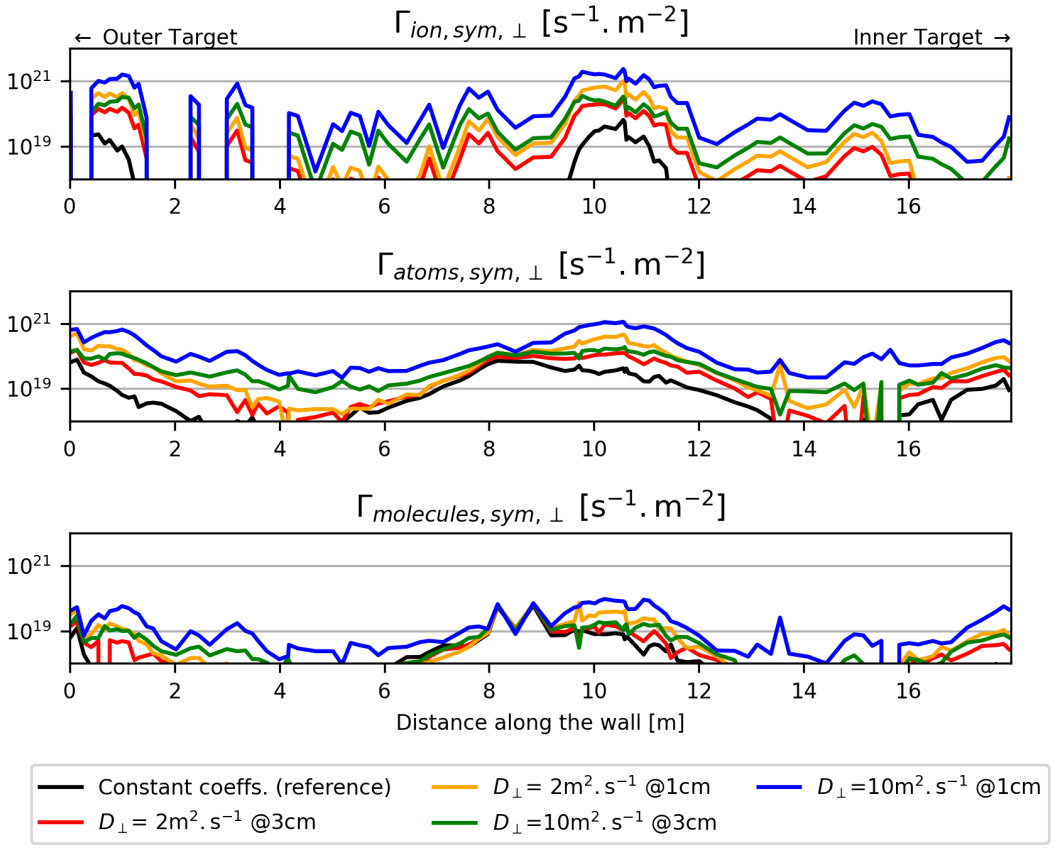

Figure 6.10.: Impact of enhanced far-SOL transport on incident particle flux decomposition along the first wall between ions, atoms, and molecules. The curvilinear coordinate is oriented counterclockwise in 2D: it starts on the left above the outer baffle, and finishes above the inner baffle. Same color scheme as in Figure 6.1.

Heat load Since the shoulder is formed by increasing both heat and particle diffusivity, the overall impact is to raise both the particle flux and the particles' energy at the first wall. This results in a combined effect that increases the heat load (plasma, neutrals, boundary plasma radiation) Figure 6.11 up to 40 kW/m² at the machine top. This increase is larger than for the throughput scan section 5.3.1 where opposite effects were observed on the two quantities: the particle flux increased, but the particles' energy decreased.

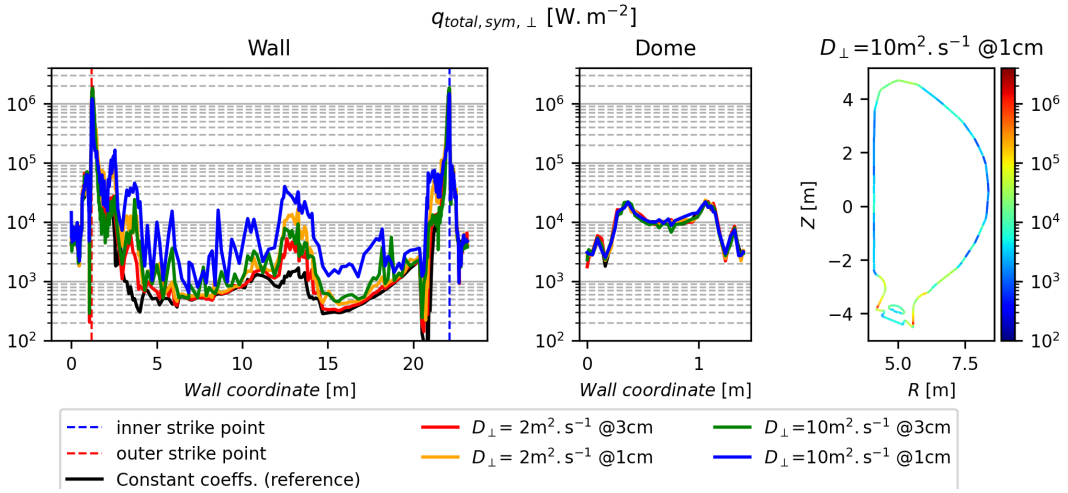

Figure 6.11.: 1D plot of the total perpendicular toroidally symmetric heat flux (including contributions from plasma, neutrals, and radiation) against the wall curvilinear coordinate for the far-SOL diffusivity scan. 0 starts at the bottom of the machine and then increases counterclockwise, starting from the outer target and ending on the inner target. Each color represents a case with a specific throughput. The leftmost plot shows the same quantity in 2D for the most diffusive case (i.e., the blue curve on the previous plots). This heat flux does not include radiation from the core region (not included in the numerical domain), which would add 10kW/m² (10MW spread over 1000m²) on top of the plotted quantity.

It must be noted here that the increased loading on the high field side is probably overestimated, because under the assumption that the perpendicular diffusion is driven by filamentary transport, these filaments would not propagate outwards on the high field side. In this case, such strong diffusion on the high field side is not expected to take place, while in the diffusion maps used here, the same radial profiles are used all around the poloidal cross-section, which is somewhat artificial.

Figure 6.12 breaks down the total integrated heat flux on the machine vessel by the flux received on each section (targets, first wall, dome). In total up to 30% of the input power is deposited on the first wall in the most diffusive case (labeled as 'D=10 @ 1cm' in the x-axis), corresponding to a threefold increase versus uniform coefficients. Two-thirds of this additional power on the first wall is taken from the initial deposition on the outer target, and one-third from that at the inner target. It can also be noted that apart from this extreme case, others do not show significant redistribution in terms of power among the vessel wall sections. In the reference case, the plasma ion flux impinging on the first wall is insignificant, but rises to 12% of the total ion flux in the most diffusive case. Other cases show only very low fluxes, below 3% of total ion flux over the whole vessel.

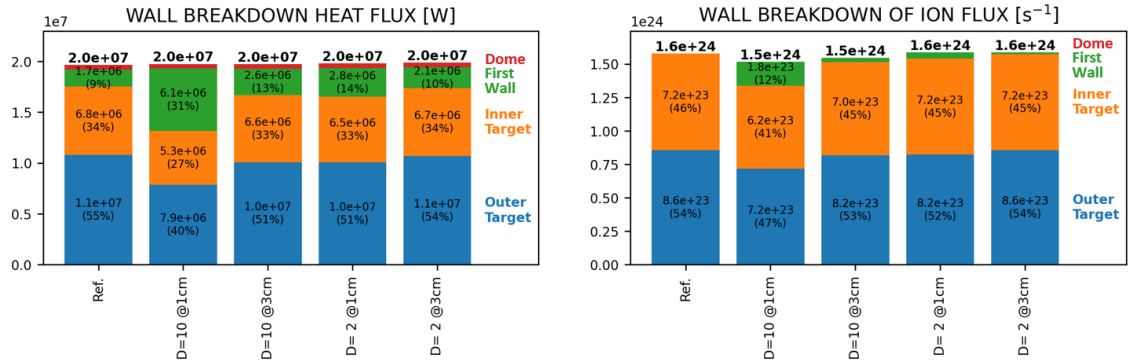

Figure 6.12.: Breakdown of the total heat flux (plasma, neutrals, radiation) on the left, and ion particle flux on the right, received by the sections of the machine.

Far-SOL flows Ranges for the Mach number are shown in Figure 6.13 for three cases, low, high throughput, and with the most enhanced far-SOL transport. The direction and patterns of flows seem unaffected by neither the throughput nor the increased transport, with the stagnation point in the far-SOL around the top outer wall. The Mach numbers increase with throughput, while the presence of a shoulder makes them decrease. Rough estimates of the amplitude for the main SOL are given in Table 6.2.

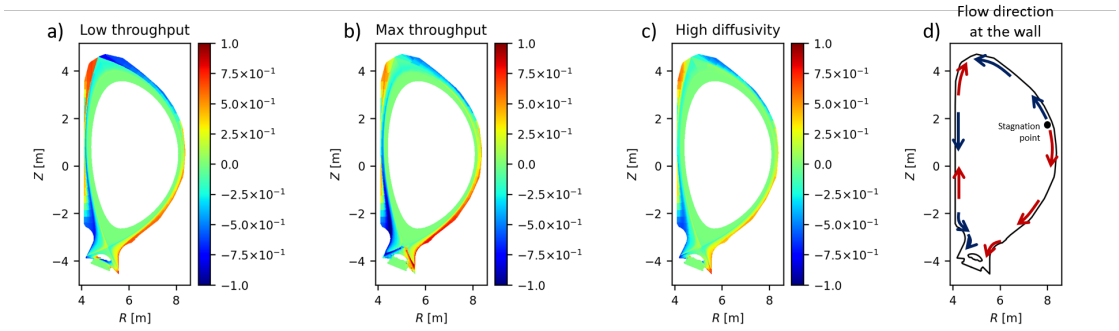

Figure 6.13.: Mach number for three cases: a) low throughput (1.46×10^{21} e^-/s), b) maximum throughput (1.76×10^{23} e^-/s), c) strongly enhanced far-SOL transport (shoulder @1cm, $D_\perp$=10m²/s in far-SOL), and d) overall direction of the plasma flow at the wall (common to all cases)

Table 6.2.: Ranges of estimates of the Mach number at four key locations, for both throughput and diffusivity scan

Region	Mach number range (est.)
Outer midplane	0.1-0.2
Inner midplane	0.1-0.4
Machine top	0.4-0.7
Inner divertor entrance	0.1-0.3
Outer divertor entrance	0.2-0.5

6.5.2. Estimating the impact on Beryllium erosion

In the same fashion as section 5.3.2.1, this section focuses on the estimations of the first wall erosion, and the impact of density shoulders in the far-SOL.

6.5.2.1. Impact of the presence of shoulders on fluxes & energies of CX atoms

Figure 6.14 shows, as in the last section, the atom particle fluxes across the first wall, and the associated average energy. A significant increase in the incident atom flux is seen with increased far-SOL transport, everywhere around the first wall, by factors of 10 to 20.

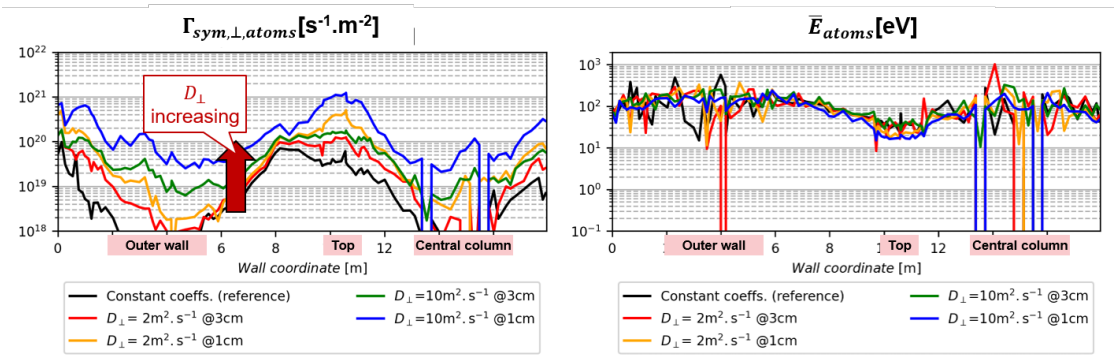

Figure 6.14.: Impact of throughput on FW atom flux and average atom energy

On the contrary, the average energy of these atoms at the first wall is almost completely unchanged. Figure 6.15 indicates that most of these collisions occur within 5 cm of the separatrix. In the previous section, it was seen that the presence of shoulders

almost does not affect the temperatures around the separatrix, and at 5cm in the SOL, profiles have not yet changed dramatically.

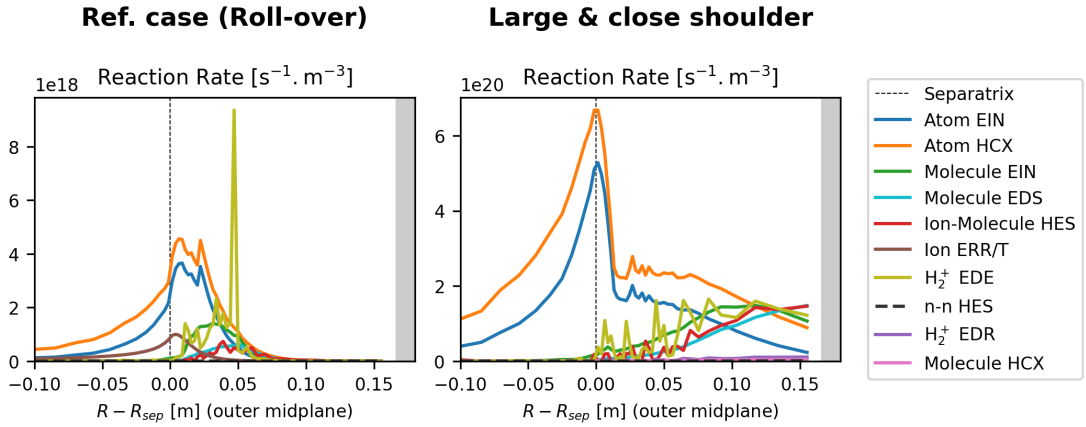

Figure 6.15.: Reactions rates at the outer midplane for the reference case (flat diffusion coefficient profiles) and the most diffusive case (shoulder at 1cm of the separatrix, $D_\perp$=10m²/s in the far-SOL). Note: the spike in the far-SOL is due to statistical noise, reactions are rare at this location without shoulders.

However, the number of reactions increases very significantly by a factor 100 with enhanced transport. On the right of Figure 6.15 in the far-SOL, many charge exchanges occur, which was not the case in the reference simulation, indicating that atoms at lower energies (i.e., with a shorter mean free path) are getting increasingly screened by the colder far-SOL plasma.

Additionally, Figure 6.16 shows the neutral densities at the outer midplane. The molecule density at the wall is raised by a factor of 100 between the scan's extremes, while the atom density gains a factor 10 at then separatrix. This illustrates the increase in main chamber recycling, and the frequency of other reactions, such as the molecular ionization and dissociation in Figure 6.15.

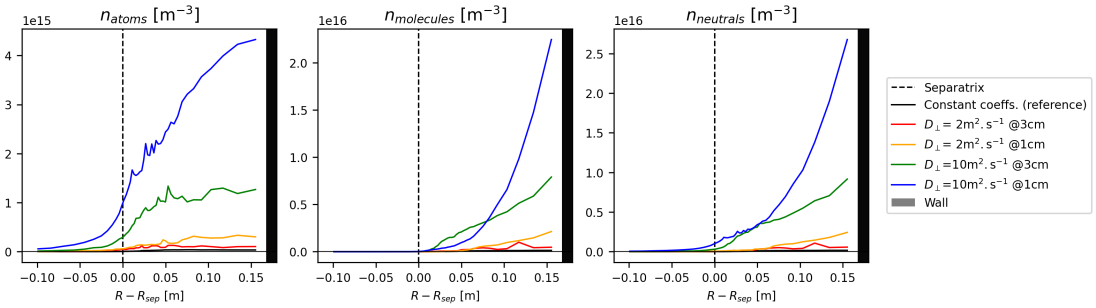

Figure 6.16.: Atom, molecule and total neutral density at the outer midplane for the enhanced far-SOL transport scan.

Energy distribution of incident atoms As in the previous chapter, the energy distribution of the atoms incident to two sections of the first wall are shown in Figure 6.17, for the two extreme cases in rows: the reference case, and the highest diffusivity case.

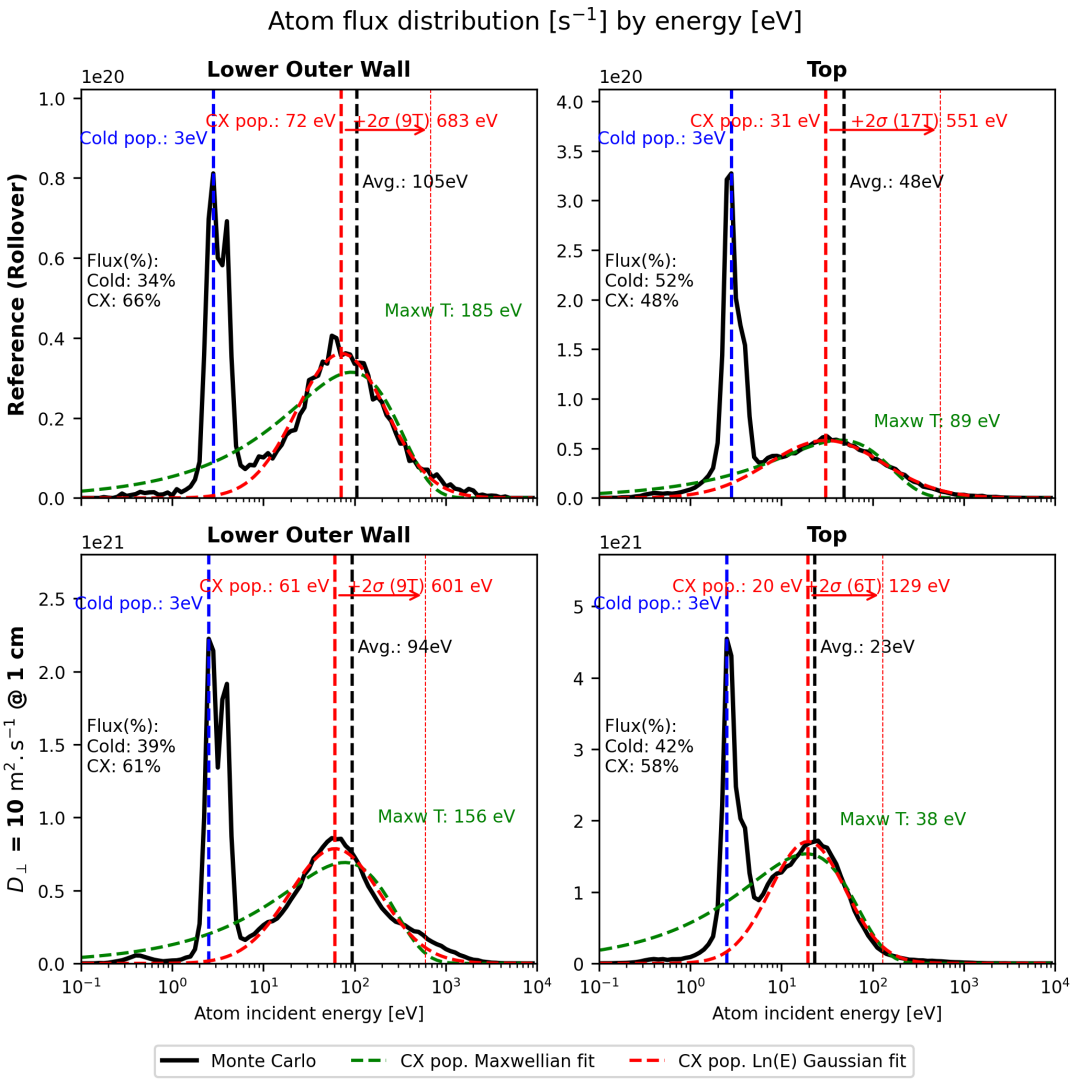

Figure 6.17.: Energy distribution of atoms incident to two of the first wall sections (see Figure 6.22 for a 2D view), for two cases (in rows) representing the reference case at rollover with uniform transport coefficients, and the most diffusive case with a shoulder at 1cm of the separatrix, $D_\perp$=10m²/s in the far-SOL. The black vertical line is the total average energy. Two fits are carried out: from a Maxwellian distribution in green with moderate success, and a more successful fit with a Gaussian law in logarithmic space in red. The vertical red dashed line represents the center of this fit, and the red arrow shows the energy upper bound required to capture 95% of the distribution (i.e. 2σ).

The observed effect is that on the lower outer wall, the shape of the distribution does not vary and is simply scaled up in amplitude, while at the machine top, two effects are opposed: the share of the CX population increases with diffusivity, but its

width narrows, and its center energy is lowered. The global effect is a reduction by a factor two of the average energy (vertical dashed lines), as was observed in Figure 6.14 (at wall coordinate ~ 11 m).

6.5.2.2. Reduced model for estimating of the CX atoms average energy

This section investigates the possibility of building a simple model to provide an estimation of the energy of charge exchange atoms at the first wall without a neutral particle kinetic solver, i.e. only using as input the plasma density and ion temperature profiles.

Since the charge exchange atoms which can lead to sputtering are at high energy, and are very fast moving particles, they interact very little with the lower density regions of the SOL. When the charge transfer collision occurs, an atom is produced at the energy of the incident ion, which is sampled from a Maxwellian at T_i, and in many cases flies through the SOL without any other collisions and impacts the wall at this T_i. This is especially true because because the reaction rate coefficient $\langle \sigma v \rangle$ is almost independent on T_i, and therefore their mean free path is mainly driven by the ion density and their velocity. Using rough numbers, a CX atom at energy T_i = 100 eV (it was seen in section 5.3.2.2 and section 6.5.2.1 that they occur predominantly near the separatrix), and taking $\langle \sigma v \rangle = 5 \times 10^{-14} \mathrm{m}^3.\mathrm{s}^{-1}$, requiring a mean free path smaller than the distance to the wall, i.e. 10 cm, gives a ion density of $2 \times 10^{19} \mathrm{m}^{-3}$, which is very far from the values in the far-SOL.

Using these considerations, the overall picture can be simplified by saying that the energy of the fast atoms on the wall is simply an average of T_i where collisions occur.

Using a 1D model, it is possible to build an average atom energy $\overline{E_{CXN}}$ at the wall as such: by weighting the T_i profile by the number of atom CX collisions along a radial profile.

More precisely, this model is a decaying atom beam from the wall to the core Figure 6.18, and is build on the following assumptions:

1. All 2D/3D effects are neglected
2. All neutrals initially come from the wall: an initial flux at s=0 is the starting point as a beam at E_0 = 3 eV, under the assumption that these atoms are initially part of the "cold", almost mono-energetic population from the breakdown of molecules and H_2^+ molecular ions, see section 5.3.2.2.
3. the charge exchange reactions remove atoms of the beam as they are sent back to the wall
4. The atom CX energy is counted directly at the wall at the energy equals to T_i, which is taken at the location where the collision occurred (assuming no additional collisions on the way back to the wall)
5. $\langle \sigma v \rangle^{CX}$ is taken as a constant at 5×10^{-14} [$\mathrm{m}^3.\mathrm{s}^{-1}$]

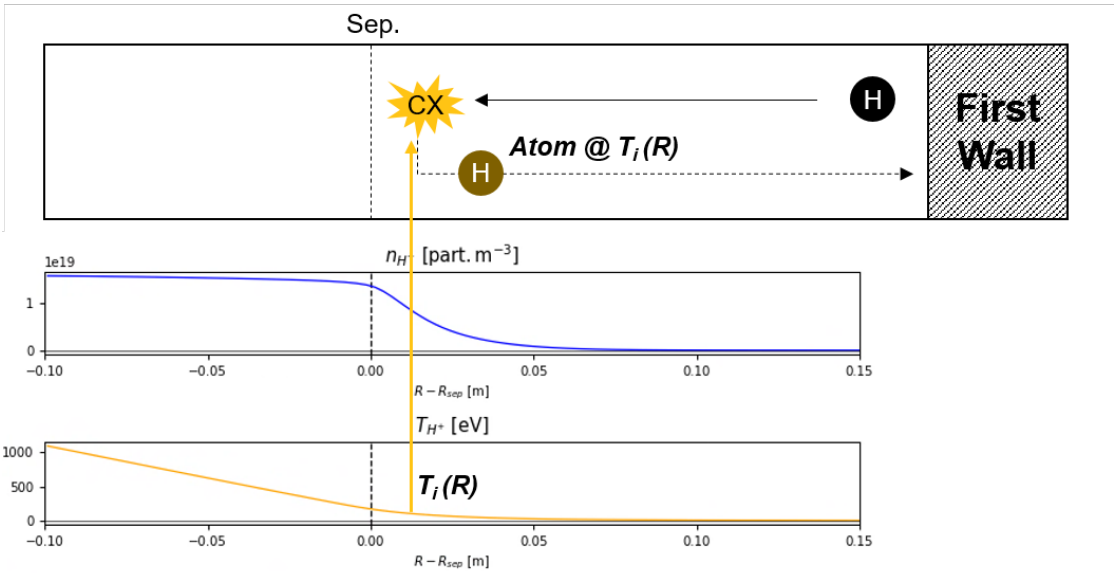

Figure 6.18.: Schema of the proxy model for computing the atom average energy at the wall. Atoms are assumed incoming with an energy of 3 eV, and to take the energy of T_i where they undergo a charge exchange. This atom then is assumed to fly back unimpeded to the wall, where its energy is counted.

The computation boils down to solving the following equation in n_a, and then recomputing the reaction rates N and averaging over the 1D coordinate with weights T_i. In the following:

- s is the radial curvilinear 1D coordinate
- n_a is the atom density
- n_i is the ion density
- N is the CX reaction rate
- E_0 is the atom beam initial energy

$$N(s) = n_a(s) n_i(s) \langle \sigma v \rangle^{CX} \tag{6.1}$$

$$\frac{\partial n_a}{\partial s} = -n_a \frac{n_i \langle \sigma v \rangle^{CX}}{\sqrt{E_0 e / m_i}} \tag{6.2}$$

$$\overline{E_{CXN}} = \frac{1}{\int_0^{s_{\text{edge}}} N(s) ds} \int_0^{s_{\text{edge}}} N(s) T_i(s) ds \tag{6.3}$$

This can be computed numerically with the n_i and T_i profiles as input. The results are shown in Figure 6.19, where the star symbols in represent the results of this model $\overline{E_{CXN}}$ for the throughput scan and the enhanced far-SOL transport scan. The orders of magnitudes and the trends are recovered, meaning that such computations could be used for rough estimates without needing full 2D EIRENE simulations, if only the the density and ion temperature profiles are available.

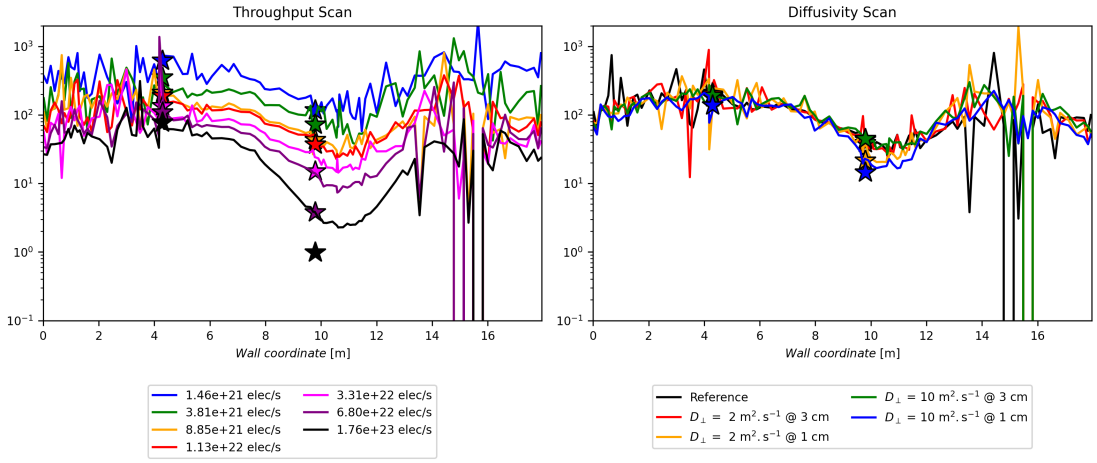

Figure 6.19.: Average energy of the atoms reaching the first wall for the throughput scan (left) and enhanced far-SOL transport scan (right), compared with the computed proxy $\overline{E_{CXN}}$ as stars (see in the text for the description). The proxy is calculated at two locations, at the outer mid plane (left stars), and the machine top (right stars)

Charge exchange reactions localisation Furthermore, this simplified model can also help interpret the reason these collisions occur mainly near the separatrix.

Using this simple approach to compute the mean free path of the 3 eV incident atoms, it is possible to obtain the order of magnitude of the density for which it falls beneath the system length, i.e. 10 cm:

$$\lambda_{mfp} = \frac{\sqrt{E_0 e/m_i}}{\langle \sigma v \rangle^{CX} n_i} \tag{6.4}$$

$$n_i^{\lambda_{mfp}=10\text{cm}} = \frac{\sqrt{E_0 e/m_i}}{\langle \sigma v \rangle^{CX} \lambda_{mfp}} \sim 1 \times 10^{19} \text{m}^{-3} \tag{6.5}$$

This is indeed the range of densities obtained at the separatrix.

Further simplifications, limitations, and outlook This model could however be refined, by including the contributions of fast atoms that could penetrate even

deeper, and also the probability that the fast atoms loses its energy via another charge exchange on the way back to the wall.

It could also be further simplified to rely only on the density and temperatures at the separatrix, at the cost of assuming a profile shape (e.g., hyperbolic tangent tanh).

As a caveat, this model could be useful if the obtained energy is not too close from the sputtering threshold, otherwise the exact energy distribution matters more for erosion yield. For beryllium walls, which has a sputtering threshold with H projectiles at 13 eV [21, 88], it should remain valid. For H on tungsten, which has a threshold of 447 eV[21, 88], it is much less the case.

Such kinds of models with further refinements have been derived and compares to experiments [89, 90], further work could also involve comparison with those, and current experimental data.

6.5.2.3. Gross erosion estimations

As was done in the throughput section section 5.3.2.4, the sensitivity of the computed gross erosion rate to the enhanced transport is studied. Of course, the same caveats as mentioned previously apply.

Figure 6.20 illustrates the total integrated gross erosion rate across the first wall, with the ion contribution in red and the atom contribution in blue. The 2D plot on the right shows the location in 2D of the highest gross erosion rate density in each part of the wall. Sputtering from ions is now dominant (50-70%), while they were minor contributors in the throughput scan. This enhanced far-SOL transport leads to much larger increases than the throughput scan (factor 6 increase), with a factor of 40 between the scan's extremes.

When throughput was increased, two effects balanced each other: neutral particle fluxes were increased, but the energy of atoms which were inducing erosion was decreased (the contribution from ions was low). Now, with enhanced transport, both ion particle and energy transports increase, and the two effects cumulate. Ion-related sputtering increases drastically to become now dominant. The neutral-induced sputtering is raised as well, but not as strongly as the ions.

In 2D, again, the top and outer lower tiles (#8,#9 & #18) show the highest sputtering rate.

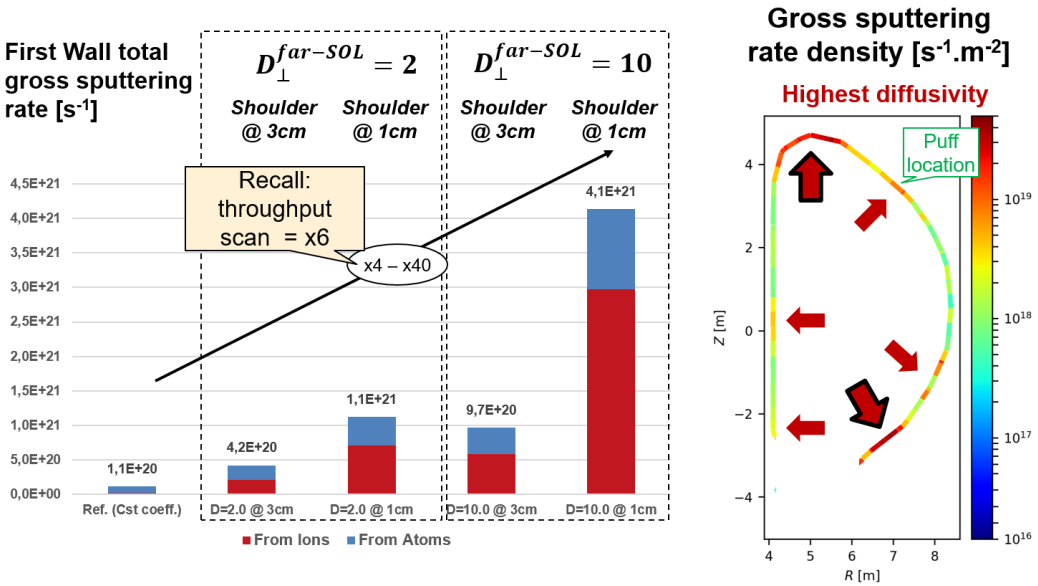

Figure 6.20.: Impact of enhanced transport on the first wall erosion, left: gross erosion rate, right: 2D plot of the gross erosion rate for the most diffusive case. The arrow illustrates the factor of increase w.r.t. the reference case.

6.6. Influence of first wall recycling on bulk plasma conditions

It was seen in section 6.3 that strongly increasing diffusivity in the far-SOL had a significant impact on density and temperatures inside the separatrix (+50% and -27% respectively). Here is investigated the origin of this effect.

In terms of particles, inside the separatrix there is only a fixed particle influx at the core-edge interface at the boundary condition of the numerical grid of 6.14×10^{20} ion/s, and the volume particle source from neutral ionization of neutrals that may have reached inside the separatrix. The transport coefficients are unchanged at the separatrix, and the value of the density there is almost unchanged as well. It is therefore most likely that there is an increased penetration of neutrals there.

Figure 6.21 shows that indeed when going to very strong diffusivity, the source from ionization of neutrals inside the separatrix becomes much larger, by a factor 60, than the core influx, increasing the density there.

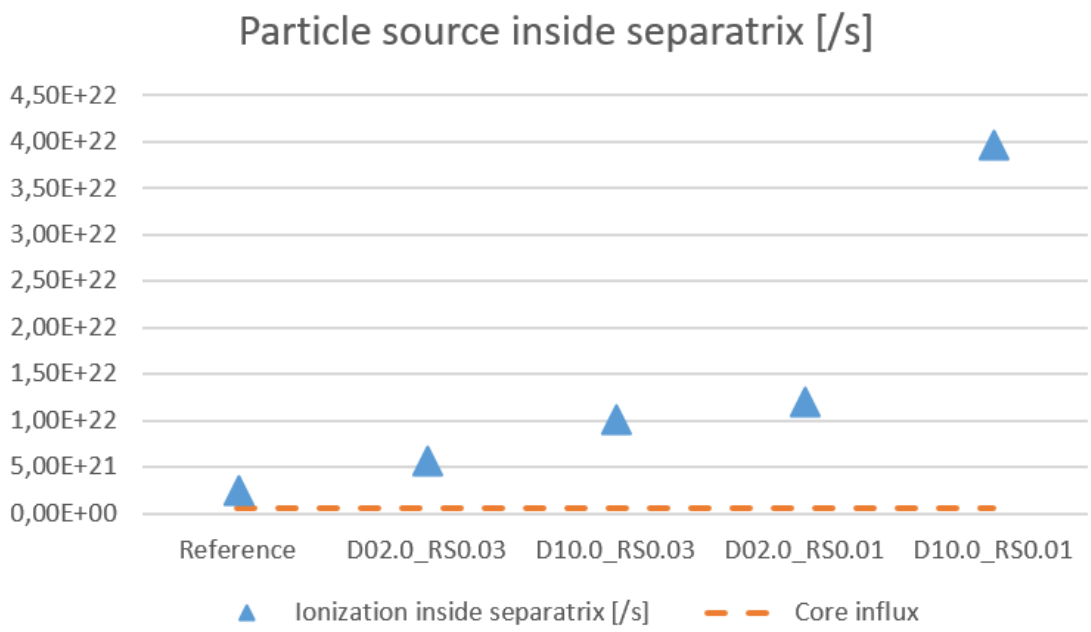

Figure 6.21.: Particle source inside the separatrix, vs the core influx in orange for the far-SOL enhanced transport scan

The origin of these neutrals may relate to different mechanisms: recycling, from the divertor targets or the first wall, from the gas injection valves, or from volumetric recombination. Since the gas injection does not change, and it was seen in the previous section that divertor conditions do not change, then also the target recycling and volumetric recombination there should not drive the observed increased neutral densities. This indicates that the first wall recycling must be the cause.

To gain more insight on which sections of the first wall are involved in this recycling, an analysis is carried out using the "strata" mechanism in EIRENE, and splitting of the contour of the vessel wall in 12 parts shown in Figure 6.22.

The following will only investigate the most diffusive case ($D_\perp = 10\text{m}^2/\text{s}$ at 1cm) so that effects are emphasized.

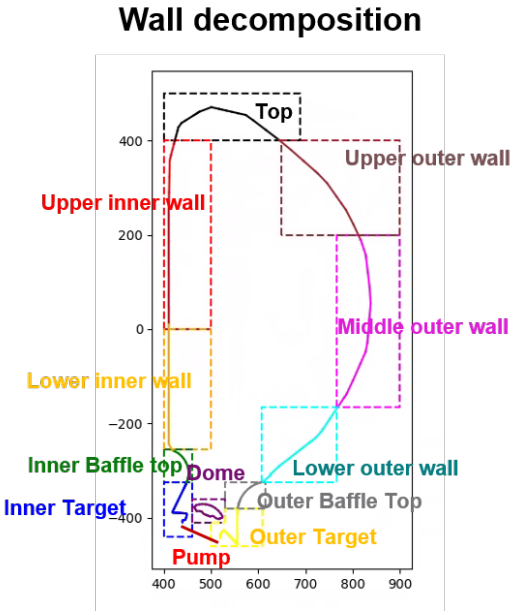

Figure 6.22.: Segments of the wall to decompose the plasma source into the recycling origin.

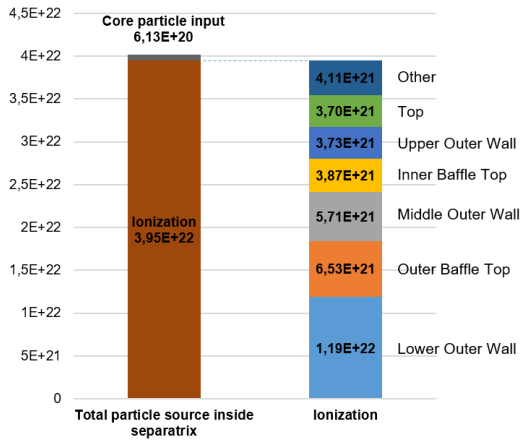

Figure 6.23.: Breakdown by origin of the total particle source inside the separatrix for the most diffusive case of the enhanced far-SOL transport scan

Figure 6.23 shows that the largest contributors are the parts of the outer lower wall. This section was already identified in the previous section as being subject to the largest erosion across the first wall. The whole outer wall contributes largely, because it is directly facing the plasma edge and the increased diffusion fuels the recycling there. The top of the machine also contributes, and was also identified previously as receiving increased ion flux. It is also notable that the targets do not contribute much: the penetration fraction inside the separatrix of the neutrals coming from the targets is very low (0.04%), meaning that divertor in this regime contains them very efficiently. The top 6 wall sections discussed here and their associated volume particle source is provided in Figure 6.24.

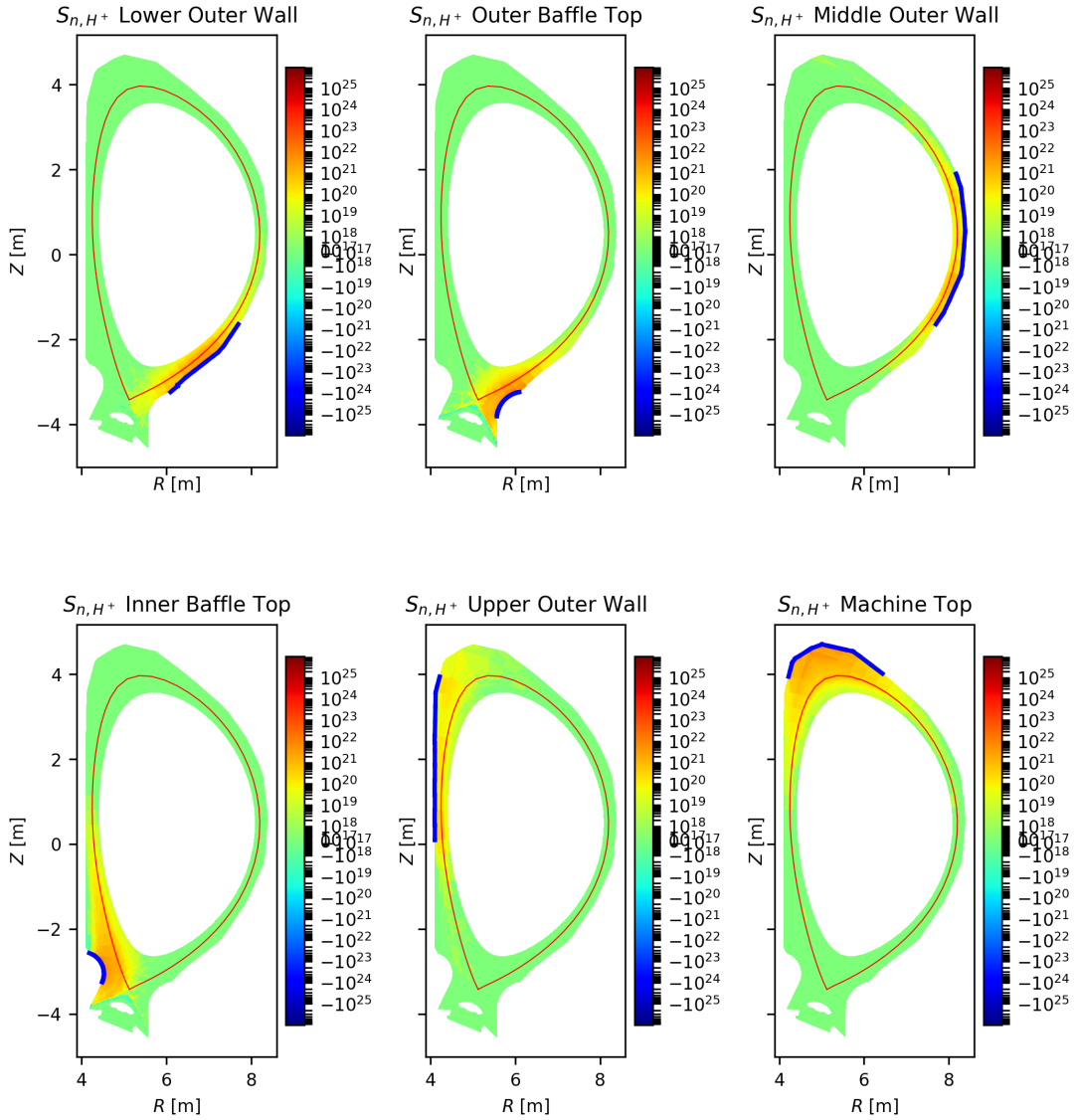

Figure 6.24.: 2D plots of the plasma particle source linked to the recycling along specific parts of the first wall, for the most diffusive case. The section in blue corresponds to the region of the wall whose recycling is plotted in the volume.

This phenomenon illustrates the sensitivity to the inner regions of the plasma to the increased transport. In the considered cases, the transport coefficients were kept identical inside the separatrix and in the near-SOL. Therefore this effect is expected to increase even further in the case of the inclusion of a H-mode transport barrier, at least in the simulations: indeed, the penetrating neutrals do not see the plasma transport barrier, therefore the resulting increase in plasma after their ionisation

can accumulate much more behind the separatrix. However, they would still see the density and temperature pedestals, which could localise the ionisation source outward closer to the separatrix instead of further in. Further simulations of the ITER H-mode PFPO-2 cases are ongoing which could address this question.

7. Conclusion

7.1. Key results

In this work, the different divertor regimes and their consequences on the first wall were studied for the ITER's first non-active phase at 20MW (PFPO-1), along with some outlook on PFO $Q = 10$ plasmas. This study was carried out with the SOLEDGE3X code, which includes a coupling to EIRENE, and has the particularity to simulate plasma up to the wall to provide an accurate description of fluxes to the wall as well as plasma conditions in its vicinity. This exercise consisted of two phases: the improvement of the code and the analysis of the results.

First, we reported on the improvements of the SOLEDGE3X physics model so that it includes phenomena relevant to the ITER machine, leading to a model that is more complex than the one that is used for medium-sized tokamaks. For this, several additions have been implemented: the Molecule Assisted Recombination channel through H_2^+, the ion-molecules elastic collisions, neutral-neutral collisions, density dependencies of the reaction rate coefficients to account for population effects, and a description of the H_2^+ ion transport dynamics. This also mandated improvements on the code's numerical scheme, including an implicitation of the friction force and energy equipartition, an improved perpendicular diffusion operator and computing time optimization from a multi-grid approach, and optimization of the EIRENE calls through a first evaluation of their validity duration. Following this, results obtained with SOLEDGE3X were compared to cases with similar parameters in SOLPS-ITER from the ITER database and were found to be in good agreement. The upstream profiles are similar, along with target density and electron temperature profiles. Ion temperature profiles at the strike points are similar, but differ away from the strike points in attached cases, being a factor two lower in SOLEDGE3X. Particle fluxes and total heat fluxes to the targets match very well. Divertor neutral pressures match for attached cases, but show a slower increase in SOLEDGE3X.

Then, an analysis of density regimes was presented, ranging from the high-recycling regime to the partial detachment regime at the maximum throughput of the machine. Upstream, it was observed that the electron parallel power decay length increased quickly by 60%, then even up to 300% at the maximum throughput. This lead to the conclusion that for the simulation of high-density regimes, one should not attempt to fix transport coefficients to match the Eich's scaling law. Rather, the approach would be first to tune the perpendicular transport coefficients to match Eich's law in sheath-limited simulations, then to keep the obtained values for high-density simulations. Such procedure is then valid provided one assumes that the characteristics of the

transverse transport which we represent through the diffusion coefficients are not impacted by divertor regimes and would need additional correction if this were the case. The decomposition of plasma-neutral interactions was analyzed for the three regimes attached, rollover, and partial detachment. At the rollover, the first dominant particle sink is the MAR, while the electron-H^+ recombination is negligible. The latter turns important in the partial detachment state. An overall picture of the main reactions for the three states was provided, highlighting the different roles of the reactions, especially the contributions of the H_2^+ ions.

Our simulations also allowed to analyse the plasma conditions and fluxes at the first wall, and their evolution across divertor density regimes. Two opposite effects were observed, particle fluxes increased with throughput, but their energy decreased. Total heat flux densities (<10kW/m²) remained largely below the design limits, in spite of increasing with throughput. Estimations of the gross Be erosion rates showed a six-fold increase with throughput, mainly driven by charge exchange atoms, as very few ions reach the first wall. The atom energy distribution features two populations, a cold 3 eV Frank-Condon population and a high energy charge exchange population which can reach 3 or 4 keV. However, the particle fluxes of those are extremely low. The segments of the first wall most prone to erosion are the machine top, the gas puff injection port, and the tiles above the outer baffle.

Then, a sensitivity study was carried out to assess the impact of the potential formation of density shoulders in the far-SOL, by enhancing perpendicular transport coefficients there. This was observed to have very little effect on the divertor conditions, and the divertor regime was unchanged. At the first wall, both particle fluxes and energies are increased. Heat flux densities increased up to 40kW/m², yet still far below the design limits. Now gross erosion is rather dominated by the ion contribution, with a much stronger increase by a factor of 60 across the scan.

7.2. Outlook

Finally, we suggest some outlook on potential future next steps.

Regarding the PFPO-1 results, the density shoulder scan was only carried out for a relatively low throughput case (the rollover case at 8.85e^-/s). It is unclear yet if the presence of shoulder affects the results in the same way at different divertor regimes. Thus, the present results could be complemented by carrying the same density shoulder scan on the attached and partially detached cases to evaluate this.

The erosion aspects were studied in this work as a post processing of the cases run without impurities, however as was mentioned in introduction, the objective of reducing the wall material sputtering is to prevent plasma contamination and impacts on its performance. To include and assess the effects of the eroded beryllium on the plasma, the presented cases could be rerun with the sputtering sources turned on in EIRENE evolving the beryllium plasma and neutrals species along with the hydrogen. This feature is already implemented and used for simulations of other machines, for example carbon sputtered impurities on JT-60SA cases in [91].

The present cases were run without fluid drifts, which is a important ingredient of the SOL physics. It was found in SOLPS-ITER cases in [80] that significant impact was found for high-power Neon seeded cases at low and medium throughput. Thus, the present cases could be rerun with the drifts activated (which are implemented in SOLEDGE3X and used in simulations of other machines), to analyse their impact.

As current discussion includes the relevance of a first wall made of tungsten instead of beryllium, the results shown here could also be compared with new runs which could be executed with a fully tungsten divertor and first wall. This material sensitivity was carried out for the divertor plates in [42] with SOLPS-ITER, but with the first wall still in beryllium (and without the extended grid). The results presented here could also be used as plasma backgrounds for ERO2.0 or WALLDYN for erosion computations.

Another angle for analysis would also be to lift the axisymmetry assumption and carry out a sensitivity analysis on the 3D localization of the gas puff.

Also, as detachment control is of particular importance for the operation of ITER, the temporal aspects of detachment could be investigated by lifting the time-independent assumption in the EIRENE setup in our simulations. Indeed, it was observed during the numerical stability investigations during this work that the lifetime of particles tracked in a single EIRENE call could largely exceed the plasma solver time step, thus indicating that the dynamics of neutrals may not be accurately resolved.

The next main focus would be pursuing the 100MW FPO Neon seeded cases, which were demonstrated to be now feasible with SOLEDGE3X during this thesis, see the proof-of-concept in section E. The same detachment reactions and contribution analysis could be extended to cases with impurities.

On the modeling side, several leads for future improvements were mentioned in section 3.3.3, as some aspects of the model are still very rough (such as the prescription of the perpendicular transport coefficients). Some potential improvements to address this include hybrid fluid-kinetic neutrals, investigate the relevance of fully fluid descriptions of neutrals with two-population atoms and Kotov-like molecule chemistry, time dependant kinetic neutrals, the inclusion of Collisional-Radiative Models, improvements on the description of the sheath, the addition of the H^- MAR channel, charge exchanges between different chemical elements, and activating reduced turbulence models instead of prescribed coefficients (e.g., the $k-\varepsilon$ model SOLEDGE3X).

Also, the decomposition of plasma-neutral interaction processes and the improved model could be confronted with current experiments, especially in cold divertor machines such as MAST-U.

Finally, regarding the supporting tools for SOLEDGE3X, the `pySOLEDGE3X` Python package and graphical user interface that was developed during this work for post-treatment and plotting (see more details in section H could be further improved, both in terms of standard routines and performance (especially for 3D cases). Also, since the data model for the plasma inside this package has strong similarities with the IMAS data structure and philosophy, and it includes an IMAS reading and plotting interface (which was developed for plotting SOLPS data), it may be worth investigating the merging of some of these components with the official IMAS python tools so that

they can benefit a larger community.

Thus we conclude this work, with the hope that it contributed a little to improving the understanding of boundary plasmas, and brought predictive simulations a step closer, which we believe would be a considerable accelerator for fusion energy.

Bibliography

[1] *File:Binding energy curve - common isotopes.svg - Wikimedia Commons*. URL: https://commons.wikimedia.org/wiki/File:Binding_energy_curve_-_common_isotopes.svg (visited on 02/11/2023) (cit. on p. 21).

[2] G. Audi, O. Bersillon, J. Blachot, et al. "The Nubase evaluation of nuclear and decay properties". In: *Nuclear Physics A* 729.1 (Dec. 2003), pp. 3–128. ISSN: 03759474. DOI: 10.1016/j.nuclphysa.2003.11.001. URL: https://linkinghub.elsevier.com/retrieve/pii/S0375947403018074 (visited on 02/11/2023) (cit. on p. 21).

[3] *Inertial Electrostatic Confinement Project - University of Wisconsin - Madison*. URL: https://iec.neep.wisc.edu/operation.php (visited on 02/11/2023) (cit. on p. 22).

[4] Mohamed Abdou, Marco Riva, Alice Ying, et al. "Physics and technology considerations for the deuterium–tritium fuel cycle and conditions for tritium fuel self sufficiency". In: *Nuclear Fusion* 61.1 (Jan. 1, 2021), p. 013001. ISSN: 0029-5515, 1741-4326. DOI: 10.1088/1741-4326/abbf35. URL: https://iopscience.iop.org/article/10.1088/1741-4326/abbf35 (visited on 02/11/2023) (cit. on p. 22).

[5] IRSN. *Nuclear Fusion Reactors - Safety and radiation protection considerations for demonstration reactors that follow the ITER facility*. Nov. 2017. ISBN: ISSN 2117-7791. URL: https://www.irsn.fr/EN/Research/publications-documentation/Scientific-books/Pages/reference-documents.aspx (cit. on p. 23).

[6] J D Lawson. "Some Criteria for a Power Producing Thermonuclear Reactor". In: *Proceedings of the Physical Society. Section B* 70.1 (Jan. 1, 1957), pp. 6–10. ISSN: 0370-1301. DOI: 10.1088/0370-1301/70/1/303. URL: https://iopscience.iop.org/article/10.1088/0370-1301/70/1/303 (visited on 01/22/2023) (cit. on p. 24).

[7] M Keilhacker, A Gibson, C Gormezano, et al. "The scientific success of JET". In: *Nuclear Fusion* 41.12 (Dec. 2001), pp. 1925–1966. ISSN: 0029-5515. DOI: 10.1088/0029-5515/41/12/217. URL: https://iopscience.iop.org/article/10.1088/0029-5515/41/12/217 (visited on 01/22/2023) (cit. on p. 25).

[8] Elizabeth Gibney. “Nuclear-fusion reactor smashes energy record”. In: *Nature* 602.7897 (Feb. 9, 2022). Bandiera_abtest: a Cg_type: News Number: 7897 Publisher: Nature Publishing Group Subject_term: Energy, Nuclear physics, pp. 371–371. DOI: 10.1038/d41586-022-00391-1. URL: https://www.nature.com/articles/d41586-022-00391-1 (visited on 01/23/2023) (cit. on p. 25).

[9] Sabina Griffith. *ITER Newsline Oct. 2008*. ITER website. Oct. 2008. URL: https://www.iter.org/fr/newsline/53/1589 (visited on 01/23/2023) (cit. on p. 25).

[10] Samuel E. Wurzel and Scott C. Hsu. “Progress toward fusion energy breakeven and gain as measured against the Lawson criterion”. In: *Physics of Plasmas* 29.6 (June 2022), p. 062103. ISSN: 1070-664X, 1089-7674. DOI: 10.1063/5.0083990. URL: https://aip.scitation.org/doi/10.1063/5.0083990 (visited on 02/11/2023) (cit. on p. 26).

[11] Roberto Bilato, Ralf Kleiber, C. Angioni, et al. “IPP Summer University for Plasma Physics 2016”. In: (2016) (cit. on p. 29).

[12] *nucleaire-info-com*. URL: http://www.nucleaire-info.com/confinement_magnetique.htm (visited on 02/11/2023) (cit. on p. 31).

[13] ITER Physics Expert Group. “Chapter 2: Plasma confinement and transport”. In: *Nuclear Fusion* 39.12 (Dec. 1999), pp. 2175–2249. ISSN: 0029-5515. DOI: 10.1088/0029-5515/39/12/302. URL: https://iopscience.iop.org/article/10.1088/0029-5515/39/12/302 (visited on 01/25/2023) (cit. on p. 32).

[14] P. C. Stangeby. *The plasma boundary of magnetic fusion devices*. Plasma physics series. Bristol ; Philadelphia: Institute of Physics Pub, 2000. 717 pp. ISBN: 978-0-7503-0559-4 (cit. on pp. 43–45, 47, 51, 134, 164, 166, 167).

[15] Fulvio Militello. *Boundary Plasma Physics: An Accessible Guide to Transport, Detachment, and Divertor Design*. Vol. 123. Springer Series on Atomic, Optical, and Plasma Physics. Cham: Springer International Publishing, 2022. ISBN: 978-3-031-17338-7 978-3-031-17339-4. DOI: 10.1007/978-3-031-17339-4. URL: https://link.springer.com/10.1007/978-3-031-17339-4 (visited on 02/11/2023) (cit. on p. 46).

[16] S. Potzel, M. Wischmeier, M. Bernert, et al. “A new experimental classification of divertor detachment in ASDEX Upgrade”. In: *Nuclear Fusion* 54.1 (Jan. 1, 2014), p. 013001. ISSN: 0029-5515, 1741-4326. DOI: 10.1088/0029-5515/54/1/013001. URL: https://iopscience.iop.org/article/10.1088/0029-5515/54/1/013001 (visited on 01/23/2023) (cit. on p. 46).

[17] A Loarte, R.D Monk, J.R Martín-Solís, et al. “Plasma detachment in JET Mark I divertor experiments”. In: *Nuclear Fusion* 38.3 (Mar. 1998), pp. 331–371. ISSN: 0029-5515. DOI: 10.1088/0029-5515/38/3/303. URL: https://iopscience.iop.org/article/10.1088/0029-5515/38/3/303 (visited on 01/11/2023) (cit. on pp. 51, 188).

[18] S I Krasheninnikov, A S Kukushkin, and A A Pshenov. “Divertor plasma detachment: roles of plasma momentum, energy, and particle balances”. In: *Plasma Physics and Controlled Fusion* 64.12 (Dec. 1, 2022), p. 125011. ISSN: 0741-3335, 1361-6587. DOI: 10.1088/1361-6587/ac9a6f. URL: https://iopscience.iop.org/article/10.1088/1361-6587/ac9a6f (visited on 01/03/2023) (cit. on pp. 51, 155).

[19] V Kotov and D Reiter. “Two-point analysis of the numerical modelling of detached divertor plasmas”. In: *Plasma Physics and Controlled Fusion* 51.11 (Nov. 1, 2009), p. 115002. ISSN: 0741-3335, 1361-6587. DOI: 10.1088/0741-3335/51/11/115002. URL: https://iopscience.iop.org/article/10.1088/0741-3335/51/11/115002 (visited on 01/03/2023) (cit. on pp. 51, 155).

[20] A.A. Pshenov, A.S. Kukushkin, A.V. Gorbunov, et al. “Divertor plasma opacity effects”. In: *Nuclear Materials and Energy* 34 (Mar. 2023), p. 101342. ISSN: 23521791. DOI: 10.1016/j.nme.2022.101342. URL: https://linkinghub.elsevier.com/retrieve/pii/S235217912200223X (visited on 01/24/2023) (cit. on pp. 56, 78, 100).

[21] J. P. Biersack and W. Eckstein. “Sputtering studies with the Monte Carlo Program TRIM.SP”. In: *Applied Physics A Solids and Surfaces* 34.2 (June 1984), pp. 73–94. ISSN: 0721-7250, 1432-0630. DOI: 10.1007/BF00614759. URL: http://link.springer.com/10.1007/BF00614759 (visited on 01/16/2023) (cit. on pp. 57, 201).

[22] W. Eckstein, C. Garcia-Rosales, J. Roth, et al. “Sputtering Data”. In: (1993). Publisher: Max-Planck-Institut für Plasmaphysik. URL: https://hdl.handle.net/11858/00-001M-0000-0027-6325-4 (visited on 12/14/2022) (cit. on pp. 57, 171).

[23] K. Ghoos, P. Börner, W. Dekeyser, et al. “Grid resolution study for B2-EIRENE simulation of partially detached ITER divertor plasma”. In: *Nuclear Fusion* 59.2 (Feb. 1, 2019), p. 026001. ISSN: 0029-5515, 1741-4326. DOI: 10.1088/1741-4326/aaf30f. URL: https://iopscience.iop.org/article/10.1088/1741-4326/aaf30f (visited on 06/03/2023) (cit. on pp. 59, 105).

[24] D. Tskhakaya, K. Matyash, R. Schneider, et al. “The Particle-In-Cell Method”. In: *Contributions to Plasma Physics* 47.8 (Dec. 2007), pp. 563–594. ISSN: 08631042, 15213986. DOI: 10.1002/ctpp.200710072. URL: https://onlinelibrary.wiley.com/doi/10.1002/ctpp.200710072 (visited on 01/31/2023) (cit. on p. 60).

[25] Harold Grad. “On the kinetic theory of rarefied gases”. In: *Communications on Pure and Applied Mathematics* 2.4 (Dec. 1949), pp. 331–407. ISSN: 00103640, 10970312. DOI: 10.1002/cpa.3160020403. URL: https://onlinelibrary.wiley.com/doi/10.1002/cpa.3160020403 (visited on 01/31/2023) (cit. on p. 63).

[26] V.M. Zhdanov. *Transport Processes in Multicomponent Plasma*. 0th ed. CRC Press, Apr. 11, 2002. ISBN: 978-0-429-17709-5. DOI: 10.1201/9781482265101. URL: https://www.taylorfrancis.com/books/9781482265101 (visited on 12/19/2022) (cit. on pp. 63, 106, 124, 231, 233).

[27] S. I. Braginskii. "Transport Processes in a Plasma". In: *Reviews of Plasma Physics* 1 (Jan. 1, 1965). ADS Bibcode: 1965RvPP....1..205B, p. 205. URL: https://ui.adsabs.harvard.edu/abs/1965RvPP....1..205B (visited on 12/19/2022) (cit. on p. 63).

[28] H Bufferand, J Balbin, S Baschetti, et al. "Implementation of multi-component Zhdanov closure in SOLEDGE3X". In: *Plasma Physics and Controlled Fusion* 64.5 (May 1, 2022), p. 055001. ISSN: 0741-3335, 1361-6587. DOI: 10.1088/1361-6587/ac4fac. URL: https://iopscience.iop.org/article/10.1088/1361-6587/ac4fac (visited on 10/11/2022) (cit. on pp. 63, 106, 124).

[29] M Raghunathan, Y Marandet, H Bufferand, et al. "Generalized collisional fluid theory for multi-component, multi-temperature plasma using the linearized Boltzmann collision operator for scrape-off layer/edge applications". In: *Plasma Physics and Controlled Fusion* 63.6 (June 1, 2021), p. 064005. ISSN: 0741-3335, 1361-6587. DOI: 10.1088/1361-6587/abf670. URL: https://iopscience.iop.org/article/10.1088/1361-6587/abf670 (visited on 01/30/2023) (cit. on p. 63).

[30] H. Bufferand, G. Ciraolo, Y. Marandet, et al. "Numerical modelling for divertor design of the WEST device with a focus on plasma–wall interactions". In: *Nuclear Fusion* 55.5 (May 1, 2015), p. 053025. ISSN: 0029-5515, 1741-4326. DOI: 10.1088/0029-5515/55/5/053025. URL: https://iopscience.iop.org/article/10.1088/0029-5515/55/5/053025 (visited on 09/23/2022) (cit. on pp. 63, 100, 146).

[31] P. Tamain, H. Bufferand, G. Ciraolo, et al. "The TOKAM3X code for edge turbulence fluid simulations of tokamak plasmas in versatile magnetic geometries". In: *Journal of Computational Physics* 321 (Sept. 2016), pp. 606–623. ISSN: 00219991. DOI: 10.1016/j.jcp.2016.05.038. URL: https://linkinghub.elsevier.com/retrieve/pii/S0021999116301838 (visited on 02/01/2023) (cit. on p. 63).

[32] G. Giorgiani, H. Bufferand, G. Ciraolo, et al. "A magnetic-field independent approach for strongly anisotropic equations arising plasma-edge transport simulations". In: *Nuclear Materials and Energy* 19 (May 2019), pp. 340–345. ISSN: 23521791. DOI: 10.1016/j.nme.2019.03.002. URL: https://linkinghub.elsevier.com/retrieve/pii/S2352179118302357 (visited on 02/01/2023) (cit. on p. 64).

[33] M. Scotto d'Abusco, G. Giorgiani, J.F. Artaud, et al. "Core-edge 2D fluid modeling of full tokamak discharge with varying magnetic equilibrium: from WEST start-up to ramp-down". In: *Nuclear Fusion* 62.8 (Aug. 1, 2022), p. 086002. ISSN: 0029-5515, 1741-4326. DOI: 10.1088/1741-4326/ac47ad. URL: https://

iopscience.iop.org/article/10.1088/1741-4326/ac47ad (visited on 02/01/2023) (cit. on p. 64).

[34] H. Bufferand, J. Bucalossi, G. Ciraolo, et al. "Progress in edge plasma turbulence modelling—hierarchy of models from 2D transport application to 3D fluid simulations in realistic tokamak geometry". In: *Nuclear Fusion* 61.11 (Nov. 1, 2021), p. 116052. ISSN: 0029-5515, 1741-4326. DOI: 10.1088/1741-4326/ac2873. URL: https://iopscience.iop.org/article/10.1088/1741-4326/ac2873 (visited on 10/11/2022) (cit. on pp. 64, 69, 100).

[35] R. A. Pitts, X. Bonnin, F. Escourbiac, et al. "Physics basis for the first ITER tungsten divertor". In: *Nuclear Materials and Energy* 20 (Aug. 1, 2019), p. 100696. ISSN: 2352-1791. DOI: 10.1016/j.nme.2019.100696. URL: https://www.sciencedirect.com/science/article/pii/S2352179119300237 (visited on 11/17/2022) (cit. on pp. 64, 88, 132, 157, 162).

[36] A.S. Kukushkin, A.R. Polevoi, H.D. Pacher, et al. "Physics requirements on fuel throughput in ITER". In: *Journal of Nuclear Materials* 415.1 (Aug. 2011), S497–S500. ISSN: 00223115. DOI: 10.1016/j.jnucmat.2010.08.050. URL: https://linkinghub.elsevier.com/retrieve/pii/S0022311510004411 (visited on 02/20/2023) (cit. on p. 70).

[37] D. Reiter. *The EIRENE Code User Manual*. 2019. URL: http://eirene.de/eirene.pdf (cit. on pp. 71, 75, 79, 97, 146, 171, 251).

[38] Wolfgang Eckstein. *Computer Simulation of Ion-Solid Interactions*. Google-Books-ID: 4h3rCAAAQBAJ. Springer Science & Business Media, 1991. 303 pp. ISBN: 978-3-642-73513-4 (cit. on p. 76).

[39] Jerome Spanier and Ely M. Gelbard. *Monte Carlo Principles and Neutron Transport Problems*. Google-Books-ID: SrFFEgzMJpoC. Courier Corporation, 1969. 258 pp. ISBN: 978-0-486-46293-6 (cit. on p. 77).

[40] T.E. Sharp. "Potential-energy curves for molecular hydrogen and its ions". In: *Atomic Data and Nuclear Data Tables* 2 (Dec. 1970), pp. 119–169. ISSN: 0092640X. DOI: 10.1016/S0092-640X(70)80007-9. URL: https://linkinghub.elsevier.com/retrieve/pii/S0092640X70800079 (visited on 02/09/2023) (cit. on pp. 80, 81).

[41] T. Eich, A.W. Leonard, R.A. Pitts, et al. "Scaling of the tokamak near the scrape-off layer H-mode power width and implications for ITER". In: *Nuclear Fusion* 53.9 (Sept. 1, 2013), p. 093031. ISSN: 0029-5515, 1741-4326. DOI: 10.1088/0029-5515/53/9/093031. URL: https://iopscience.iop.org/article/10.1088/0029-5515/53/9/093031 (visited on 12/07/2022) (cit. on pp. 84, 160, 161, 229).

[42] Jae-Sun Park, Xavier Bonnin, and Richard Pitts. “Assessment of ITER divertor performance during early operation phases”. In: *Nuclear Fusion* 61.1 (Jan. 1, 2021), p. 016021. ISSN: 0029-5515, 1741-4326. DOI: 10.1088/1741-4326/abc1ce. URL: https://iopscience.iop.org/article/10.1088/1741-4326/abc1ce (visited on 10/05/2022) (cit. on pp. 84, 85, 123, 157, 162, 209).

[43] K. Schmid, K. Krieger, S.W. Lisgo, et al. “WALLDYN simulations of global impurity migration in JET and extrapolations to ITER”. In: *Nuclear Fusion* 55.5 (May 1, 2015), p. 053015. ISSN: 0029-5515, 1741-4326. DOI: 10.1088/0029-5515/55/5/053015. URL: https://iopscience.iop.org/article/10.1088/0029-5515/55/5/053015 (visited on 12/12/2022) (cit. on pp. 88, 171).

[44] *Fuel Cycle*. ITER. URL: http://www.iter.org/mach/fuelcycle (visited on 02/05/2023) (cit. on p. 88).

[45] *V throughput*. URL: https://www.pfeiffer-vacuum.com/en/know-how/introduction-to-vacuum-technology/fundamentals/pv-throughput/ (visited on 02/05/2023) (cit. on p. 88).

[46] V Kotov, D Reiter, R A Pitts, et al. “Numerical modelling of high density JET divertor plasma with the SOLPS4.2 (B2-EIRENE) code”. In: *Plasma Physics and Controlled Fusion* 50.10 (Oct. 1, 2008), p. 105012. ISSN: 0741-3335, 1361-6587. DOI: 10.1088/0741-3335/50/10/105012. URL: https://iopscience.iop.org/article/10.1088/0741-3335/50/10/105012 (visited on 09/22/2022) (cit. on p. 90).

[47] Vladislav Kotov, Detlev Reiter, and Andrey S Kukushkin. “Numerical study of the ITER divertor plasma with the B2-EIRENE code package”. In: (Nov. 2007). URL: https://www.eirene.de/kotov_solps42_report.pdf (cit. on pp. 90, 91).

[48] D. Reiter. *The AMJUEL Database*. 2020. URL: http://www.eirene.de/amjuel.pdf (cit. on pp. 91, 149).

[49] S. Touchard, J. Mougenot, C. Rond, et al. “AMMONX: A kinetic ammonia production scheme for EIRENE implementation”. In: *Nuclear Materials and Energy* 18 (Jan. 2019), pp. 12–17. ISSN: 23521791. DOI: 10.1016/j.nme.2018.11.020. URL: https://linkinghub.elsevier.com/retrieve/pii/S2352179118301054 (visited on 06/02/2023) (cit. on p. 98).

[50] D. Reiter. *Private communication*. 2023 (cit. on pp. 98, 118).

[51] K. Verhaegh, B. Lipschultz, J.R. Harrison, et al. “The role of plasma-molecule interactions on power and particle balance during detachment on the TCV tokamak”. In: *Nuclear Fusion* 61.10 (Oct. 1, 2021), p. 106014. ISSN: 0029-5515, 1741-4326. DOI: 10.1088/1741-4326/ac1dc5. URL: https://iopscience.iop.org/article/10.1088/1741-4326/ac1dc5 (visited on 12/06/2022) (cit. on p. 100).

[52] A. Holm, P. Börner, T.D. Rognlien, et al. “Comparison of a collisional-radiative fluid model of H2 in UEDGE to the kinetic neutral code EIRENE”. In: *Nuclear Materials and Energy* 27 (June 2021), p. 100982. ISSN: 23521791. DOI: 10.1016/j.nme.2021.100982. URL: https://linkinghub.elsevier.com/retrieve/pii/S235217912100065X (visited on 01/24/2023) (cit. on p. 100).

[53] V. Kotov, D. Reiter, A. S. Kukushkin, et al. “Radiation Absorption Effects in B2-EIRENE Divertor Modelling”. In: *Contributions to Plasma Physics* 46.7 (Sept. 2006), pp. 635–642. ISSN: 0863-1042, 1521-3986. DOI: 10.1002/ctpp.200610056. URL: https://onlinelibrary.wiley.com/doi/10.1002/ctpp.200610056 (visited on 01/24/2023) (cit. on p. 100).

[54] K. Verhaegh, B. Lipschultz, J.R. Harrison, et al. “Spectroscopic investigations of detachment on the MAST Upgrade Super-X divertor”. In: *Nuclear Fusion* 63.1 (Jan. 1, 2023), p. 016014. ISSN: 0029-5515, 1741-4326. DOI: 10.1088/1741-4326/aca10a. URL: https://iopscience.iop.org/article/10.1088/1741-4326/aca10a (visited on 02/08/2023) (cit. on p. 100).

[55] S. Di Genova, A. Gallo, N. Fedorczak, et al. “Modelling of tungsten contamination and screening in WEST plasma discharges”. In: *Nuclear Fusion* 61.10 (Oct. 1, 2021), p. 106019. ISSN: 0029-5515, 1741-4326. DOI: 10.1088/1741-4326/ac2026. URL: https://iopscience.iop.org/article/10.1088/1741-4326/ac2026 (visited on 12/12/2022) (cit. on pp. 100, 171).

[56] H. Yang, G. Ciraolo, J. Bucalossi, et al. “Numerical modelling of the impact of leakage under divertor baffle in WEST”. In: *Nuclear Materials and Energy* 33 (Oct. 2022), p. 101302. ISSN: 23521791. DOI: 10.1016/j.nme.2022.101302. URL: https://linkinghub.elsevier.com/retrieve/pii/S2352179122001831 (visited on 02/01/2023) (cit. on p. 100).

[57] G. Ciraolo, S. Baschetti, H. Bufferand, et al. “A self-consistent cross-field transport model for edge tokamak plasma simulations: SOLEDGE modelling and comparison with experiments”. In: 48th EPS conference on plasma physics. June 27, 2022. URL: https://hal-cea.archives-ouvertes.fr/cea-03766468 (visited on 02/01/2023) (cit. on p. 100).

[58] H. Bufferand, P. Tamain, S. Baschetti, et al. “Description of the model Application to 2D transport modelling Application to 3D turbulence modelling”. In: IAEA. Nov. 4, 2019. URL: https://hal.science/hal-02903014 (visited on 02/01/2023) (cit. on p. 100).

[59] Ulrich Trottenberg, Cornelius W. Oosterlee, and Anton Schuller. *Multigrid*. Google-Books-ID: 9ysyNPZoR24C. Elsevier, Nov. 20, 2000. 648 pp. ISBN: 978-0-08-047956-9 (cit. on p. 102).

[60] Prateek Sharma and Gregory W. Hammett. “Preserving monotonicity in anisotropic diffusion”. In: *Journal of Computational Physics* 227.1 (Nov. 2007), pp. 123–142. ISSN: 00219991. DOI: 10.1016/j.jcp.2007.07.026. URL: https://

linkinghub.elsevier.com/retrieve/pii/S0021999107003233 (visited on 01/18/2023) (cit. on p. 114).

[61] D.V. Borodin, F. Schluck, S. Wiesen, et al. "Fluid, kinetic and hybrid approaches for neutral and trace ion edge transport modelling in fusion devices". In: *Nuclear Fusion* 62.8 (Aug. 1, 2022), p. 086051. ISSN: 0029-5515, 1741-4326. DOI: 10.1088/1741-4326/ac3fe8. URL: https://iopscience.iop.org/article/10.1088/1741-4326/ac3fe8 (visited on 01/18/2023) (cit. on pp. 118, 122).

[62] W. Van Uytven, W. Dekeyser, M. Blommaert, et al. "Advanced spatially hybrid fluid-kinetic modelling of plasma-edge neutrals and application to ITER case using SOLPS-ITER". In: *Contributions to Plasma Physics* 62.5 (June 2022). ISSN: 0863-1042, 1521-3986. DOI: 10.1002/ctpp.202100191. URL: https://onlinelibrary.wiley.com/doi/10.1002/ctpp.202100191 (visited on 01/18/2023) (cit. on pp. 118, 122).

[63] M. Valentinuzzi, Y. Marandet, H. Bufferand, et al. "Two-phases hybrid model for neutrals". In: *Nuclear Materials and Energy* 18 (Jan. 2019), pp. 41–45. ISSN: 23521791. DOI: 10.1016/j.nme.2018.12.003. URL: https://linkinghub.elsevier.com/retrieve/pii/S2352179118301856 (visited on 01/18/2023) (cit. on pp. 118, 122).

[64] N. Horsten, M. Groth, W. Dekeyser, et al. "Validation of SOLPS-ITER simulations with kinetic, fluid, and hybrid neutral models for JET-ILW low-confinement mode plasmas". In: *Nuclear Materials and Energy* 33 (Oct. 2022), p. 101247. ISSN: 23521791. DOI: 10.1016/j.nme.2022.101247. URL: https://linkinghub.elsevier.com/retrieve/pii/S2352179122001284 (visited on 01/18/2023) (cit. on pp. 118, 122).

[65] Kristel Ghoos, Heinke Frerichs, Wouter Dekeyser, et al. "Numerical accuracy and convergence with EMC3-EIRENE". In: *Plasma Science and Technology* 22.5 (May 2020), p. 054001. ISSN: 1009-0630. DOI: 10.1088/2058-6272/ab5866. URL: https://iopscience.iop.org/article/10.1088/2058-6272/ab5866 (visited on 01/29/2023) (cit. on pp. 118, 239).

[66] K. Ghoos, W. Dekeyser, G. Samaey, et al. "Accuracy and convergence of coupled finite-volume/Monte Carlo codes for plasma edge simulations of nuclear fusion reactors". In: *Journal of Computational Physics* 322 (Oct. 2016), pp. 162–182. ISSN: 00219991. DOI: 10.1016/j.jcp.2016.06.049. URL: https://linkinghub.elsevier.com/retrieve/pii/S0021999116302741 (visited on 01/29/2023) (cit. on pp. 118, 239).

[67] M. Baeten, K. Ghoos, M. Baelmans, et al. "Analytical study of statistical error in coupled finite-volume/Monte Carlo simulations of the plasma edge". In: *Contributions to Plasma Physics* 58.6 (July 2018), pp. 659–665. ISSN: 08631042. DOI: 10.1002/ctpp.201700177. URL: https://onlinelibrary.wiley.com/doi/10.1002/ctpp.201700177 (visited on 01/29/2023) (cit. on pp. 118, 119).

[68] Y. Marandet, H. Bufferand, G. Ciraolo, et al. “Effect of Statistical Noise on Simulation Results with a Plasma Fluid Code Coupled to a Monte Carlo Kinetic Neutral Code: Effect of Statistical Noise on Simulation Results with a Plasma Fluid Code Coupled to a Monte Carlo Kinetic Neutral Code”. In: *Contributions to Plasma Physics* 56.6 (Aug. 2016), pp. 604–609. ISSN: 08631042. DOI: 10.1002/ctpp.201610009. URL: https://onlinelibrary.wiley.com/doi/10.1002/ctpp.201610009 (visited on 01/18/2023) (cit. on p. 119).

[69] G Maddison and D Reiter. *Maddison-coupling-report.pdf*. Juel-2872. 1994. URL: http://eirene.de/Maddison-coupling-report.pdf (visited on 02/07/2023) (cit. on p. 119).

[70] Kristel Ghoos, Giovanni Samaey, and Martine Baelmans. “Accuracy and convergence of iteratively solved Monte Carlo codes for simulations in the plasma edge of nuclear fusion reactors”. In: *Contributions to Plasma Physics* 58.6 (July 2018), pp. 652–658. ISSN: 08631042. DOI: 10.1002/ctpp.201700181. URL: https://onlinelibrary.wiley.com/doi/10.1002/ctpp.201700181 (visited on 01/29/2023) (cit. on p. 122).

[71] K. Ghoos, W. Dekeyser, G. Samaey, et al. “Accuracy and Convergence of Coupled Finite-Volume / Monte-Carlo Codes for Plasma Edge Simulations: Accuracy and Convergence of Coupled Finite-Volume / Monte-Carlo Codes for Plasma Edge Simulations”. In: *Contributions to Plasma Physics* 56.6 (Aug. 2016), pp. 616–621. ISSN: 08631042. DOI: 10.1002/ctpp.201610010. URL: https://onlinelibrary.wiley.com/doi/10.1002/ctpp.201610010 (visited on 01/29/2023) (cit. on p. 122).

[72] W. Dekeyser, P. Boerner, S. Voskoboynikov, et al. “Plasma edge simulations including realistic wall geometry with SOLPS-ITER”. In: *Nuclear Materials and Energy* 27 (June 2021), p. 100999. ISSN: 23521791. DOI: 10.1016/j.nme.2021.100999. URL: https://linkinghub.elsevier.com/retrieve/pii/S2352179121000788 (visited on 11/16/2022) (cit. on p. 124).

[73] S. O. Makarov, D. P. Coster, V. A. Rozhansky, et al. “Equations and improved coefficients for parallel transport in multicomponent collisional plasmas: Method and application for tokamak modeling”. In: *Physics of Plasmas* 28.6 (June 2021), p. 062308. ISSN: 1070-664X, 1089-7674. DOI: 10.1063/5.0047618. URL: https://aip.scitation.org/doi/10.1063/5.0047618 (visited on 12/19/2022) (cit. on p. 124).

[74] M. Moscheni, C. Meineri, M. Wigram, et al. “Cross-code comparison of the edge codes SOLPS-ITER, SOLEDGE2D and UEDGE in modelling a low-power scenario in the DTT”. In: *Nuclear Fusion* 62.5 (May 1, 2022), p. 056009. ISSN: 0029-5515, 1741-4326. DOI: 10.1088/1741-4326/ac42c4. URL: https://iopscience.iop.org/article/10.1088/1741-4326/ac42c4 (visited on 12/19/2022) (cit. on p. 129).

[75] S. I. Krasheninnikov, A. S. Kukushkin, and A. A. Pshenov. “Divertor plasma detachment”. In: *Physics of Plasmas* 23.5 (May 2016), p. 055602. ISSN: 1070-664X, 1089-7674. DOI: 10.1063/1.4948273. URL: http://aip.scitation.org/doi/10.1063/1.4948273 (visited on 12/22/2022) (cit. on p. 134).

[76] D. Tskhakaya. “On Recent Massively Parallelized PIC Simulations of the SOL”. In: *Contributions to Plasma Physics* 52.5 (June 2012), pp. 490–499. ISSN: 08631042. DOI: 10.1002/ctpp.201210038. URL: https://onlinelibrary.wiley.com/doi/10.1002/ctpp.201210038 (visited on 01/28/2023) (cit. on p. 146).

[77] S Devaux and G Manfredi. “Magnetized plasma–wall transition—consequences for wall sputtering and erosion”. In: *Plasma Physics and Controlled Fusion* 50.2 (Feb. 1, 2008), p. 025009. ISSN: 0741-3335, 1361-6587. DOI: 10.1088/0741-3335/50/2/025009. URL: https://iopscience.iop.org/article/10.1088/0741-3335/50/2/025009 (visited on 01/28/2023) (cit. on p. 146).

[78] S. I. Krasheninnikov and A. S. Kukushkin. “1D model of tokamak scrape-off layer and divertor plasmas: Dimensionless parameters and the results of numerical simulations”. In: *Physics of Plasmas* 29.12 (Dec. 2022), p. 122502. ISSN: 1070-664X, 1089-7674. DOI: 10.1063/5.0129131. URL: https://aip.scitation.org/doi/10.1063/5.0129131 (visited on 01/07/2023) (cit. on p. 155).

[79] C. Guillemaut, R.A. Pitts, A.S. Kukushkin, et al. “Influence of atomic physics on EDGE2D-EIRENE simulations of JET divertor detachment with carbon and beryllium/tungsten plasma-facing components”. In: *Nuclear Fusion* 54.9 (Sept. 1, 2014), p. 093012. ISSN: 0029-5515, 1741-4326. DOI: 10.1088/0029-5515/54/9/093012. URL: https://iopscience.iop.org/article/10.1088/0029-5515/54/9/093012 (visited on 01/07/2023) (cit. on p. 155).

[80] E. Kaveeva, V. Rozhansky, I. Senichenkov, et al. “SOLPS-ITER modelling of ITER edge plasma with drifts and currents”. In: *Nuclear Fusion* 60.4 (Apr. 1, 2020), p. 046019. ISSN: 0029-5515, 1741-4326. DOI: 10.1088/1741-4326/ab73c1. URL: https://iopscience.iop.org/article/10.1088/1741-4326/ab73c1 (visited on 12/13/2022) (cit. on pp. 161, 209, 241).

[81] X. Bonnin J.S. Park. *Private communication*. 2021 (cit. on p. 162).

[82] W Fundamenski. “Parallel heat flux limits in the tokamak scrape-off layer”. In: *Plasma Physics and Controlled Fusion* 47.11 (Nov. 1, 2005), R163–R208. ISSN: 0741-3335, 1361-6587. DOI: 10.1088/0741-3335/47/11/R01. URL: https://iopscience.iop.org/article/10.1088/0741-3335/47/11/R01 (visited on 12/01/2022) (cit. on p. 166).

[83] *ITER Research Plan within the Staged Approach (Level III-Provisional version) ITER Technical Report ITR-18-003*. https://www.iter.org/technical-reports. 2018 (cit. on p. 168).

[84] J. Romazanov, A. Kirschner, S. Brezinsek, et al. “Beryllium erosion and redeposition in ITER H, He and D–T discharges”. In: *Nuclear Fusion* 62.3 (Mar. 1, 2022), p. 036011. ISSN: 0029-5515, 1741-4326. DOI: 10.1088/1741-4326/ac4776. URL: https://iopscience.iop.org/article/10.1088/1741-4326/ac4776 (visited on 09/23/2022) (cit. on p. 171).

[85] William L. Rowan, R.D. Bengtson, X. Bonnin, et al. “Particle balance in diverted plasmas in TEXT-U”. In: *Journal of Nuclear Materials* 220-222 (Apr. 1995), pp. 668–671. ISSN: 00223115. DOI: 10.1016/0022-3115(94)00562-1. URL: https://linkinghub.elsevier.com/retrieve/pii/0022311594005621 (visited on 02/14/2023) (cit. on p. 181).

[86] N. Vianello, D. Carralero, C.K. Tsui, et al. “Scrape-off layer transport and filament characteristics in high-density tokamak regimes”. In: *Nuclear Fusion* 60.1 (Jan. 1, 2020), p. 016001. ISSN: 0029-5515, 1741-4326. DOI: 10.1088/1741-4326/ab423e. URL: https://iopscience.iop.org/article/10.1088/1741-4326/ab423e (visited on 10/12/2022) (cit. on pp. 181, 182).

[87] A. Wynn, B. Lipschultz, I. Cziegler, et al. “Investigation into the formation of the scrape-off layer density shoulder in JET ITER-like wall L-mode and H-mode plasmas”. In: *Nuclear Fusion* 58.5 (May 1, 2018), p. 056001. ISSN: 0029-5515, 1741-4326. DOI: 10.1088/1741-4326/aaad78. URL: https://iopscience.iop.org/article/10.1088/1741-4326/aaad78 (visited on 10/12/2022) (cit. on pp. 181–183).

[88] W. Eckstein. *Sputtering, reflection and range values for plasma edge codes (IPP–9/117)*. 1998. URL: https://inis.iaea.org/search/30003883 (cit. on p. 201).

[89] Jr Neilson. *Charge exchange measurements of ion behavior in the ISX tokamak*. ORNL/TM-7333. Oak Ridge National Lab. (ORNL), Oak Ridge, TN (United States), Dec. 1, 1980. DOI: 10.2172/6752774. URL: https://www.osti.gov/biblio/6752774 (visited on 02/05/2023) (cit. on p. 201).

[90] J. T. Hogan and J. F. Clarke. *Fluxes of charged and neutral particles from tokamaks*. CONF-740104-9. Oak Ridge National Lab., Tenn. (USA), Jan. 1, 1973. URL: https://www.osti.gov/biblio/4334091 (visited on 02/05/2023) (cit. on p. 201).

[91] K. Gałązka, N. Rivals, P. Tamain, et al. “Particle transport and heat loads in JT-60SA studied by SOLEDGE-EIRENE code”. In: AAPPS DPP 2022 - 6th Asia-Pacific Conference on Plasma Physics. Oct. 9, 2022. URL: https://hal-cea.archives-ouvertes.fr/cea-03949501 (visited on 02/23/2023) (cit. on p. 208).

[92] Hong-sup Hahn. “Quantum Transport Cross Sections for Ionized Gases”. In: *Physics of Fluids* 14.2 (1971), p. 278. ISSN: 00319171. DOI: 10.1063/1.1693425. URL: https://aip.scitation.org/doi/10.1063/1.1693425 (visited on 12/01/2022) (cit. on p. 232).

[93] A S Kukushkin and S I Krasheninnikov. “Bifurcations and oscillations in divertor plasma”. In: *Plasma Physics and Controlled Fusion* 61.7 (July 1, 2019), p. 074001. ISSN: 0741-3335, 1361-6587. DOI: 10.1088/1361-6587/ab1bba. URL: https://iopscience.iop.org/article/10.1088/1361-6587/ab1bba (visited on 02/14/2023) (cit. on p. 239).

[94] A S Kukushkin and H D Pacher. “Divertor modelling and extrapolation to reactor conditions”. In: *Plasma Physics and Controlled Fusion* 44.6 (June 1, 2002), pp. 931–943. ISSN: 0741-3335, 1361-6587. DOI: 10.1088/0741-3335/44/6/320. URL: https://iopscience.iop.org/article/10.1088/0741-3335/44/6/320 (visited on 02/14/2023) (cit. on p. 251).

APPENDICES

A. Impact of updated magnetic equilibrium and wall geometry

This section compares results obtained for a high throughput case (#103030) between the initial assumptions on the magnetic equilibrium and wall which were adopted for the development of the SOLPS simulation database for ITER, and updated versions in 2021. The updated configuration can be found in ITER IMAS database: magnetic equilibrium #135011 run 7, and wall #116000 run 2, as shown in Figure A.1. The key difference in these two geometries is a reduction of the outer mid-plane distance between the primary and secondary separatrices from 11cm to 6.5cm. The wall contour involves only one change: the inner wall has been brought 6.5mm closer to the plasma.

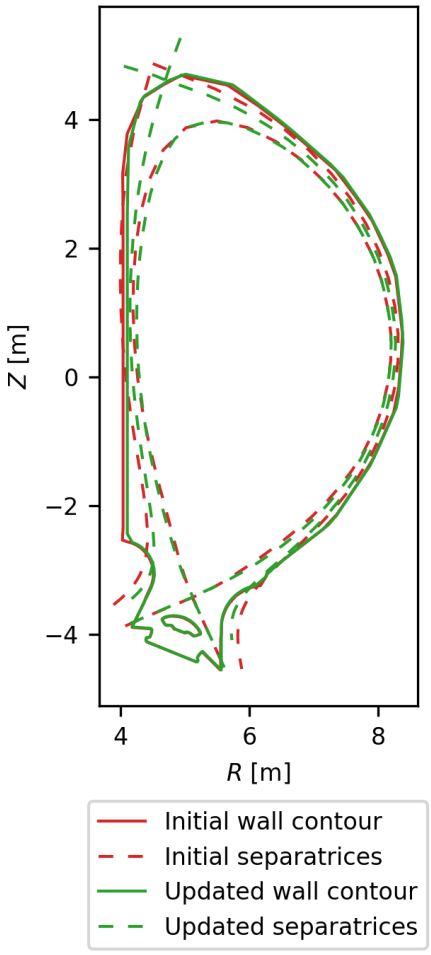

Figure A.1.: Comparison between the initial (red) and updated (green) magnetic equilibrium from recent DINA scenario (#135011 run 7) and wall contour with a central column closer to the plasma (#116000 run 2).

Overall, no significant difference on the metrics of interest considered here is observed. This was to be expected, as in both configurations, the magnetic equilibrium is consistent with the wall assumption. If one had executed the simulations with the previous magnetic equilibrium but the updated wall, in this case a large increase of fluxes on the central column could have been expected.

The details on the results are shown in the figures below, which show upstream Figure A.2 and downstream Figure A.3 conditions, as well as target fluxes Figure A.4 and first wall fluxes Figure A.5.

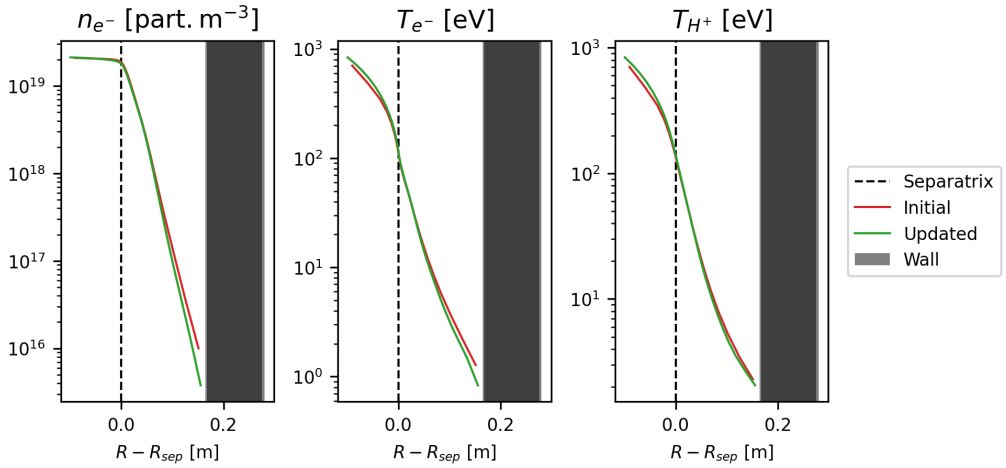

Figure A.2.: Comparison in upstream plasma conditions at the outer midplane between initial and updated magnetic equilibrium and wall.

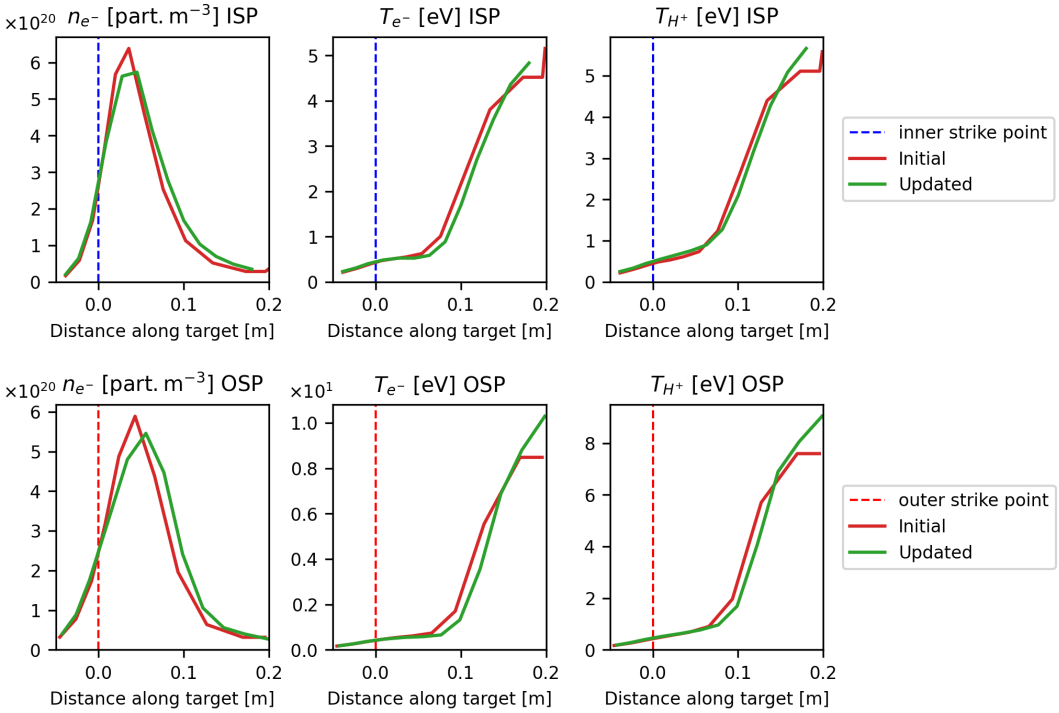

Figure A.3.: Comparison between initial and updated magnetic equilibrium and wall on the inner (top row) and outer (bottom row) target plasma conditions.

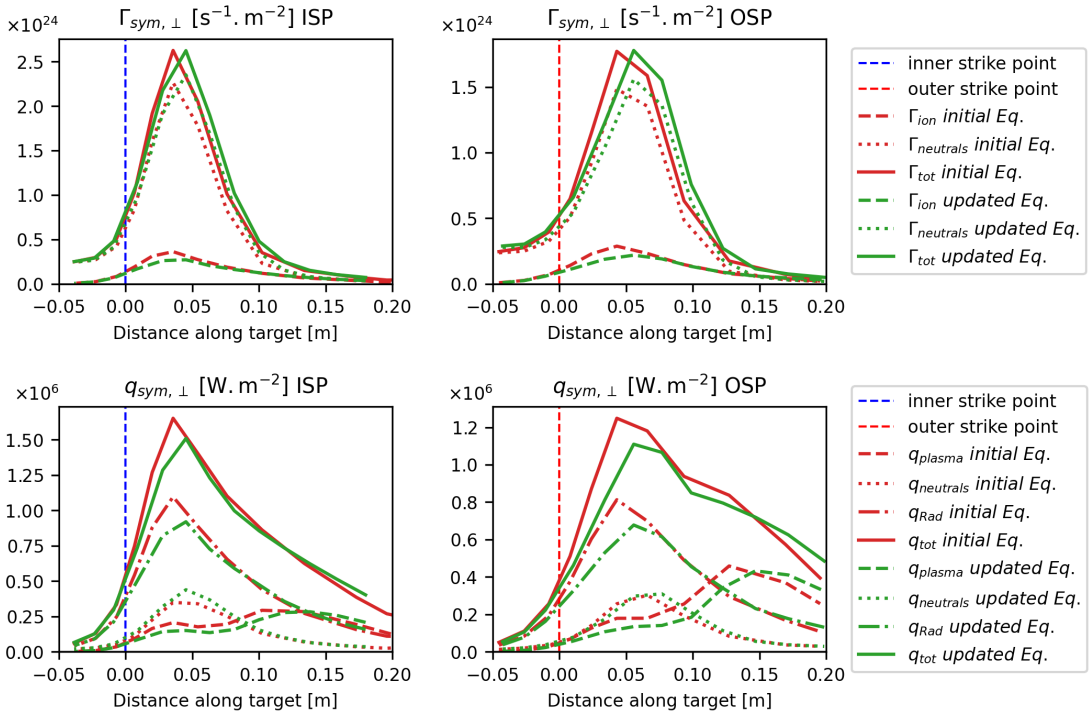

Figure A.4.: Comparison between initial and updated magnetic equilibrium and wall on the inner (left column) and outer (right column) target particle (top row) and heat (bottom row) fluxes.

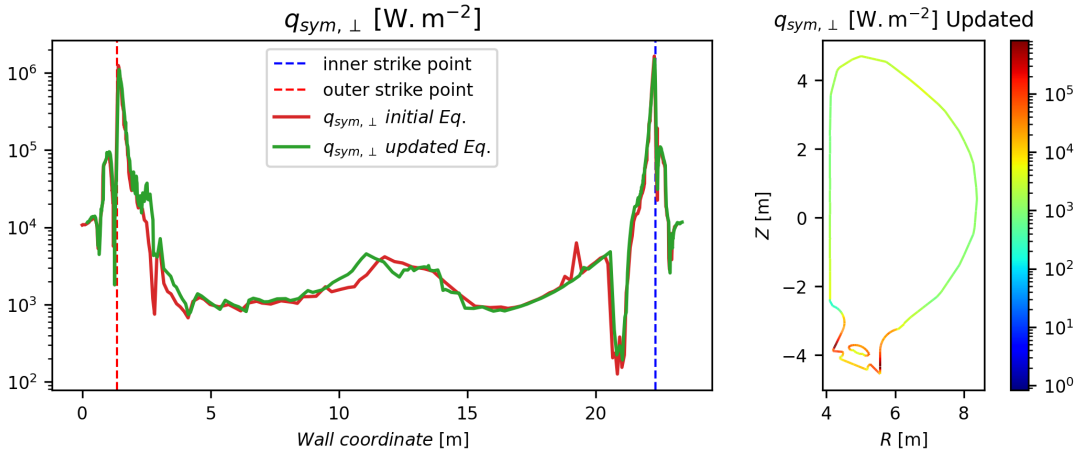

Figure A.5.: 1D plot of the total perpendicular toroidally symmetric heat flux (including contributions from plasma, neutrals, and radiation) against the wall curvilinear coordinate for the previous and updated magnetic equilibrium and wall for the initial configuration in red and the updated configuration in green. 0 starts at the bottom of the machine then increases counter clockwise, starting from the outer target and ending on the inner target.

B. Computation of $\lambda_{q,e}$

To ensure clarity of the meaning of "$\lambda_{q,e}$", a proxy for λ_q used in this document, this section describes the computation of this quantity. It is intended to be identical to the computation of the one used in SOLPS output (`xwhm_par_ol` quantity in the `peak_power_w file`) to be relevant for comparison purposes.

It is especially emphasized that what is called here λ_q is neither the definition from a parameterized fit via the Wagner-Eich method [41] which relies on quantities solely located at the target, nor solely upstream quantities at the outer mid-plane through an artificial Bohm condition there.

The following elements are the basis of the approach:

- The calculation needs to be independent of any fixed coordinate system
- The SOL width λ_q is the width at the "upstream" location, and so need to be understood as the width at the outer mid-plane.
- The width is defined here as the width where the majority of the heat transport happens, and since we are interested in upstream quantities, the parallel heat flux will be used as a base.
- This heat flux profile is expected in the form of a decaying exponential, therefore λ_q will be the parameter of this exponential profile.
- The actual quantity of interest is the heat deposition on the targets, which depend on their geometry, which is to say the angle of incidence. The exponential characteristic length λ_q will not change depending on the angle of incidence itself, only by its variation along the target. Therefore this will have to be taken into account.
- The objective is to base this computation on a profile of the upstream parallel heat flux that is devoid of as much other effects as possible. Care needs to be taken for two of them that will affect the profile shape:
  - upstream side: the proximity of the stagnation point to the outer midplane
  - downstream side: effects of interactions with neutrals

  The most simple procedure in this case is to scan between the outer midplane and the divertor entrance for the location of the maximum parallel heat flux.
- Finally, the objective is to fit a decaying exponential on the profile, however the ion parallel heat flux can flow upward near the separatrix away from the target, which would impact the quality of the fit. For this reason the heat flux is restricted to the electron heat flux which is found to be always downward in the simulations. This simplification is also supported by the fact that the electrons carry the majority of the parallel heat flux in this region.

The computation is sequenced as such:

- Scan for all poloidal indices between the outer midplane and the X point the radial profile of the plasma electron parallel heat flux, and select the poloidal index where the peak parallel heat flux density is the highest among all radial profiles.
- For each data point of that parallel heat flux profile (radial indices), follow the field line until the target, and project the parallel heat flux with the incidence angle that was found at the corresponding point on the target.
- For this selected profile, project its curviliear coordinate to the outer mid-plane
- From the peak in the profile, fit an exponential decay length by means of the half-maximum method. Here s is the curvilinear coordinate:

$$\lambda_q = \frac{s_{q_{\parallel,peak}/2} - s_{q_{\parallel,peak}}}{\ln 2} \tag{B.1}$$

C. Expressions for the collisional friction force and thermal equipartition systems

C.0.1. Friction force (momentum exchange)

The friction force from species β applied to species α $R_{\alpha\beta}^{\text{fric}}$ Equation C.1 is found in Zhdanov's work [26] by combining expression (3.1.10) p.55 with the expression for $\tau_{\alpha\beta}^{-1}$ Equation C.3 in (3.1.17) p.56.

$$R_{\alpha\beta}^{\text{fric}} = -n_\alpha \mu_{\alpha\beta} \tau_{\alpha\beta}^{-1} (w_\alpha - w_\beta) \tag{C.1}$$

where the reduced mass $\mu_{\alpha\beta}$, the inverse collision time $\tau_{\alpha\beta}^{-1}$, the relative parallel velocity w_α to the common velocity $\overline{u}$, and the effective Coulomb logarithm Λ_{eff} are defined as:

$$\mu_{\alpha\beta} = \frac{m_\alpha m_\beta}{m_\alpha + m_\beta} \tag{C.2}$$

$$\tau_{\alpha\beta}^{-1} = \frac{16\pi^{1/2}}{3} n_\beta \left(\frac{\gamma_{\alpha\beta}}{2}\right)^{3/2} \left(\frac{e_\alpha e_\beta}{4\pi\varepsilon_0 \mu_{\alpha\beta}}\right)^2 \ln\Lambda_{\alpha\beta} \tag{C.3}$$

$$w_\alpha = u_\alpha - \overline{u} \tag{C.4}$$

$$\overline{u} = \frac{\sum_\alpha m_\alpha n_\alpha u_\alpha}{\sum_\alpha m_\alpha n_\alpha} \tag{C.5}$$

$$\gamma_{\alpha\beta} = \frac{\gamma_\alpha \gamma_\beta}{\gamma_\alpha + \gamma_\beta} \tag{C.6}$$

$$\gamma_\alpha = \frac{m_\alpha}{k_B T_\alpha} \tag{C.7}$$

$$\Lambda_{\alpha\beta} \simeq \Lambda_{\text{eff}} = \frac{12\pi\varepsilon_0^{3/2} k_B T_{\text{eff}}}{Z_{\text{eff}} e^2} \left(\frac{k_B T_{\text{eff}}}{n_e e^2 (1 + Z_{\text{eff}})}\right)^{1/2} + 1 \tag{C.8}$$

Here we also make a note of two specific points regarding the treatment of the Coulomb Logarithm in SOLEDGE3X (Equation C.8):

- it is taken as the "common" Coulomb Logarithm (i.e. identical for all species)

based on the common temperature and effective charge Z_{eff}, as described in chapter 8 in expression 8.1.5 which assumes $|T_\alpha - T_\beta| \ll T_\alpha$. In this case, as each ion possesses its own temperature in SOLEDGE3X, the common temperature for this expression is chosen as the effective temperature T_{eff}.

- at very low temperature < 0.2 eV for plasma dense regions, which can sometimes occur in computing transients in ITER's divertor in SOLEDGE3X, the expression for Λ found in Zhdanov's work can become smaller than 1, producing a negative Coulomb Logarithm, which would nonphysically invert the computed heat flux. This behavior is due to the classical approach to collisions that was used by Zhdanov and is valid at high temperatures, however for low temperatures, quantum effects have to be accounted for. Corrections for this case were carried out by Hahn et al. in [92], where they compute cross sections for Coulomb collisions in the quantum case, then bridge the gap to the classical model at high temperature. This results in the addition of a "+1" correction term in the logarithm computation and produces a well-behaved asymptotic limit at the low-T range, preventing negative values, which can be seen in Equation C.8.

We can rewrite this force to make the quantity $\Gamma_\alpha = n_\alpha u_\alpha$ solved by the code appear from the double dependence in density in $\lambda_{\alpha\beta}$, and using $w_\alpha - w_\beta = u_\alpha - u_\beta$:

$$R_{\alpha\beta}^{\text{fric}} = -\frac{1}{3}(2\pi)^{-3/2} Z_\alpha^2 Z_\beta^2 e^4 \mu_{\alpha\beta}^{1/2} \frac{\ln \Lambda_{\text{eff}}}{(k_B T_{\text{eff}})^{3/2} \varepsilon_0^2} (n_\beta n_\alpha u_\alpha - n_\alpha n_\beta u_\beta) \tag{C.9}$$

$$R_{\alpha\beta}^{\text{fric}} = -\frac{1}{3}(2\pi)^{-3/2} Z_\alpha^2 Z_\beta^2 e^4 \mu_{\alpha\beta}^{1/2} \frac{\ln \Lambda_{\text{eff}}}{(k_B T_{\text{eff}})^{3/2} \varepsilon_0^2} (n_\beta \Gamma_\alpha - n_\alpha \Gamma_\beta) \tag{C.10}$$

Let us now define the coefficient $B_{\alpha\beta}$:

$$B_{\alpha\beta} = \frac{1}{3}(2\pi)^{-3/2} Z_\alpha^2 Z_\beta^2 e^4 \mu_{\alpha\beta}^{1/2} \frac{\ln \Lambda_{\text{eff}}}{(k_B T_{\text{eff}})^{3/2} \varepsilon_0^2} \tag{C.11}$$

The force from β to α now reads:

$$R_{\alpha\beta}^{\text{fric}} = B_{\alpha\beta}(n_\alpha \Gamma_\beta - n_\beta \Gamma_\alpha) \tag{C.12}$$

Summing over all species to get the total friction force on α:

$$R_\alpha^{\text{fric}} = \sum_\beta B_{\alpha\beta}(n_\alpha \Gamma_\beta - n_\beta \Gamma_\alpha) \tag{C.13}$$

$$= \sum_\beta B_{\alpha\beta} n_\alpha \Gamma_\beta - \left(\sum_\beta B_{\alpha\beta} n_\beta \right) \Gamma_\alpha \tag{C.14}$$

Now, since this expression will be used in a system for solving the parallel particle flux Γ (which is also the quantity solved by the code), and we recall that $R_{\alpha\beta}$ is a force, we need to divide by the mass of species α to recover a rate of Γ:

$$R^{\text{fric},\Gamma}_{\alpha\beta} = \frac{R^{\text{fric}}_{\alpha\beta}}{m_\alpha} \tag{C.15}$$

This can be written for all species in matrix form:

$$R^{\text{fric},\Gamma} = M^R.\Gamma \tag{C.16}$$

$$M^R_{\alpha\beta} = \begin{cases} \frac{B_{\alpha\beta} n_\alpha}{m_\alpha} & \text{if } \alpha \neq \beta \\ -\sum_{k\neq\alpha} \frac{B_{\alpha k} n_k}{m_\alpha} & \text{if } \alpha = \beta \end{cases} \tag{C.17}$$

C.0.2. Energy equipartition (thermal energy exchange)

The expression of the energy equipartition heat flux from species β received by species α $Q_{\alpha\beta}$ is found in Zhdanov's work [26] by combining expression 3.1.11 p.55 with $\tau^{-1}_{\alpha\beta}$ in expression 3.1.17 p.56 (Equation C.3).

$$Q^{th}_{\alpha\beta} = 3 k_B n_\alpha \left(\frac{\mu_{\alpha\beta}}{m_\alpha + m_\beta}\right) \tau^{-1}_{\alpha\beta} (T_\beta - T_\alpha) \tag{C.18}$$

We define here the $A_{\alpha\beta}$ coefficient such as:

$$Q^{th}_{\alpha\beta} = \frac{3}{2} n_\alpha n_\beta A_{\alpha\beta} (T_\beta - T_\alpha) \tag{C.19}$$

$$A_{\alpha\beta} = 2 k_B \left(\frac{\mu_{\alpha\beta}}{m_\alpha + m_\beta}\right) \frac{16\pi^{1/2}}{3} \left(\frac{\gamma_{\alpha\beta}}{2}\right)^{3/2} \left(\frac{e_\alpha e_\beta}{4\pi\varepsilon_0 \mu_{\alpha\beta}}\right)^2 \ln\Lambda_{\text{eff}} \tag{C.20}$$

The total equipartition heat flux Q^{th}_α received by species α is the sum of all elemental equipartition heat fluxes coming from all other species, expressed using the thermal energy densities.

$$E_{th,\alpha} = \frac{3}{2} n_\alpha T_\alpha \tag{C.21}$$

$$Q^{th}_\alpha = \sum_\beta Q^{th}_{\alpha\beta} = \sum_\beta \frac{3}{2} n_\alpha n_\beta A_{\alpha\beta} (T_\beta - T_\alpha) = \sum_\beta A_{\alpha\beta} (n_\alpha E_{th,\beta} - n_\beta E_{th,\alpha}) \tag{C.22}$$

$$= \sum_\beta A_{\alpha\beta} n_\alpha E_{th,\beta} - \left(\sum_\beta A_{\alpha\beta} n_\beta\right) E_{th,\alpha} \tag{C.23}$$

We obtain the following form with the matrix M and its $M_{\alpha\beta}$ coefficients:

$$Q^{th} = M^Q.E_{th} \tag{C.24}$$

$$M^Q = \begin{cases} A_{\alpha\beta} n_\alpha & \text{if } \alpha \neq \beta \\ -\sum_{k\neq\alpha} A_{\alpha k} n_k & \text{if } \alpha = \beta \end{cases} \tag{C.25}$$

Turning back from the internal energy E_{th} to the total energy E equation which includes the kinetic energy E_{kin}:

$$E = E_{th} + E_{kin} = E_{th} + \frac{1}{2}\frac{m}{n}\Gamma^2 \tag{C.26}$$

$$Q^{th} = M^Q.E_{th} = M^Q.(E - \frac{1}{2}m\frac{\Gamma^2}{n}) = M^Q.E - M^Q.\frac{1}{2}m\frac{\Gamma^2}{n} \tag{C.27}$$

$$Q^{th} = M^Q.E + C_{kin} \quad \text{with} \quad C_{kin} = -M^Q.\frac{1}{2}m\frac{\Gamma^2}{n} \tag{C.28}$$

Again, no linearization is necessary here for Γ which can be calculated directly.

C.0.3. Work of collisional forces

We turn now to the energy transfers associated with the collisional forces $R^{\text{fric}}_{\alpha\beta}$ and $R^{\text{therm}}_{\alpha\beta}$. Since the Q^{th}_α and R_α from Zhdanov's formulations are computed in the common velocity frame of reference, and the equations of the code are solved in the frame of the laboratory, this makes appear a non-symmetric force work term in the form of $w_\alpha R\alpha$ in the equations p.44 (2.4.8). In order to conserve energy (i.e., $\sum_\alpha Q^W_\alpha = 0$), a correction term was added which reduces to the Bragingskii formulation for single species plasmas. The following generalization conserves energy for multi-species, but could be refined and is under discussions.

The term from Zhdanov's expression in 2.4.8 applied to α from collisions with species β take the following form:

$$Q^W_{\alpha\beta} = R_{\alpha\beta} u_\alpha = \left(R^{\text{fric}}_{\alpha\beta} + R^{\text{therm}}_{\alpha\beta}\right) u_\alpha \tag{C.29}$$

With now the added correction:

$$Q^W_{\alpha\beta} = R_{\alpha\beta} u_\alpha - R_{\alpha\beta}\frac{m_\beta}{m_\alpha + m_\beta}(u_\alpha - u_\beta) \tag{C.30}$$

$$Q^W_{\alpha\beta} = R_{\alpha\beta}\frac{m_\alpha u_\alpha + m_\beta u_\beta}{m_\alpha + m_\beta} \tag{C.31}$$

Since $R_{\alpha\beta} = -R_{\beta\alpha}$ it follows that $Q_{\alpha\beta} = -Q_{\beta\alpha}$, i.e. we recover the energy conservation for the whole system.

$$Q^W_{\alpha\beta} = \left(\frac{m_\alpha}{m_\alpha + m_\beta} \frac{\Gamma_\alpha}{n_\alpha} + \frac{m_\beta}{m_\alpha + m_\beta} \frac{\Gamma_\beta}{n_\beta} \right) R_{\alpha\beta} \tag{C.32}$$

Let us note:

$$\mu'_\alpha = \frac{m_\alpha}{m_\alpha + m_\beta} \qquad \text{and} \qquad \mu'_\beta = \frac{m_\beta}{m_\alpha + m_\beta} \tag{C.33}$$

$$Q^W_{\alpha\beta} = \left(\mu'_\alpha \frac{\Gamma_\alpha}{n_\alpha} + \mu'_\beta \frac{\Gamma_\beta}{n_\beta} \right) \left(R^{\text{fric}}_{\alpha\beta} + R^{\text{therm}}_{\alpha\beta} \right) \tag{C.34}$$

Substituting Equation C.12 in Equation C.34:

$$Q^W_{\alpha\beta} = \mu'_\alpha \frac{\Gamma_\alpha}{n_\alpha} B_{\alpha\beta}(n_\alpha \Gamma_\beta - n_\beta \Gamma_\alpha) + \mu'_\beta \frac{\Gamma_\beta}{n_\beta} B_{\alpha\beta}(n_\alpha \Gamma_\beta - n_\beta \Gamma_\alpha) + \left(\mu'_\alpha \frac{\Gamma_\alpha}{n_\alpha} + \mu'_\beta \frac{\Gamma_\beta}{n_\beta} \right) R^{\text{therm}}_{\alpha\beta} \tag{C.35}$$

$$Q^W_{\alpha\beta} = B_{\alpha\beta} \left[(\mu'_\alpha - \mu'_\beta) \Gamma_\alpha \Gamma_\beta - \mu'_\alpha \frac{n_\beta}{n_\alpha} \Gamma^2_\alpha + \mu'_\beta \frac{n_\alpha}{n_\beta} \Gamma^2_\beta \right] + \left(\mu'_\alpha \frac{\Gamma_\alpha}{n_\alpha} + \mu'_\beta \frac{\Gamma_\beta}{n_\beta} \right) R^{\text{therm}}_{\alpha\beta} \tag{C.36}$$

Where finally:

$$Q^W_\alpha = \sum_\beta Q^W_{\alpha\beta} \tag{C.37}$$

One possible approach would be to linearize the latter expression in terms of Γ and build a system that includes Γ and E and solve it in one go. However, since Γ does not depend on E here, this linearization is not necessary and it is possible to use in this expression directly the values of Γ obtained from solving the Γ-only system (i.e. the new values of Γ for the next time step). Also, the linearization approach was attempted and did not improve sufficiently the stability of the case, and this was attributed to the approximation in the linearization.

D. Numerical matters related to multispecies case at high power

D.1. Challenges

While running the low-power, single-species ITER runs presented in the previous sections of this work proved to be very challenging, the full-power multi-species case with a transport barrier raises the bar on a whole other level. This section introduces the different aspects that factor into such an increased challenge.

Those were, in fact, the drivers of some of the development mentioned in chapter 3. The collisional closure coupling terms between species can become very large (friction forces, energy equipartition), and neutral interaction terms become very strong and unstable. Therefore, time scales become very short, especially the one from plasma neutral interactions, and the computation time becomes unreasonably long. The reasons for this are detailed below. Therefore with the transport barrier, which results in an equilibrium time of the plasma to the order of the second, the order of magnitude of computation time is the year. However, the multigrid approach largely speeds up the process, as the simulation can be very strongly accelerated at the start. The computation time for such an ITER case is now around three months.

D.2. Effect of the number of particles

This can be seen on Figure D.1, which shows on the left the evolution of the integrated deuterium particle source, for 10,000 time-steps for an FPO 100MW Deuterium-Neon-Helium case. Each curve corresponds to a different number of particles in the Monte Carlo solver. Even with 500 particles per stratum, a very low number, the solution is stable and does not drift. The variations can be seen in the middle plot, where the y-axis focuses just on the range of plotted values. Increasing the number of particles presents a minimal gain in this case, and is immensely expensive, as is seen on the right plot showing the number of wall-clock hours to compute a millisecond of plasma versus the number of particles. It increases very rapidly from 7 hours with 500 particles to more than 250 with 40,000. However, it must be noted that the time step is rather small (3.8×10^{-8}s) in this case.

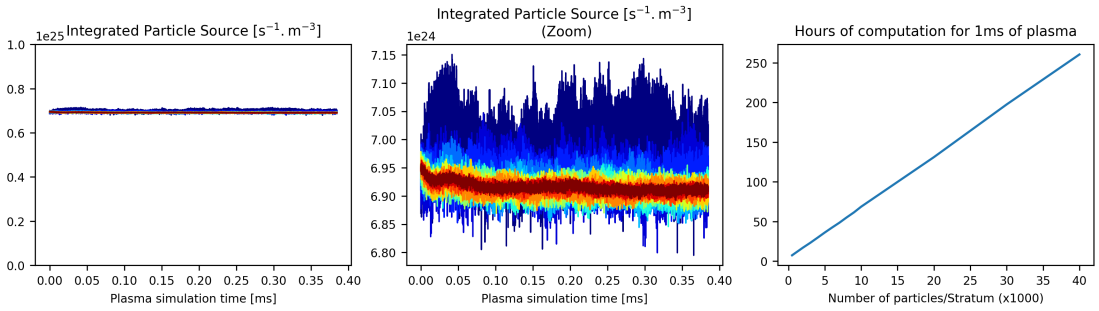

Figure D.1.: Effect of scanning of the number of particles per EIRENE stratum, from 500 to 40,000, for an FPO ITER case with Deuterium, Neon, and Helium on the coarse grid (6mm at the target). 10,000 time-steps, an EIRENE call at each time step, at a fixed time step of 3.8×10^{-8}s. Left and middle graph: volume integral of the deuterium D^+ particle source. Each curve corresponds to a different number of particles, as mentioned in the legend. The middle graph is the same data, with the y-axis zoomed to see variations. Right: computation speed, displayed as hours of wall clock time to compute one millisecond of plasma, as a function of the number of particles. Computed on the ITER cluster, with 36 cores.

D.3. Effect of the time between EIRENE calls

This effect is illustrated in Figure D.2, where the evolution of the integrated particle source is plotted, for different values of the time step, i.e. the duration between EIRENE calls (EIRENE is called at every time step of the SOLEDGE3X time stepper). It can be noted that those values of the time step are below the maximum allowed value for the plasma solver via its CFL condition so that any change in the stability of the solution is more likely to be an effect of the frequency of calls to the neutrals solver and not an effect of the numerical stability of the plasma solver itself. Two scans are performed, one with 1,000 particles on the left, and one with 10,000 particles on the middle. Two conclusions can be drawn:

- Contrary to the number of particles, the time step length has a very strong influence on the noise and stability of the code. Going beyond 5.0×10^{-7} s proved to be unsuccessful in the considered case, showing two symptoms:
  - If the time step is moderately too large, case 9.6×10^{-7} s in royal blue, the solution is biased and bifurcates, as can be seen by the shape of the curve, very different from other runs. In fact, in this case, the dense plasma blob at the targets is pushed to the target and disappears; and the plasma reattaches abruptly.
  - If the time step becomes large at 1.9×10^{-6} s in dark blue, the case becomes so unstable that it simply crashes.

- Increasing the number of particles by one order of magnitude does not compensate for the decreased stability of raising the time step, and has no beneficial effects, as the exact same behaviors, including bifurcation and crash, are obtained. It simply translates as an increase in the computation time.

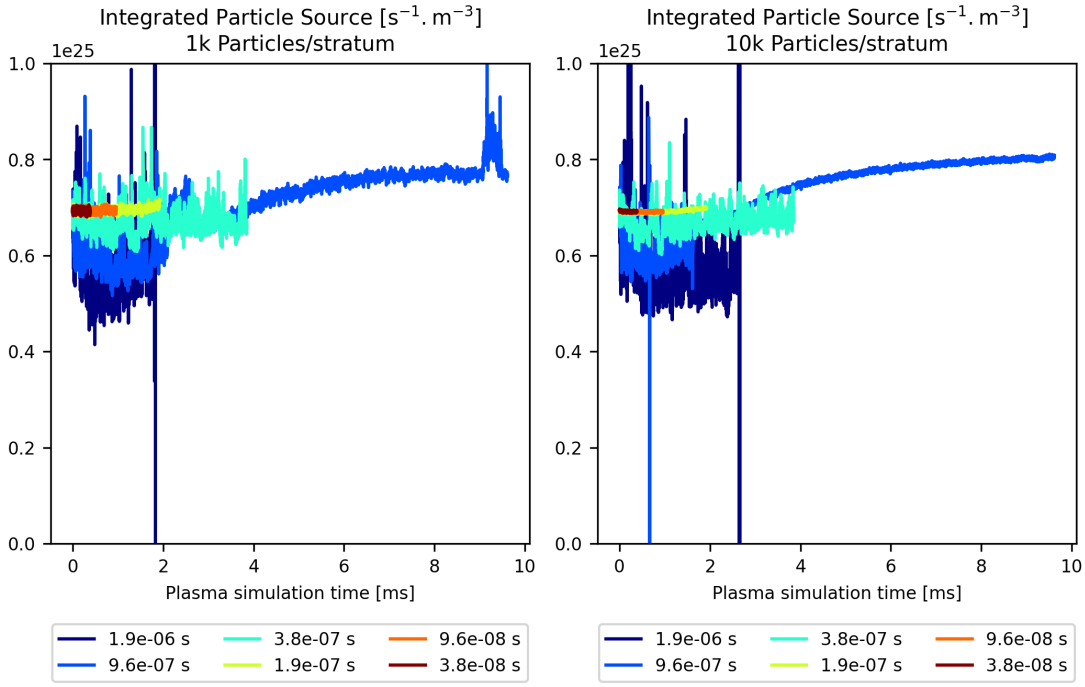

Figure D.2.: Impact of time step length, i.e., duration between EIRENE calls, on the time evolution of the volume integral of the deuterium D^+ particle source. The time step is scanned from 3.8×10^{-8}s to 1.9×10^{-6}s, for an FPO ITER case with Deuterium, Neon, and Helium on the coarse grid (6mm at the target). 10,000 time steps were performed in all cases, with an EIRENE call at each time step, for 1,000 particles (left) and 10,000 particles (right). The case at 1.9×10^{-6}s crashed after 2 ms, and the behavior is vastly changed for 9.6×10^{-7} s.

Oscillating regimes as an effect of mesh resolution In spite of the rapid convergence of the solution with the grid resolution, it is important to highlight that one may also encounter, in certain cases, issues with the ability of the code to find a stable converged solution when the grid is too coarse.

As an illustration, it was observed that for the FPO 100MW Deuterium-Neon-Helium case, the low-resolution coarse grid produces an oscillating regime, which was never observed in any of the pure-H 20MW runs. Figure D.3 shows the temporal evolution of the integrated particle source for two cases with the same number of EIRENE particles, same time step length, one on the coarse mesh which has a 6 mm poloidal resolution

at the targets, and one on a finer mesh, which has a 3 mm poloidal resolution at the targets. The coarser mesh shows oscillations that do not decay, with a period of around a period of 50 ms, while the more resolved mesh at 3 mm shows none for the same parameters. This illustrates what was shown in [65] and [66], i.e., the spatial discretization of the plasma solver can be the largest source of error if the grid is too coarse.

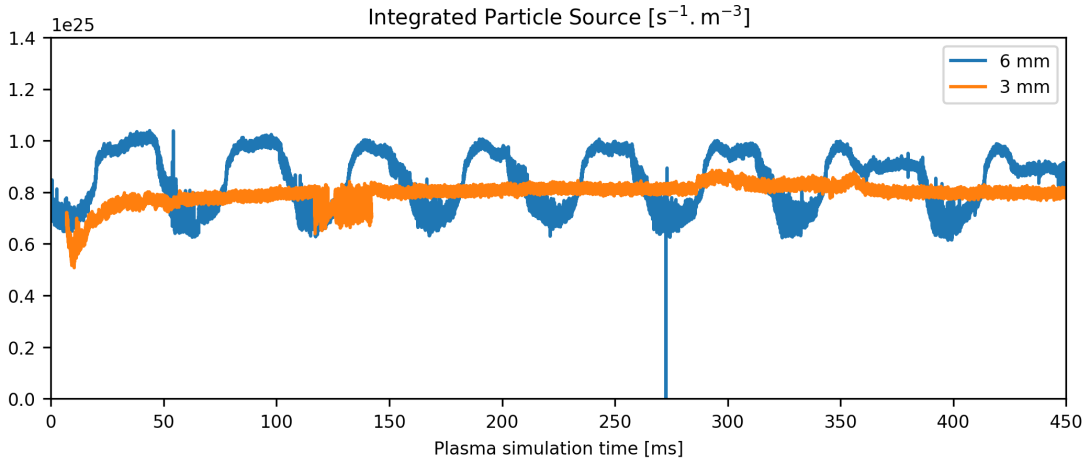

Figure D.3.: Temporal evolution of the integrated particle source from neutrals, for an FPO ITER case with Deuterium, Neon, and Helium, 1000 EIRENE particles per stratum, with a time step of $\sim 4 \times 10^{-7}$ s.

This way, the use of the multigrid approach cannot be made fully automatic and must be carefully monitored by the code user.

However, it is possible that in some cases, oscillations appear and are driven by physical phenomena, as is shown in [93]. Therefore, upon observations of oscillating divertor regimes, attention should be paid to investigating whether they are of physical or numerical nature.

E. Proof-of-concept for full power case at 100MW neon-seeded with helium ashes

Here in this section are presented some preliminary elements of the overall initial objective of the improvements of the SOLEDGE3X: reaching simulations of a target Q=10 plasma of ITER.

The work in this PhD included the implementation of all elements that were described chapter on the improvement of the model and the codes, however the remaining time was insufficient to bring those cases to convergence. Rather, in this section presents the plasma state roughly half-way until convergence, to show as a proof-of-concept that following this work, the code is now able to run such scenarios. Convergence should be reached in a few weeks.

At the time of writing the convergence levels (0% means converged) are for particles: D:~5%, Ne:50%, He:50%, and for total energy: ~0%. Thus, the results still show a "reasonnable" plasma, but should nevertheless not be taken as simulation results for the modelled case. Therefore, some elements in the following may appear surprising to the reader, which may be related to the unconverged state of the simulation at the present time.

E.1. Simulation setup

The simulation setup is similar that for other cases presented here, with the following changes:

- **Composition**: The plasma contains 3 elements: Deuterium as main species (Tritium is not included here), Neon for impurity seeding, and Helium ash from the fusion reactions.
  - **Electrons**:
    - Core input power: 50 MW
  - **Deuterium**:
    - Core input power: 50 MW
    - Gas injection rate: 4.9×10^{22} electrons/s
    - Core outflux: 9.1×10^{21} ion/s
    - Recycling coefficient of the pump: 0.9928
  - **Neon**:
    - Gas injection rate: 1×10^{21} electrons/s
    - Recycling coefficient of the pump: 0.9928
  - **Helium**:
    - Core outflux: 2.14×10^{20} ion/s at fixed 1800 eV

    - Recycling coefficient of the pump: 0.9928

- **Transport coefficients**: The transport coefficients is not uniform, and includes a transport barrier to model for the H-mode behavior. The values are taken identically as in [80], is shown as in Figure E.1.

The value of the neon seeding rate was chosen to match the SOLPS-4.3 case #122399 (which does not have the transport barrier), which was driven to have a neon impurity concentration (as defined by the ratio of element nuclei to electron density, averaged along the separatrix) of 0.6%.

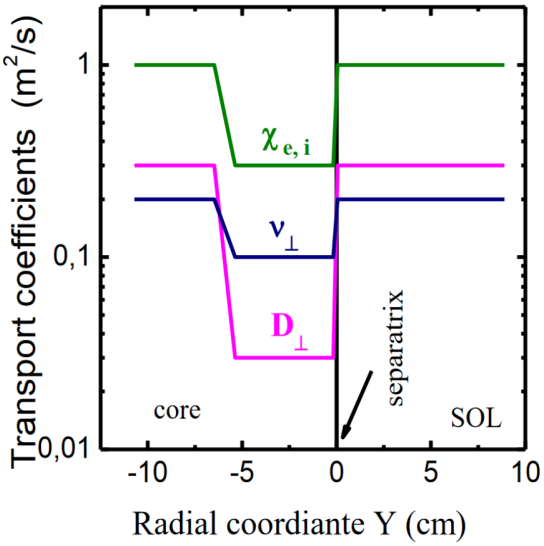

Figure E.1.: Assumptions on perpendicular transport coefficients for particles, momentum and energy for the FPO 100MW ITER case.

E.2. Plasma state

In Figure E.2 are shown the profiles of density and temperatures at the midplane, for each plasma species. Highly charged Neon species (Ne^{8+}, Ne^{9+}, Ne^{10+}) are obtained near and inside the separatrix, as expected. Ion temperatures of Neon species are quite close to each other,

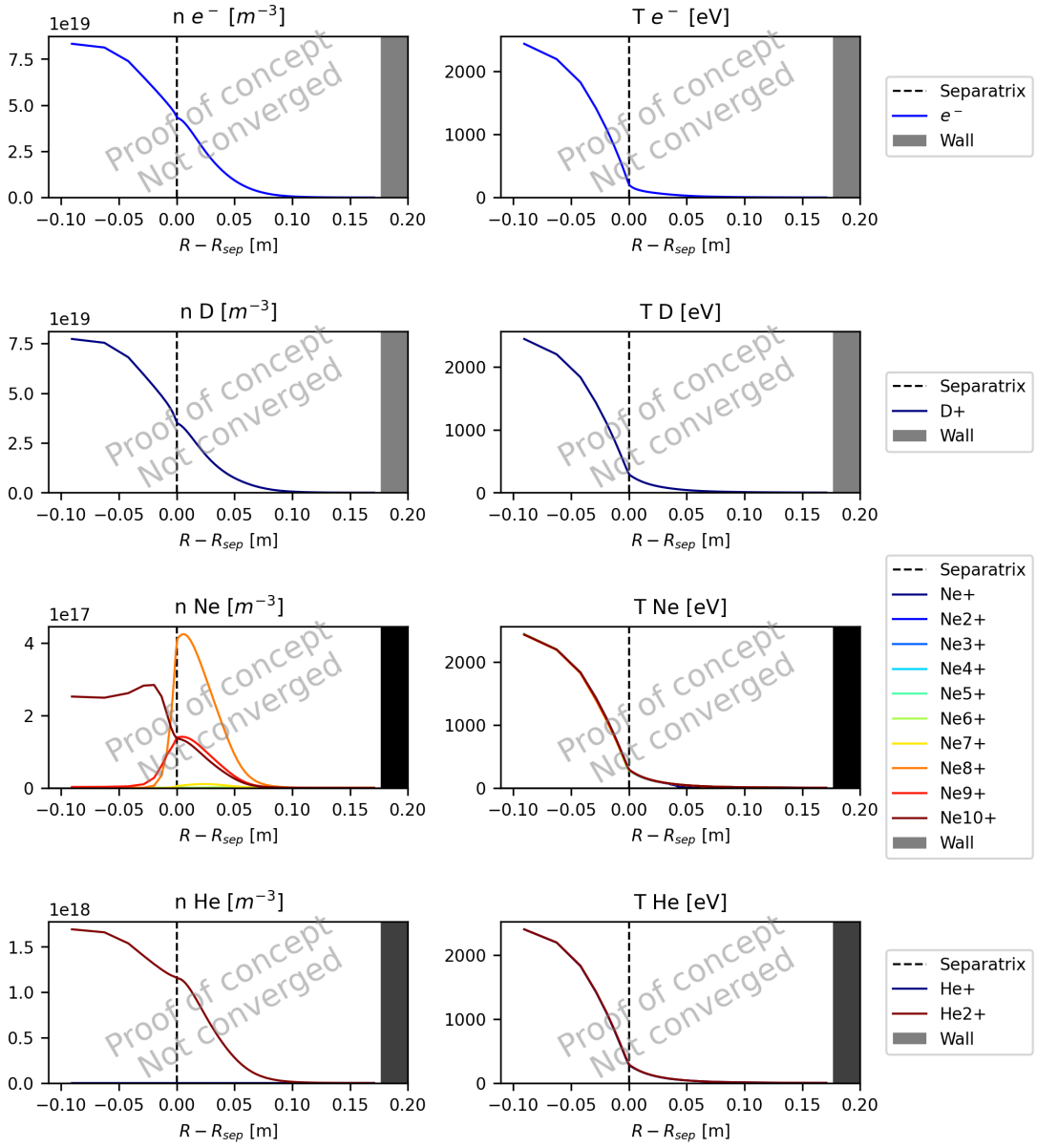

Figure E.2.: Outer midplane density and temperature profiles for species included in the FPO 100MW case

In the volume Figure E.3, a significant plasma density is obtained at the machine top near the secondary X-point. The neutral pressure at the divertor entrance is around 5 Pa.

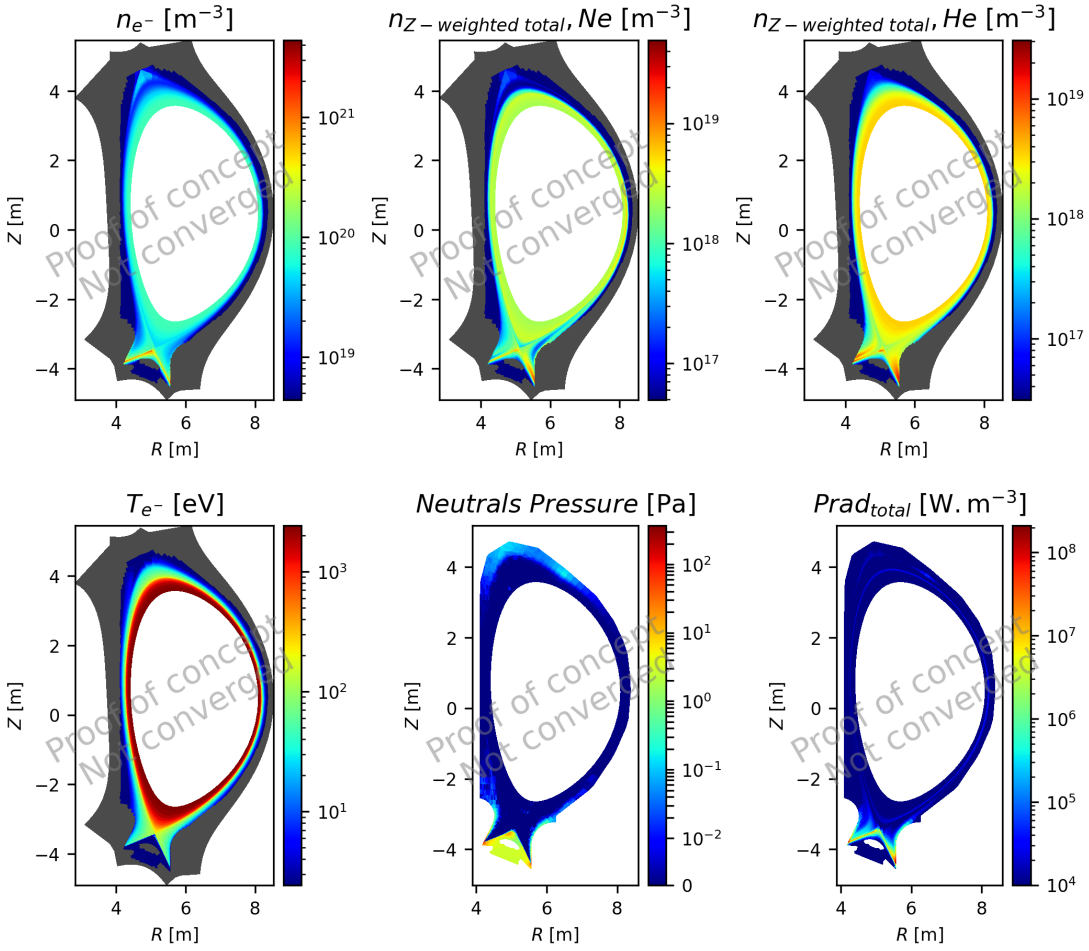

Figure E.3.: Electron density, total Neon and Helium Z-weighed density, radiated power and neutral pressure

Then turning to the targets Figure E.4, the obtained temperatures at the target are of the order of a few eV, i.e. lower than 10eV, and peak heat fluxes at around 7 and 8 MW/m², i.e. within the 10MW/m² design limits. A significant asymmetry is obtained, the inner target being around twice as dense and cold as the outer target.

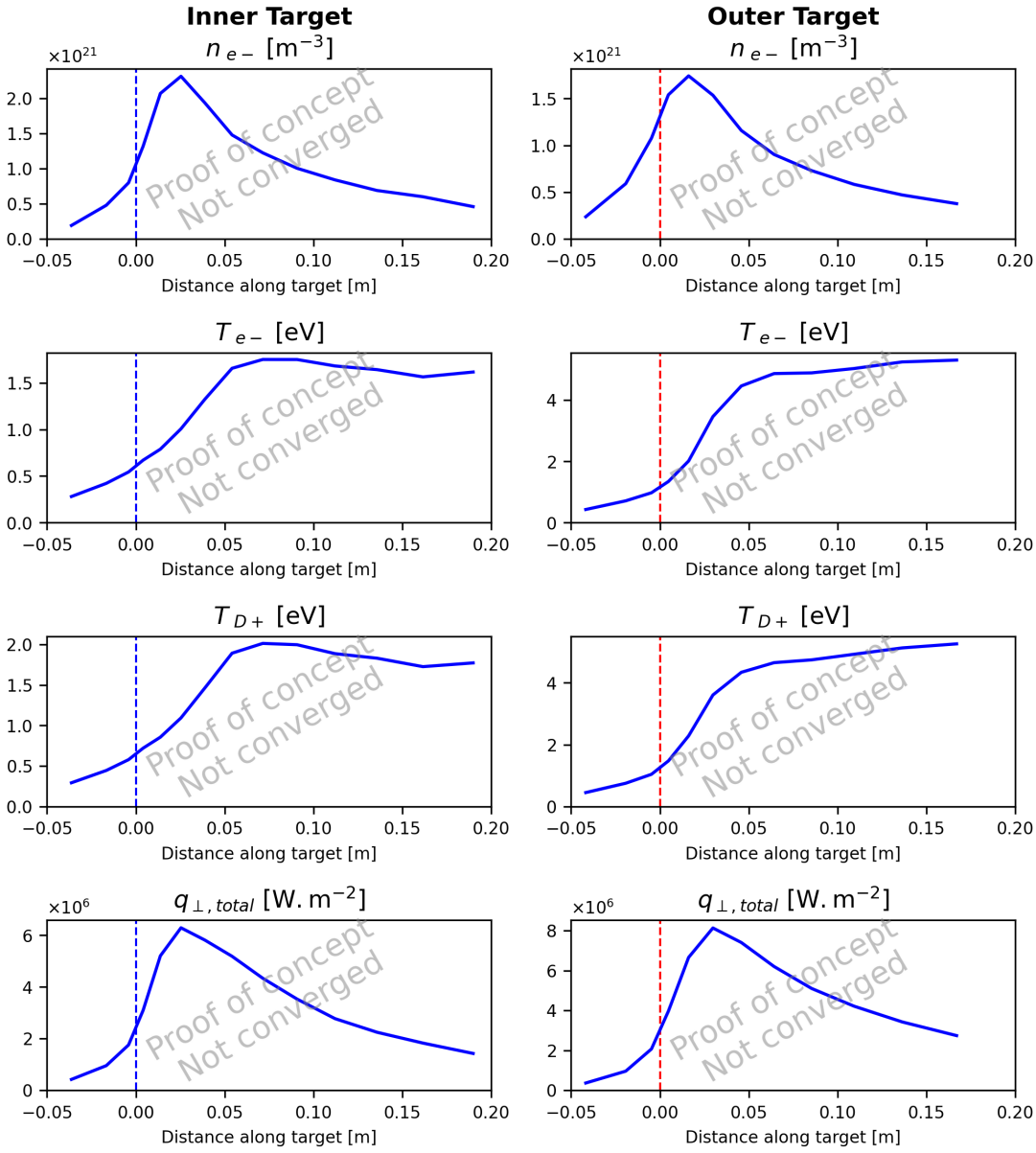

Figure E.4.: Plasma conditions and total power deposition at the outer target (top row) and inner target (bottom row)

Finally, across the first wall, ion and electron temperatures are within 1 to 10 eV. At the top of the machine, plasma density can reach 4×10^{19}[m^{-3}].

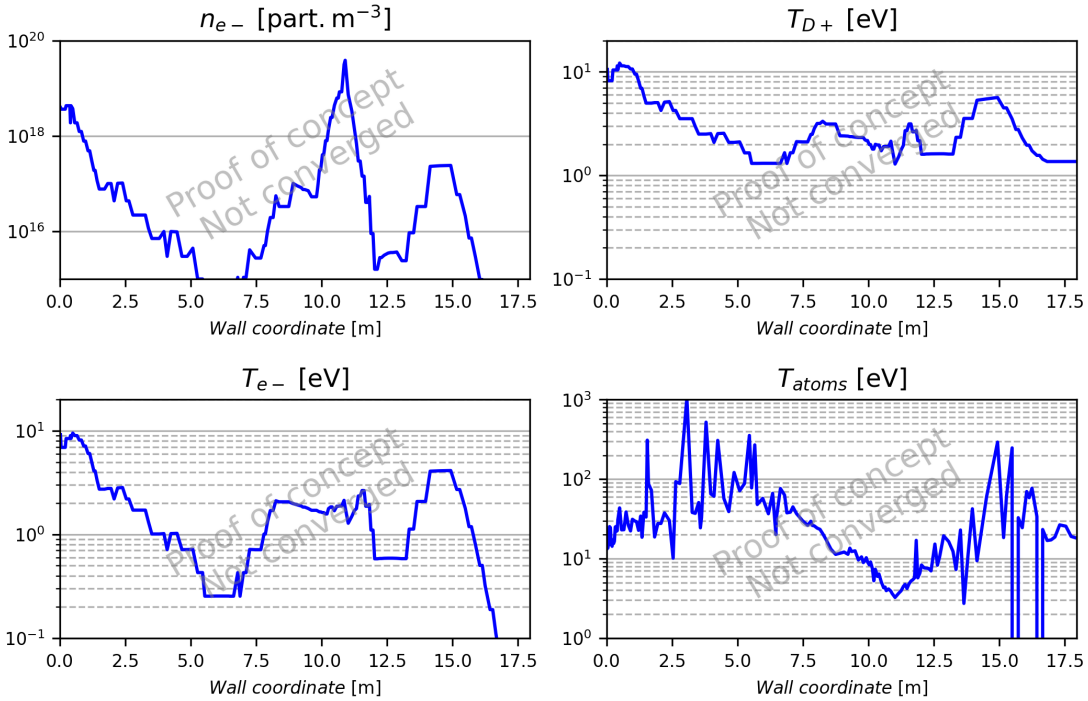

Figure E.5.: Plasma density temperatures, and charge transfer atoms average energy across the first wall

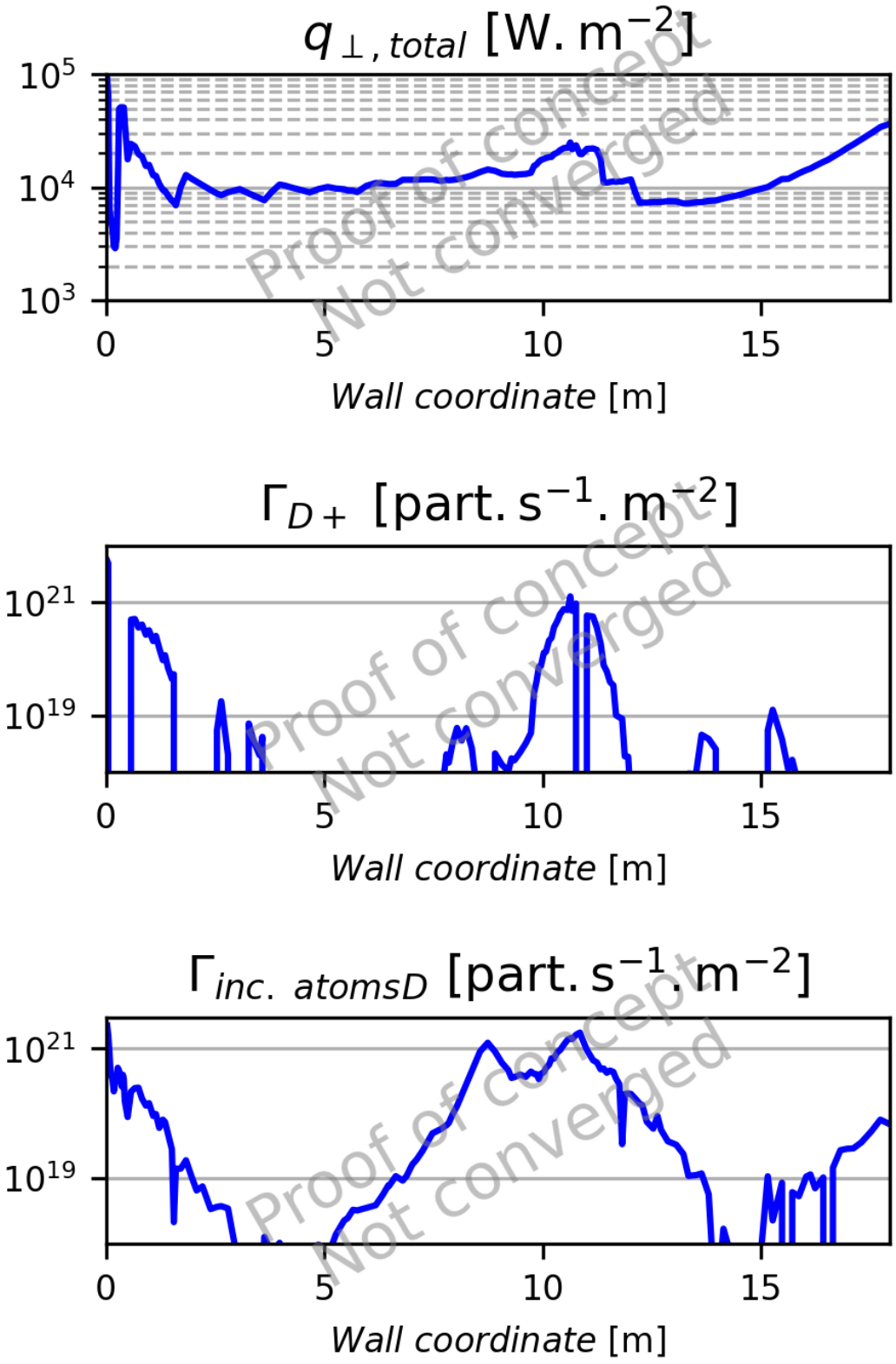

Figure E.6.: Total heat flux, ion particle flux, atom incident particle flux across the first wall

F. Computation of $\partial_{T_e} SE_{e-}^{RC}$

This section aims at computing the derivative w.r.t. T_e of the EIRENE electron energy source for the volumetric recombination reaction in units of W.cm^{-3}.eV^{-1}.

$$\frac{\partial SE_{e-}^{RC}}{\partial T_e} = -n_i n_e \frac{\partial}{\partial T_e}(\langle \sigma \upsilon E \rangle_{RC,cool}) e \tag{F.1}$$

It must be clarified here that in the AMJUEL database, the energy fit for the 3-body recombination is actually the **radiation rate $\langle \sigma \upsilon E \rangle_{RC,rad}$ and not the electron population cooling rate** $\langle \sigma \upsilon E \rangle_{RC,cool}$ as is the case for other reactions, and for the ADAS database. The reason for this is that the cooling rate can be positive (loss of energy for the electrons) at high temperature or negative (electron heating) at low temperature, while the database only contains log quantities that cannot represent signed quantities. The two quantities are related:

$$\langle \sigma \upsilon E \rangle_{RC,cool} = \langle \sigma \upsilon E \rangle_{RC,rad} - E_{iz} \langle \sigma \upsilon \rangle_{RC} \tag{F.2}$$

Where:

- $\langle \sigma \upsilon E \rangle_{RC,cool}$: Electron population cooling rate coefficient (convention: positive mean electrons lose energy) in eV.cm^3.s^{-1}. This is a signed quantity.
- $\langle \sigma \upsilon E \rangle_{RC,rad}$: Radiation rate coefficient (convention: always positive) in eV.cm^3.s^{-1}
- E_{iz}: Ionization energy of the considered atom in eV
- $\langle \sigma \upsilon \rangle_{RC}$: reaction rate coefficient in cm^3.s^{-1}

These coefficients are stored in log-log form in the AMJUEL database:

$$\frac{\partial}{\partial T_e}(\langle \sigma \upsilon \rangle_{RC}) = \frac{\partial (\ln T_e)}{\partial T_e} \frac{\partial}{\partial \ln T_e}(\langle \sigma \upsilon \rangle_{RC}) = \frac{1}{T_e} \frac{\partial}{\partial \ln T_e}(\langle \sigma \upsilon \rangle_{RC}) = \frac{\langle \sigma \upsilon \rangle_{RC}}{T_e} \frac{\partial}{\partial \ln T_e}(\ln \langle \sigma \upsilon \rangle_{RC})$$

Their representation consists in polynomials of order 8 in $\ln \tilde{n}_e$ and $\ln T_e$, with $\ln \tilde{n}_e = n_e / 10^8$, with n_e being expressed in cm^{-3} and T_e in eV. Let i the index of the reaction considered:

$$\ln(\langle \sigma \upsilon \rangle_i) = \sum_{k=0}^{8} \sum_{l=0}^{8} \alpha_{k,l} (\ln \tilde{n}_e)^k (\ln T_e)^l$$

$$\begin{aligned}\frac{\partial}{\partial \ln T_e}\ln\left(\langle\sigma v\rangle_i\right) &= \sum_{k=0}^{8}\sum_{l=0}^{8}\alpha_{k,l}\,l\,(\ln\tilde{n}_e)^k(\ln T_e)^{l-1}\\ &= \sum_{k=0}^{8}\sum_{l=0}^{8}\alpha_{k,l}\,l\,(\ln n_e-\ln 10^8)^k(\ln T_e)^{l-1}\end{aligned}\tag{F.3}$$

Similarly:

$$\begin{aligned}\frac{\partial}{\partial \ln n_e}\ln\left(\langle\sigma v\rangle_i\right) &= \sum_{k=0}^{8}\sum_{l=0}^{8}\alpha_{k,l}\,k\,(\ln\tilde{n}_e)^{k-1}(\ln T_e)^{l}\\ &= \sum_{k=0}^{8}\sum_{l=0}^{8}\alpha_{k,l}\,k\,(\ln n_e-\ln 10^8)^{k-1}(\ln T_e)^{l}\end{aligned}\tag{F.4}$$

We can then evaluate these in $n_e = n_e^0$ and $T_e = T_e^0$, and we note, where "primed T" quantities represent the derivatives w.r.t. T, the ^{0} represent the direct coefficients:

$$\begin{aligned}R_i^0 &= \langle\sigma v\rangle_i(n_e^0, T_e^0)\\ R_i'^T &= \frac{\partial}{\partial \ln T_e}\ln\langle\sigma v\rangle_i(n_e^0, T_e^0)\\ R_{E,i}^0 &= \langle\sigma vE\rangle_i(n_e^0, T_e^0)\\ R_{E,i}'^T &= \frac{\partial}{\partial \ln T_e}\ln\langle\sigma vE\rangle_i(n_e^0, T_e^0)\end{aligned}$$

The final expression for the derivative is then:

$$\frac{\partial SE_{e-}^{RC}}{\partial T_e} = n_e n_i\left(-\frac{R_{E,RC}^0}{T_e}R_{E,RC}'^T + E_{iz}\frac{R_{RC}^0}{T_e}R_{RC}'^T\right)e\tag{F.5}$$

G. Source rescaling procedures ("short-cycling")

In this section we discuss matters regarding the coupling of the EIRENE kinetic neutral code, which computes the sources of particles, momentum, and energy for plasma species (ions and electrons), which are used by the SOLEDGE3X plasma solver. This topic is of particular importance for two reasons: strong neutral sources increase the potential for instabilities, the neutral sources computation is the main driver of the run time. The EIRENE code is a Monte Carlo solver, which is quite expensive in terms of computation time (1 EIRENE call is of the order of the second), and this part completely dominates the total computation time. This is especially the case in cold and dense regions where tracked neutrals can undergo a very large number of collisions before being ionized or pumped. As a consequence, any improvement on this section will have a very large impact on the total computation time.

One of the key characteristics of the coupling of SOLEDGE3X with EIRENE, is that the sources returned by EIRENE are fully explicit in the SOLEDGE3X numerical scheme, which, as can be expected by the strength of plasma-neutral interaction processes, will pose numerical stability challenges.

An initial (and more precise) numerical approach would be to update the neutral sources at each time step of the run. This would require running EIRENE at each plasma time step, as since the computation of a full Monte Carlo is of the order a few seconds, the computation time becomes quickly unmanageable if the plasma solver time step (i.e. simulation time step) is too small. Therefore one of the main features of the coupling between SOLEDGE3X and EIRENE, is the capability to skip the full and expensive Monte Carlo calculation for a certain number of time steps, and make certain sets of assumptions on neutrals until the next EIRENE call. This approach is motivated mainly by the assumption that the response time of the plasma sources from neutrals (the EIRENE sources) is much longer than the evolution time of the plasma, which is the plasma solver time step. For how long the sources from neutrals sources remain valid is a key question to the computation time challenge, and is the main focus of the next section. The time steps, or "cycles", during which EIRENE is not called, and other assumptions are used to extrapolate the evolution of sources without requiring a full EIRENE run, are referred here as "short cycles". This section will discuss these sets of assumptions for the short cycling scheme used in SOLEDGE3X.

The extrapolation schemes for the sources in short-cycles can be understood by looking at the formulation of such sources:

$$S_X = \underbrace{\langle \sigma v \rangle_{i_{reac}} n_{\alpha_b}}_{①} \; \underbrace{n_{\alpha_t}}_{②} \; \underbrace{\delta X_{i_{reac}}}_{③} \tag{G.1}$$

Where:

- S_X is the volume source of quantity X (i.e. particles, momentum, or energy)
- $\langle \sigma v \rangle i_{reac}$ is the reaction rate coefficient of the reaction index i_{reac}, reaction

between particles of species α_b and α_t

- n is the particle density
- α_b is taken as the incident particle type that is from a "bulk" species, in the sense of a species described by fluid quantities. This will be in many cases (but not all) the electrons.
- α_t the species of the so-called "test" incident particle, which is treated kinetically by EIRENE during Monte Carlo particle tracking. This will be in many cases neutral particles.
- $\delta X_{i_{reac}}$ is the elementary plasma source of X for each occurrence of this reaction.

The coupling interface between the codes allows for different treatments the plasma sources from neutrals during the short cycles, depending on which of the above ①, ②, ③ terms are updated during each short cycle. At the moment, the code includes 3 "short cycling" schemes:

1. "Constant" mode
2. "Rescaled" mode
3. "Updated" mode

G.0.1. "Constant" mode

This mode is activated in SOLEDGE3X by setting the short-cycling mode parameter `sc_mode = 1` *in the eirene_coupling.txt parameter file.*

In this mode, none of the ①, ②, ③ terms are updated.

Advantages This is the most simple mode, under which all particle, momentum, and energy sources remain constant during the short cycles. The assumption here is that the complete sources does not change too much during short cycling. This mode also has the advantage of using EIRENE's output as is, without any need for post processing or recomputation, and therefore is fully independent of the choice of reactions that is used in EIRENE's databases.

Limitations This was found to be sufficient for SOLEDGE3X runs for devices other (i.e. smaller) than ITER, and using a simplified atomic and molecular model, which is not used in the context of this work. For ITER cases, the strength of these sources is such that this mode led to numerical instabilities on temperature and parallel velocity, when used for more than a few time steps. Additionally, for ITER cases, using this mode was found to produce a wrong solution, because of the introduction of a bias on the particle balance. The initial issue with this mode is that it breaks the particle

conservation: for the recycling mechanism, the sources returned by EIRENE are based on the amount of plasma flux outgoing to the wall at the time step where EIRENE is called. This plasma flux is given by the plasma solver, and so evolves at each time step. However during the short cycles, the sources do not change, while the plasma wall flux does. Therefore the total number of neutrals, which are either deposited on the plasma after ionization or pumped, does not match the particle flux received by the wall, leading to artificial creation or destruction of particles. This was found to nonphysically fill the machine with artificially created particles, because the plasma outflux would systematically decrease after an EIRENE call, and then increase again over the course of the next time steps, so the wall flux would have a large probability to stay below the flux used in the Monte Carlo for a period of time. The reason for this systematic decrease is not understood at the moment, but this motivated the use of the next modes, which conserve particles.

G.0.2. "Rescaled" mode

This mode is activated in SOLEDGE3X by setting the short-cycling mode parameter `sc_mode = 6` *in the eirene_coupling.txt parameter file.*

The objective of this mode is to ensure particle conservation to address the issue left out by the previous "constant" mode. This mode is similar to the one that was implemented in SOLPS to enable particle convergence of Helium impurities and mentioned by Kukushkin et al. in [94]. In the following paragraphs, we refer as "primary source" the amplitude of the neutral particle source linked to a mechanism that generate neutrals tracked by EIRENE, These mechanisms are defined in more details below, in the "stratum" section. In this mode, the neutral densities ② are updated by a rescaling factor to account for the overall integrated variation of the primary source. The underlying assumptions are that the spatial distribution of both the primary sources (e.g. the plasma wall flux is still deposited at the targets) and the resulting plasma sources in the volume do not change much. The per-particle reaction rates ① are assumed constant. The EIRENE Monte Carlo solver computes the density of neutrals as the response rescaled by the integral of the primary source, as explained in the EIRENE documentation [37].

$$S_X = \frac{s}{V_m N} \sum_{i=1}^{N} X_g(\omega_i) \tag{G.2}$$

$$s = \int d^3r d^3v dt S_p(\mathbf{r}, \mathbf{v}, t) \tag{G.3}$$

With V_m the cell-volume is space-time, N the number of sampled particle histories ω_i, and S_p the primary source density in phase space, and X_g an unbiased estimator of the detector function g which is chosen adequately to compute the desired source S_X. It follows then that the plasma source computed has a linear dependency in the integral of the primary source s, which justifies that a rescaling of the sources map by

the relative variation of s is a relevant approximation.

EIRENE uses a "stratified sampling" technique, which is used to decompose the calculations of plasma sources deposited by neutrals depending on the mechanism that has initially generated these neutrals: their "primary" source. The advantage of such a decomposition is that the final source is computed by simply summing the contributions from all strata, and each one of these contributions has a linear dependency in the primary source integral amplitude. For the simulations we consider, there are three types of primary sources, or "strata":

1. The recycling stratum: the neutrals generated by recombination of the plasma outflux to the wall, which recombines there, and is reinjected as neutrals in the chamber from the wall.

2. The recombination stratum: When the electron temperature decreases below 1 eV, plasma starts recombining into atoms, and this process generated neutral atoms that are sampled and tracked directly from the simulation volume (vs. from the wall for the recycling stratum)

3. The gas puff stratum: neutrals generated constantly at the point indicated as gas puff location (here at the top of the machine).

From this description of the intensity of the primary source of each stratum, it is possible to ensure particle conservation even during short cycling through rescaling of the last plasma sources returned by EIRENE. Let us now detail for each stratum the followed procedure.

First, we define the plasma sources from the interaction with neutrals returned by EIRENE.

- $S_X^t(i_{cell})$ is the plasma source for any X quantity (X=n/m/E for particles/momentum/energy) in the cell number i_{cell} at any time t during the short cycling

- $S_X^{MC}(i_{cell})$ is the plasma source for any X quantity (X=n/m/E for particles/momentum/energy) in the cell number i_{cell} at the time of the last Monte Carlo call

Recycling stratum:
The primary source is the integral of the plasma wall flux.

$$S_X^t(i_{cell}) = S_X^{MC}(i_{cell}) \frac{\Gamma_{TOT}^t}{\Gamma_{TOT}^{MC}} \tag{G.4}$$

Where:

- Γ_{TOT}^t is the total wall particle flux at any time t during the short cycling

- Γ_{TOT}^{MC} is the total wall particle flux at the time of the last Monte Carlo call

Recombination stratum:
The primary source is the integral of the recombined plasma into atoms, generated in the volume. It must be emphasized that in the case of the recombination stratum this source S_X is not the total source for the plasma, it is the plasma source deposited by the neutrals that have been generated by the recombination, but does not include the plasma particles/momentum/energy lost by the process of recombination itself, which is called $S_{X,RC}$ here, and has to be added on top of the former before being passed to the plasma solver.

$$S_X^t(i_{cell}) = S_X^{MC}(i_{cell}) \frac{\int_{cells} S_{n,RC}^t}{\int_{cells} S_{n,RC}^{MC}} \tag{G.5}$$

$$S_{n,RC} = n_e n_i \langle \sigma v \rangle_{RC} \tag{G.6}$$

Where:

- $S_{n,RC}$ is the volume recombination rate, i.e. the volume rate of generation of atoms in each cell
- $\langle \sigma v \rangle_{RC}$ is the recombination rate coefficient, read from the atomic and molecular database AMJUEL.

This mode however has a special behavior for this stratum: to enable this rescaling, the $\langle \sigma v \rangle_{RC}$ rate coefficient is updated at each time step in the short cycling. No other reaction rate coefficient is updated in this mode, which is the main difference with the "Rates-updated" mode. A choice could have been made to not update/rescale the recombination stratum in this mode, however, seeing the importance and sensitivity of the recombination in ITER cases as will be discussed later, this behavior produced an additional layer of stability.

Gas puff stratum:
The primary source is simply the gas puff rate. It may only need rescaling when this rate is not constant throughout the run, for example in the case of feedback scheme to reach a desired other parameter. The rescaling factor is the ratio of the gas puff at Monte Carlo call to the current gas puff rate.

Advantages This mode is still relatively simple in its concept, as the sources only vary by scaling factors, while retaining spatial distributions. It also conserves particles, and is still independent of the type of reactions in the database.

Limitations While particle sources in this scheme do not pose stability issues, the limitations are related to momentum and energy sources, which can produce numerical instabilities. Neutral-plasma interactions usually produce strong friction forces against the plasma flow, which are only rescaled via an integral on particle, therefore its sign will not change. Therefore, if such source is kept for too long, an

inversion of the local plasma velocity can occur in cells, while still having a decrease in energy. The amplitude of the velocity can even grow indefinitely after having changed sign. This issue arises because the per-collision momentum and energy exchange ③ term is not updated. This is addressed in "Updated" mode below.

G.0.3. "Updated" mode

This mode is activated in SOLEDGE3X by setting the short-cycling mode parameter `sc_mode = 3` *in the eirene_coupling.txt parameter file.*

This mode is the most complex extrapolation scheme. Here the per-particle reaction rate ①, the test particle densities ②, and per-collision elementary exchange ③ are updated. Only the spatial distribution of the neutrals are assumed constant. This requires re-computation of all sources from all reactions from fluid quantities (or other moments) outside EIRENE. The computation is as follows:

- Rescale the neutrals density fields with the primary source amplitude (see "rescaling" mode)
- Update the reaction rate coefficients from the reaction databases using updated T_e, T_i, n_e and n_i from the plasma solver.
- Fully recompute the sources from all reactions, with updated per-collision exchange quantities.
- Rescale once again the newly obtained sources to ensure particle conservation

The first step is similar to the "rescaling" mode, but applied to the neutral densities.

The second step, where we update the reaction rate coefficients, involves some external re-use of EIRENE's routine to read from the database using the updated plasma parameters at the current time step. In that process, a specific point is non trivial and needs special care: updating rate coefficients for reactions that have fits which depend on the kinetic energy of the tracked neutral. This is the case for the molecule-ion elastic collisions and the atom charge-exchange (H.3 fits). The short cycle procedure is not kinetic in nature and can only handle moments of the distribution functions as produced by EIRENE, therefore some assumption has to be made: the fits are recomputed using a velocity computed from the average neutral kinetic energy in the cell, and its average direction, which are both moments available in EIRENE output.

The third step, the full re-computation of sources, proceeds as follows, by summing

over all reactions:

$$
\begin{aligned}
S_n^t &= \sum_{i_{REAC}} n_{ispec_1} n_{ispec_2} \langle \sigma v \rangle_{i_{REAC}} \\
S_m^t &= \sum_{i_{REAC}} n_{ispec_1} n_{ispec_2} \langle \sigma v \rangle_{i_{REAC}} \delta m_{i_{REAC}} \\
S_E^t &= \sum_{i_{REAC}} n_{ispec_1} n_{ispec_2} \langle \sigma v \rangle_{i_{REAC}} \delta E_{i_{REAC}} \\
&or \\
S_E^t &= \sum_{i_{REAC}} n_{ispec_1} n_{ispec_2} \langle \sigma v E \rangle_{i_{REAC}} \text{if this data is available in databases}
\end{aligned}
$$

In some case, special attention is required to $\langle \sigma v \rangle_{i_{REAC}} \delta m_{i_{REAC}}$ and $\langle \sigma v \rangle_{i_{REAC}} \delta E_{i_{REAC}}$ terms. For inelastic collisions, when one of the incident particle is consumed, computing these terms can be done simply by adding or subtracting the fluid moment of momentum or energy of the involved plasma particles or neutrals. However, for elastic collisions or reaction whose collision characteristics depend on the neutral velocity (such as the atom charge exchange), this term can not be computed a posteriori because the distribution of the neutrals velocity is not saved. In these cases, they are computed as the average momentum and energy exchange, i.e. the total reaction source returned by EIRENE divided by its number of reactions.

Now, a second level of care needs to be taken at this stage for these rates: since they cannot be computed a posteriori, this means an assumption on their evolution during the short-cycling procedure has to be taken. The option to assume them constant was found to be unstable, because these two reactions are very large contributors to the overall sources, and, as momentum source, they can produce flow reversals if kept for too long. This happens when a strong friction force with the neutrals is maintained as is, the flow velocity will not converge to zero, it will decrease then be accelerated on the other direction indefinitely. Therefore, it was found crucial for the stability of the code to rescale them via the parallel velocity of the plasma (when it is above a certain threshold to avoid instabilities) between the Monte Carlo call and the current time step. For the energy, the square of that scaling is used. One could note that only the parallel velocity of the plasma is used for this rescaling, and not the difference between the parallel velocity of the plasma and the neutrals, which would be expected for generic friction forces. Indeed, it was found that in some cells, the resulting momentum source as computed by EIRENE after the Monte Carlo run, was not in the direction that a friction force would have if computed from the difference between the plasma and neutral parallel fluid velocities, therefore this approach would produce instabilities. The reason for this behavior is not clear, whether it is from special cases in the distribution of neutrals, or unlucky statistical sampling.

Finally, the last source rescaling step is needed because when all sources were recomputed, any value of the reaction rates coefficients can be obtained from the databases without constraint, and would break particle conservation. At this stage,

the integral of the new particle source is computed for each stratum, then, assuming the ratio between the pumped particles and the primary source for each stratum is constant, the scaling factor is computed so that the integral of the particle source matches the new primary source adjusted by the pumping ratio. The same scaling factor is applied to momentum and energy.

A small note has to be made here on the Fokker-Planck slowing of ions against "test" ions tracked by EIRENE: this reaction does not appear in the reaction set, but is automatically added to create a momentum and energy loss for the plasma as soon as "test" ions are tracked by EIRENE. This is not the case if they are in the "static" approximation, which consists in assuming that their transport can be neglected because of their short life time and is the approximation made in SOLPS-ITER simulations. This assumption is not made in SOLEDGE3X because it was found to generate spikes in the particle source map, and therefore a specific tally for the Fokker-Planck term had to be created (its reaction number is NREACI+1).

Advantages This mode is the most stable, as both reaction rates and momentum and energy per-collision exchanges are updated with the new plasma fields.

Limitations This mode is most complex to implement and requires significant development work for proper recomputation of all sources for all reactions. It is also highly dependant on the type of reaction used: for reactions that depend on the velocity of the tracked particles, such as elastic collisions, or exchanges which take into account the energy in the computation of the cross section, the computation of specific moments (or "tallies" in EIRENE language) have to be implemented for each of them.

G.0.4. Choice of "Rates-updated" mode for ITER runs, and limitations

The chosen mode for running ITER cases has been the "Rates-updated" mode, because it is the most stable, due to the update of the reaction rate coefficient, which are by far the most sensitive variable. This enables in particular to account for changes in T_e that drives strong changes at low temperature. However, the stability vanishes as soon as the change in rates coefficients are too severe, leading to a very different particle source integral.

Let us consider an example of this behavior which comes from the combination of the ion molecule charge exchange and the atom charge exchange reactions. In regions below the separatrix legs in the divertor, the plasma gets colder, and get actually reheated by atom charge exchange from the atoms that have themselves undergone a charge exchange with the very hot portion of the plasma that is just above. The plasma energy source from neutrals is positive in this case, the ion temperature rises. However, the rate coefficient of the molecule charge exchange (ion conversion) that consumes one ion and produces a molecular ion H_2^+ and an atom, has as very sharp positive slope in T_i in this temperature range. The ion consumption rate will strongly increase, reducing in turn the total plasma source integral. Then, at the second rescaling step,

the scaling factor gets large to compensate for that particle source reduction, and is also applied to the energy source, which is already positive and heating the ion. This positive feedback loop leads then to an ion temperature blow-up, that is only avoidable by executing again a full EIRENE call.

It is difficult to anticipate in advance how often it is necessary to call EIRENE to avoid such type of behaviour. A safe choice for robustness would consist in reducing to a minimum value the number of short-cycling steps between EIRENE calls, but this can prove extremely and unnecessarily costly in terms of computing time when difficulties arise only in transient phases of the simulation. In order to find an adequate compromise between robustness and rapidity, one has to design a scheme in which the frequency of EIRENE calls is determined automatically based on current plasma conditions. Such a scheme has been designed and implemented in SOLEDGE3X. We describe this in the next section.

H. pySOLEDGE3X post processing & visualisation package and its GUI

In this section, we present a high-level overview of the Python package and a Graphical User Interface (GUI) that was developed in the context of the present work for post-processing and plotting of the code's outputs. It is located on SOLEDGE3X's git repository. It actually includes two components: a Python package to be loaded as a Python module, "pySOLEDGE3X", and a pyQT5 GUI, which uses this package. It is also available as a pre-packaged standalone binary executable for Linux (used on the ITER and MARCONI clusters). It consists of a "pre-processor" to load the raw data and transform it into a physics-oriented data model similar to IMAS in philosophy, a post-processing layer, and plotting routines. The GUI is based on those and offers a way to call those functions in a quick, user-friendly way.

H.1. Pre-processing

The data structure is based on mesh+fields couples, where 4 "plasma" types exist. Below in Figure H.1 is presented an overview of the data model.

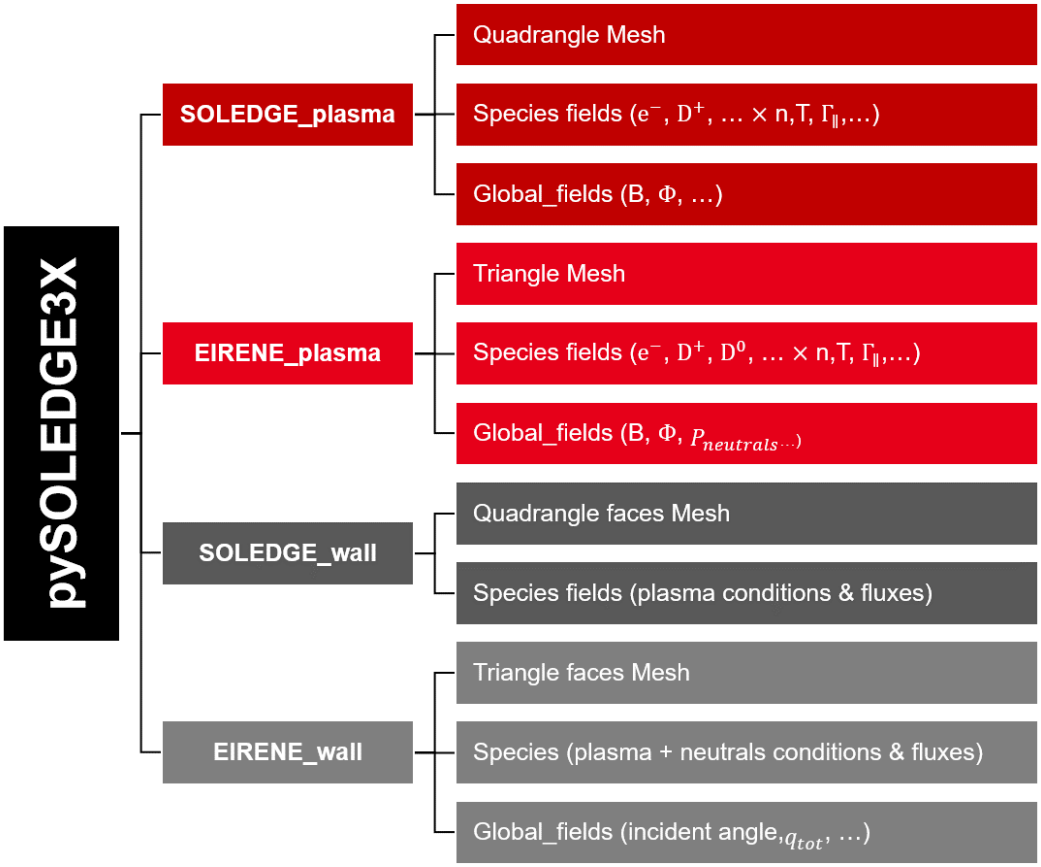

Figure H.1.: Overview of the Python pySOLEDGE3X package data model.

It includes four plasma container types:

- Volume "plasma" containers:
    1 SOLEDGE (quadrangles)
    2 EIRENE (triangles)
- Wall (surfaces) "plasma" containers:
    3 SOLEDGE (Quadrangle faces)
    4 EIRENE (triangle faces)

Each plasma object structure contains the associated mesh data, species-independent fields, and species-related fields (with space + time dimensions). All data is denormalized and in SI units. Field objects have their own attributes (unit, short name, LaTeX name, presence of ghost cells, volume or flux field, and the direction of flux...).

H.2. Post-processing

Additional calculated fields based on the code raw output are made available:

- Plasma sound speed
- Mach number
- Parallel velocity
- Thermal energy
- Neutral pressure
- Kinetic energy
- Parallel flux fields
- Flux expansion
- Particle and Energy balances
- Convergence levels
- Integrals (volume, over wall segments)

H.3. High-level operations

High-level operations are implemented on `Field` objects for convenient field-wise operations:

- Addition, subtraction, multiplication, division, power.
- Field slicing (triangle, psi, theta, phi, time)
- Type plasma conversion/interpolation (e.g. triangles -> quadrangles)

Example for computing and plotting the electron pressure:

```
ne = simulation.SOLEDGE_plasma.species["e-"]["n"]
Te = simulation.SOLEDGE_plasma.species["e-"]["T"]
pe = ne * Te
simulation.plotter.SOLEDGE_plotter.plot_outer_mid_plane(pe, matplotlibAxis)
```

H.4. Plotting

Each of the plasma object has its own associated plotter object, which can produce a set of specific plots to this plasma. For example: For SOLEDGE plasma plots:

- 2D plot
- Radial profile
- Outer mid plane profile
- poloidal profiles

For EIRENE wall plasma plots:

- Color coded wall contour in 2D
- 1D plots for the whole wall.
- Inner/Outer target plots

All plotter functions take a `Field` of the corresponding type as input

H.5. GUI

A Graphical User Interface is available to enable quick and no-code visualisation.

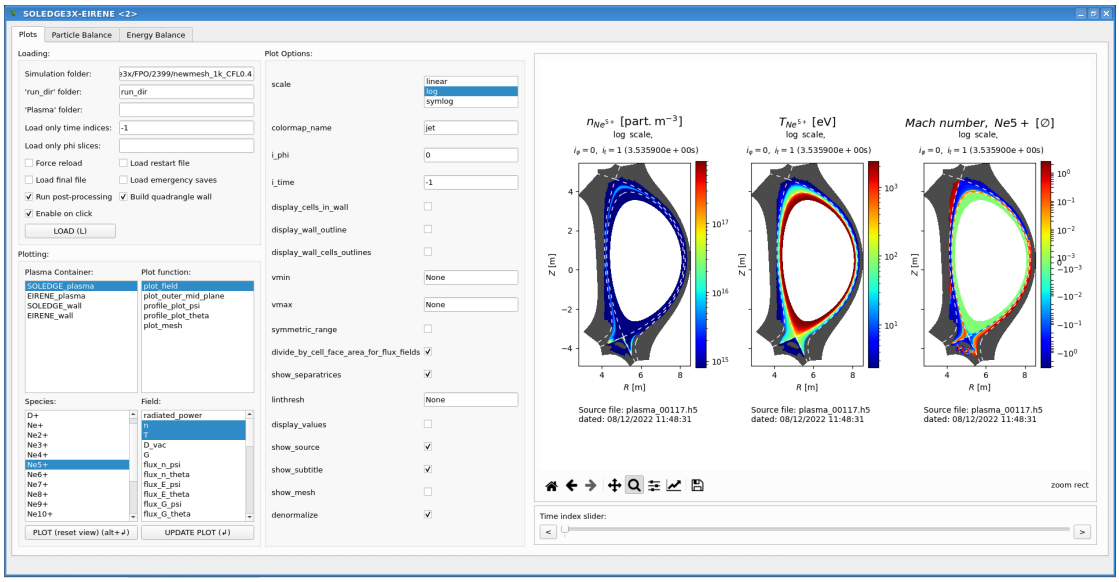

Figure H.2.: Example of plots from the GUI